

## Boundary Layer Response to Combustion Instabilities and Associated Heat Transfer

Dipl.-Ing. Daniele Panara

Deutsches Zentrum für Luft- und Raumfahrt e.V.  
Institut für Verbrennungstechnik  
Stuttgart



**DLR**

**Deutsches Zentrum  
für Luft- und Raumfahrt e.V.**

in der Helmholtz-Gemeinschaft



# Boundary Layer Response to Combustion Instabilities and Associated Heat Transfer

A thesis accepted by the Faculty of Aerospace Engineering and Geodesy of the  
Universität Stuttgart in partial fulfillment of the requirements for the degree of  
Doctor of Engineering Sciences (Dr.-Ing.)

by

**Dipl.-Ing. Daniele Panara**

born in Guardiagrele

main referee: Prof. Dr.-Ing. M. Aigner

co-referee: Prof. Dr.-Ing. J. von Wolfersdorf

Date of defence: 24.03.2010

Institute of Combustion Technology for Aerospace Engineering  
Universität Stuttgart

2010



# Acknowledgments

Most part of the present work has been undertaken within the collaborative research project FLUISTCOM (Fluid-Structure Interaction in Combustion Chamber Applications) under the founding of the European commission during the 6th Framework Program. For this reason I would like to thank the European Community that allowed me to research and travel among all the partners of the FLUISTCOM research training network: CERFACS, CIMNE, Queen's University of Belfast, Siemens, University of Twente and DLR as my host research institute. Especially I want to thank all the nice people that supervised me at the DLR Institute for Combustion Technology in Stuttgart: Dr. Robert Dannecker, Dr. Berthold Noll, Prof. Manfred Aigner and Prof. von Wolfersdorf from the University of Stuttgart who accepted to be the co-referee of my work. A more personal thanks goes to all the other people who were close to me in the every day life at the institute and outside: Francesca Rebosio, Karina Nold, Massimiliano di Domenico, Stefan Werrer, Elizaveta Ivanova, Jutta Lotz, Martin Liu and Patrick Le Clerq with his wife Tiffany and his fantastic son Nicola. A special thanks goes to Sini Pöyhönen for the love and support she gave me in this and all the other nice adventure we had together across Europe. I want to thank also my friends in Florence and Grazia who shared with me the difficulties of working and studying during the PhD thesis finalization in Italy. The last thank, but the more important one, goes to my family and especially to Nonna Augusta for the support they are able to give me just with their strong presence in my heart.



# Contents

<b>Acknowledgments</b>	<b>2</b>
<b>List of Figures</b>	<b>7</b>
<b>List of Tables</b>	<b>13</b>
<b>List of Symbols</b>	<b>15</b>
<b>Zusammenfassung</b>	<b>19</b>
<b>Abstract</b>	<b>21</b>
<b>1 Introduction</b>	<b>23</b>
<b>2 Industrial Burner Simulation and Heat Load</b>	<b>29</b>
2.1 Introduction . . . . .	30
2.2 ITS Test Rig . . . . .	30
2.3 CFD Set-up and Comparison with Previous Calculations . . . . .	31
2.4 Results and Comparison . . . . .	34
2.5 Conclusions . . . . .	40
<b>3 Conjugate Heat Transfer Modeling</b>	<b>43</b>
3.1 Introduction . . . . .	44
3.2 Code Description . . . . .	44
3.3 Code Validation . . . . .	45
3.4 Conclusions . . . . .	48
<b>4 Thermo-Fluid Dynamics Problem: Fundamental Equations</b>	<b>49</b>
4.1 Stability of the Fundamental Equations and Transition to Turbulence . . . . .	51
4.2 URANS - Unsteady Reynolds Averaged Navier-Stokes Equations . . . . .	52
4.3 Turbulent Boundary Layers: the Law of the Wall . . . . .	55
4.4 Turbulence Modeling . . . . .	57
4.5 LES - Large Eddy Simulation . . . . .	68
<b>5 Simple Channel and Pipe Configuration: Analytical Laminar Solutions and Turbulent Flow Correlations</b>	<b>71</b>

5.1	Laminar Channel Flow . . . . .	72
5.2	Laminar Pipe Flow . . . . .	77
5.3	Steady Turbulent Pipe and Channel Flow Correlations . . . . .	80
<b>6</b>	<b>Pulsating Flows without Heat Transfer</b>	<b>83</b>
6.1	Overview on Pulsating and Oscillating Pipe and Channel Flow . . . . .	84
6.2	LES simulation of Oscillating Turbulent Flow . . . . .	90
6.3	Conclusions . . . . .	94
6.4	URANS simulation of Pulsating Turbulent Flow . . . . .	102
6.5	LES and URANS Near Wall Numerical Predictions in Turbulent Pulsating Flows	105
6.6	Conclusions . . . . .	107
<b>7</b>	<b>Pulsating Flows with Heat Transfer - The Ishino et al. Test Case</b>	<b>109</b>
7.1	Test Case Description . . . . .	110
7.2	Numerical Simulations . . . . .	112
7.3	Numerical Results . . . . .	114
7.4	Conclusions . . . . .	116
<b>8</b>	<b>DNS of a Channel Flow with Heat Transfer</b>	<b>119</b>
8.1	Steady Channel Flow with Heat Transfer . . . . .	120
8.2	Fundamental Equations and Numerical Solution . . . . .	121
8.3	DNS Calculations of Steady Channel Flow . . . . .	121
8.4	Results . . . . .	122
8.5	Unsteady Channel Flow with Heat Transfer . . . . .	125
8.6	Conclusions . . . . .	155
<b>9</b>	<b>Turbulent Heat Transfer Modeling</b>	<b>159</b>
9.1	Two Equation Turbulent Heat Transfer Closures . . . . .	160
9.2	Model Validation . . . . .	164
9.3	Model Modification . . . . .	173
9.4	Pulsating Channel Flow . . . . .	179
<b>10</b>	<b>Conclusions</b>	<b>195</b>
<b>A</b>	<b>- Tensor Notation in General Coordinates Systems</b>	<b>201</b>
	<b>Bibliography</b>	<b>209</b>



# List of Figures

1.0.1	Wall heat transfer discrepancy in URANS and RANS numerical simulations . .	25
2.1.1	Air Management Strategy, source SIEMENS Power Generation, Mülheim [46] .	31
2.2.1	Siemens burner, courtesy of SIEMENS Power Generation, Mülheim . . . . .	31
2.3.1	Diagonal swirler mixing passage, Methane mass fraction. . . . .	32
2.3.2	Computational Domain and sample line positions . . . . .	33
2.4.1	Wall temperature profiles . . . . .	34
2.4.2	Transverse temperature profile, $x/D = 0.226$ . . . . .	36
2.4.3	Wall temperature profile . . . . .	37
2.4.4	Wall heat flux profiles, unsteady results reported as in figure 2.4.3 . . . . .	38
2.4.5	Transverse temperature profile, $x/D = 0.226$ , unsteady results reported as in figure 2.4.3 . . . . .	39
2.4.6	Unsteady simulation, instantaneous stream lines and vorticity plots. . . . .	40
2.4.7	Unsteady simulation, Heat flux (a) and wall normal vorticity (b). . . . .	41
2.4.8	Velocity magnitude, longitudinal cuts, $\phi = 0$ (a) and $\phi = 12\pi/11$ (b). . . . .	41
3.3.1	Composite slab case, configuration (a) and temperature profiles at different time steps(b). . . . .	46
3.3.2	Forced convection in a laminar pipe flow. Case configuration. . . . .	47
3.3.3	Temperature distribution, conjugate laminar pipe flow. . . . .	47
3.3.4	Wall and center line temperature, conjugate laminar pipe flow with oscillating inlet temperature. . . . .	48
5.1.1	Channel flow configuration, coordinate system and velocity decomposition . . .	72
5.1.2	Channel flow configuration, velocity and shear stress profiles . . . . .	74
5.2.1	Pipe flow configuration, coordinate system and velocity decomposition . . . . .	78
5.3.1	Nomenclature for flow and heat transfer in a circular-tube annulus. . . . .	82
6.1.1	Triple decomposition of a periodic velocity signal . . . . .	85
6.1.2	Transition to turbulence in oscillatory flow alone.(source [51]) . . . . .	87
6.1.3	Transition to turbulence in combined current and oscillatory flow. (source [51])	88
6.1.4	Turbulent Pulsating flow regimes. a) Quasi steady b) Intermediate Frequency c) Quasi Laminar . . . . .	90
6.2.1	Typical velocity profile near the wall and notation used for near-wall quantities.	91

6.3.1	Phase $\pi/6$ , Fine grid, Wall-Function Computation. . . . .	96
6.3.2	Phase $\pi/3$ , Fine grid, Wall-Function Computation. . . . .	96
6.3.3	Phase $2\pi/3$ , Fine grid, Wall-Function Computation. . . . .	97
6.3.4	Phase $5\pi/6$ , Fine grid, Wall-Function Computation. . . . .	97
6.3.5	Phase $\pi$ , Fine grid, Wall-Function Computation. . . . .	98
6.3.6	Phase $\pi/6$ , Fine grid, Wall-Normal Resolved Computation. . . . .	98
6.3.7	Phase $\pi/3$ , Fine grid, Wall-Normal Resolved Computation. . . . .	99
6.3.8	Phase $2\pi/3$ , Fine grid, Wall-Normal Resolved Computation. . . . .	99
6.3.9	Phase $5\pi/6$ , Fine grid, Wall-Normal Resolved Computation. . . . .	100
6.3.10	Phase $\pi$ , Fine grid, Wall-Normal Resolved Computation. . . . .	100
6.3.11	a) Wall-shear stress vs. oscillation phase, Fine grid, Wall-Normal Resolved and Wall Function Computation. b) pressure source term and center line velocity vs. oscillation phase . . . . .	101
6.3.12	Pressure term profiles. Comparison with DNS [76] . . . . .	101
6.4.1	Instantaneous velocity profiles in the presence of reverse flow. $U_c = 16.9 \text{ cm/s}$ , $a_{\bar{u}c} = 0.64$ , $l_s^+ = 8.1$ . Symbols from Tardu et al. [79], solid lines: High Reynolds (HR) number model with wall functions, dashed lines: $k$ - $\epsilon$ Launder and Sharma low reynolds (LR) number model. . . . .	104
6.6.1	Wall shear stress phase shift dependence on pulsation frequency . . . . .	107
7.1.1	Ishino et. al. experimental apparatus, simplified sketch . . . . .	110
7.2.1	LES grid, transversal cut . . . . .	113
7.3.1	Effect of the amplitude ratio on heat transfer enhancement ratio, comparison with numerical results ( $U_m = 5 \text{ m/s}$ ) . . . . .	115
8.1.1	Flow geometry, velocity and temperature layout . . . . .	120
8.4.1	Temperature profiles. Comparison with experimental data from [58] . . . . .	122
8.4.2	Dimensionless temperature profiles. Comparison with DNS data from [42] . . .	123
8.4.3	Dimensionless $k_\theta$ budget. Comparison with DNS data from Lyons et al. [52], Kasagi et al. [42] and experiments from Krishnamoorthy and Antonia [47]. . .	125
8.4.4	Dimensionless $\epsilon_\theta$ budget. Comparison with DNS data from, Kasagi et al. [42] .	126
8.4.5	Dimensionless turbulent kinetic energy budget. Comparison with DNS data from, Kasagi et al. [42] . . . . .	127
8.5.1	Velocity profiles, comparison with LES data from [72], $l_s^+ = 7$ . Profiles are plot- ted every $T/4$ and offset in the vertical direction; the bottom plot corresponds to phase $\pi$ with respect to the pressure forcing. . . . .	128
8.5.2	Velocity profiles, comparison with LES data from [72], $l_s^+ = 14$ . Profiles are plotted every $T/4$ and offset in the vertical direction; the bottom plot corre- sponds to phase $\pi$ with respect to the pressure forcing. . . . .	129

8.5.3	Velocity profiles, comparison with LES data from [72], $l_s^+ = 32$ . Profiles are plotted every $T/4$ and offset in the vertical direction; the bottom plot corresponds to phase $\pi$ with respect to the pressure forcing. . . . .	130
8.5.4	Reynolds stress profiles, comparison with LES data from [72], $l_s^+ = 7$ . Profiles are plotted every $T/4$ and offset in the vertical direction; the bottom plot corresponds to phase $\pi$ with respect to the pressure forcing. . . . .	131
8.5.5	Reynolds stress profiles, comparison with LES data from [72], $l_s^+ = 14$ . Profiles are plotted every $T/4$ and offset in the vertical direction; the bottom plot corresponds to phase $\pi$ with respect to the pressure forcing. . . . .	132
8.5.6	Reynolds stress profiles, comparison with LES data from [72], $l_s^+ = 35$ . Profiles are plotted every $T/4$ and offset in the vertical direction; the bottom plot corresponds to phase $\pi$ with respect to the pressure forcing. . . . .	133
8.5.7	Pulsating channel flow, Phase-locked averaged Nusselt number comparison . .	133
8.5.8	Budget of $k_\theta$ , pulsating flow computations on fine and coarse grid, $a_{uc} = 0.7$ , $l_s^+ = 7$ , comparison with steady channel flow DNS data from [52] . . . . .	135
8.5.8	Budget of $k_\theta$ , pulsating flow computations on fine and coarse grid, $a_{uc} = 0.7$ , $l_s^+ = 7$ , comparison with steady channel flow DNS data from [52] (continue) . .	136
8.5.9	Budget of kinetic energy, pulsating flow computations on fine and coarse grid, $a_{uc} = 0.7$ , $l_s^+ = 7$ , comparison with steady channel flow DNS data from [42] . .	137
8.5.9	Budget of kinetic energy, pulsating flow computations on fine and coarse grid, $a_{uc} = 0.7$ , $l_s^+ = 7$ , comparison with steady channel flow DNS data from [42] (continue) . . . . .	138
8.5.10	Budget of $\epsilon_\theta$ , pulsating flow computations on fine and coarse grid, $a_{uc} = 0.7$ , $l_s^+ = 7$ , comparison with steady channel flow DNS data from [42] . . . . .	139
8.5.10	Budget of $\epsilon_\theta$ , pulsating flow computations on fine and coarse grid, $a_{uc} = 0.7$ , $l_s^+ = 7$ , comparison with steady channel flow DNS data from [42] (continue) . .	140
8.5.11	Budget of $k_\theta$ , pulsating flow computations on fine and coarse grid, $a_{uc} = 0.7$ , $l_s^+ = 14$ , comparison with steady channel flow DNS data from [52] . . . . .	141
8.5.11	Budget of $k_\theta$ , pulsating flow computations on fine and coarse grid, $a_{uc} = 0.7$ , $l_s^+ = 14$ , comparison with steady channel flow DNS data from [52] (continue) .	142
8.5.12	Budget of kinetic energy, pulsating flow computations on coarse grid, $a_{uc} = 0.7$ , $l_s^+ = 14$ , comparison with steady channel flow DNS data from [42] . . . . .	143
8.5.12	Budget of kinetic energy, pulsating flow computations on coarse grid, $a_{uc} = 0.7$ , $l_s^+ = 14$ , comparison with steady channel flow DNS data from [42] (continue) .	144
8.5.13	Budget of $\epsilon_\theta$ , pulsating flow computations on fine and coarse grid, $a_{uc} = 0.7$ , $l_s^+ = 14$ , comparison with steady channel flow DNS data from [42] . . . . .	145
8.5.13	Budget of $\epsilon_\theta$ , pulsating flow computations on fine and coarse grid, $a_{uc} = 0.7$ , $l_s^+ = 14$ , comparison with steady channel flow DNS data from [42](continue) .	146
8.5.14	Budget of $k_\theta$ , pulsating flow computations on fine and coarse grid, $a_{uc} = 0.7$ , $l_s^+ = 35$ , comparison with steady channel flow DNS data from [52] . . . . .	147

8.5.14	Budget of $k_\theta$ , pulsating flow computations on fine and coarse grid, $a_{uc} = 0.7$ , $l_s^+ = 35$ , comparison with steady channel flow DNS data from [52] (continue) . . . . .	148
8.5.15	Budget of kinetic energy, pulsating flow computations on coarse grid, $a_{uc} = 0.7$ , $l_s^+ = 35$ , comparison with steady channel flow DNS data from [42] . . . . .	149
8.5.15	Budget of kinetic energy, pulsating flow computations on coarse grid, $a_{uc} = 0.7$ , $l_s^+ = 35$ , comparison with steady channel flow DNS data from [42] (continue) . . . . .	150
8.5.16	Budget of $\epsilon_\theta$ , pulsating flow computations on fine and coarse grid, $a_{uc} = 0.7$ , $l_s^+ = 35$ , comparison with steady channel flow DNS data from [42] . . . . .	151
8.5.16	Budget of $\epsilon_\theta$ , pulsating flow computations on fine and coarse grid, $a_{uc} = 0.7$ , $l_s^+ = 35$ , comparison with steady channel flow DNS data from [42] (continue) . . . . .	152
8.5.17	Phase-locked averaged Turbulent Prandtl Number, case $a_{uc} = 0.7$ $l_s^+ = 7$ . . . . .	153
8.5.18	Phaselocked averaged turbulent Prandtl Number, case $a_{uc} = 0.7$ $l_s^+ = 14$ . . . . .	154
8.5.19	Phase-locked averaged turbulent Prandtl Number, case $a_{uc} = 0.7$ $l_s^+ = 35$ . . . . .	155
8.5.20	Averaged turbulent Prandtl Number, comparison with steady flow. . . . .	156
8.5.21	Pulsating channel flow, Phase-locked averaged Nusselt number comparison, wave dominated flow. . . . .	157
9.2.1	Velocity (a) and Temperature (b) profiles. Comparisons with DNS data from [42]. . . . .	166
9.2.2	Budget of $k_\theta$ (a) and $\epsilon_\theta$ (b). Comparison with DNS data from [42] . . . . .	166
9.2.3	Experimental setup and coordinate system . . . . .	167
9.2.4	Computational domain, cut off . . . . .	168
9.2.5	Velocity (a) and Temperature (b) distributions. Comparison with experimental data from [81] (LS=Lauder and Sharma, AKN= Abe et al., NTT=Nagano and Tagawa . . . . .	169
9.2.6	Skin friction coefficient (a) and Stanton number (b) wall distributions. Comparison with experimental data from [81] . . . . .	170
9.2.7	AKN model, comparison with DNS in the SChF-FWTD configuration, turbulent kinetic energy, $k$ (a), turbulent kinetic energy dissipation rate, $\epsilon$ (b), turbulent temperature variance, $k_\theta$ (c) and turbulent temperature variance dissipation rate, $\epsilon_\theta$ (d). . . . .	172
9.2.8	AKN model, comparison with DNS in the SChF-FWTD configuration, turbulent temperature variance budget, $k_\theta$ (a), turbulent temperature variance dissipation rate budget, $\epsilon_\theta$ (b). . . . .	173
9.2.9	Temperature profiles, comparison between URANS, DNS and experimental data from [58] . . . . .	173
9.3.1	AKN <sub>D</sub> model, comparison with DNS in the SChF-FWTD configuration, turbulent kinetic energy, $k$ (a), turbulent kinetic energy dissipation rate, $\epsilon$ (b), turbulent temperature variance, $k_\theta$ (c) and turbulent temperature variance dissipation rate, $\epsilon_\theta$ (d). . . . .	176

9.3.2	AKN <sub>D</sub> model, comparison with DNS in the SChF-FWTD configuration, turbulent temperature variance budget, $k_\theta$ (a), turbulent temperature variance dissipation rate budget, $\epsilon_\theta$ (b). . . . .	177
9.3.3	Temperature profiles, comparison between URANS, DNS and experimental data from [58] . . . . .	177
9.3.4	Budget of $k_\theta$ (a) and $\epsilon_\theta$ (b). AKN <sub>D</sub> model, comparison with DNS data from [42]	178
9.3.5	AKN <sub>D</sub> model. Comparisons with DNS data from [42]. . . . .	179
9.3.6	AKN <sub>D</sub> model. Backward facing step case, Stanton number, comparisons with experimental data from [81]. . . . .	180
9.3.7	AKN <sub>D</sub> model. Backward facing step case, temperature profiles comparison. . .	181
9.4.1	Nusselt number predictions. Comparison with DNS results from Section 8.5. AKN model (a) and proposed AKN <sub>D</sub> modification (b). . . . .	181
9.4.2	Budget of $\epsilon_\theta$ , AKN <sub>D</sub> model results with pulsating flow ( $a_{uc} = 0.7, l_s^+ = 7$ ). Comparison with DNS on coarse grid. . . . .	183
9.4.2	Budget of $\epsilon_\theta$ , AKN <sub>D</sub> model results with pulsating flow ( $a_{uc} = 0.7, l_s^+ = 7$ ). Comparison with DNS on coarse grid (continue). . . . .	184
9.4.3	Budget of $k_\theta$ , AKN <sub>D</sub> model results with pulsating flow ( $a_{uc} = 0.7, l_s^+ = 7$ ). Comparison with DNS on coarse grid and steady channel flow DNS data from [52] . . . . .	185
9.4.3	Budget of $k_\theta$ , AKN <sub>D</sub> model results with pulsating flow ( $a_{uc} = 0.7, l_s^+ = 7$ ). Comparison with DNS on coarse grid and steady channel flow DNS data from [52] (continue) . . . . .	186
9.4.4	Budget of $\epsilon_\theta$ , AKN <sub>D</sub> model results with pulsating flow ( $a_{uc} = 0.7, l_s^+ = 14$ ). Comparison with DNS on coarse grid . . . . .	187
9.4.4	Budget of $\epsilon_\theta$ , AKN <sub>D</sub> model results with pulsating flow ( $a_{uc} = 0.7, l_s^+ = 14$ ). Comparison with DNS on coarse grid (continue) . . . . .	188
9.4.5	Budget of $k_\theta$ , AKN <sub>D</sub> model results with pulsating flow ( $a_{uc} = 0.7, l_s^+ = 35$ ). Comparison with DNS on coarse grid and steady channel flow DNS data from [52] . . . . .	189
9.4.5	Budget of $k_\theta$ , AKN <sub>D</sub> model results with pulsating flow ( $a_{uc} = 0.7, l_s^+ = 35$ ). Comparison with DNS on coarse grid and steady channel flow DNS data from [52] (continue) . . . . .	190
9.4.6	Budget of $\epsilon_\theta$ , AKN <sub>D</sub> model results with pulsating flow ( $a_{uc} = 0.7, l_s^+ = 14$ ). Comparison with DNS on coarse grid . . . . .	191
9.4.6	Budget of $\epsilon_\theta$ , AKN <sub>D</sub> model results with pulsating flow ( $a_{uc} = 0.7, l_s^+ = 14$ ). Comparison with DNS on coarse grid (continue) . . . . .	192
9.4.7	Budget of $k_\theta$ , AKN <sub>D</sub> model results with pulsating flow ( $a_{uc} = 0.7, l_s^+ = 35$ ). Comparison with DNS on coarse grid and steady channel flow DNS data from [52] . . . . .	193

---

9.4.7 Budget of $k_\theta$ , $AKN_D$ model results with pulsating flow ( $a_{uc} = 0.7, l_s^+ = 35$ ).	
Comparison with DNS on coarse grid and steady channel flow DNS data from	
[52](continue) . . . . .	194

# List of Tables

4.1	Constants and functions for the Launder and Sharma $k$ - $\epsilon$ model [49]. ( $R_T = \frac{k^2}{\nu \bar{\epsilon}}$ )	61
4.2	Constants and functions for the Wilcox and Rubesin $k$ - $\omega$ model. ( $l = \frac{\sqrt{k}}{\omega}, R_T = \frac{\sqrt{k}l}{\nu}$ )	64
4.3	Constants and functions for the $k$ - $\omega$ BSL model. . . . .	65
4.4	Constants and functions for the $k$ - $\omega$ BSL model. . . . .	65
4.5	Constants for the Abe, Kim and Nagano [10] (AKN) model, $k_\theta$ and $\epsilon_\theta$ equations.	67
4.6	functions for the AKN model, $k_\theta$ and $\epsilon_\theta$ equations. . . . .	68
6.1	Working principle of the wall-function boundary condition. . . . .	92
6.2	grid points and reference directory table . . . . .	92
7.1	Experimental Conditions of Pulsating Flows from Ishino et al. [38] . . . . .	112
8.1	DNS computations, pulsating parameter and investigated flow regimes. . . . .	126
9.1	$k_\theta$ transport equation: turbulent production, dissipation, molecular diffusion and turbulent diffusion terms. . . . .	160
9.2	$\epsilon_\theta$ transport equation, mean gradient production terms: production by mean temperature gradient, gradient production, production by mean velocity gradient.	161
9.3	$\epsilon_\theta$ transport equation: turbulent production, dissipation, molecular diffusion and turbulent diffusion terms. . . . .	161
9.4	Flow reattachment length ( $X_r$ ) comparisons. . . . .	169
9.5	Constants for the AKN model modification (AKN <sub>D</sub> ), $k_\theta$ and $\epsilon_\theta$ equations. . . . .	175
9.6	functions for the AKN model modification (AKN <sub>D</sub> ), $k_\theta$ and $\epsilon_\theta$ equations. . . . .	175





# List of Symbols

---

*Roman symbols*

---

$C_f$	friction coefficient
$D$	characteristic diameter
$f$	generic fluid property / pulsation frequency
$h$	fluid enthalpy / channel height / heat transfer coefficient
$I$	identity matrix
$K$	material heat conductivity
$k$	turbulent kinetic energy
$k_\theta$	fluctuating temperature variance
$l_s^+$	non dimensional Stokes length, $l_s^+ = \frac{\delta_s \bar{u}_\tau}{\nu}$
$p$	fluid pressure
$\vec{q}$	heat flux vector
$R$	perfect gas constant
$R$	characteristic time scale ratio, $R = \frac{\tau_\theta}{\tau_t}$ / pipe radius
$S_{ij}$	strain tensor
$T$	fluid temperature / pulsation period
$t$	time unit
$\vec{u}$	velocity vector
$U$	characteristic velocity
$Ue$	free stream velocity
$u^+$	non-dimensional velocity, $u^+ = \frac{\bar{u}}{\bar{u}_\tau}$

---

$u_\tau$	skin friction velocity, $u_\tau = \sqrt{\frac{\tau_w}{\rho}}$
$x$	generic axial coordinate
$y$	generic wall-normal coordinate
$y^+$	non-dimensional wall distance, $y^+ = \frac{\bar{u}_\tau y}{\nu}$
$z$	generic span-wise coordinate

---

*Greek symbols*

---

$\alpha$	fluid heat diffusivity, $\alpha = \frac{\lambda}{\rho c_p}$
$\delta$	boundary layer thickness
$\delta_s$	Stokes length, $\delta_s = \sqrt{\frac{2\nu}{\omega}}$
$\delta$	boundary layer thickness
$\epsilon$	turbulent kinetic energy dissipation rate
$\epsilon_{ij}$	Reynolds stress dissipation tensor
$\epsilon_\theta$	fluctuating temperature variance dissipation rate
$\kappa$	von Karman constant
$\lambda$	fluid heat conductivity
$\mu$	fluid molecular viscosity
$\omega$	rate of dissipation of turbulence per unit energy / angular pulsation, $\omega = 2\pi f$
$\omega^+$	non dimensional frequency parameter, $\omega^+ = \frac{\omega\nu}{\bar{u}_\tau^2}$
$\phi$	angular phase / angular coordinate
$\rho$	fluid density
$\underline{\tau}$	fluid shear stress tensor
$\theta$	non-dimensional temperature, $\theta^+ = \frac{\bar{T} - T_w}{T_\tau}$
$\tau_t$	velocity fluctuation characteristic time scale
$\tau_\theta$	temperature fluctuation characteristic time scale
$\tau_w$	wall shear stress

---

*Superscripts*

---

---

$\bar{\phantom{x}}$	time averaging operator (Reynolds averaging)
$\tilde{\phantom{x}}$	Favre averaging operator
$'$	turbulent fluctuations
$''$	turbulent fluctuating quantity (Favre averaging)
$\sim$	phase locked averaging operator
$+$	non-dimensional wall units
$c_p$	specific heat capacity (at constant pressure)

---

*Subscripts*

---

$c$	relative to the channel centerline
$f$	relative to fluid quantities
$s$	relative to solid quantities
$t$	turbulent quantity
$uc$	relative to the velocity at channel centerline
$w$	wall quantity

---

*Miscellaneous*

---

$\Delta$	characteristic LES filter length
$\Delta\theta$	logarithmic mean temperature difference
$\langle \phantom{x} \rangle$	ensemble averaging operator
$J_0$	zero-th order Bessel function
$\nabla$	gradient operator: $\nabla = (\frac{\partial}{\partial x}, \frac{\partial}{\partial y}, \frac{\partial}{\partial z})$
$Nu$	Nusselt number
$P_{ij}$	Reynolds stress velocity-pressure-gradient tensor
$\mathcal{P}_{ij}$	Reynolds stress production tensor
$Pr$	Prandtl Number
$Re$	Reynolds Number
$\mathcal{R}_e$	Real part of a complex number

$Tr$  trace operator  $Tr = \sum_i a_{ii}$

$(u, v, w)$  velocity components

$(x, r, \phi)$  cylindrical coordinates

# Zusammenfassung

Die Entwicklung effizienter, nachhaltiger Verbrennungssysteme stellt im heutigen Umfeld einer stark wettbewerbsorientierten Wirtschaft eine anspruchsvolle Aufgabe dar.

Durch die starke Temperaturabhängigkeit der Stickstoffoxidbildung muss hierbei ein Temperaturoptimum gefunden werden, das den maximal möglichen Wirkungsgrad des Kreisprozesses bei gleichzeitig minimalen Emissionen, in den Grenzen der Materialfestigkeit, gewährleistet. Diese Anforderungen führten in der Brennkammerentwicklung zur Einführung magerer Vormischflammen, bei denen lokale Temperaturspitzen durch exakte Lufteinblasung verringert werden. Ein bedeutender Nachteil dieser innovativen Systeme ist ihre Anfälligkeit für Verbrennungsinstabilitäten sowie größere Wandwärmebelastungen.

In der vorliegenden Arbeit wird unter Verwendung numerischer Simulationen das Verhalten der wandnahen Grenzschicht gegenüber auftretenden Verbrennungsinstabilitäten untersucht, um den Einfluß von Strömungspulsationen auf den Wärmeübergang zu charakterisieren.

In Kapitel 2 wird die Simulation einer Brennkammer in technisch relevantem Maßstab vorgestellt. Die Simulation wurde mit einem kommerziellen CFD (Computational Fluid Dynamic) Code durchgeführt dessen Methoden dem aktuellen Stand der Technik entsprechen. Die Ergebnisse zeigen, dass in komplexen Simulationen, in denen Verbrennungsinstabilitäten auftreten, die Wandwärmebelastung nicht nur von der korrekten Modellierung der Brennstoff-Luft Mischung, der chemischen Reaktionen, der Wärmeleitung im Festkörper und der Wärmestrahlung abhängt, sondern auch stark von der Modellierung der Turbulenz im wandnahen Bereich beeinflusst wird. Des Weiteren spielt auch die korrekte Lösung des gekoppelten Festkörper/Fluid Wärmeübergangs eine maßgebliche Rolle (siehe genaue Ausführungen in Kapitel 3).

Das Hauptinteresse dieser Arbeit liegt jedoch auf der Untersuchung der Wechselwirkung zwischen wandnaher Turbulenz und dem Wandwärmübergang bei instationären Strömungskonfigurationen.

Kapitel 4 konzentriert sich auf die Interaktion zwischen Wärmefreisetzung und Fluidmechanik in turbulenten, instationären Strömungen und stellt die beschreibenden, mathematischen Gleichungen vor. Anschließend präsentiert Kapitel 5 analytische Lösungen dieser Gleichungen für einfache Kanal- und Rohrströmungen. Des Weiteren werden die grundlegenden Korrelationen zwischen turbulenten Kanal- und Rohrströmungen und den dort auftretenden viskosen Verlusttermen erläutert.

Kapitel 6 und 7 widmen sich der Analyse verschiedener Turbulenzmodelle bei der Modellierung des Wandwärmübergangs unter dem Einfluß von thermo-akustischen Schwingungen. Die

Genauigkeit der Modelle wird anhand vereinfachter, aber gut definierter akademischer Testfälle bestimmt. Die Ergebnisse zeigen Abweichungen gegenüber den experimentellen Daten und veranschaulichen so deutlich die Grenzen von Wandfunktionen, sowohl bei der Verwendung in URANS als auch in LES Simulationen.

Die interessantesten Ergebnisse sind in Kapitel 8 zu finden, in dem eine detaillierte Untersuchung der turbulenten Strukturen im wandnahen Bereich bei Wärmeübergang anhand von DNS (Direct Numerical Simulation) Simulationen von pulsierenden Strömungen vorgestellt wird. Das Verhalten der turbulenten kinetischen Energie, der Temperaturfluktuationen sowie deren Dissipationsraten werden für verschiedene Schwingungsfrequenzen und -amplituden analysiert.

Die DNS Ergebnisse zeigen eine starke Abhängigkeit der turbulenten Größen von der Strömungspulsation und deren Amplitude. Jeder Term in den Erhaltungsgleichungen von  $k$ ,  $k_\theta$  und  $\epsilon_\theta$  antwortet mit einer unterschiedlichen Phasenverschiebung auf die anliegende Schwingungsfrequenz und -amplitude. Sowohl die phasengemittelte als auch die gemittelte turbulente Prandtl Zahl wird von der Strömungspulsation sowie dem instationären Wärmeübergang beeinflusst. Eine Erhöhung der Schwingungsfrequenz bewirkt eine Verringerung der Amplitude des instationären Wärmeübergangs. Der globale Gesamtwärmeübergang wird von der Schwingungsamplitude beeinflusst. Mit zunehmender Amplitude vergrößert sich der globale Wärmeübergang bis zum doppelten Wert des stationären Strömungsfalls.

Die DNS Datenbank stellte eine wertvolle und einzigartige Arbeit dar, die zum Verbessern und/oder Entwickeln neuer Modelle für den instationären, turbulenten Wärmeübergang verwendet werden kann.

Abschließend wird in Kapitel 9, von den DNS Daten ausgehend ein neues Schließungsmodell für den instationären, turbulenten Wärmeübergang hergeleitet. Für alle untersuchten Strömungszustände gibt das Modell die Mittelwerte des instationären Wärmeübergangs sowie die Schwingungsamplitude sehr gut wieder. Die DNS Datenbank konnte hier direkt für ein vertieftes Verständnis der Wechselwirkung zwischen wandnaher Turbulenz und dem Wandwärmeübergang bei instationären Strömungskonfigurationen verwendet werden.

# Abstract

The development of efficient and environmental sustainable combustion systems is critical in the nowadays economy. The efficiency of an energy cycle is proportional to the highest cycle temperature but unfortunately, due to the major mechanism of nitric oxide formation, there is a temperature trade off between improved cycle efficiency, material constraints and low emissions. This considerations have pushed combustion chamber technology towards lean premixed flames where the tendency is to reduce local temperature peaks making use of a well studied air management. Unfortunately this kind of innovative systems have shown to be prone to combustion instabilities and higher wall heat load.

In the present work, making use of numerical simulations, the wall boundary layer response to combustion instabilities has been studied in order to asses the effect of flow pulsations on heat transfer.

In Chapter 2 the status of the art of combustor simulation has been presented. A full scale burner has been simulated with a commercial CFD (Computational Fluid Dynamic) code. The results have shown that in such complex simulations and in the presence of combustion instabilities, the correct predictions of wall heat load rely not only on the correct modeling of air-fuel turbulent mixing, chemical reactions and heat radiation, but also depend strongly on the near wall turbulence treatment and on the correct solution of the unsteady conjugate solid-fluid heat transfer problem at the wall (which details are discussed in Chapter 3).

The main interest of the work is however the study of the near wall turbulence and the associated heat transfer in the presence of flow unsteadiness. In Chapter 4 the fundamental equations for the solution of the thermo-Fluid dynamic problem in turbulent unsteady flows have been introduced. Moreover, in Chapter 5 some unsteady analytical solutions in simple channel and pipe configurations as well as turbulent channel and pipe flow heat transfer and viscous loss correlations have been presented.

In Chapter 6 and 7, making use of simplified but well defined academic test cases, the accuracy of different turbulence models for the prediction of the wall heat transfer response in presence of thermo-acoustic instabilities has been discussed. The results have shown the clear limitation of the use of wall functions both in URANS and LES applications and discrepancies with some experimental results.

The most interesting results are however presented In Chapter 8 where the turbulent near wall structures and the associated heat transfer were in detail investigated by means of pulsating channel flow DNS (Direct Numerical Simulation) simulations.

The response of the turbulent kinetic energy ( $k$ ) and fluctuating temperature variance ( $k_\theta$ ) as well as their dissipation rates ( $\epsilon$  and  $\epsilon_\theta$ ) were reported at different flow pulsations and amplitudes. In order to highlight the most critical (for the turbulence models) flow conditions, the pulsation amplitudes and frequencies were chosen so to span different pulsating flow regimes.

The DNS results have shown very complex turbulence unbalance phenomena depending on the flow pulsation and amplitude. Each term on the budget equation of  $k$ ,  $k_\theta$  and  $\epsilon_\theta$  have shown different answer to pulsation frequency and amplitude. The mean and phase locked averaged turbulent Prandtl number seems to be affected by flow pulsation as well as the unsteady heat transfer. The pulsation frequency increase determines an unsteady heat transfer amplitude decrease. The flow pulsation amplitude seems to affect the overall mean heat transfer value increasing up to two times its steady value with the increasing of pulsation amplitude.

The present DNS database represents a highly valuable and unique work which can serve as a reference for the development of innovative unsteady turbulent heat transfer models.

Finally, in Chapter 9, starting from the DNS data, a new turbulent heat transfer closure has been proposed. The new model was capable, in all the flow condition studied, to correctly predict the unsteady heat transfer mean value and pulsating amplitude showing the added value of the present DNS database for the understanding of the near wall turbulence behavior and the associated heat transfer in presence of flow unsteadiness.



# 1 Introduction

In order to meet worldwide sustainability targets in terms of energy supply, lean gas turbine combustion technology will play a crucial role in the short and middle term. Unfortunately, lean premix combustion technology with high power density often leads to the appearance of combustion instabilities which may cause severe damages to the combustor structures.

Combustion instabilities are due to different feedback cycles that may take place in the combustion chamber. A common interpretation of the phenomenon [46] makes use of the following steps. Unsteady pressure oscillations can induce volume flow oscillations at the burner exit. These volume flow oscillations cause an oscillating heat release. In technically premixed systems the heat release oscillations may depend on the acoustic answer of both the air and fuel supply system and in general results in the propagation of pressure waves in the combustion chamber. The geometry of the combustion chamber and the acoustic boundary conditions at the combustor exit determine the shape of the acoustic modes. Depending on their intensity and phase, pressure fluctuation can then affect the heat release rate in a self-sustaining process. Following Lord Rayleigh, in absence of acoustic damping a positive correlation of the pressure fluctuations  $p'$  and the heat release fluctuations  $q'$  results in combustion instabilities. Here a qualitative cause-and-effect chain is established. However, in practical applications, the individuation and suppression of the initiating perturbations and the quantitative evaluation of the complex interacting physical phenomena remain still very challenging [46].

In order to understand in more details the physical phenomena involved in such a complex mechanism, the present work has been focused on the effect of flow pulsations on the unsteady wall heat transfer. The questions that have been addressed are the following: can flow pulsation affect the overall wall heat transfer? If yes, could it be a danger for the thermal resistance of the combustion chamber materials? Can flow simulations help in predicting unsteady flow effects on wall heat transfer? Which available near wall numerical models are the more accurate and what are their limitations?

The determination of the wall heat load in combustion chamber applications is a complex problem which involves the modeling of different interacting physical phenomena. Turbulent mixing, chemical reactions, turbulent heat convection, heat conduction and heat radiation are just the principal aspects to be modeled. In order to have a clear perspective of the physical phenomena involved, in Chapter 2 a commercial multi-physics code is validated against experimental data from a Siemens burner test bench. Despite the stable operating condition and the simplified geometry, the simulations exhibit some flow unsteadiness and can be used as the starting point of the present investigation. Discrepancies in the wall heat load prediction between steady and unsteady simulations have been observed as well as the result dependence on the near wall turbulence modeling.

An important role on the wall heat load prediction is played by the solution of the conjugate heat transfer problem. Commercial multi-physics codes have the capability of coupling different domains with different thermal properties. This is often not the case for dedicated academic software.

In Chapter 3 some details are given about the solution of the unsteady conjugate heat transfer problem. A coupled solver has been developed and validated against analytical solutions. The results have confirmed the accuracy of the solution method in time and its suitability for the coupling of different specific numerical solvers in a multi-physics environment.

The main topic of the present work remains however the study of the wall heat transfer in presence of unsteady flow conditions and the discrepancy between steady and unsteady numerical predictions.

A discrepancy in predicting wall heat transfer have been observed not only in the above mentioned SIEMENS validation case, but also in many other combustion chamber simulations. In figure 1.0.1 heat transfer results are reported for another validation case, the Twente test rig (details are given in [5]). Here the averaged wall heat flux computed using the Reynolds Averaged Navier-Stokes (RANS) and Unsteady Reynolds Averaged Navier-Stokes approach (URANS) is reported. The calculation have been done using the  $k - \omega$  SST turbulence model and the

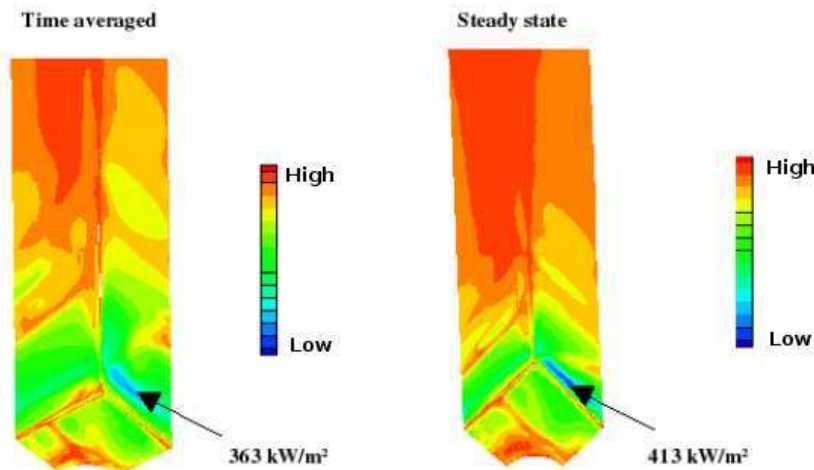


Figure 1.0.1: Wall heat transfer discrepancy in URANS and RANS numerical simulations

EDM combustion model. In this case, the boundary layer was resolved using a wall-stretched grid. According to the convention, the highest heat flux takes place in the blue area (most negative values of heat flux leaving the calculation domain). The transient case (URANS) was calculated over several periods, with a periodic fuel mass flow excitation. Here we see, that the time averaging of unsteady values leads to a wider distribution of the overall heat flux, whereas the peak values diminish comparing with the results obtained in the steady case (RANS). This finding is moreover in contradiction with preceding calculations performed using the  $k - \epsilon$  model and the so called 'wall function' approach. The wall function approach is often preferred in complex industrial applications due to the coarser near wall grid resolution required. However, as will be discussed in details in Chapter 7, its application in unsteady flow condition can be questionable.

Later on in this work the effect of pulsation on unsteady heat transfer has been more systematically investigated shifting the attention from the complex combustion chamber problem to much simpler pulsating pipe and channel flow configurations.

A literature survey on simple pulsating flows with heat transfer, such as pulsating channel and pipe flows, shows disagreement between the different experimental results in both laminar and turbulent flow conditions.

Despite the fact that one of the first experiments on the effect of pulsation on heat transfer was conducted already in 1952 [84] little attention was given later on a comprehensive understanding of pulsating flows and heat transfer phenomena.

Traditionally, the thermo-fluid design was made in order to avoid unsteady regimes and in this sense the attention was always focused on the modeling of mean flow quantities. Nevertheless the attention on transient behavior of the energy-related systems during the period of startup, shutdown or any off-normal operation conditions, such as the changing of loading conditions, grew in the years together with the increasing need to procure precise thermal control of the various heat exchange devices involved in chemical process, nuclear and non conventional energy systems ( such as the Stirling motors ).

Starting from the pioniering work of West in the 1952 [84], the possibility of increasing the overall heat transfer adding fluid pulsations interested many authors ( [50], [45], [34], [28] [32] ). The intrinsic difficulties in modeling the complex flow dynamics together with (this is the author opinion) the complications and the extra costs needed for the design and the operation of an efficient pulsating device, could have been the possible cause for the lack of industrial interest in this field, which probably contributed to limit the number of scientific work done in this direction.

In compressible flows, as shown already by Lemlich [50] in the 1961 the heat transfer seems to be effectively enhanced through flow resonance. In this case the flow pulsations are obtained inducing the system resonance without the necessity of adding complicating pulsating devices. In the author opinion, this interesting phenomenon as well has not been enough investigated due, not only to the complexity of the phenomena itself, but also due to the industrial distrust in the possibility of reliably control resonance phenomena which are often the cause of mechanical system failure.

Recently, the interest on pulsating turbulent flows has been increasing. The need of lower the level of  $NO_x$  emissions pushed the combustion chamber air management towards lean premixed combustion. As mentioned already, lean premixed combustion is often characterized by the appearance of combustion instabilities that can lead to severe component damages.

A correct prevention of material failure requires a better understanding of the high mechanical and thermal stresses induced by the thermo-acoustic flow instabilities. For this reason, the todays renewed interest on unsteady turbulent heat transfer phenomena regards not only the possibility of improving the heat exchange and the overall system efficiency but also the necessity of enhance the reliability of the new generation - low emission energy systems.

Moreover, the exigence of a clean combustion technology, pushed the scientific community towards the experimentation of non conventional systems. One interesting possibility seem to be the pulse combustion technology. Pulse combustion systems have shown many advantages over conventional burners such as higher thermal efficiency, low pollutant emissions, and high

---

rates of heat transfer. In all cases low  $NO_x$  emissions and high wall heat transfer seem to be connected with flow pulsations and in this sense a better understanding of the aero-thermodynamic behaviors of wall bounded pulsating flows become more and more of crucial interest [13], [22], [24], [23].

In Chapter 6 different turbulent pulsating flow regimes were distinguished making use of experimental results on isothermal pulsating pipe and channel flows. The main non-dimensional parameter, able to characterize the turbulent pulsating flow conditions, have been discussed. In Chapter 7 different available turbulent model were compared in a non-isothermal pulsating turbulent pipe flow testcase from Ishino.

Finally in Chapter 8 pulsating channel flow DNS simulations have been performed with fixed wall temperature differences. Turbulent temperature and velocity statistics have been collected in order to study the effect of different pulsation amplitudes and frequency on the wall heat transfer.

In Chapter 9 the DNS data have been used as a database for the validation and development of a heat transfer turbulent closure model. The proposed new closure seems to be able to correctly predict the mean and pulsating amplitude values of the wall heat flux in presence of unsteady, separating and reattaching flow.

The model was validated in pulsating non reacting flow conditions. It is however possible to apply successfull the model to the complex combustion chamber starting problem.



## 2 Industrial Burner Simulation and Heat Load

## 2.1 Introduction

Due to the major mechanism of  $NO_x$  generation, there is generally a temperature trade off between improved cycle efficiency, material constraints and low  $NO_x$  emission. The cycle efficiency is proportional to the highest cycle temperature, but unfortunately also the  $NO_x$  production increases with increasing combustion temperature. As already mentioned,  $NO_x$  limitation have pushed the gas turbine technology towards combustion chamber designs with leaner premixed flames. The tendency, as sketched in figure 2.1.1, is to reduce the zones with local temperature peaks. This can be achieved improving the air management between primary and secondary combustion chamber zones and progressively reducing the pilot flames till their complete elimination. Pilot turbulent diffusion flames are intrinsically prone to local high combustion temperature due to the fact that the flow must span locally from rich to leaner combustion zones passing through stoichiometric states which realize the highest temperature. Improved air management can help in reducing the temperatures in the primary flame zone. This is normally done redirecting fresh gas from the secondary flame zone and improving the thermal mixing. One draw back of this strategy is the fact that less fresh air is then left in the secondary flame zone for the liner cooling. The cooling air management becomes then a major challenge for the combustion chamber technology [60].

In this sense a correct prediction of the wall heat load and more in general of the combustion chamber temperature field becomes of strategic importance for the design of low emission devices. In the frame of these considerations, in the present work the capability of a commercial multi-physics code ( ANSYS CFX ) to correctly predict the wall heat load and the core flow temperature field has been investigated. Comparison have been made with the experimental results from the ITS test rig at the University of Karlsruhe [70] and with a preceding numerical campaign from [21]. The present results have been also published in [61].

## 2.2 ITS Test Rig

The ITS test facility consists of a square-cross-section combustion chamber equipped with a full scale Siemens burner. Details of the facility are available in references [21]. The burner consists of a so called axial swirler, through which the pilot air flow is swirled before entering the combustion chamber. Furthermore the burner includes a so called diagonal swirler, in which a technical premix of the fuel gas and air is obtained (see figure 2.2.1). The test rig is operated at atmospheric condition and at an equivalence ratio of 0.5. The combustion chamber is fired by natural gas and the numerical simulations refer to the operating condition with 7% pilot gas injection. The combustion chamber casing consists of a ceramic heat shield (CHS) used in Siemens engines. Span-wise temperature measurements are available at different axial positions on the combustion chamber symmetry plane as reported in [21] and wall temperature measurements within the ceramic material are given in reference [7].



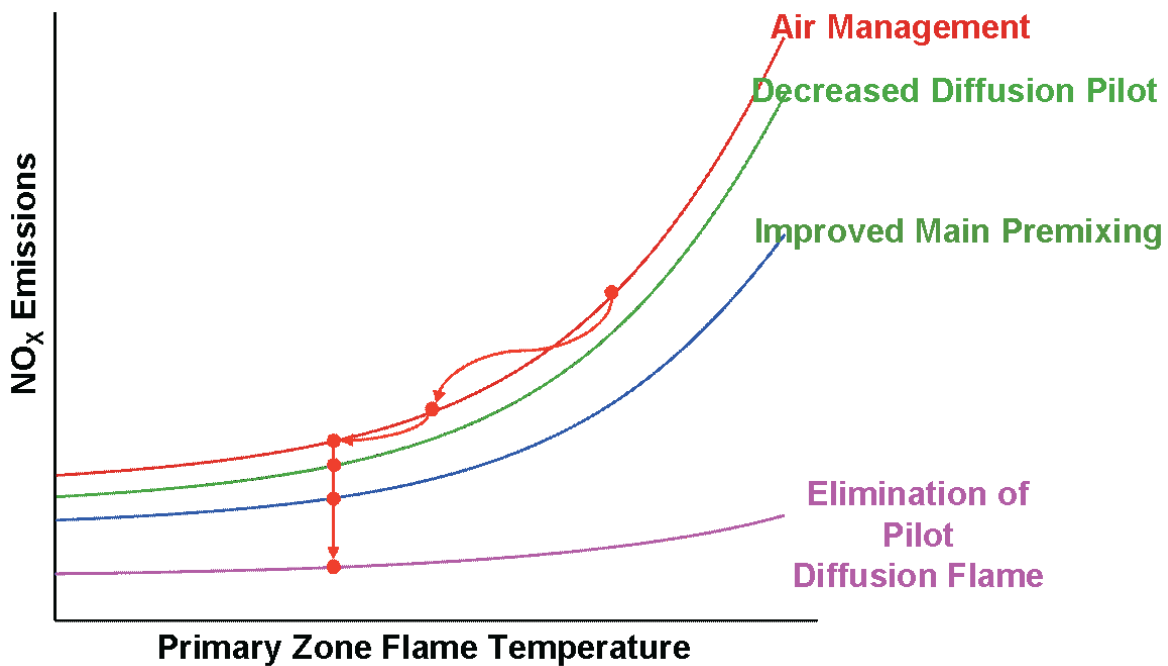


Figure 2.1.1: Air Management Strategy, source SIEMENS Power Generation, Mülheim [46]

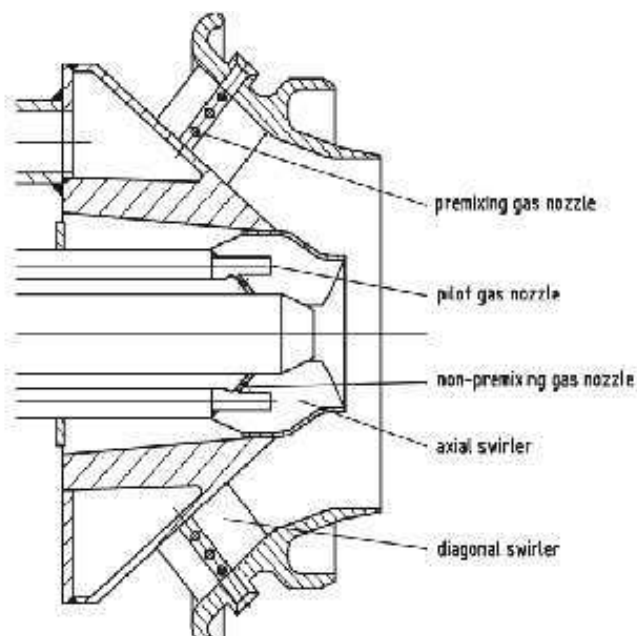


Figure 2.2.1: Siemens burner, courtesy of SIEMENS Power Generation, Mülheim

## 2.3 CFD Set-up and Comparison with Previous Calculations

The following work can be viewed as a continuation of the work made by Dannecker et al. in [21]. In [21] the impact of radiation on the wall heat load has been investigated. Despite the

sensible improvement of the numerical predictions due to the radiation modeling, the presence of a mismatch between experimental and numerical data suggested a further investigation in the direction of improving the wall boundary layer resolution. As already mentioned, the correct prediction of the wall heat load in such a complex simulation rely on the correct modeling of turbulent mixing, chemical reaction, turbulent convection, heat conduction in the solid and radiation. Dannecker et al. studied the effect of improving the radiation modeling. In the present work the computational domain and boundary condition used in [21] have been modified in order to improve the predictions of the fuel air turbulent mixing, the near wall turbulent heat convection and the conjugate heat transfer between the fluid and the ceramic solid walls. Regarding the fuel air turbulent mixing, the accuracy of the diagonal swirler boundary conditions is improved through a preceding simulation of a diagonal swirler mixing passage. The inflow profiles of velocity and species at the diagonal swirler inlet section were specified in [21] through a rough interpolation of experimental data. In the present case the diagonal swirler inlet boundary condition are interpolated from the simulation of a diagonal swirler sector (see figure 2.3.1).

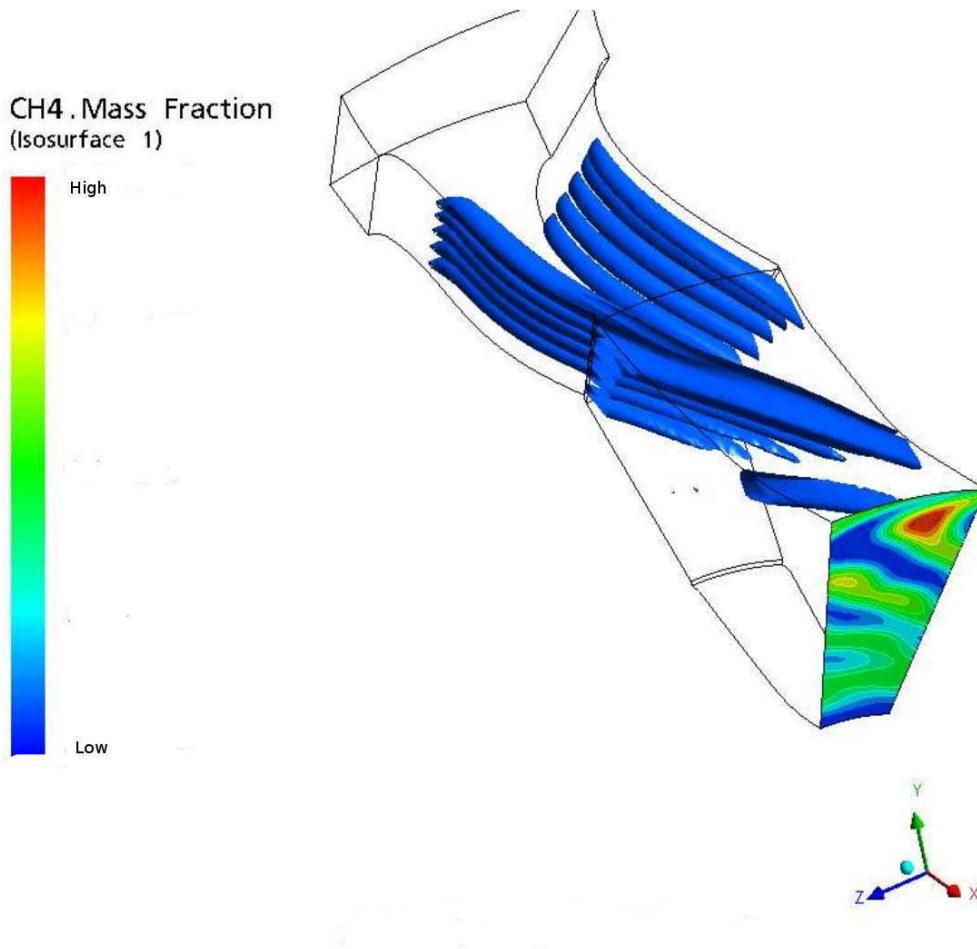


Figure 2.3.1: Diagonal swirler mixing passage, Methane mass fraction.

In order to increase accuracy in the prediction of the near wall turbulent convection, the computational domain was refined at the wall up to values of  $y^+$  of the order of one. The  $k-\omega$

*SST* turbulence model was used permitting a boundary layer resolution down to the laminar sublayer which was not allowed with the previous grid spacing. Concerning the heat conduction in the solid boundaries, the conjugate heat transfer section was extended to the complete liner down to the convergent exit nozzle (see figure 2.3.2).

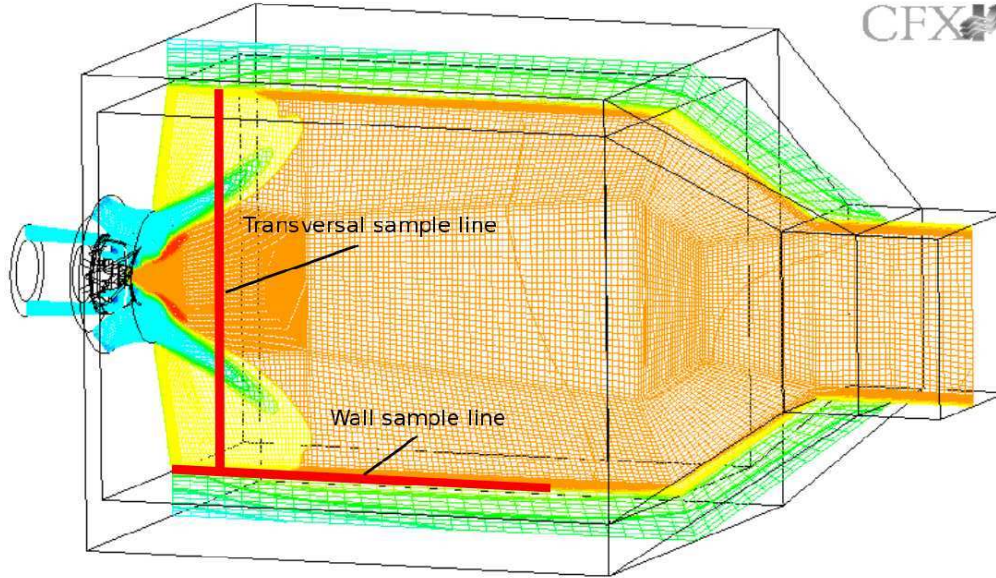


Figure 2.3.2: Computational Domain and sample line positions

In order to save computational points, Dannecker et al. [21], considered just one of the four walls that compose the combustion chamber square cross section. The remaining wall temperature was calculated assuming a prescribed wall heat transfer coefficient. The heat flux at the wall was calculated according to the following formula,

$$q_w = \frac{k_c}{t_c}(T_w - T_{out}). \quad (2.3.1)$$

where  $q_w$  represents the wall heat flux,  $k_c$  is the ceramic wall heat conductivity and  $t_c$  is the wall thickness.  $T_w$  represent the computed wall temperature and  $T_{out}$  is the prescribed temperature profile at the cold side of the liner walls. The heat transfer coefficient ( $h_c = \frac{k_c}{t_c}$ ) was assumed to be function of temperature considering the temperature dependence of the wall heat conductivity. In the present work, same  $k_c$  temperature dependence and  $T_{out}$  profile have been considered for the solution of the conjugate heat transfer problem. The radiation model considered hereinafter is the discrete transfer model (DT) [1] and the fluid has been modeled as a weighted multigray sum of gas species (WSGG) [3]. Details about the WSGG model used are available in [21], [54]. The ceramic wall emissivity,  $\epsilon$ , has been considered as a function of temperature according to measurements on heat shield material samples. Dannecker et al. [21] considered, instead, a constant emissivity value. The eddy dissipation model (EDM) [2] and a simplified two step mechanism has been used for the reaction model as in [21].

## 2.4 Results and Comparison

### 2.4.1 Wall Temperature Profiles

The wall temperature profiles are compared in figure 2.4.1. A steady numerical simulation has been performed. The temperature data are non dimensionalized with the adiabatic flame temperature and expressed in function of the non-dimensionalized axial distance,  $x/D$ , where  $D$  represents the transverse dimension of the combustion chamber. Three wall normal positions are considered at  $z = z_w$ ,  $z = z_w + 0.1mm$  and  $z = z_w + 0.2mm$ . The profile at  $z = z_w$  refers to the solid-fluid interface. At this location, the present numerical results are compared with the results from Dannecker et al. [21] showing a quite sensitive mismatch with the experimental data. A closer look on the numerical temperature field revealed that little error in the thermocouple positioning of the order of a tenth of a millimeter, due to the presence of strong temperature gradient, could sensibly affect the temperature predictions. In order to quantify such an effect, the temperature profiles at  $0.1mm$  and  $0.2mm$  from the solid-fluid interface in the fluid flow direction are reported in figure 2.4.1 with black continuous lines. The profile at the location  $z = z_w + 0.1mm$  matches quite well with the experimental data especially for  $x/D$  values below 0.5.

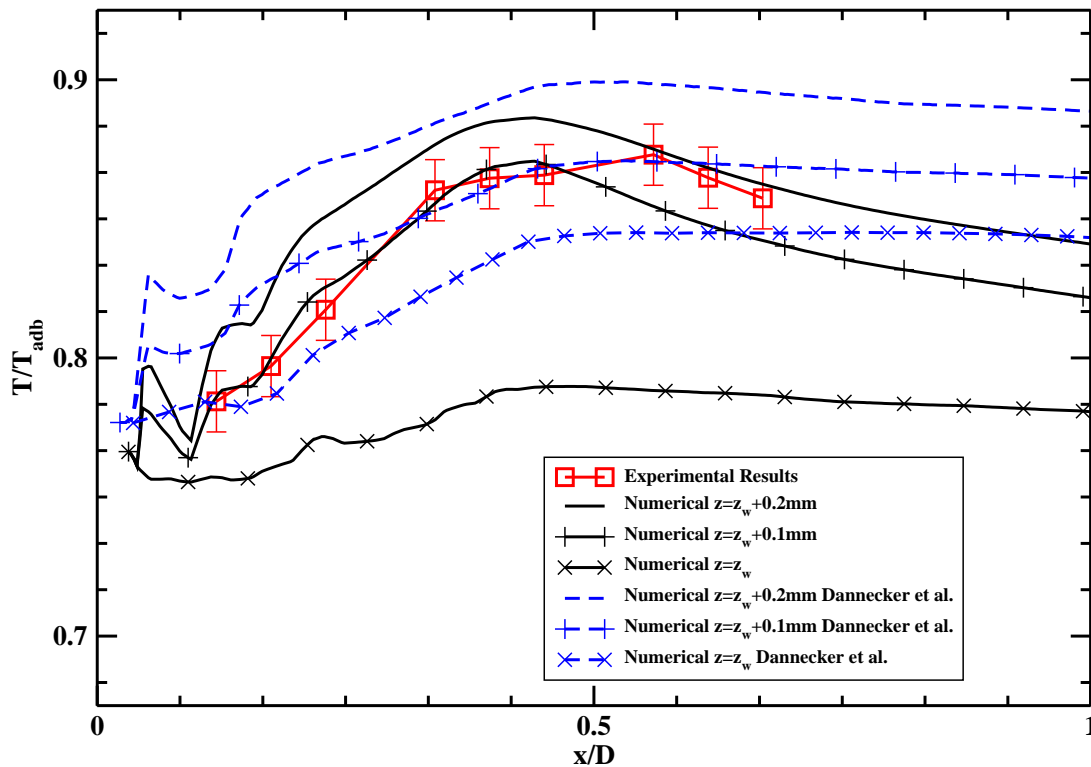


Figure 2.4.1: Wall temperature profiles

Above 0.5 the numerical prediction underestimates the temperature level but exhibits the same temperature profile trend. On the contrary, at  $z = z_w + 0.2mm$  the numerical prediction matches with the experimental values downstream  $x/D = 0.5$  and upstream that value a temperature over prediction is observed. Both the under and over estimation seem to have the same order of magnitude. A comparison of the numerical results obtained at the wall and at a positive displacement inside the fluid flow suggest the existence of a systematic experimental error in the thermocouple positioning. Two concurrent causes exist for such a possible mismatch [8]: the difficulty of machining the thermocouples slots into the ceramic material and the difficulty of correct shaping the thermocouples wires within the slot. Both the imprecise wire bending and the intrinsic difficulty of removing material from the hard ceramic surface could have concurred to a positive shift of the measurement line. Furthermore negative displacement of the thermocouple inside the solid material does not affect much the temperature profiles, which remain very close to the temperature values at  $z = z_w$ . In this sense, even considering a symmetric displacement statistical errors of  $\pm 0.2mm$  the temperature values must have been biased towards higher temperature levels. The thermocouple itself possesses a certain measurement volume due to its thickness of the order of a millimeter. Thus a resolution of  $0.1mm$  seems to be impossible even if the positioning were better performed. In figure 2.4.1 the temperature profiles at the same locations are compared with the results obtained using the Dannecker et al. numerical setup and with the same radiation, turbulence and chemical model. Wall emissivity and conductivity were considered function of temperature for both simulations. The results are reported with the dashed blue lines and referred hereafter as Dannecker et al. numerical results. It is interesting to notice that the temperature prediction at the solid-wall interface seem to be in better agreement with the experimental data compared with the present simulation. The mismatch with the experiments is however quite sensitive especially in the downstream section of the graph. At  $z = z_w + 0.1mm$  and  $z = z_w + 0.2mm$ , on the contrary, the present calculation reproduces quite well the experimental temperature profiles. At those locations the Dannecker et al. computation predicts similar temperature maxima but the temperature profile behaviors do not compare so well with the experiments. A temperature plateau in the downstream section is predicted but not observed in the experiments. In conclusion, considering the mentioned systematic experimental error in the thermocouple positioning the present calculation is much more in agreement with the experimental data.

### 2.4.2 Core Flow Temperature Profiles

In figure 2.4.2 the temperature profiles along a transverse sample line at  $x/D = 0.226$  (see figure 2.3.2 for the sample line positioning) is shown. Due to the improved boundary conditions at the diagonal swirler inlet section, the present numerical results (black solid line) agree very well with the experimental values especially close to the combustion chamber symmetry line ( $z/D = 0$ ) and near the wall. The improved boundary layer resolution seems to have a positive effect on the temperature prediction close to the wall. This improvement, from the fluid side, further validate the present numerical setup and reinforce the possibility of the existence of

a systematic error in the positioning of the wall thermocouples. The numerical results in the Dannecker et al. configuration over predict in general the temperature level in the core flow zone and in particular close to the wall. This temperature over prediction results in a higher wall temperature and explains the temperature profile differences in figure 2.4.1. The refined computation in figure 2.4.2 (black line), as already mentioned, reveals very steep temperature gradients close to the wall which must be taken into account at least for the determination of the experimental data errors. The transverse position ( $z/D$ ) of the temperature minimum seems to be over predicted by both numerical simulations as well as the thickness of the temperature mixing zone. It is important at this point to mention that the steady calculations showed oscillating residuals and non symmetrical temperature profiles. Thus, the question arises if the numerical instabilities found could be due to the existence of real physical flow unsteadiness and, in the positive case, if an averaged unsteady computation could be than capable of better predicting the measured temperature wake. This issues are investigated in the next section.

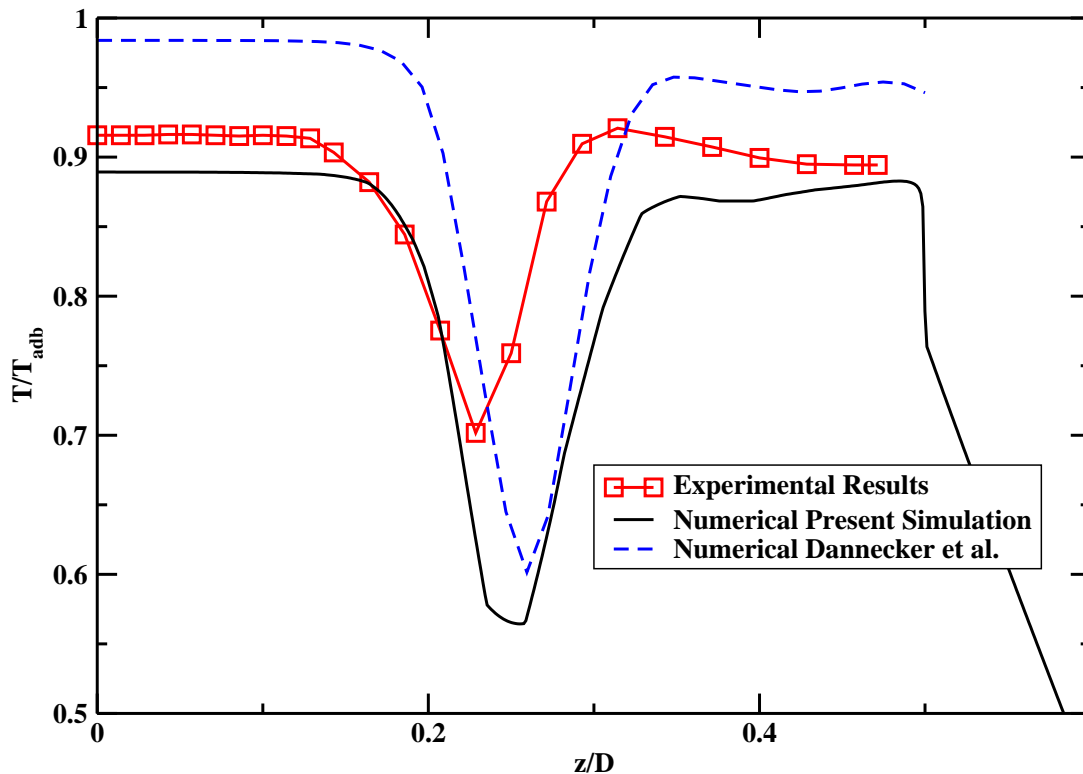


Figure 2.4.2: Transverse temperature profile,  $x/D = 0.226$

### 2.4.3 Effect of Flow Unsteadiness

As already mentioned in the previous section, the steady calculation performed with the new numerical setup showed unstable residuals suggesting the presence of physical flow instabilities.

In the following, the numerical results obtained performing an unsteady calculation are presented. The computational domain, boundary condition and numerical models are the same as in the previous case. The time resolved simulation showed the existence of self excited oscillations at the frequency of circa  $20Hz$ . The isotherm plot analysis showed the existency of a weak flame core precession in that frequency range. The effect of the flame unsteadiness on the wall temperature is reported in figure 2.4.3

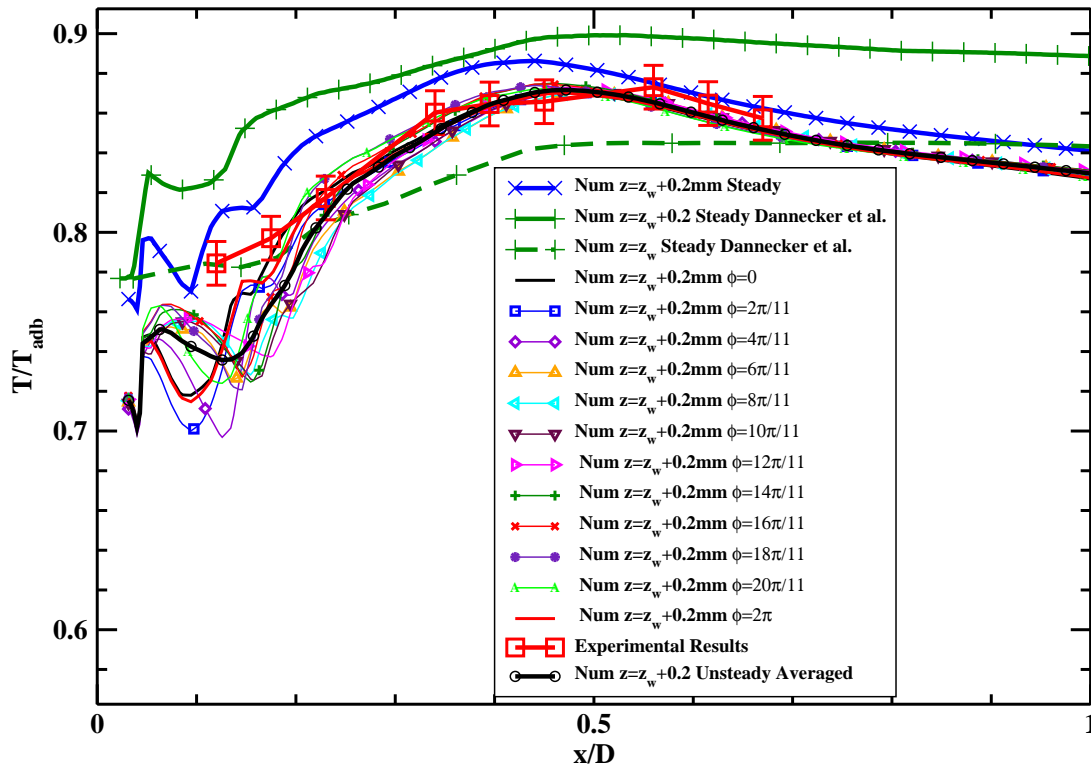


Figure 2.4.3: Wall temperature profile

At the wall a temperature profile periodicity of  $18Hz$  has been found. The colored thin lines with symbols refer to different time step at  $0.2mm$  above the fluid-solid interface. The thicker red and black continuous lines are considered as the phase zero and  $2\pi$  of a cycle. As can be seen in figure 2.4.3, the effect of flow unsteadiness on the temperature profiles seems to be limited to the first wall section ( $x/D < 0.3$ ). For comparison the average temperature profile is reported. It is interesting to point out the differences between the averaged unsteady results and the steady results. The steady results are reported with the thick blue line with crosses. Both profiles are taken at the location  $z = z_w + 0.2mm$ . The averaged unsteady results seems to agree better with the experimental results at  $x/D > 0.25$ . This is the zone in which the profiles variations in time are less sensitive. For comparison, in green, the temperature profile obtained in the Dannecker et al. configuration is reported at  $z = z_w$  and  $z = z_w + 0.2mm$ . The mismatch

between those results and the experimental data is quite evident. Probably due to the limited conjugate heat transfer section considered, the numerical temperature profile obtained in the Dannecker et al. configuration seems to predict a plateau in the downstream section which is not given in the experimental data. The temperature profiles at  $z = z_w + 0.2mm$  in the unsteady simulation, instead, agree very well with the experimental temperature decreasing at that location.

The convective wall heat transfer non dimensionalized by its maximum value has been plotted in figure 2.4.4. The unsteady results at each phase are reported as in figure 2.4.3 with thin colored lines with symbols. As in figure 2.4.3 the thicker red and black continuous lines indicate the phase zero and  $2\pi$  of the cycle. The heat flux wall profile obtained in the present configuration for the steady simulation is reported in the figure together with the averaged unsteady wall heat flux distribution. The difference between the two lines are quite large especially in the maxima and minima prediction. The flow instabilities seem to have quite a big impact on the wall heat flux prediction.

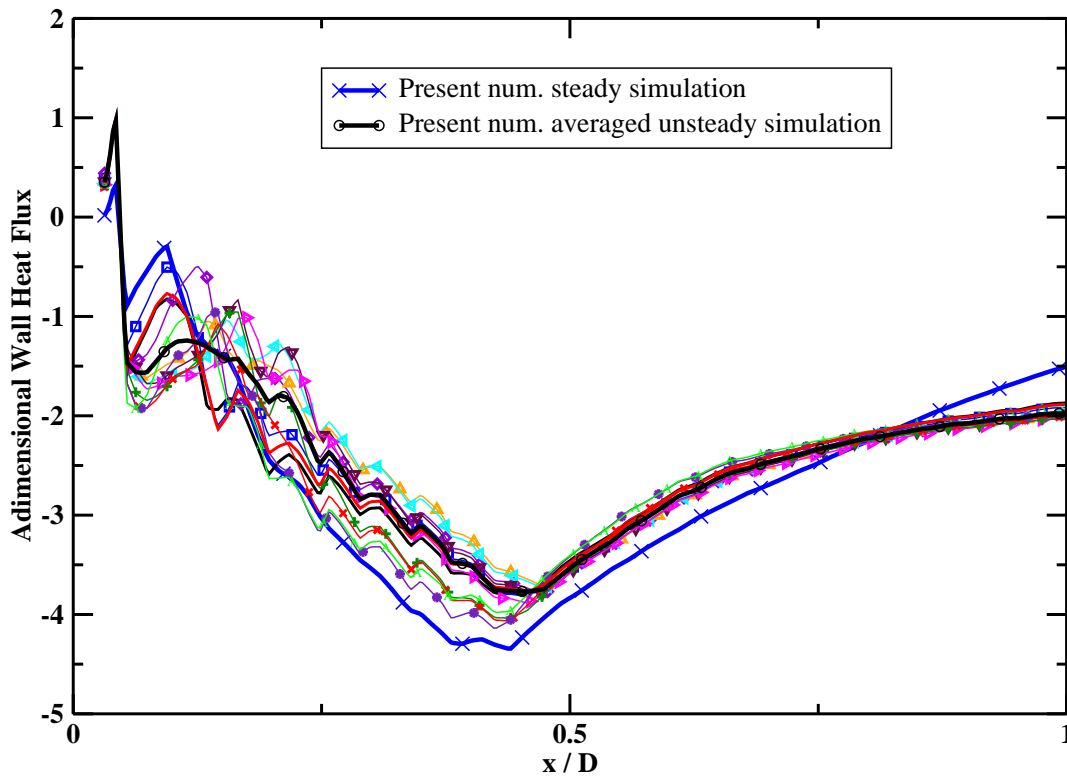


Figure 2.4.4: Wall heat flux profiles, unsteady results reported as in figure 2.4.3

On the contrary, the core flow temperature profiles are little affected by the flow unsteadiness as shown in figure 2.4.5. The instabilities mainly determine an oscillation of the minimum temperature in the diagonal swirler mixing region and of course more strongly affect the near



wall region ( $z/D > 0.35$ ). The physical temperature oscillations might be a reason for the numerical residual oscillations and the asymmetrical temperature field experienced in the steady calculations.

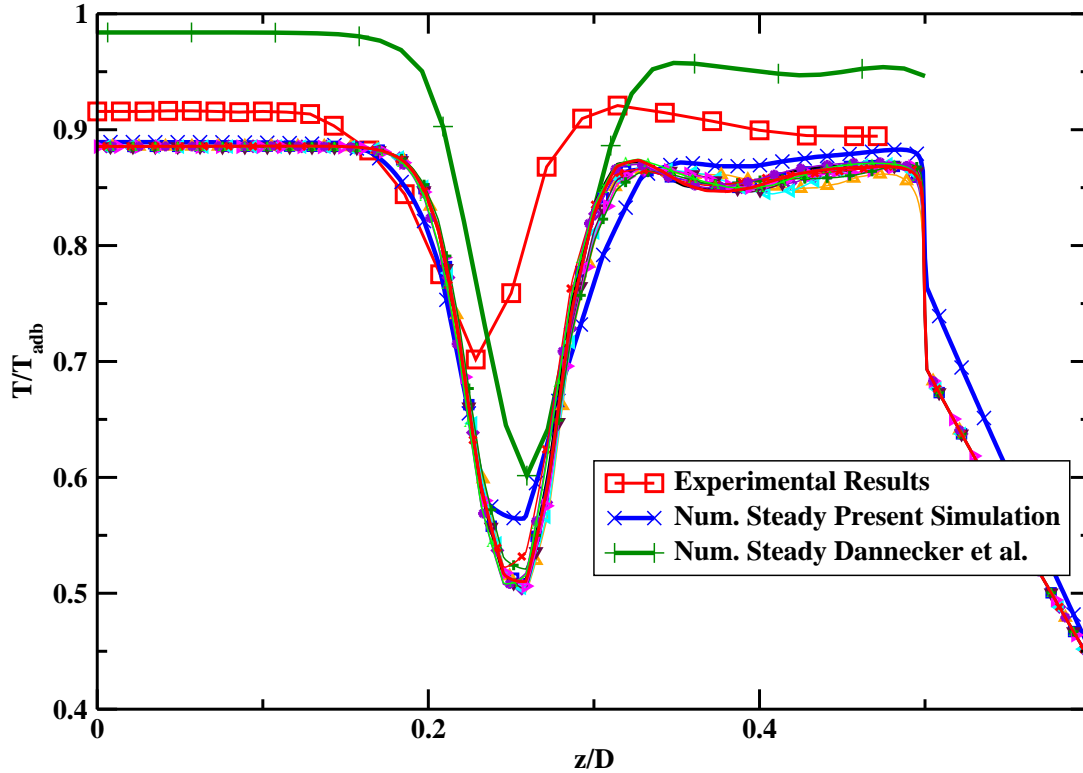


Figure 2.4.5: Transverse temperature profile,  $x/D = 0.226$ , unsteady results reported as in figure 2.4.3

The flow instabilities seem to have quite a big impact on the wall heat flux prediction which sensibly differs from the values predicted in the steady state simulation. In figure 2.4.4, the increasing and decreasing of heat flux values corresponds to the cooling and heating of the solid walls by the gas flow. The positive heat flux peak corresponds infact at the corner recirculation zones where the cold gases coming from the diagonal swirler have a cooling effect on the hot solid ceramic boundary. As can be seen from figure 2.4.6 there is a quite complicate flow pattern in the proximity of the combustion chamber back corners. As can be seen from the velocity cuts of figures 2.4.8 (a) and (b), a macro recirculation zone which reattaches at  $x/D = 0.43$  is evident and explains the global minimum of heat transfer in figure 2.4.4 at the same x coordinate. Within this macro vortical structure several vortex pairs can be recognized by means of vorticity plots. In figure 2.4.6 a) and b) the vorticity normal to the sample cuts is reported. An interesting correlation between the vorticity in the direction normal to the wall and the wall heat flux is presented in figure 2.4.7. Local maxima of heat transfer (minimum

heat transferred from the gas to the wall) seem to be correlated with the presence of counter rotating vortical structure with rotational axis normal to the wall figure 2.4.7 b ). The vortical structure pattern changes in time revealing a connection with the flow unsteadiness. Some vortical structure belonging to the macro recirculation zone seem to interact with the swirling flow coming from the diagonal swirler creating a peripheral swirler flow distortions that moves in a clockwise direction. In the instantaneous plot of figure 2.4.6 c) the distorted diagonal swirled flow corresponds to the distorted red ring in the middle of the transversal cut. In figure 2.4.8 a) and b) two velocity longitudinal cuts are reported at two different times in opposition of phase. It is evident that a similar flow pattern reproduce itself alternatively in the two opposite combustion chamber corners. The asymmetric flow patterns at the corners drift periodically the diagonal swirler incoming flow affecting the temperature field and more in particular the wall heat flux as reported in figure 2.4.4.

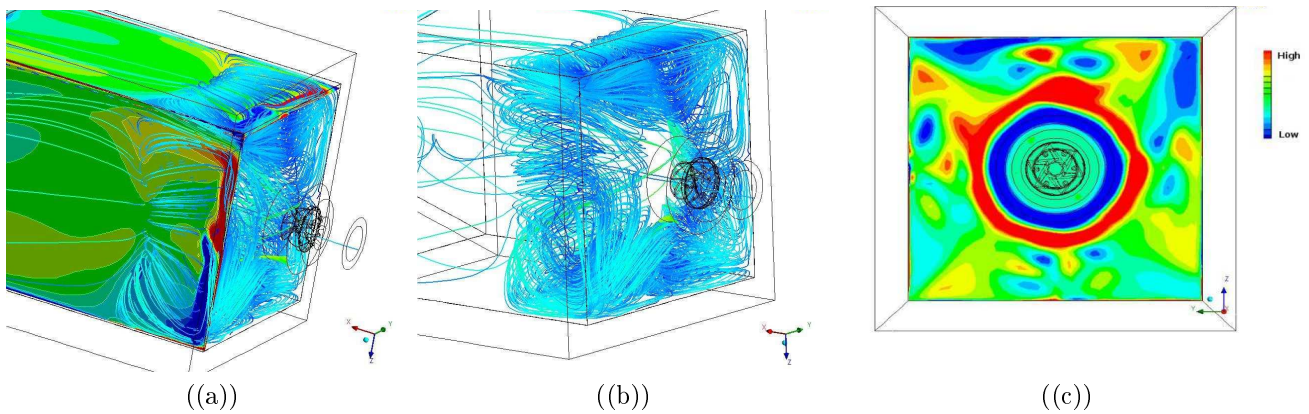


Figure 2.4.6: Unsteady simulation, instantaneous stream lines and vorticity plots.

## 2.5 Conclusions

The prediction of the wall heat load in combustion chamber applications is a complex task that involves the correct modeling of turbulent mixing, chemical reaction, turbulent convection, heat conduction in the solid and heat radiation. The capability of a commercial multi physics code ( ANSYS CFX ) to correctly predict the temperature level at the wall and in the core flow zone has been tested by experiments done at the University of Karlsruhe [70]. The work extend the results obtained in a previous numerical campaign from [21]. Improved results for the wall heat load prediction are obtained improving the wall grid resolution and the diagonal swirler inlet boundary conditions and by extending the conjugate heat transfer section to the entire liner walls.

The present numerical results suggest the existence of a systematic error in the positioning of the thermal probes. Due to the strong temperature gradient near the walls, the experimental results match well with the numerical results at  $0.2mm$  above the solid fluid interface. In addition the numerical simulations showed the presence of little flow instabilities that seem to affect the wall heat load predictions. The convective wall heat flux and temperature profiles are affected by the presence of flow unsteadiness. As it is shown in figure 2.4.4 the averaged

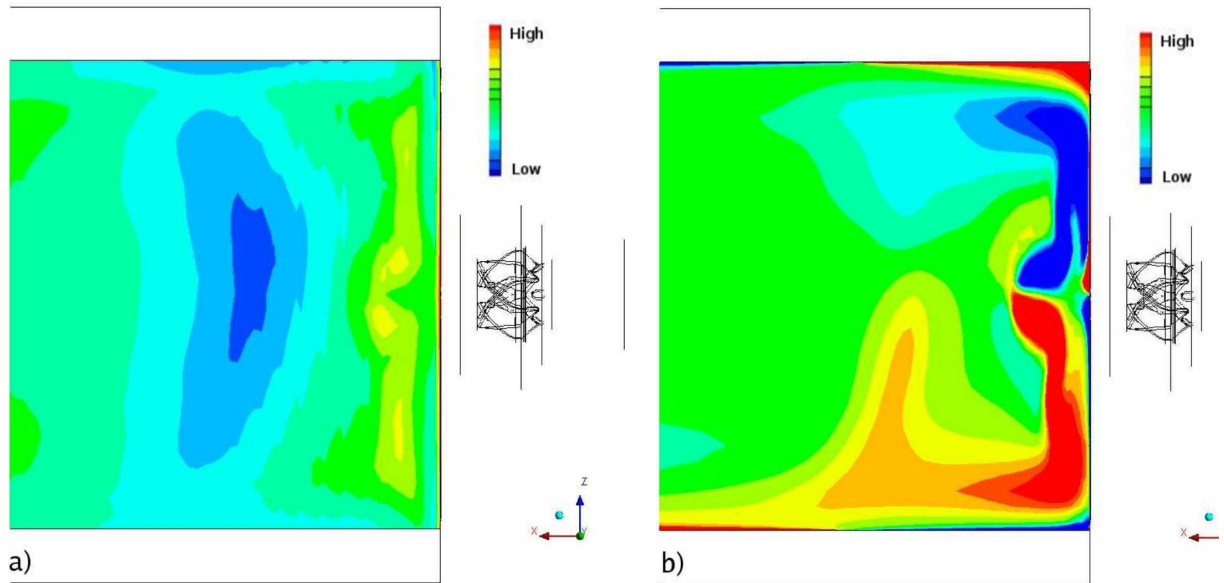


Figure 2.4.7: Unsteady simulation, Heat flux (a) and wall normal vorticity (b).

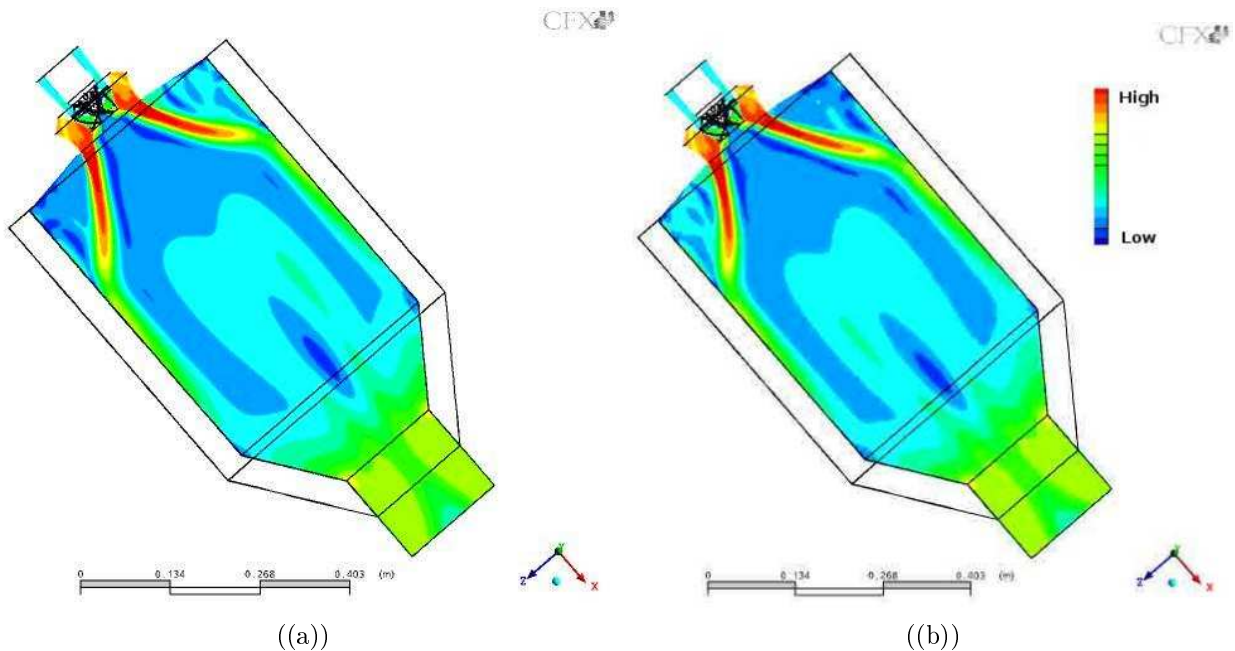


Figure 2.4.8: Velocity magnitude, longitudinal cuts,  $\phi = 0$  (a) and  $\phi = 12\pi/11$  (b).

unsteady numerical results predict both increasing and decreasing values of wall heat transfer with respect to the steady state numerical predictions. This effects are strong close to the corner recirculating zones. The position of the impinging point at the wall oscillates due to flow unsteadiness and the thermal boundary layer conditions are influenced by the consequent

longitudinal flow pulsations. The amplitude of the flow pulsations depend on the distance from the moving reattachment zone. In the present operating conditions relatively low frequency instabilities have been found (range of  $20Hz$ ). Higher frequencies have been however reported for the same test rig operating at other equivalence ratios. Since there is not much known on how flow pulsation can affect the thermal boundary layer and the wall heat load, the present findings reinforce the need for a more systematic investigation. However the agreement between numerical and experimental data for the temperature field prediction in this particular case with low unsteadiness is quite satisfactory but the non negligible effects of unsteadiness on the wall heat flux suggest that for the thermal design of such components, further investigations on the effects of frequency and pulsation amplitude on the thermal boundary layer are required.

# 3 Conjugate Heat Transfer Modeling

In the frame of the present work a coupled solver for the solution of the transient conjugate heat transfer problem was developed and validated against analytical solutions. The present results have been also reported in [62].

Time varying solutions were obtained in a multiphysics and multidomain configuration through an iterative boundary condition exchange procedure. Several transient problem were investigated: transient heat transfer in composite solids; the effect of oscillating inlet temperature in laminar forced convection and the transient heat transfer problem in developing and fully developed laminar pipe flow. The method seems to be accurate in time and well suited for the coupling of different specific numerical solvers in a multiphysics environment.

### 3.1 Introduction

Traditionally, the thermo-fluid design was primarily made for steady regimes and in this sense was always focused on the modeling of mean flow quantities. Nevertheless the attention on transient behavior of the energy-related systems during the period of start up, shutdown, changing of loading conditions or any off-normal operational conditions grew in the years together with the increasing need to procure precise thermal control of various heat exchange devices encountered in chemical processes, nuclear and non conventional energy systems ( such as the Stirling engines ). Such devices consist often of different composite material parts dynamically interacting with a thermo-fluid vector. Classically, for the solution of each particular thermal problem, different numerical approaches were used and different commercial programs were developed. With the growing attention on transient behaviors, the developed tools were often upgraded in order to handle specific unsteady problems. However, as soon as a more time accurate thermal control is sought, each single unsteady problem has to be combined in order to model all the thermally interacting parts. In this sense, instead of tackling the conjugate heat transfer problem developing a third problem-specific tool, a more comprehensive strategy is the development of a time accurate communication tool which can combine each fully validated existing solvers. The coupling is then made trough the inter-exchange of interface conditions between the codes. In the following an evaluation of this approach against available analytical solutions in different solid-fluid and solid-solid simple configurations is reported. The geometries considered are simple but representative of heat exchanger or combustor liner configurations. The domain coupling was simple but the problem formulation was kept quite general. Data interpolation problems between different domain discretizations were not addressed and the main objective of this investigation is to show that also a so called weak coupling (by means of interface conditions exchanging), thanks to sub iterative loops, can give good time accurate results.

### 3.2 Code Description

The calculations where performed using the OpenFoam solver [6], [83]. OpenFoam (Open Field Operation and Manipulation) is a CFD toolbox that uses finite volume numeric to solve systems of partial differential equations ascribed on any 3D unstructured mesh of polyhedral

cells. OpenFOAM is designed to be a flexible, programmable environment for simulation by having top-level code that is a direct representation of the equations being solved. The solver can handle multiple domains and different equations can be solved in each domain. The top-level code used for our computations has been customized to each case depending on the physics to be solved in each sub-domain. For the transient heat transfer simulation in composite solids the Laplace equations for heat conduction is solved separately in each sub domain with different thermal material properties. For the unsteady forced convection cases the laminar Navier-Stokes equations were solved in the fluid region and the Laplace equations were solved in the solid material.

The coupling between different region is ensured at the interfaces using a FFTB method (Flux Forward, Temperature Back) [25]. The method is briefly described in the following. At the interface of two different regions the heat flux and the temperature must be conserved.

$$T_1|_{\partial_{1-2}} = T_2|_{\partial_{2-1}} \quad (3.2.1)$$

$$K_1 \frac{\partial T_1}{\partial n}|_{\partial_{1-2}} = K_2 \frac{\partial T_2}{\partial n}|_{\partial_{2-1}} \quad (3.2.2)$$

This can be achieved using an inner iterative loop. The boundary heat flux at the common interface in the second domain is prescribed equal to the calculated heat flux in the first domain (Flux Forward). With this Neumann boundary condition the temperature distribution on the second domain can be computed and the temperature profile at the common interface obtained is prescribed back to the first domain as a Dirichlet boundary condition (Temperature Back). The temperature distribution and the heat flux are then computed in the first domain and the loop is iterated till the temperature and heat flux differences at the two domain common interface are below the desired numerical error. When the convergence is reached the physical time step is incremented.

$$K_2 \frac{\partial T_2^{n+1}}{\partial n}|_{\partial_{2-1}} = K_1 \frac{\partial T_1^n}{\partial n}|_{\partial_{1-2}} \quad (3.2.3)$$

$$T_1^{n+1}|_{\partial_{1-2}} = T_2^n|_{\partial_{2-1}} \quad (3.2.4)$$

### 3.3 Code Validation

The code has been validated against analytical results in the case of transient heat transfer in a composite slab [15] and forced convection in laminar flow [57]. A comparison with the numerical results of Sucec and Sawant [78] in the case of oscillating inlet condition in laminar plate duct is also reported.

In figure 3.3.1 (b) the temperature distribution in a composite slab of thickness  $2t$  is plotted at different times ( $\tau$ ). The slab consists of two solidly joined plates of thickness  $t$  with different thermal conductivity ( $K_1 = 34[Wm^{-1}K^{-1}]$ ,  $K_2 = 65[Wm^{-1}K^{-1}]$ ) and same thermal diffusivity ( $\alpha_1 = \alpha_2 = 2.4 \cdot 10^{-5}[m^2s^{-1}]$ ). The slab at time,  $\tau = 0$  is supposed at the same temperature

$T_2 = 0[K]$  and at time  $\tau > 0$  one external surface is abruptly set at  $T = T_1 = 400[K]$  while the other is kept at  $T = T_2$ . A sketch of the case is reported in figure 3.3.1 (a).

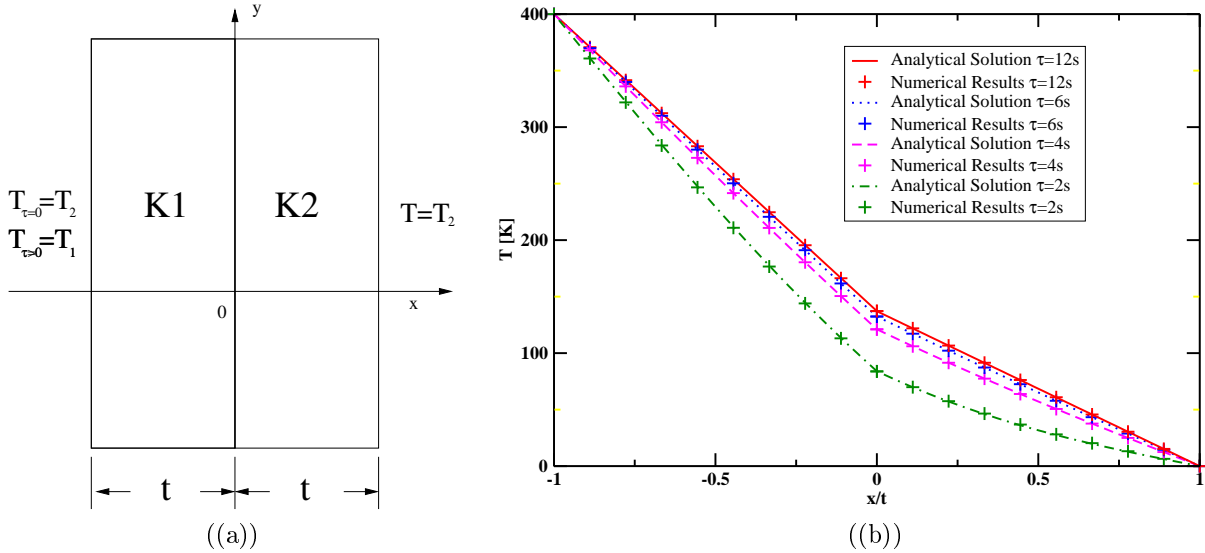


Figure 3.3.1: Composite slab case, configuration (a) and temperature profiles at different time steps(b).

In figure 3.3.3 forced convection in a laminar pipe flow is considered. The non-dimensional temperature distribution in the fluid and solid pipe wall region is displayed at different non-dimensional time steps ( $\tau = \frac{\nu_f t}{R_i^2}$ , where  $\nu_f$  is the fluid kinematic viscosity and  $R_i$  is the pipe inner radius, see figure 3.3.2). The pipe and the fluid considered have a heat conductivity ( $K_r = \frac{K_s}{K_f}$ ) and heat diffusivity ratio ( $\alpha_r = \frac{\alpha_s}{\alpha_f}$ ) of 10 and 1. The fluid enters the pipe at the axial position  $x = 0$  with inlet temperature  $T_i$ . The outer pipe wall, initially at the same temperature of the fluid, at time  $\tau > 0$ , is suddenly set at a different temperature  $T_w$ , with  $T_w < T_i$ . In the figure 3.3.3, two flow conditions were considered. In figure 3.3.3 (a) the flow is considered hydraulically developing along the pipe and the temperature profiles refers to the non-dimensional axial position  $X = \frac{2x}{R_i Re} = 0.1$  where  $Re$  is the fluid Reynolds number ( $Re = \frac{2R_1 U_m}{\nu_f}$ ) based on the averaged pipe flow velocity  $U_m$ . The results are compared with the numerical data from Al-Nimr [12]. In figure 3.3.3 (b) the flow is hydraulically fully developed and it thermally develops along the pipe. The plot in this case refers to the non-dimensional axial position  $X = 0.7$  and the results are compared with the analytical solution [57].

The last comparison has been done with the numerical results from Sucec and Sawant [78]. They considered a fully developed laminar flow in a parallel plate duct. The outer solid wall were considered thermally insulated and the inlet temperature oscillates as follows:

$$T_i = T_m + \Delta T_0 \sin(\omega t) \quad (3.3.1)$$



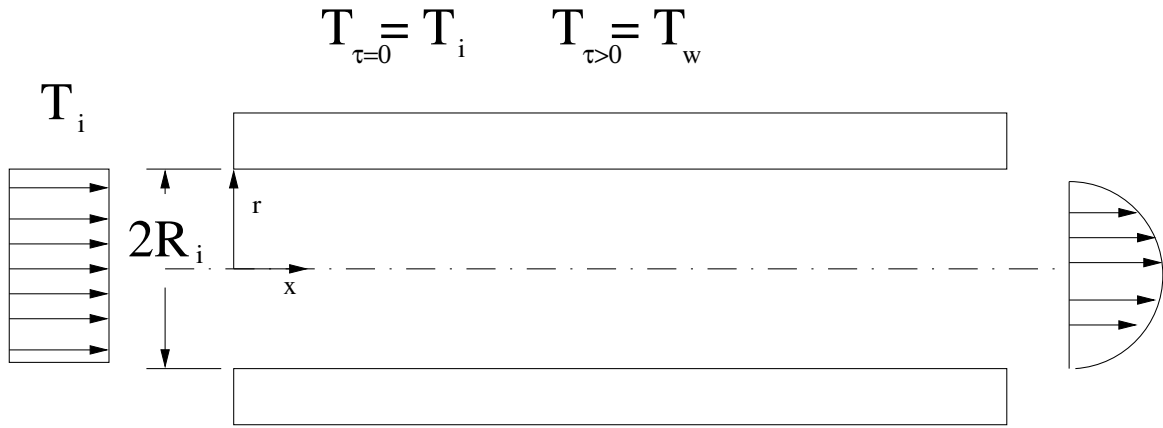


Figure 3.3.2: Forced convection in a laminar pipe flow. Case configuration.

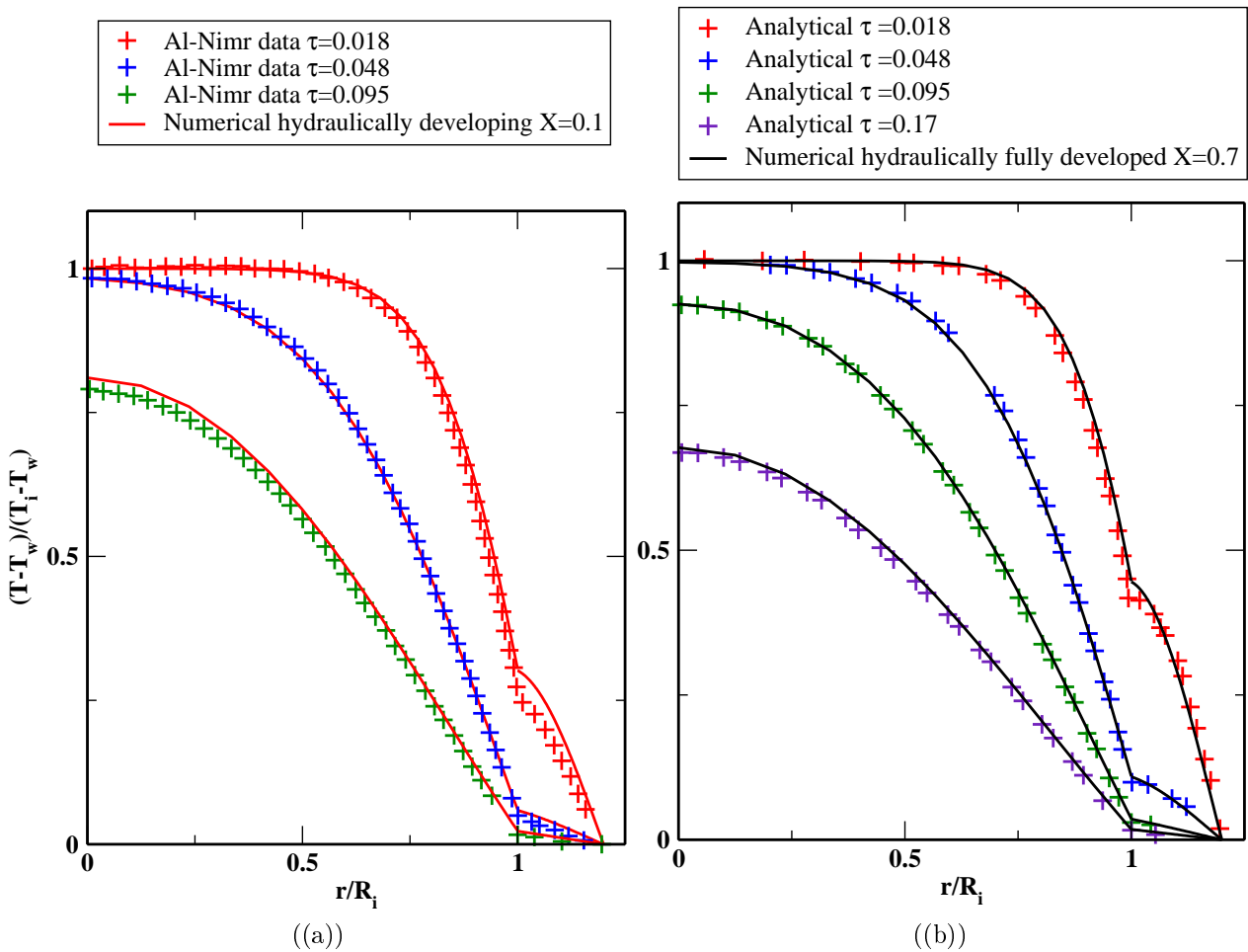


Figure 3.3.3: Temperature distribution, conjugate laminar pipe flow.

In figure 3.3.4 the non-dimensional wall ( $\theta_w/\Delta T_0$ ) and bulk ( $\theta_b/\Delta T_0$ ) flow temperature are reported in time for different value of the non-dimensional axial position  $X = \alpha_f x / R^2 U_m$  where R is the half distance between the flat plates.

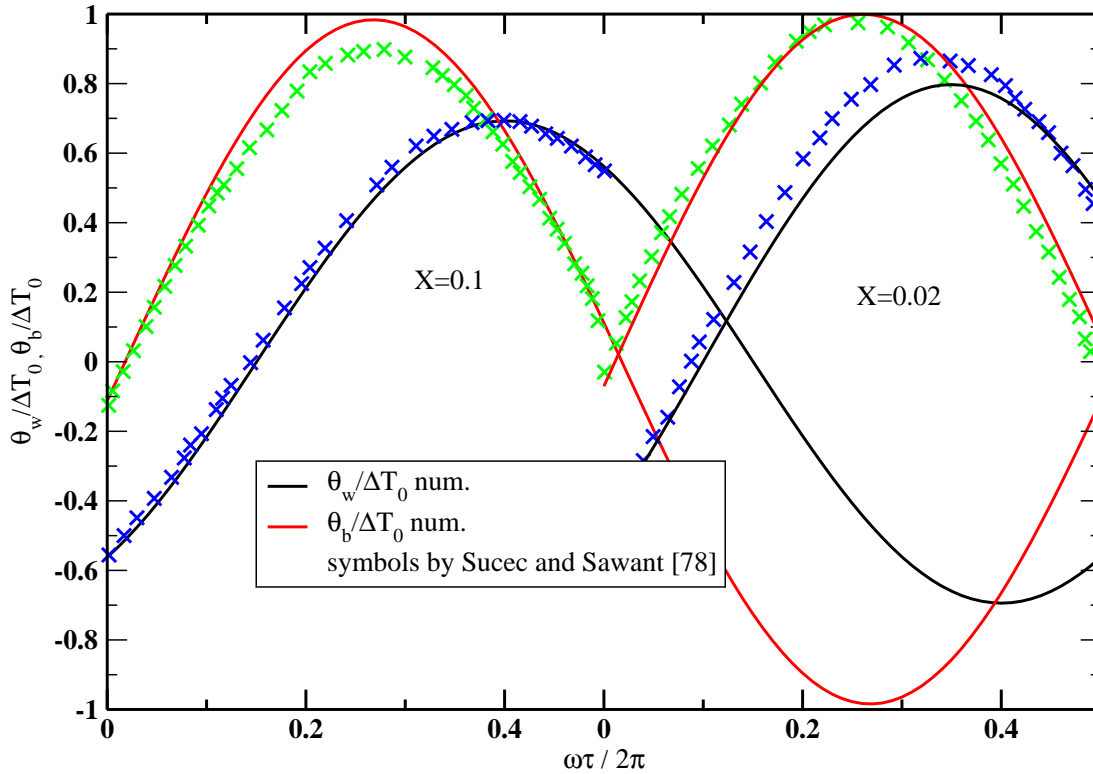


Figure 3.3.4: Wall and center line temperature, conjugate laminar pipe flow with oscillating inlet temperature.

### 3.4 Conclusions

For the solution of the thermal coupled problem, the interface coupling presented is an alternative to the solution of a fully coupled monolithic system. The advantage resides in the possibility of utilizing existing dedicated solvers for the coupled solution of specific interacting thermo-physical problems. Regarding the computational time, the method effectiveness depends strongly on the problem size. In the test cases presented, for each time step the number of sub iterative steps rarely exceeded 10. The number of sub-steps depends on the physical time step chosen and could be easily problem optimized. Despite their simplicity, it is however important to point out that the presented test cases are representative of many interesting industrial problems which could be effectively solved using the proposed approach.

## 4 Thermo-Fluid Dynamics Problem: Fundamental Equations

The conservation laws of mass, momentum and energy can be written in a generic curvilinear coordinate system and for a single species compressible gas as follows:

$$\frac{\partial \rho}{\partial t} + \nabla \cdot (\rho \vec{u}) = 0 \quad (4.0.1)$$

$$\frac{\partial \rho \vec{u}}{\partial t} + \nabla \cdot (\rho \vec{u} \vec{u}) - \nabla \cdot \underline{\tau} + \nabla p = 0 \quad (4.0.2)$$

$$\frac{\partial \rho h}{\partial t} + \nabla \cdot (\rho h \vec{u}) = \frac{Dp}{Dt} + \underline{\tau} : \nabla \vec{u} - \nabla \cdot \vec{q} \quad (4.0.3)$$

where  $\rho$  is the fluid density,  $\vec{u}$  is the velocity vector,  $\underline{\tau}$  is the shear stress tensor,  $p$  the fluid pressure,  $h$  the fluid enthalpy,  $\vec{q}$  the heat flux vector and the double dot product is defined as follows [73]:

$$\nabla \cdot (\underline{\tau} \vec{u}) = \underline{\tau} : \nabla \vec{u} + \vec{u} \cdot \nabla \cdot \underline{\tau} \quad (4.0.4)$$

The tensorial notation which makes use of the nabla operator,  $\nabla$  is very convenient for its generality and compactness. For a Cartesian coordinate system the above equation can be easily converted in the more familiar Einstein notation considering the nabla operator as a simple vector of the form:

$$\nabla = \left( \frac{\partial}{\partial x}, \frac{\partial}{\partial y}, \frac{\partial}{\partial z} \right) \quad (4.0.5)$$

Unfortunately even expressing the nabla operator in the right form depending on the reference system, this analogy is not consistent for a general curvilinear coordinate system and each term involving nabla must be reformulate using the covariant differentiation notation [73](see appendix A).

For a Newtonian fluid,  $\underline{\tau}$  can be expressed in both the Einstein and tensorial notation as

$$\tau_{ij} = \mu \left( \frac{\partial u_i}{\partial x_j} + \frac{\partial u_j}{\partial x_i} \right) - \frac{2}{3} \mu \delta_{ij} \frac{\partial u_k}{\partial x_k} \quad (4.0.6)$$

$$\underline{\tau} = \mu \nabla \vec{u} + \mu \nabla \vec{u}^T - \mu \frac{2}{3} Tr(\nabla \vec{u}^T) I. \quad (4.0.7)$$

Where  $Tr$  is the operator trace and  $I$  is the identity matrix. The heat flux vector can be modeled using the Fourier law:

$$\vec{q} = -\lambda \nabla T = -\rho \alpha \nabla h. \quad (4.0.8)$$

In the hypothesis of constant density flow (low speed and small temperature differences) the energy equation can be transformed in the temperature equation:

$$\frac{\partial T}{\partial t} + \nabla \cdot (T \vec{u}) = \alpha \nabla^2 T \quad (4.0.9)$$

where the viscous term  $\underline{\tau} : \nabla \vec{u}$  has been neglected and the fluid thermal capacity  $c_p$  has been considered constant. The pressure term  $\frac{Dp}{Dt}$  can also be neglected due to the incompressibility assumption.

Equations 4.0.1 to 4.0.3, together with the constitutive equations 4.0.6, 4.0.8 and a fluid specific thermodynamic relation between pressure density and temperature (for air, the law of perfect gas:  $p = \rho RT$ ) represent a closed system of partial differential equations. Providing the necessary temporal and spatial accuracy the equation system can be directly numerically solved (Direct Numerical Simulation or DNS). In the range of validity of the continuum hypothesis, DNS simulations are able to describe with great accuracy all the fluid flow structures down to the Kolmogorov length scale.

## 4.1 Stability of the Fundamental Equations and Transition to Turbulence

Due to the non-linearities present in the fundamental equations (4.0.1 to 4.0.3), for specific flow conditions, the system solution can be strongly unstable. This reflects the physical laminar-turbulent behavior of viscous flows. Stable solutions correspond to laminar flow conditions. Following the mathematical definition of stability, a system of equations admits a stable solution when small perturbations in the boundary conditions determine small (bounded) and continuous variations of the system solution. A flow in a so-called laminar regime, when perturbed tends either to fall back in its unperturbed configuration or exhibits periodical (bounded) oscillations which eventually die in the far field flow (i.e. laminar vortex shedding). The flow stability depends on the particular flow condition and an important stability parameter is represented by the so-called flow Reynolds Number:

$$Re = \frac{UD}{\nu}, \quad (4.1.1)$$

where  $\nu$  is the flow viscosity and  $U$  and  $D$  represent respectively a characteristic flow velocity and dimension. For Reynolds Numbers above a critical value the flow is unstable and small perturbations can lead to the appearance of chaotic flow structures typical of turbulent flow regimes. As already mentioned, providing the necessary accuracy required to resolve all the small turbulent structures, DNS is able to describe accurately high complex turbulent flows. Unfortunately, due to the high spatial and temporal resolution required, DNS computational time is unrealistic for practical applications. In those cases turbulence modeling can help to reduce the spatial and temporal resolution and different approaches are available and will be discussed in Chapter 4.2 and 4.5.

## 4.2 URANS - Unsteady Reynolds Averaged Navier-Stokes Equations

In turbulent flow condition, a possible alternative to the direct numerical simulation (DNS) of the Navier-Stokes equations, without the already mentioned strong restrictions on the spatial and temporal accuracy, is the so called Unsteady Reynolds Averaged Navier-Stokes (URANS) approach [27]. Extending the idea of Reynolds [68] for steady turbulent flows to general unsteady flows, an instantaneous turbulent fluid characteristics  $f(\vec{x}, t)$  (being  $f$  velocity, temperature, pressure etc.) can be expressed as the summation of an ensemble averaged value  $\langle f(\vec{x}, t) \rangle$  and a turbulent fluctuation  $f'(\vec{x}, t)$ :

$$f(\vec{x}, t) = \langle f(\vec{x}, t) \rangle + f'(\vec{x}, t), \quad (4.2.1)$$

where  $\vec{x}$  and  $t$  represent respectively a coordinate and time position. The ensemble averaging operator can be defined as

$$\langle f(\vec{x}, t) \rangle = \lim_{n \rightarrow \infty} \left( \frac{1}{n} \sum_{k=1}^n f^k(\vec{x}, t) \right), \quad (4.2.2)$$

where  $f^k$  represents, physically, the value of the quantity  $f$  at time  $t$  and at position  $\vec{x}$  during the  $k^{th}$  experiment realization. The probability density function of  $f$  depends on the flow turbulence. The ensemble averaging operator filters out the contribution of the turbulence fluctuations and the Navier-Stokes equations can be then rewritten just in terms of the averaged variables. The effect of the turbulence is then assembled in the additional terms of the equations which need a closure for its determination.

In steady flow applications, the ensemble average operator is often confused with the so called Reynolds averaging operator which, for historical reason, names the method:

$$\bar{f}(\vec{x}) = \lim_{T \rightarrow \infty} \left( \frac{1}{T} \int_0^T f(\vec{x}, t) dt \right). \quad (4.2.3)$$

For steady flows,  $\bar{f}(\vec{x}) = \langle f(\vec{x}, t) \rangle$  and  $\langle f(\vec{x}, t) \rangle$  is constant in time. A generic quantity  $f$  can be expressed then as:

$$f(\vec{x}, t) = \bar{f}(\vec{x}) + f'(\vec{x}, t). \quad (4.2.4)$$

For unsteady flows, a triple decomposition can be also performed, which also explains the difference between Reynolds averaging and ensemble averaging operators:

$$f(\vec{x}, t) = \langle f(\vec{x}, t) \rangle + f'(\vec{x}, t) = \bar{f}(\vec{x}) + \check{f}(\vec{x}, t) + f'(\vec{x}, t) \quad (4.2.5)$$

For a detailed explanation on the terms involved in the triple decomposition see chapter 6.1.

Due to the properties of turbulence and the definition of the averaging operators, the following properties are valid:

$$\langle f'(\vec{x}, t) \rangle = 0 \quad (4.2.6)$$

$$\langle \langle f(\vec{x}, t) \rangle \rangle = \langle f(\vec{x}, t) \rangle \quad (4.2.7)$$

For compressible flows another useful averaging operator called the Favre operator can be defined as follows:

$$\tilde{f}(\vec{x}, t) = \frac{1}{\langle \rho \rangle} \lim_{n \rightarrow \infty} \left( \frac{1}{n} \sum_{k=1}^n \rho^k f^k(\vec{x}, t) \right) \quad (4.2.8)$$

An instantaneous value of  $f$  can be then expressed also in the form:

$$f(\vec{x}, t) = \tilde{f}(\vec{x}, t) + f''(\vec{x}, t), \quad (4.2.9)$$

and the following are valid:

$$\tilde{f}(\vec{x}, t) = \frac{\langle \rho f(\vec{x}, t) \rangle}{\langle \rho \rangle} \quad (4.2.10)$$

$$\langle \rho f g \rangle = \langle \rho \rangle \tilde{f} \tilde{g} + \langle \rho f'' g'' \rangle \quad (4.2.11)$$

where  $g$  is another generic fluid characteristics.

For compressible flows, the application of the Favre averaging to equations from 4.0.1 to 4.0.3 leads to the following system of equations:

$$\frac{\partial \langle \rho \rangle}{\partial t} + \nabla \cdot (\langle \rho \rangle \vec{u}) = 0 \quad (4.2.12)$$

$$\frac{\partial \langle \rho \rangle \vec{u}}{\partial t} + \nabla \cdot (\langle \rho \rangle \vec{u} \vec{u}) = \nabla \cdot (\langle \tau \rangle - \langle \rho \vec{u}'' \vec{u}'' \rangle) - \nabla \langle p \rangle \quad (4.2.13)$$

$$\frac{\partial \langle \rho \rangle \tilde{h}}{\partial t} + \nabla \cdot (\langle \rho \rangle \tilde{h} \vec{u}) = \frac{D \langle p \rangle}{Dt} + \langle \tau : \nabla \vec{u} \rangle - \nabla \cdot (\langle \vec{q} \rangle - \langle \rho h'' \vec{u}'' \rangle) \quad (4.2.14)$$

In analogy with 4.0.7 the averaged stress tensor becomes :

$$\langle \tau \rangle = \tilde{\mu} \nabla \vec{u} + \tilde{\mu} \nabla \vec{u}^T - \tilde{\mu} \frac{2}{3} Tr(\tilde{\mu} \nabla \vec{u}^T) \quad (4.2.15)$$

where

$$\tilde{\mu} = \mu(\tilde{T}). \quad (4.2.16)$$

The averaged heat flux can be written as:

$$\langle \vec{q} \rangle = -\langle \lambda \nabla T \rangle = -\langle \rho \alpha \nabla h \rangle = -\langle \rho \rangle \alpha \nabla \tilde{h}. \quad (4.2.17)$$

Neglecting the second term of the right hand side of the equation 4.2.14, two new unknowns appear in the set of equations:

the turbulence stress tensor

$$\langle \underline{\tau} \rangle_t = -\langle \rho \vec{u}'' \vec{u}'' \rangle \quad (4.2.18)$$

and the turbulent heat flux

$$\langle \vec{q} \rangle_t = \langle \rho h'' \vec{u}'' \rangle \quad (4.2.19)$$

The modeling of these two new terms generally make use of the Boussinesq analogy ( for the turbulent Reynolds stress tensor ) and the Reynolds analogy ( for the turbulent heat flux ) as follows:

$$\langle \underline{\tau} \rangle_t = \mu_t \nabla \vec{u} + \mu_t \nabla \vec{u}^T - \mu_t \frac{2}{3} Tr(\nabla \vec{u}^T) \quad (4.2.20)$$

and

$$\langle \vec{q} \rangle_t = -\langle \rho \rangle \alpha_t \nabla \tilde{h} \quad (4.2.21)$$

where  $\mu_t$  and  $\alpha_t$  are the turbulent viscosity and the turbulent heat diffusivity. The heat diffusivity as well as its turbulent counterpart are generally derived from the assumption of a constant Prandtl Number:

$$Pr_t = \frac{\nu_t}{\alpha_t} \quad (4.2.22)$$

$$Pr = \frac{\nu}{\alpha} \quad (4.2.23)$$

In this hypothesis, the energy and momentum equation are assumed to be similar:

$$\begin{aligned} \frac{\partial \langle \rho \rangle}{\partial t} + \nabla \cdot (\langle \rho \rangle \vec{u}) &= 0 \\ \frac{\partial \langle \rho \rangle \vec{u}}{\partial t} + \nabla \cdot (\langle \rho \rangle \vec{u} \vec{u}) &= \nabla \cdot \left[ (\tilde{\mu} + \mu_t) \left( \nabla \vec{u} + \nabla \vec{u}^T - \frac{2}{3} Tr(\nabla \vec{u}^T) \right) \right] - \nabla \langle p \rangle v \quad (4.2.24) \\ \frac{\partial \langle \rho \rangle \tilde{h}}{\partial t} + \nabla \cdot (\langle \rho \rangle \tilde{h} \vec{u}) &= \nabla \cdot \left( \left( \frac{\tilde{\mu}}{Pr} + \frac{\mu_t}{Pr_t} \right) \nabla \tilde{h} \right) - \frac{D \langle p \rangle}{Dt} \end{aligned}$$

In a boundary layer flow, neglecting the flow derivative in the stream-wise direction, the heat transfer and the wall shear stress can be expressed as:



$$\langle \vec{q} \rangle = -\langle \rho \rangle (\alpha + \alpha_t) \frac{d\bar{h}}{dy} = -\left( \frac{\bar{\mu}}{Pr} + \frac{\mu_t}{Pr_t} \right) \frac{d\bar{h}}{dy}$$

$$\langle \vec{\tau} \rangle = (\mu + \mu_t) \frac{d\bar{u}}{dy}.$$

The wall heat transfer and the wall shear stress are then proportional and, since the Prandtl numbers (  $Pr$  and  $Pr_t$  ) are considered fixed, they depend strongly on the turbulent viscosity modeling.

For an incompressible flow, if the flow unsteadiness occurs at a time scale considerably different from the turbulence time scales, the ensemble average operator can be replaced with the Reynolds averaging operator assuming:

$$\langle f(\vec{x}, t) \rangle = \overline{f(\vec{x}, t)} = \lim_{n \rightarrow \infty} \left( \frac{1}{n} \sum_{k=1}^n f^k(\vec{x}, t) \right) = \frac{1}{\mathcal{T}} \int_{-\mathcal{T}/2}^{\mathcal{T}/2} f(\vec{x}, t + \tau) d\tau \quad (4.2.25)$$

The time integration period  $\mathcal{T}$  is to be chosen large enough compared with the turbulence time scale but still small compared with the time scale of all the other unsteady phenomena [36].

The fundamental system of equation can be then rewritten as

$$\nabla \cdot (\vec{u}) = 0 \quad (4.2.26)$$

$$\frac{\partial \vec{u}}{\partial t} + \nabla \cdot (\vec{u}\vec{u}) = \nabla \cdot \left( \frac{\vec{\tau}}{\bar{\rho}} - \overline{u'u'} \right) - \frac{\nabla \bar{p}}{\bar{\rho}} \quad (4.2.27)$$

$$\frac{\partial \bar{T}}{\partial t} + \nabla \cdot (\bar{T}\vec{u}) = \nabla \cdot \left( \alpha \nabla \bar{T} - \overline{u'T'} \right) \quad (4.2.28)$$

Here the energy equation has been substituted with the temperature equation 4.0.9.

## 4.3 Turbulent Boundary Layers: the Law of the Wall

The effect of solid boundaries on turbulent viscous fluid flows resides often just in a thin layer called the turbulent boundary layer. Turbulent boundary layer have been intensively studied since the early 30<sup>s</sup> and many attempts to derive an universal law for the boundary layer velocity profile have been made in different flow conditions ( see [67], [82], [56], [17], [18] and [77])

Outside the boundary layer the so called free-stream velocity conditions ( $Ue$ ) can be determined assuming the flow practically inviscid. The boundary layer thickness ( $\delta$ ) is defined as the distance from the wall where the fluid velocity is  $0.99Ue$  [37].

Inside the boundary layer thanks to the studies of Prandtl and von Karman on steady flows over a flat plate, two sub-layers, the so called inner and outer layer can be recognized. Indicating with  $y$  the normal distance to the wall, the outer layer resides generally in between  $0.2\delta$  and  $\delta$  [85]. The outer layer is affected by the free-stream velocity and pressure gradient. The inner layer instead has a more universal character and can be decomposed in three sub-layers: the

logarithmic region, the buffer layer and the linear sub-layer [85], [37]. If a non-dimensional velocity and wall distance is introduced as follows:

$$y^+ = \frac{\bar{u}_\tau y}{\nu} \quad (4.3.1)$$

$$u^+ = \frac{\bar{u}}{\bar{u}_\tau}, \quad (4.3.2)$$

where  $\bar{u}_\tau$  is the skin friction velocity,

$$\bar{u}_\tau = \sqrt{\frac{\bar{\tau}_w}{\bar{\rho}}} \quad (4.3.3)$$

it can be observed that the linear sub-layer is confined between  $0 < y^+ < 5$ , the buffer layer between  $5 < y^+ < 40$  and the logarithmic region extends from the limit of the inner layer,  $y^+ = 40$  to the beginning of the outer layer. The velocity profiles in the linear sub-layer and in the logarithmic layer can be analytically expressed as follows

$$u^+ = \begin{cases} y^+ & 0 < y^+ < 5 \\ \frac{1}{\kappa} \ln y^+ + C & y^+ > 40. \end{cases} \quad (4.3.4)$$

where  $\kappa$  and  $C$  are equal to 0.41 and 5.2 respectively. Note that the Reynolds averaging operator (over bar) has been used for the velocity ( $\bar{u}$ ) since a steady flow is considered.

If heat transfer is also present, in analogy to the skin friction velocity, a skin friction temperature can be defined as:

$$\bar{T}_\tau = -\frac{\bar{q}_w}{\bar{\rho}c_p\bar{u}_\tau} \quad (4.3.5)$$

and a non-dimensional wall temperature as

$$\theta^+ = \frac{\bar{T} - T_w}{T_\tau}. \quad (4.3.6)$$

It can be shown that in analogy to the logarithmic law for the velocity a logarithmic law for the temperature profile is also valid:

$$\theta^+ = \frac{1}{\kappa_\theta} \ln y^+ + A_\theta \quad (4.3.7)$$

where

$$A_\theta = 3.7Pr^{2/3} - 7.5 \quad (4.3.8)$$

and for the Reynolds analogy [37] the ratio of  $\kappa$  and  $\kappa_\theta$  is a constant and equal to the turbulent Prandtl number:

$$Pr_t = \frac{\nu_t}{\alpha_t} = \frac{\kappa}{\kappa_\Theta} \quad (4.3.9)$$

The turbulence model and hence the definition of the turbulent viscosity have to take into account these so called universal laws of the wall. It is important to notice that all these findings are valid for steady and in equilibrium boundary layers and cannot be in general extended to unsteady boundary layers without a deeper investigation on the phenomena involved.

## 4.4 Turbulence Modeling

### 4.4.1 High Reynolds Number Turbulence Model with Wall Functions

Several turbulence closure are available. Depending on the number of partial differential transport equations needed for the definition of the turbulent viscosity, one, two or more equation models can be distinguished. In the following the attention will be focused just on the first-order closure models which refer on the already mentioned Boussinesq analogy.

Assuming valid (4.2.20) and (4.2.21), the turbulence closure problem is then shifted on the determination of  $\nu_t$  and  $\alpha_t$ . A further assumption can be made, for many common flows, on the constancy of the turbulent Prandtl number. As pointed out by [44], the simplest assumption of  $Pr_t = 1.0$  is quite accurate for air, water and even oil boundary layer flows. The only unknown remains the turbulent viscosity.

Since  $\nu_t$  has the dimensions of  $[m^2/s]$ , the turbulence closure problem can be viewed as the problem of the determination of a suitable turbulent time and length scale which can univocally define  $\nu_t$ . A turbulent energy scale is in general offered by the modeling of the transport equation of the turbulent kinetic energy defined as:

$$k = \frac{1}{2} \langle u'_i u'_i \rangle \quad \text{or} \quad k = \frac{1}{2} \overline{u'_i u'_i}.$$

In the following, in order to simplify the notation, the Reynolds averaging will be used instead of the ensemble averaging operator.

The transport equation for the turbulent kinetic energy can be obtained by a simple contraction of the Reynolds stress equations [59]. For an incompressible flow the Reynolds stress equation:

$$\frac{\partial \overline{u'_i u'_j}}{\partial t} + \bar{u}_j \frac{\partial \overline{u'_i u'_j}}{\partial x_j} = \nu \nabla^2 \overline{u'_i u'_j} + \mathcal{P}_{ij} + \Pi_{ij} - \epsilon_{ij} \quad (4.4.1)$$

can be easily obtained manipulating equation (4.0.2) and (4.2.13) [59].  $\mathcal{P}_{ij}$ ,  $\Pi_{ij}$  and  $\epsilon_{ij}$  are respectively the production tensor,

$$\mathcal{P}_{ij} = -\overline{u'_i u'_k} \frac{\partial \bar{u}_j}{\partial x_k} - \overline{u'_j u'_k} \frac{\partial \bar{u}_i}{\partial x_k}, \quad (4.4.2)$$

the velocity-pressure-gradient tensor,

$$\Pi_{ij} = -\frac{1}{\bar{\rho}} \overline{u'_i \frac{\partial p'}{\partial x_j}} + \overline{u'_j \frac{\partial p'}{\partial x_i}}, \quad (4.4.3)$$

and the dissipation tensor [66]

$$\epsilon_{ij} = 2\nu \overline{\frac{\partial u'_i}{\partial x_k} \frac{\partial u'_j}{\partial x_k}}. \quad (4.4.4)$$

The complete form of the turbulent kinetic energy transport equation for incompressible flows can be than written:

$$\frac{\partial k}{\partial t} + \bar{u}_j \frac{\partial k}{\partial x_j} = \mathcal{P} - \epsilon - \frac{\partial}{\partial x_j} \left( \frac{1}{2} \overline{u'_i u'_i u'_j} - \frac{\overline{P' u'_j}}{\rho} \right) + \nu \nabla^2 k. \quad (4.4.5)$$

The terms on the right hand side represent the turbulent kinetic energy production and its dissipation rate:

$$\mathcal{P} = -\overline{u'_i u'_j} \frac{\partial \bar{u}_i}{\partial x_j} \quad (4.4.6)$$

$$\epsilon = \nu \overline{\frac{\partial u'_i}{\partial x_j} \frac{\partial u'_i}{\partial x_j}} \quad (4.4.7)$$

For an homogeneous turbulence flow, it is possible to neglect the spatial derivative of all turbulence statistics and (4.4.5) simplifies as:

$$\frac{\partial k}{\partial t} + \bar{u}_j \frac{\partial k}{\partial x_j} = \mathcal{P} - \epsilon. \quad (4.4.8)$$

Depending on the turbulence model chosen, there are several possibilities for the definition of the other missing turbulent scales for the determination of  $\nu_t$ . Here we will refer to one of the most used two-equation turbulence model, the  $k - \epsilon$  turbulence model, widely used in industry for its robustness and accuracy. In its classical formulations, referred also as High Reynolds Number formulations, the turbulent viscosity is obtained as follows:

$$\nu_t = C_\mu \frac{k^2}{\epsilon} \quad (4.4.9)$$

and  $k$  and  $\epsilon$  are obtained by solving the following partial differential equations:

$$\frac{\partial k}{\partial t} + \bar{u}_j \frac{\partial k}{\partial x_j} = \mathcal{P} - \epsilon \quad (4.4.10)$$

$$\frac{\partial \epsilon}{\partial t} + \bar{u}_j \frac{\partial \epsilon}{\partial x_j} = C_{\epsilon 1} \frac{\epsilon}{k} \mathcal{P} - C_{\epsilon 2} \frac{\epsilon^2}{k} \quad (4.4.11)$$

It can be shown [59] that the above formulation is valid in the hypothesis of high Reynolds number flow conditions and assuming the turbulence isotropic and in equilibrium. Unfortunately, those conditions are not valid at the wall. In order to have a right estimation of  $k$  and  $\epsilon$  near the solid boundaries the so called wall-function approach has to be used. Due to the importance and its wide use in combustion chamber applications (and more in general, in industrial flow applications), the wall-function approach will be briefly described. In the near wall flow, two main hypothesis are made: the validity of the logarithmic law at the first computational point near the wall, and the hypothesis of local equilibrium at the wall:

$$\begin{aligned}\mathcal{P} &= \epsilon && \text{local equilibrium} \\ u^+ &= \frac{1}{\kappa} \ln y^+ + C && \text{law of the wall}\end{aligned}$$

From the local equilibrium and the definition of the turbulent kinetic energy production we have:

$$\epsilon = \mathcal{P} = -\overline{u'_i u'_j} \frac{\partial \bar{u}_i}{\partial x_j} = \nu_t \frac{\partial \bar{u}}{\partial y} \frac{\partial \bar{u}}{\partial y}. \quad (4.4.12)$$

From the validity of the logarithmic law of the wall is easy to obtain:

$$\bar{u} = \frac{\bar{u}_\tau}{\kappa} \ln y^+ + C \quad (4.4.13)$$

$$\frac{\partial \bar{u}}{\partial y} = \frac{\bar{u}_\tau}{\kappa} \frac{1}{y^+} \frac{\bar{u}_\tau}{\nu} = \frac{\bar{u}_\tau}{\kappa y}. \quad (4.4.14)$$

From the definition of  $\bar{\tau}_w$ ,  $\bar{u}_\tau$  and (4.4.14)

$$\bar{\tau}_w = \bar{\rho} \nu_t \frac{\partial \bar{u}}{\partial y} \quad (4.4.15)$$

$$\bar{u}_\tau = \sqrt{\frac{\bar{\tau}_w}{\bar{\rho}}}, \quad (4.4.16)$$

$\epsilon$  can be expressed as:

$$\epsilon = \mathcal{P} = \nu_t \frac{\partial \bar{u}}{\partial y} \frac{\partial \bar{u}}{\partial y} = \frac{\bar{\tau}_w}{\bar{\rho}} \frac{\partial \bar{u}}{\partial y} = \bar{u}_\tau^2 \frac{\bar{u}_\tau}{\kappa y} \quad (4.4.17)$$

or using the  $\nu_t$  formulation for the  $k$ - $\epsilon$  model

$$\epsilon = \mathcal{P} = \nu_t \frac{\partial \bar{u}}{\partial y} \frac{\partial \bar{u}}{\partial y} = C_\mu \frac{k^2}{\epsilon} \frac{\bar{u}_\tau^2}{\kappa^2 y^2} \quad (4.4.18)$$

and solving for  $\epsilon$

$$\epsilon = \frac{\bar{u}_\tau}{\kappa y} (\kappa C_\mu^{1/2}). \quad (4.4.19)$$

Comparing (4.4.19) and (4.4.17) the skin friction velocity can be written as:

$$\bar{u}_\tau = C_\mu^{1/4} k^{1/2} \quad (4.4.20)$$

and substituting the above expression in (4.4.19),  $\epsilon$  at the first grid point can be expressed as:

$$\epsilon = \frac{k^{3/2} C_\mu^{3/4}}{\kappa y} \quad (4.4.21)$$

In conclusion, assuming that the turbulent kinetic energy at the first grid point is  $k_p$ ,  $\epsilon_p$  can be computed from (4.4.21) and the resulting turbulent viscosity will be then in accordance with the law of the wall. For the determination of  $k$  the wall boundary condition  $\frac{\partial k}{\partial y}|_w = 0$  is used.

The wall shear stress can be then computed as follows:

$$\begin{aligned} \frac{\bar{u}\bar{u}_\tau}{\bar{u}_\tau^2} &= \frac{1}{\kappa} \ln y^+ + C = \frac{1}{\kappa} \ln Ey^+ \\ \bar{u} \frac{\bar{\rho}}{\bar{\tau}_w} (C_\mu^{1/4} k^{1/2}) &= \frac{1}{\kappa} \ln \left( Ey (C_\mu^{1/4} k^{1/2}) \frac{\bar{\rho}}{\mu} \right) \\ \bar{\tau}_w &= \frac{\bar{\rho} \bar{u} (C_\mu^{1/4} k^{1/2}) \kappa}{\ln \left( Ey (C_\mu^{1/4} k^{1/2}) \frac{\bar{\rho}}{\mu} \right)}. \end{aligned} \quad (4.4.22)$$

it is important to remark that the use of wall functions is valid only when the first computational point is in the range of validity of the logarithmic law, it means for value of  $y^+$  above 40 (compare with (4.3.4)).

#### 4.4.2 Low Reynolds Number Turbulence Models

As we have already stressed in the previous section the hypothesis on which the High Reynolds Number formulation is based are not valid in the near wall region where the turbulence is anisotropic and the local Reynolds number is small. For this reason, many researchers have tried to develop so called Low Reynolds Number formulations that are valid not only in the far field regions but also accurate close to the solid boundaries. We distinguish here between two major classes of Low Reynolds Number Turbulence models: the  $k - \epsilon$  and  $k - \omega$  models. As already mentioned in section 4.4.1, the different turbulence models can be classified according to the turbulent time and length scales chosen for the determination of the turbulent viscosity.

$D$	$C_\mu$	$C_{\epsilon 1}$	$C_{\epsilon 2}$	$\sigma_k$	$\sigma_\epsilon$	$f_\mu$	$f_1$	$f_2$	$E$
$2\nu\left(\frac{\partial\sqrt{k}}{\partial x_j}\right)$	0.09	1.44	1.92	1.0	1.3	$e^{-\left[\frac{3.4}{(1+R_T/50)^2}\right]}$	1.0	$1 - 0.3e^{-R_T^2}$	$2\nu\nu_t\left(\frac{\partial^2 u}{\partial x_j^2}\right)^2$

Table 4.1: Constants and functions for the Launder and Sharma  $k$ - $\epsilon$  model [49]. ( $R_T = \frac{k^2}{\nu\tilde{\epsilon}}$ )

#### 4.4.2.1 low Reynolds Number $k$ - $\epsilon$ Modifications

For the  $k$ - $\epsilon$  models, the turbulent kinetic energy,  $k$  and the rate of dissipation of turbulent energy,  $\epsilon$  are used. Most of the different  $k$ - $\epsilon$  Low Reynolds Number formulations can be rewritten in the following general form [65]:

$$\begin{aligned}
\frac{\partial k}{\partial t} + \bar{u}_j \frac{\partial k}{\partial x_j} &= \mathcal{P} - \epsilon + \frac{\partial}{\partial x_j} \left[ \left( \nu + \frac{\nu_t}{\sigma_k} \right) \frac{\partial k}{\partial x_j} \right] \\
\frac{\partial \tilde{\epsilon}}{\partial t} + \bar{u}_j \frac{\partial \tilde{\epsilon}}{\partial x_j} &= C_{\epsilon 1} f_1 \frac{\tilde{\epsilon}}{k} \mathcal{P} - C_{\epsilon 2} f_2 \frac{\tilde{\epsilon}^2}{k} + \frac{\partial}{\partial x_j} \left[ \left( \nu + \frac{\nu_t}{\sigma_\epsilon} \right) \frac{\partial \tilde{\epsilon}}{\partial x_j} \right] + E \\
\epsilon &= \tilde{\epsilon} + \mathcal{D} \\
\nu_t &= C_\mu f_\mu \frac{k^2}{\tilde{\epsilon}}
\end{aligned} \tag{4.4.23}$$

Where  $C_\mu$ ,  $C_{\epsilon 1}$ ,  $C_{\epsilon 2}$ ,  $\sigma_k$ ,  $\sigma_\epsilon$ , are constants and  $f_1$ ,  $f_2$ ,  $f_\mu$ ,  $\mathcal{D}$  and  $E$  are different quantities depending on the specific Low Reynolds Number turbulence model employed. The Low Reynolds Number formulation differs from the High Reynolds Number formulation by the inclusion of the viscous diffusion terms and of the functions  $f$ . Also the  $\mathcal{D}$  and  $E$  terms are added in some cases to better represent the near-wall behavior. A quite extensive review on Low Reynolds Number turbulence model and their applications to unsteady flow is given in [29] and [65]. In Table 4.1 functions and constants are reported for the Launder and Sharma  $k$ - $\epsilon$  turbulence model. In general the term  $f_2$  is introduced to incorporate low Reynolds effect found experimentally in the decay law of turbulence. The terms  $f_1$ ,  $\mathcal{D}$  and  $E$  are introduced to recover the behavior of  $k$  and  $\epsilon$  at the wall for steady flows. The term  $D$  in fact, is introduced to take into account the non zero value of epsilon at the wall. The diffusion terms in general introduce more physics in the transport equations and the term  $f_\mu$  is the most important term that should model the viscous and pressure strain effects. In general the term  $f_\mu$  takes into account the fact that the turbulent viscosity cannot be modeled just as a scalar field but in complex flow conditions has more likely a tensor field character which can take better into account the anisotropy of the flow due to unsteadiness and curvature-pressure gradient effects. Far from the wall, all the low Reynolds additional functions ( $f_1, f_2$  and  $f_\mu$ ) tend to approach the unity recovering the original high Reynolds number formulation. The models are then suited for both high and low Reynolds number regions.

In conclusion the Low Reynolds Number formulation, even if it is still based on steady flow measurements, introduces a better physical understanding on the turbulence phenomena and for this reason it is certainly more suitable for unsteady calculations.

#### 4.4.2.2 $k$ - $\omega$ Models

In their original form from Wilcox [86] the  $k$ - $\omega$  turbulence model equations are reported below:

$$\begin{aligned} \frac{\partial k}{\partial t} + \bar{u}_j \frac{\partial k}{\partial x_j} &= \mathcal{P} - C_\mu k \omega + \frac{\partial}{\partial x_j} \left[ \left( \nu + \frac{\nu_t}{\sigma_k} \right) \frac{\partial k}{\partial x_j} \right] \\ \frac{\partial \omega}{\partial t} + \bar{u}_j \frac{\partial \omega}{\partial x_j} &= \frac{C_{\omega 1}}{\nu_t} \mathcal{P} - C_{\omega 2} \omega^2 + \frac{\partial}{\partial x_j} \left[ \left( \nu + \frac{\nu_t}{\sigma_\omega} \right) \frac{\partial \omega}{\partial x_j} \right] \\ \nu_t &= \frac{k}{\omega}. \end{aligned} \quad (4.4.24)$$

The equations can be integrated through the viscous sublayer and no wall functions are required. Despite the use of the same symbol,  $k$  is considered a measure of the turbulent kinetic energy or the kinetic energy of the fluctuations in the direction of shear and do not represent directly the turbulent kinetic energy itself.  $\omega$  as well, can be interpreted as the rate of dissipation of turbulence per unit energy or formally as  $\epsilon/(C_\mu k)$  and has the dimension of a frequency. The main point is that  $\omega$  and  $k$  do not attempt to mimic the behavior of a specific turbulent quantities but rather the scale-determining the turbulent viscosity. For Wilcox [86] it is just required for  $k$  being proportional to the square of the velocity at which local turbulent mixing occurs and gives different physical interpretation for  $\omega$ . Despite the simplicity of the approach and the capability of the model to predict correctly the effect of pressure gradients, an important source of criticism resides in the difficulties of directly compare the turbulent scales with measurable turbulence quantities or DNS data. This results in the difficulties to define univocally the  $\omega$  boundary conditions at the wall and in the far field.

At the wall an asymptotic behavior of  $\omega$ ,

$$\omega = \frac{6\nu}{C_\omega 2y^2} \rightarrow \infty \quad \text{as } y^+ \rightarrow 0, \quad (4.4.25)$$

is suggested, which leaves quite a freedom in the actual numerical definition of  $\omega$  at the wall. This additional freedom on the other hand gives the possibility to simulate the effect of roughness and porosities. Wilcox in [86] suggested specific values of  $\omega$  depending on the surface finishing of the wall ( $S_R$ ) and the surface blowing rate ( $S_B$ ):

$$\omega_p = \begin{cases} \frac{20\nu}{C_\omega 2\Delta y^2} & \text{for smooth wall} \\ \frac{S_R S_B}{S_R + S_B} \frac{u_\tau^2}{\sqrt{C_\mu \nu}} & \text{for rough and/or porous walls} \end{cases} \quad (4.4.26)$$

For the far field  $\omega$  boundary conditions Wilcox does not suggest any particular relation. Menter in [53] instead recommends values ranging from



$$\omega_\infty = (1 \div 10) \frac{U_\infty}{L} \quad (4.4.27)$$

where  $L$  represents the approximate length of the computational domain.

#### 4.4.2.3 low Reynolds Number $k - \omega$ Modifications

As already mentioned the  $k - \omega$  model in its original formulation permits by itself the integration of the model equations down to the viscous sublayer without the necessity of additional wall functions. However, due to their empirical nature, several modifications were proposed in order to, not only reproduce the overall turbulence viscosity, but also to correlate the turbulent quantities  $k$  and  $\omega$  to the measured values of Reynolds stresses in complex turbulent shear layer flows [87]. Due to the similarity of the models with the  $k - \epsilon$  Low Reynolds Number formulations and to the fact that the proposed modifications are introduced in order to take into account the effect of turbulence anisotropy in the boundary layers (low Reynolds Number effect), such models are often referred as low Reynolds  $k - \omega$  models:

$$\begin{aligned} \frac{\partial k}{\partial t} + \bar{u}_j \frac{\partial k}{\partial x_j} &= \mathcal{P} - C_\mu k \omega + \frac{\partial}{\partial x_j} \left[ \left( \nu + \frac{\nu_t}{\sigma_k} \right) \frac{\partial k}{\partial x_j} \right] \\ \frac{\partial \omega}{\partial t} + \bar{u}_j \frac{\partial \omega}{\partial x_j} &= f_1 \frac{C_{\omega 1}}{\nu_t} \mathcal{P} - C_{\omega 2} \omega^2 + \frac{\partial}{\partial x_j} \left[ \left( \nu + \frac{\nu_t}{\sigma_\omega} \right) \frac{\partial \omega}{\partial x_j} \right] + E \\ \nu_t &= f_\mu \frac{k}{\omega}. \end{aligned} \quad (4.4.28)$$

In Table 4.2 the constant and functions for the Wilcox and Rubesin  $k - \omega$  model are reported. In this case the relation between  $k$ ,  $\omega$  and the Reynolds stresses is given below

$$\langle \tau_t \rangle_{ij} = -\frac{2}{3} k \delta_{ij} + 2\nu_t \left( S_{ij} - \frac{1}{3} \frac{\partial \bar{u}_k}{\partial x_k} \delta_{ij} \right) + \frac{8}{9} \frac{k}{C_\mu \omega^2 + 2S_{mn} S_{nm}} (S_{im} \Omega_{mj} + S_{jm} \Omega_{mi}) \quad (4.4.29)$$

where

$$S_{ij} = \frac{1}{2} \left( \frac{\partial \bar{u}_i}{\partial x_j} + \frac{\partial \bar{u}_j}{\partial x_i} \right) \quad (4.4.30)$$

$$\Omega_{ij} = \frac{1}{2} \left( \frac{\partial \bar{u}_i}{\partial x_j} - \frac{\partial \bar{u}_j}{\partial x_i} \right) \quad (4.4.31)$$

#### 4.4.2.4 Hybrid Turbulence Model: Shear-Stress Transport Model (SST)

Besides the two important families of turbulent model described above Menter [53] proposed a hybrid model which combines the advantages of both  $k - \epsilon$  and  $k - \omega$  formulations. As already mentioned, the major point of criticism in the  $k - \omega$  model is the strong sensitivity to the (quite

$C_\mu$	$C_{\omega 1}$	$C_{\omega 2}$	$\sigma_k$	$\sigma_\omega$	$f_\mu$	$f_1$	$E$
0.09	1.11	0.15	2.0	2.0	$1 - 0.992e^{-R_T}$	$1 - 0.992e^{-R_T/2}$	$-\frac{2}{\sigma_\omega} \left( \frac{\partial l}{\partial x_j} \right)^2 \omega^2$

Table 4.2: Constants and functions for the Wilcox and Rubesin  $k$ - $\omega$  model. ( $l = \frac{\sqrt{k}}{\omega}$ ,  $R_T = \frac{\sqrt{k}l}{\nu}$ )

arbitrary) free-stream values of  $\omega$  outside the boundary-layer. On the other side, even if several Low Reynolds  $k$ - $\epsilon$  corrections are available, the use of near wall damping functions is often prone to numerical instabilities. At the wall, the simplicity of the  $k$ - $\omega$  model, which makes use of simple Dirichlet boundary conditions certainly improve the model stabilities without loss of accuracy in the prediction of the main flow characteristics (velocity profiles, wall skin friction and eddy viscosity). Another point of criticism, for the  $k$ - $\omega$  model, is the poor correlations between the predicted  $k$  and  $\omega$  near wall behavior with high resolved DNS data. However, only for cold flow simulations and more in general in all the cases in which near wall turbulent mixing is not important, the inconsistency in the asymptotic behavior of turbulence in the near wall region affects just the eddy viscosity limiting behavior, which can be neglected since the molecular viscosity in this region is of some order of magnitude greater. As pointed out by Menter [53] in these cases it is not clear why fitting the DNS data for the turbulence quantities such  $k$  and  $\epsilon$  should lead to an improved eddy-viscosity distribution.

In order to gain the best features from both the  $k$ - $\epsilon$  and  $k$ - $\omega$  turbulence models, Menter [53] suggested a blending between the two formulations as follows: the  $k$ - $\epsilon$  model is transformed in a  $k$ - $\omega$  formulation. The transformed transport equations are multiplied by a blending function  $(1 - \mathcal{F}_1)$  and added to the original  $k$ - $\omega$  equation times  $\mathcal{F}_1$ . The blending function is designed to be one in the sublayer and logarithmic region of the boundary layer and to gradually switch to zero in the wake region. This means that near the wall a  $k$ - $\omega$  formulation is used and in the outer wake region, as well as in the free shear layers, a  $k$ - $\epsilon$  model is activated. This simple blended version is often referred as the  $k$ - $\omega$  Baseline Model ( $k$ - $\omega$  BSL) and it is reported below (for details see [53]):

$$\begin{aligned}
\frac{\partial k}{\partial t} + \bar{u}_j \frac{\partial k}{\partial x_j} &= \mathcal{P} - C_\mu k \omega + \frac{\partial}{\partial x_j} \left[ (\nu + \sigma'_k \nu_t) \frac{\partial k}{\partial x_j} \right] \\
\frac{\partial \omega}{\partial t} + \bar{u}_j \frac{\partial \omega}{\partial x_j} &= \frac{C1_\omega \mathcal{P}}{\nu_t} - C2_\omega \omega^2 + \frac{\partial}{\partial x_j} \left[ (\nu + \sigma'_\omega \nu_t) \frac{\partial \omega}{\partial x_j} \right] + 2(1 - \mathcal{F}_1) \sigma'_{\omega 2} \frac{1}{\omega} \frac{\partial k}{\partial x_j} \frac{\partial \omega}{\partial x_j} \\
\nu_t &= \frac{k}{\omega} \\
C_\eta &= \mathcal{F}_1 C_{\eta 1} + (1 - \mathcal{F}_1) C_{\eta 2} \\
\mathcal{F}_1 &= \tanh \left\{ \min \left[ \max \left( \frac{\sqrt{k}}{0.09 \omega y}; \frac{500 \nu}{y^2 \omega} \right); \frac{4 \sigma'_{\omega 2} k}{CD_{k\omega} y^2} \right]^4 \right\} \\
CD_{k\omega} &= \max \left( 2 \sigma'_{\omega 2} \frac{1}{\omega} \frac{\partial k}{\partial x_j} \frac{\partial \omega}{\partial x_j}; 10^{-20} \right)
\end{aligned} \tag{4.4.32}$$

$C_{\mu 1}$	$C_{\mu 2}$	$C1_{\omega 1}$	$C1_{\omega 2}$	$C2_{\omega 1}$	$C2_{\omega 2}$	$\sigma'_{k1}$	$\sigma'_{k2}$	$\sigma'_{\omega 1}$	$\sigma'_{\omega 2}$
0.09	0.09	0.503167	0.44035	0.0750	0.0828	0.5	1.0	0.5	0.856

Table 4.3: Constants and functions for the  $k$ - $\omega$  BSL model.

$C_{\mu 1}$	$C_{\mu 2}$	$C1_{\omega 1}$	$C1_{\omega 2}$	$C2_{\omega 1}$	$C2_{\omega 2}$	$\sigma'_{k1}$	$\sigma'_{k2}$	$\sigma'_{\omega 1}$	$\sigma'_{\omega 2}$	$a_1$
0.09	0.09	0.503167	0.44035	0.0750	0.0828	0.85	1.0	0.5	0.856	0.31

Table 4.4: Constants and functions for the  $k$ - $\omega$  BSL model.

where each constant is blended between the values reported in Table 4.3 using the formula reported in 4.4.32 for a generic constant  $C_\eta$ .

A further improvement of the model for strong adverse pressure gradient flow can be obtained enforcing the so called Bradshaw's hypothesis in the wake region of the boundary layer [14] [53]. Bradshaw, Ferris and Atwel in [14] observed that the principal turbulent shear stress is proportional to the turbulent kinetic energy not only in the log layer but also in the wake region of the boundary layer. This experimental evidence is not recovered by the classical two-equation models eventhough the turbulence level in the log-layer is well predicted. In flows with strong adverse pressure gradient, it is the level of eddy viscosity in the wake region (outer edge of the boundary layer) that ultimately determines the ability of an eddy-viscosity model to predict correctly the flow behavior. This is the reason why the  $k$ - $\omega$  model performs better than  $k$ - $\epsilon$  models [86] in moderate adverse pressure gradient flow. Menter in [53] found an elegant way to combine the Bradshaw assumption to the BSL model. He proposed the so called Shear-Stress transport model SST reported below:

$$\begin{aligned}
\frac{\partial k}{\partial t} + \bar{u}_j \frac{\partial k}{\partial x_j} &= \mathcal{P} - C_\mu k \omega + \frac{\partial}{\partial x_j} \left[ (\nu + \sigma'_k \nu_t) \frac{\partial k}{\partial x_j} \right] \\
\frac{\partial \omega}{\partial t} + \bar{u}_j \frac{\partial \omega}{\partial x_j} &= \frac{C1_\omega}{\nu_t} \mathcal{P} - C2_\omega \omega^2 + \frac{\partial}{\partial x_j} \left[ (\nu + \sigma'_\omega \nu_t) \frac{\partial \omega}{\partial x_j} \right] + 2(1 - \mathcal{F}_1) \sigma'_{\omega 2} \frac{1}{\omega} \frac{\partial k}{\partial x_j} \frac{\partial \omega}{\partial x_j} \\
\nu_t &= \frac{a_1 k}{\max(a_1 \omega; \Omega \mathcal{F}_2)} \\
C_\eta &= \mathcal{F}_1 C_{\eta 1} + (1 - \mathcal{F}_1) C_{\eta 2} \\
\mathcal{F}_1 &= \tanh \left\{ \min \left[ \max \left( \frac{\sqrt{k}}{0.09 \omega y}; \frac{500 \nu}{y^2 \omega} \right); \frac{4 \sigma'_{\omega 2} k}{CD_{k\omega} y^2} \right]^4 \right\} \\
\mathcal{F}_2 &= \tanh \left\{ \left[ \max \left( 2 \frac{\sqrt{k}}{0.09 \omega y}; \frac{500 \nu}{y^2 \omega} \right) \right]^2 \right\} \\
CD_{k\omega} &= \max \left( 2 \sigma'_{\omega 2} \frac{1}{\omega} \frac{\partial k}{\partial x_j} \frac{\partial \omega}{\partial x_j}; 10^{-20} \right) \\
\Omega &= \left| \frac{1}{2} \left( \frac{\partial \bar{u}_i}{\partial x_j} - \frac{\partial \bar{u}_j}{\partial x_i} \right) \right|
\end{aligned} \tag{4.4.33}$$

The model constants are reported in Table 4.4.

The main modifications resides in the definition of the turbulent viscosity in 4.4.33. In a standard two-equation model, in the near wall region the turbulent shear stress can be expressed as

$$\overline{u'_i u'_j} = \nu_t \Omega \quad (4.4.34)$$

where  $\Omega = \frac{\partial \bar{u}}{\partial y}$  and  $\nu_t = \frac{k}{\omega}$ . In the Bradshaw assumption:

$$\overline{u'_i u'_j} = a_1 k. \quad (4.4.35)$$

The definition of  $\nu_t$  in this case should be modified as:

$$\nu_t \Omega = a_1 k \quad (4.4.36)$$

thus

$$\nu_t = \frac{a_1 k}{\Omega}. \quad (4.4.37)$$

A general expression for  $\nu_t$  which combines both formulation (4.4.37) and (4.4.32) in their hypothesis of validity is then (4.4.33), where  $\mathcal{F}_2$  is a function that is one for boundary layer flows and zero for free shear layers. In adverse pressure gradient boundary layer,  $\Omega$  is larger than  $a_1 \omega$  and (4.4.33) guarantees that (4.4.37) is satisfied whereas the original formulation (4.4.32) is used for the rest of the flow.

### 4.4.3 Two-Equation Turbulent Heat Transfer Models

In non-isothermal flow, the turbulent heat flux in (4.2.19) is generally modelled using a constant turbulent Prandtl number. Such assumption can be released trough the definition of a turbulent thermal diffusivity which can be modelled with first or second order closures similarly to the the turbulent viscosity. An example of first order closure which makes use of two additional transport equations is given by [55] and will be briefly discussed below.

As proposed by Nagano in [55], in analogy with the  $k$ - $\epsilon$  turbulence models, two additional transport equations for the fluctuating temperature variance ( $k_\theta$ ) and its dissipation rate ( $\epsilon_\theta$ ) can be derived from the URANS equation system.

The exact transport equation for  $k_\theta$ , according to [48] has been presented first by Corrsin [19] and can be obtained by multiplying the instantaneous temperature equation by  $T'$  and ensemble averaging:

$$\frac{Dk_\theta}{Dt} = -\overline{u'_j T'} \frac{\partial \bar{T}}{\partial x_j} - \alpha \frac{\partial T'}{\partial x_j} \frac{\partial T'}{\partial x_j} - \frac{\partial \overline{u'_j k'_\theta}}{\partial x_j} + \frac{\partial}{\partial x_j} \left( \alpha \frac{\partial k_\theta}{\partial x_j} \right). \quad (4.4.38)$$

The terms on the right hand side are often referred as: Production, Dissipation, Turbulent Diffusion and Molecular Diffusion respectively. A transport equation can be derived also for  $\epsilon_\theta$  which corresponds to the second term in (4.4.38) ( $\epsilon_\theta = \alpha \frac{\partial T'}{\partial x_j} \frac{\partial T'}{\partial x_j}$ ):

$C_\lambda$	$C_{D1}$	$C_{D2}$	$C_{P1}$	$C_{P2}$	$A_{D1}$	$A_{D2}$	$\sigma_h$	$\sigma_{\epsilon_\theta}$	$Cm$
0.1	2.0	0.9	1.9	0.6	1.0	5.7	1.6	1.6	0.5

Table 4.5: Constants for the Abe, Kim and Nagano [10] (AKN) model,  $k_\theta$  and  $\epsilon_\theta$  equations.

$$\begin{aligned}
\frac{D\epsilon_\theta}{Dt} = & -2\alpha \frac{\overline{\partial T' \partial u'_k}}{\partial x_j \partial x_j} \frac{\partial \bar{T}}{\partial x_k} - 2\alpha u'_k \frac{\overline{\partial T'}}{\partial x_j} \frac{\partial^2 \bar{T}}{\partial x_k \partial x_j} \\
& -2\alpha \frac{\overline{\partial T' \partial T'}}{\partial x_j \partial x_j} \frac{\partial \bar{u}_k}{\partial x_j} - 2\alpha \frac{\overline{\partial T' \partial u'_k}}{\partial x_j \partial x_j} \frac{\partial T'}{\partial x_k} \\
& -2 \left( \alpha \frac{\partial^2 T'}{\partial x_j \partial x_k} \right)^2 - \frac{\partial \overline{\epsilon'_\theta u'_k}}{\partial x_k} + \frac{\partial}{\partial x_k} \left( \alpha \frac{\partial \epsilon_\theta}{\partial x_k} \right). \tag{4.4.39}
\end{aligned}$$

The  $\epsilon_\theta$  transport equation can be obtained by taking the derivative of the temperature equation (4.0.9) with respect of  $x_k$ , multiplying by  $2\alpha \frac{\partial T'}{\partial x_k}$  and ensemble averaging. The terms on the right hand side of (4.4.39) are often referred as: Production by Mean Temperature Gradient, Gradient Production, Production by Mean Velocity Gradient, Turbulent Production, Dissipation, Turbulent Diffusion, Molecular Diffusion.

Using the eddy diffusivity concept

$$-\overline{u'T'} = \alpha_t \frac{\partial \bar{T}}{\partial x_j} \tag{4.4.40}$$

and according to the models of [55] and [10], Equations (4.4.39) and (4.4.38) can be closed as follows

$$\begin{aligned}
\frac{\partial k_\theta}{\partial t} + \bar{u}_j \frac{\partial k_\theta}{\partial x_j} &= \frac{\partial}{\partial x_j} \left\{ \left( \alpha + \frac{\alpha_t}{\sigma_h} \right) \frac{\partial k_\theta}{\partial x_j} \right\} - \alpha_t \frac{\partial \bar{T}}{\partial x_j} \frac{\partial \bar{T}}{\partial x_j} - \epsilon_\theta \\
\frac{\partial \epsilon_\theta}{\partial t} + \bar{u}_j \frac{\partial \epsilon_\theta}{\partial x_j} &= \frac{\partial}{\partial x_j} \left\{ \left( \alpha + \frac{\alpha_t}{\sigma_{\epsilon_\theta}} \right) \frac{\partial \epsilon_\theta}{\partial x_j} \right\} - C_{P1} f_{P1} \frac{\epsilon_\theta}{k_\theta} \alpha_t \frac{\partial \bar{T}}{\partial x_j} \frac{\partial \bar{T}}{\partial x_j} \\
&\quad - C_{P2} f_{P2} \frac{\epsilon_\theta}{k_\theta} \nu_t \left( \frac{\partial \bar{u}_j}{\partial x_i} + \frac{\partial \bar{u}_i}{\partial x_j} \right) \frac{\partial \bar{u}_i}{\partial x_j} - C_{D1} f_{D1} \frac{\epsilon_\theta^2}{k_\theta} - C_{D2} f_{D2} \frac{\epsilon_\theta}{k} \tag{4.4.41}
\end{aligned}$$

where  $\alpha_t$  is defined below

$$\alpha_t = C_\lambda \left[ \frac{k^2}{\epsilon} \left( \frac{2R}{Cm + R} \right) + 3\sqrt{k} \left( \frac{\nu^3}{\epsilon} \right)^{1/4} \frac{\sqrt{2R}}{Pr} f_d \right] \left[ 1 - e^{-\frac{(\nu\epsilon)^{1/4} y}{14\nu}} \right] \left[ 1 - e^{-\frac{Pr^{1/2} (\nu\epsilon)^{1/4}}{14\nu}} \right] \tag{4.4.42}$$

and the model constants and functions are summarized in Tables 4.5 and 4.6

$f_{D1}$	$f_{D2}$	$f_{P1}$	$f_{P2}$	$f_d$	$R$
$f_{P1}$	$-\frac{0.3C_{\epsilon 2}e^{-(R_t/6.5)^2}}{C_{D2}} \left\{ 1 - e^{-\frac{(\nu\epsilon)^{1/4}y}{AD2\nu}} \right\}$	$\left\{ 1 - e^{-\frac{(\nu\epsilon)^{1/4}y}{\nu}} \right\}^2$	1.0	$e^{-(R_t/200)^2}$	$\frac{k_{\theta}\epsilon}{2\epsilon_{\theta}k}$

Table 4.6: functions for the AKN model,  $k_{\theta}$  and  $\epsilon_{\theta}$  equations.

## 4.5 LES - Large Eddy Simulation

As shown in section 4.2, the URANS equations are obtained from the conservation equations performing a time average (Reynolds averaging) or, more in general, a statistical average (ensemble averaging) of the turbulent flow field. This operation filters out the small turbulence structures but introduces new unresolved equation terms which can be modelled using different turbulence closure approaches.

In the so called Large Eddy Simulation approach, a spatial filtering instead of a “temporal filtering” is performed:

$$\vec{u}(\vec{x}) = \int G(\vec{x} - \vec{\xi}) \vec{u}(\vec{\xi}) d\vec{\xi} \quad (4.5.1)$$

where  $G$  represents a generic spatial filtering function which is meant to filter out all the turbulent structures smaller than the computational grid resolution. The instantaneous flow field can be decomposed in a numerically resolved field ( $\vec{u}$ ) and an unresolved turbulent (subgrid) fluctuation ( $\vec{u}'$ )

$$\vec{u} = \vec{u} + \vec{u}' \quad (4.5.2)$$

The advantage of this approach is that performing a spatial filtering, the turbulent macro structures which generally depend on the flow geometry are separated from the turbulent micro structures which tend to have a more universal character. Performing for each quantity the decomposition given in (4.5.2), substituting in equations (4.0.1) to (4.0.3) and filtering, additional unresolved terms appear in the convective fluxes:

$$\overline{\tau_{ij_t}} = -\bar{\rho}(\widetilde{u_i u_j} - \tilde{u}_i \tilde{u}_j) \quad (4.5.3)$$

for the Reynolds stresses and

$$\overline{q_{i_t}} = \bar{\rho}(\widetilde{u_i h} - \tilde{u}_i \tilde{h}) \quad (4.5.4)$$

for the heat flux vector. The tilde represent the Favre filtering for which a relation analogous to (4.2.10) is valid:

$$\tilde{f}(\vec{x}, t) = \frac{\overline{\rho f(\vec{x}, t)}}{\bar{\rho}}. \quad (4.5.5)$$

This time the bar operator corresponds to the LES filtering (4.5.1).

The general equation system for a compressible flow can be expressed as

$$\frac{\partial \bar{\rho}}{\partial t} + \nabla \cdot (\bar{\rho} \vec{u}) = 0 \quad (4.5.6)$$

$$\frac{\partial \bar{\rho} \vec{u}}{\partial t} + \nabla \cdot (\bar{\rho} \vec{u} \vec{u}) = \nabla \cdot (\bar{\tau} - \bar{\rho} \vec{u}' \vec{u}') - \nabla \bar{p} \quad (4.5.7)$$

$$\frac{\partial \bar{\rho} \tilde{h}}{\partial t} + \nabla \cdot (\bar{\rho} \tilde{h} \vec{u}) = \frac{D \bar{p}}{Dt} + \bar{\tau} : \nabla \vec{u} - \nabla \cdot (\vec{q} - \bar{\rho} \vec{u}' h) \quad (4.5.8)$$

The LES unresolved sub-grid scale (SGS) terms are generally closed using the following formulation:

$$\bar{\tau}_{ij} = 2\bar{\rho}\nu_t \widetilde{S}_{ij} - \frac{1}{3}\bar{\tau}_{it} \delta_{ij} \quad (4.5.9)$$

for the Reynolds stresses and

$$\bar{q}_{it} = -\lambda_t \frac{\partial \widetilde{T}}{\partial x_i} \quad (4.5.10)$$

for the heat flux vector. Where

$$\lambda_t = \frac{\nu_t \bar{\rho} \overline{C_p}}{Pr_t} \quad (4.5.11)$$

and

$$\widetilde{S}_{ij} = \frac{1}{2} \left( \frac{\partial \tilde{u}_i}{\partial x_j} + \frac{\partial \tilde{u}_j}{\partial x_i} \right) - \frac{1}{3} \frac{\partial \tilde{u}_k}{\partial x_k} \delta_{ij} \quad (4.5.12)$$

Since  $Pr_t$  is assumed to be constant (for air flow often set to 0.9) the closure of the SGS terms is shifted to the determination of  $\nu_t$ .

Hereafter the LES equation system is reported for an incompressible flow [16].

$$\nabla \cdot (\vec{u}) = 0 \quad (4.5.13)$$

$$\frac{\partial \vec{u}}{\partial t} + \nabla \cdot (\vec{u} \vec{u}) = \nabla \cdot \left( \frac{\bar{\tau}}{\bar{\rho}} - \vec{u}' \vec{u}' \right) - \frac{\nabla \bar{p}}{\bar{\rho}} \quad (4.5.14)$$

$$\frac{\partial \bar{T}}{\partial t} + \nabla \cdot (\bar{T} \vec{u}) = \nabla \cdot (\alpha \nabla \bar{T} - \vec{u}' T')$$

Where

$$\overline{\vec{u}'\vec{u}'} = \frac{1}{\bar{\rho}} \overline{\tau'_{ijt}} \quad (4.5.16)$$

$$\overline{\vec{u}'T'} = \overline{q'_{it}}. \quad (4.5.17)$$

Despite the different physical meaning, it is evident that the LES equations (4.5.13)-(4.5.14) are identical to the URANS equations (4.2.26)-(4.2.27) except for the definition of the turbulent viscosity.

In the present work two different closures are used: the classical Smagorinsky model [74]

$$\nu_t = (C_S \Delta)^2 \sqrt{2 \widetilde{S}_{ij} \widetilde{S}_{ij}} \quad (4.5.18)$$

and the WALE model [26]

$$\nu_t = (C_w \Delta)^2 \frac{(s_{ij}^d s_{ij}^d)^{3/2}}{(\widetilde{S}_{ij} \widetilde{S}_{ij})^{5/2} + (s_{ij}^d s_{ij}^d)^{5/4}} \quad (4.5.19)$$

where  $C_w$  and  $C_S$  are model constants ( $C_w = 0.4929$  and  $C_S = 0.18$ ),  $\Delta$  is the characteristic filter length and

$$s_{ij}^d = \frac{1}{2}(\tilde{g}_{ij}^2 + \tilde{g}_{ji}^2) - \frac{1}{3}\tilde{g}_{kk}^2 \delta_{ij} \quad (4.5.20)$$

$\tilde{g}_{ij}$  denotes the resolved velocity gradient. The Smagorinsky model is particularly suited for homogeneous isotropic turbulent flows. Unfortunately the model is not recommended for bounded flows where the turbulence in the near wall region is anisotropic. In this case, The WALE model represent a much better alternative. It was developed infact to recover the scaling law of the wall without the necessity of using a wall function approach [26] .



# 5 Simple Channel and Pipe Configuration: Analytical Laminar Solutions and Turbulent Flow Correlations

In the case of simple laminar channel and pipe flow configuration, equation (4.0.1)-(4.0.3) can be simplified and solved analytically. The solution in the steady and oscillating case is discussed below and will serve as a basis for the comprehension of the more complex turbulent flow case.

Due to the simple geometry, turbulent steady channel and pipe flows have been extensively investigated during the years. A number of empirical correlations exist which can help designers in the determination of the overall heat transfer and frictional losses. The empirical correlations can be useful not only to compare the overall effects of flow pulsations on the mean flow, but also constitute the basis of the quasi-steady theory.

According to the quasi-steady theory, a time varying flow can be studied as a succession of several steady state solutions. Each solution corresponds to an imposed change of the boundary conditions. The overall effect of unsteadiness can be than obtained integrating in time each steady state contribution.

In this sense the empirical correlations, which are strictly valid in steady flow conditions, can be used also for the characterization of time varying flows.

## 5.1 Laminar Channel Flow

Equation 4.0.1-4.0.3 can be written in Einstein notation as follows

$$\frac{\partial \rho}{\partial t} + \frac{\partial}{\partial x_i}(\rho u_i) = 0 \quad (5.1.1)$$

$$\frac{\partial}{\partial t}(\rho u_i) + \frac{\partial}{\partial x_j}(\rho u_i u_j) - \frac{\partial \tau_{ij}}{\partial x_j} + \frac{\partial p}{\partial x_j} = 0 \quad (5.1.2)$$

$$\frac{\partial \rho h}{\partial t} + \frac{\partial}{\partial x_j}(\rho h u_j) = \frac{Dp}{Dt} + \tau_{ij} \frac{\partial u_i}{\partial x_j} - \frac{\partial q_j}{\partial x_j} \quad (5.1.3)$$

where the heat flux vector component  $q_i$  can be modelled using the Fourier law:

$$q_i = -\lambda \frac{\partial T}{\partial x_i} \quad (5.1.4)$$

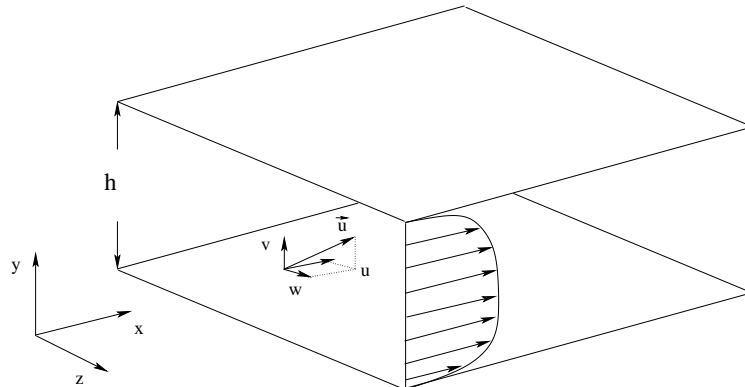


Figure 5.1.1: Channel flow configuration, coordinate system and velocity decomposition

### 5.1.1 Steady Laminar Channel Flow

In the hypothesis of

1. channel configuration ( $v = w = 0$  see fig. 5.1.1)
2. steady flow ( $\frac{\partial}{\partial t} = 0$ )
3. incompressible flow ( $\rho = \text{constant}$ )
4. distributed losses, fully developed flow ( $\frac{\partial p}{\partial x} = \text{constant}$ )
5. isothermal flow ( $T = \text{constant}$ )

Equation (5.1.1)-(5.1.3) simplify as follows:

$$\frac{\partial u}{\partial x} = \frac{\partial v}{\partial y} = \frac{\partial w}{\partial z} = 0 \quad (5.1.5)$$

$$\frac{\partial p}{\partial x} = \frac{\partial \tau_{xy}}{\partial y} \quad (5.1.6)$$

and using (4.0.6)

$$\tau_{xy} = \mu \left( \frac{\partial u}{\partial y} \right) \quad (5.1.7)$$

the system of equations reduces to a system of ordinary partial differential equation with the non-slip boundary condition at the wall

$$\frac{dp}{dx} = \frac{d\tau_{xy}}{dy} = K \quad (5.1.8)$$

$$\mu \frac{d^2 u}{dy^2} = K \quad (5.1.9)$$

$$u|_{\pm \frac{h}{2}} = 0 \quad (5.1.10)$$

The velocity profile is than obtained by integration of (5.1.9):

$$u = u_{max} \left( 1 - \left( \frac{2y}{h} \right)^2 \right) \quad (5.1.11)$$

where

$$u_{max} = -\frac{K h^2}{\mu 8} \quad (5.1.12)$$

The cross-sectional mean flow velocity is given by

$$U_b = \frac{1}{h} \int_{-\frac{h}{2}}^{\frac{h}{2}} u dy \quad (5.1.13)$$

and using (5.1.11),

$$U_b = \frac{2}{3}u_{max} \quad (5.1.14)$$

Due to the constancy of the pressure gradient in  $x$  expressed in 5.1.8, the profile of the shear stress is linear in  $y$ , having its maximum in absolute value at the wall (see fig. 5.1.2)

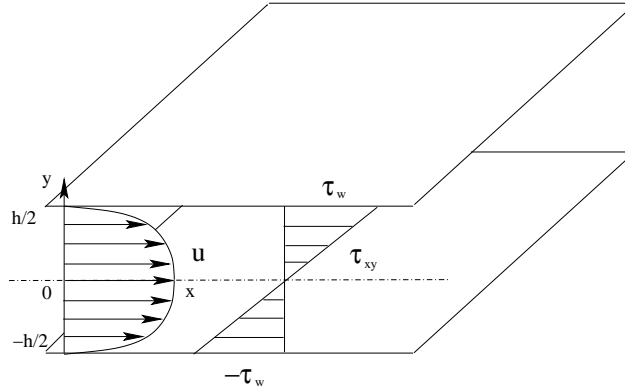


Figure 5.1.2: Channel flow configuration, velocity and shear stress profiles

$$\tau_{xy} = Ky \quad (5.1.15)$$

and using (5.1.15), (5.1.12) and (5.1.14 )

$$|\tau_w| = |\tau_{xy}|_{\pm \frac{h}{2}} = 6\mu \frac{U_b}{h} \quad (5.1.16)$$

The relation between the frictional loss and the cross-sectional mean flow velocity can be formulated in non-dimensional form as follows

$$C_f = \frac{\tau_w}{\frac{1}{2}\rho U_b^2} = 12 \frac{\mu}{\rho U_b h} = \frac{12}{Re_h} = \frac{24}{Re_{D_h}} \quad (5.1.17)$$

where  $Re_h$  and  $Re_{D_h}$  are the flow Reynolds number based on the channel wall distance  $h$  and the hydraulic diameter

$$Re_{D_h} = \frac{U_b D_h}{\nu} \quad (5.1.18)$$

$$Re_h = \frac{U_b h}{\nu} \quad (5.1.19)$$

The hydraulic diameter for a general non circular pipe is defined as

$$D_h = \frac{4A}{P} \quad (5.1.20)$$

where  $A$  is the pipe cross section and  $P$  is the wetted perimeter. In the case of a 2D-channel flow  $D_h = 2h$ .

Other characteristic scales, often used in boundary layer flows for the quantification of the viscous effects, are the boundary layer thickness  $\delta$  and the skin friction velocity  $u_\tau$  (see (4.3.3)). The resulting Reynolds numbers are  $Re_\delta$  and  $Re_{u_\tau}$  respectively:

$$Re_\delta = \frac{U_b \delta}{\nu}, \quad (5.1.21)$$

$$Re_{u_\tau} = \frac{\delta u_\tau}{\nu}. \quad (5.1.22)$$

Note that  $\delta$  in the case of fully developed laminar channel flow corresponds to  $h/2$ .

In conclusion, the Navier-Stokes equations can be solved in the case of a fully developed 2D-laminar steady channel flow. The velocity profiles are parabolic and can be expressed using (5.1.11) and (5.1.12) in function of the channel pressure gradient ( $\frac{dp}{dx} = K$ ) which is function of the mass flow rate. The channel friction losses and the mean cross sectional velocity are univocally related through the expression (5.1.17) and the definition of the channel Reynolds number.

### 5.1.2 Oscillating Laminar Channel Flow

In the case of oscillating channel flow equations (4.0.1)-(4.0.3) together with the following assumptions

1. incompressible flow ( $\rho = \text{constant}$ )
2.  $\frac{\partial p}{\partial x} = K \sin(\omega t)$
3. isothermal flow ( $T = \text{constant}$ )
4. channel configuration ( $v = w = 0$  see fig. 5.1.1)

leads to the following simplified system of differential equations:

$$\frac{dp}{dx} = \frac{d\tau_{xy}}{dy} = K \sin(\omega t) \quad (5.1.23)$$

$$\rho \frac{\partial u}{\partial t} - \mu \frac{\partial^2 u}{\partial y^2} = K \sin(\omega t) \quad (5.1.24)$$

$$u|_{\pm \frac{h}{2}} = 0 \quad (5.1.25)$$

The pulsating pressure term can be rewritten in complex notation as follows

$$\frac{dp}{dx} = -iK e^{i\omega t} \quad (5.1.26)$$

where  $i$  is the imaginary number ( $i^2 = -1$ ). If we consider the solution of the form

$$u(y, t) = f(y) e^{i\omega t} \quad (5.1.27)$$

substituting 5.1.27 in 5.1.24 leads to the following differential equation:

$$i\rho\omega f(y)e^{i\omega t} - \mu \frac{d^2 f(y)}{dy^2} e^{i\omega t} = iK e^{i\omega t} \quad (5.1.28)$$

that can be rearranged as follows

$$\frac{d^2 f(y)}{dy^2} - \frac{i\omega}{\nu} f(y) = \frac{iK_2}{\nu} \quad (5.1.29)$$

where  $K_2 = -K/\rho$  or  $\frac{dp}{dx} = -K_2\rho \sin(\omega t)$ . It can be shown [37] that the solution of 5.1.29 is:

$$u(y, t) = -\frac{K_2}{\omega} e^{i\omega t} \left[ 1 - \frac{\cosh\left(y\sqrt{\frac{i\omega}{\nu}}\right)}{\cosh\left(\frac{h}{2}\sqrt{\frac{i\omega}{\nu}}\right)} \right]. \quad (5.1.30)$$

For small frequency  $\cosh\phi \simeq 1 + \phi^2/2$  and 5.1.30 becomes

$$u(y, t) = \frac{K_2}{2\nu} \left( \frac{h^2}{4} - y^2 \right) \sin(\omega t) \quad (5.1.31)$$

Thus, for low frequencies, the flow oscillates with the same phase as the driving pressure term and the velocity profile is parabolic as in the steady case ( compare 5.1.31 and 5.1.11). For small oscillation frequency therefore the flow is quasi steady. At each time step the velocity profile is equal to the steady flow profile relative to the instantaneous pressure forcing. Equation (5.1.31) is valid with an error below 1% when

$$\mathcal{R}_e\left(\frac{h}{2}\sqrt{\frac{i\omega}{\nu}}\right) < 0.22 \quad (5.1.32)$$

where  $\mathcal{R}_e(z)$  is the real part of a complex number  $z$ . Considering the identity  $\sqrt{i} = \sqrt{1/2} + i\sqrt{1/2}$  it is easy to give a lower bound for the pulsation frequency  $\omega$  with respect to  $\nu$  and the channel height

$$\omega < 0.394 \frac{\nu}{h^2} \quad (5.1.33)$$

For very large values of  $\omega$ ,  $\cosh\phi \simeq e^\phi/2$  and the velocity profile can be simplified as follows:

$$u(y, t) = \frac{K_2}{\omega} (\cos(\omega t) - e^{-\eta_s} \cos(\omega t - \eta_s)) \quad (5.1.34)$$

where

$$\eta_s = \sqrt{\frac{\omega}{2\nu}} \left( \frac{h}{2} - y \right) = \sqrt{\frac{\omega}{2\nu}} y_w \quad (5.1.35)$$

and  $y_w$  is the distance from the channel wall. Considering Equation (5.1.34) instead of (5.1.30) for

$$\omega > 170 \frac{\nu}{h^2} \quad (5.1.36)$$

gives an error below 1%. For high values of  $\omega$  the second term in 5.1.34 is negligible compared to the first one and the flow basically oscillates inviscidly with a  $90^\circ$  phase shift with respect to the pressure forcing. The velocity at the channel centerline can be expressed as:

$$U_c = U_0 \cos(\omega t) = \frac{K_2}{\omega} \cos(\omega t) \quad (5.1.37)$$

and the oscillating pressure forcing becomes

$$\frac{dp}{dx} = -\rho K_2 \sin(\omega t) = U_0 \omega \sin(\omega t) \quad (5.1.38)$$

The term  $\frac{K_2}{\omega} e^{-\eta_s} \cos(\omega t - \eta_s)$  starts to play a role when  $\eta_s$  approaches zero. At  $\eta_s = 4.6$  the second term in 5.1.34 is 100 time smaller than the first one and for

$$y_w > 4.6 \sqrt{\frac{2\nu}{\omega}} \quad (5.1.39)$$

practically the velocity profile is accurately predicted by (5.1.37). An oscillating laminar channel flow can than be characterized through the definition of the so called Stokes length:

$$\delta_s = \sqrt{\frac{2\nu}{\omega}} \quad (5.1.40)$$

and the center-line velocity amplitude  $U_0$ , which together define the so called Stokes Reynolds number:

$$Re_{\delta_s} = \frac{U_0 \delta_s}{\nu} \quad (5.1.41)$$

For distance from the wall below  $4.6\delta_s$  the effect of pulsations can be important. For this reason  $\delta_s$  can be seen as a measure of the layer affected by the flow pulsations. It is important to notice that analogous flow solutions can be found each time an oscillatory relative motion between the flow and the wall is present ( see the oscillating outer flow and the second Stokes problem in [37] ). In the case of oscillating wall in a flow at rest  $\delta_s$  is often referred as the oscillation penetration depth. In this case it gives a measure of the distance from the wall affected by the wall oscillations.

## 5.2 Laminar Pipe Flow

In pipe flow configurations, it is convenient to rewrite the Navier-Stokes equations in cylindrical coordinates (see figure 5.2.1). Equations 5.1.1-5.1.3 become

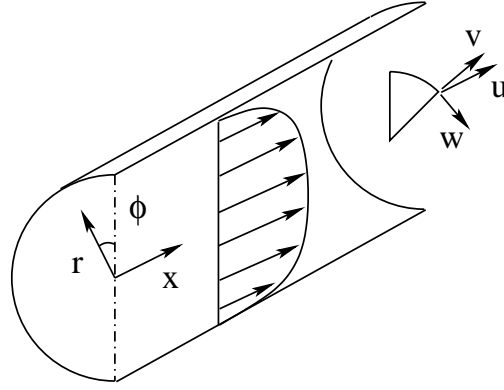


Figure 5.2.1: Pipe flow configuration, coordinate system and velocity decomposition

$$\frac{\partial \rho}{\partial t} + \frac{1}{r} \frac{\partial}{\partial r}(\rho r v) + \frac{1}{r} \frac{\partial}{\partial \phi}(\rho w) + \frac{\partial}{\partial x}(\rho u) = 0 \quad (5.2.1)$$

$$\rho \left( \frac{\partial v}{\partial t} + v \frac{\partial v}{\partial r} + \frac{w}{r} \frac{\partial v}{\partial \phi} - \frac{w^2}{r} + u \frac{\partial v}{\partial x} \right) - \frac{1}{r} \frac{\partial r \tau_{rr}}{\partial r} - \frac{1}{r} \frac{\partial \tau_{r\phi}}{\partial \phi} - \frac{\partial \tau_{rx}}{\partial x} + \frac{\partial p}{\partial r} = 0 \quad (5.2.2)$$

$$\rho \left( \frac{\partial w}{\partial t} + v \frac{\partial w}{\partial r} + \frac{w}{r} \frac{\partial w}{\partial \phi} + \frac{vw}{r} + u \frac{\partial w}{\partial x} \right) - \frac{1}{r^2} \frac{\partial r^2 \tau_{r\phi}}{\partial r} - \frac{1}{r} \frac{\partial \tau_{\phi\phi}}{\partial \phi} - \frac{\partial \tau_{\phi x}}{\partial x} + \frac{1}{r} \frac{\partial p}{\partial \phi} = 0 \quad (5.2.3)$$

$$\rho \left( \frac{\partial u}{\partial t} + v \frac{\partial u}{\partial r} + \frac{w}{r} \frac{\partial u}{\partial \phi} + u \frac{\partial u}{\partial x} \right) - \frac{1}{r} \frac{\partial r \tau_{rx}}{\partial r} - \frac{1}{r} \frac{\partial \tau_{\phi x}}{\partial \phi} - \frac{\partial \tau_{xx}}{\partial x} + \frac{\partial p}{\partial x} = 0 \quad (5.2.4)$$

$$\rho c_p \left( \frac{\partial T}{\partial t} + v \frac{\partial T}{\partial r} + \frac{w}{r} \frac{\partial T}{\partial \phi} + u \frac{\partial T}{\partial x} \right) - \frac{DP}{Dt} - \frac{1}{r} \frac{\partial}{\partial r} \left( \lambda r \frac{\partial T}{\partial r} \right) - \frac{1}{r^2} \frac{\partial}{\partial \phi} \left( \lambda \frac{\partial T}{\partial \phi} \right) - \frac{\partial}{\partial x} \left( \lambda \frac{\partial T}{\partial x} \right) = 0 \quad (5.2.5)$$

In 5.2.5 the term  $\underline{\tau} : \nabla \vec{u}$  in 4.0.3 has been neglected. This can be done when the temperature effects due to the flow viscous dissipation can be neglected. This is generally the case for low Mach number gas flows which are generally considered in combustor flows. The energy equation reduce than to a simple scalar transport equation for the temperature.

### 5.2.1 Steady Laminar Pipe Flow

In the assumptions of

1. pipe configuration ( $v = w = 0$  see fig. 5.2.1)
2. steady flow ( $\frac{\partial}{\partial t} = 0$ )
3. incompressible flow ( $\rho = \text{constant}$ )



4. fully developed pipe flow  $\frac{\partial p}{\partial x} = \text{constant}$

5. isothermal flow ( $T = \text{constant}$ )

Equation 5.2.1-5.2.5 simplify as follows:

$$\frac{\partial u}{\partial x} = \frac{\partial v}{\partial r} = \frac{\partial w}{\partial \phi} = 0 \quad (5.2.6)$$

$$\frac{\partial p}{\partial x} = \frac{1}{r} \frac{\partial r \tau_{rx}}{\partial r} \quad (5.2.7)$$

From 4.0.7  $\tau_{rx} = \mu \frac{\partial u}{\partial r}$  and the system of equations reduces to a system of ordinary differential equation with the non-slip boundary condition at the wall

$$\frac{dp}{dx} = \frac{1}{r} \frac{dr \tau_{rx}}{dr} = K \quad (5.2.8)$$

$$\mu \left( \frac{d^2 u}{dr^2} + \frac{1}{r} \frac{du}{dr} \right) = K \quad (5.2.9)$$

$$u|_{\pm R} = 0 \quad (5.2.10)$$

The velocity profile can be obtained by integration of 5.2.9:

$$u = u_{max} \left( 1 - \frac{r^2}{R^2} \right) \quad (5.2.11)$$

where

$$u_{max} = -\frac{K R^2}{\mu 4} \quad (5.2.12)$$

the cross-sectional mean flow velocity is given by

$$U_b = \frac{1}{\pi R^2} \int_{-R}^R 2\pi r u dr \quad (5.2.13)$$

and using 5.2.11,

$$U_b = \frac{1}{2} u_{max} \quad (5.2.14)$$

due to the parabolic velocity profile the shear stress is linear in  $r$ , having its maximum in absolute value at the pipe wall:

$$|\tau_w| = |\tau_{xr}|_{\pm R} = 4\mu \frac{U_b}{R} \quad (5.2.15)$$

The relation between the frictional loss and the cross-sectional mean flow velocity can be formulated in non-dimensional form as follows [85]

$$C_f = \frac{\tau_w}{\frac{1}{2}\rho U_b^2} = 8 \frac{\mu}{\rho U_b R} = \frac{16}{Re_D} \quad (5.2.16)$$

The Navier-Stokes equation can be solved in the case of a steady laminar pipe flow. The velocity profile is parabolic and expressed by 5.2.11 and 5.2.14 in function of the channel pressure gradient ( $\frac{dP}{dx} = K$ ). The channel friction losses and the mean cross sectional velocity are univocally related through the expression 5.2.16 and the definition of the channel Reynolds number.

### 5.2.2 Oscillating Laminar Pipe Flow

In analogy with the case of oscillating channel flow, assuming an harmonically oscillating pressure term of the form

$$\frac{1}{\rho} \frac{dp}{dx} = -K_2 \sin(\omega t) \quad (5.2.17)$$

an analytical solution can be obtained for the velocity field [37]:

$$u(r, t) = -\frac{K_2}{\omega} e^{i\omega t} \left[ 1 - \frac{J_0\left(r\sqrt{-\frac{i\omega}{\nu}}\right)}{J_0\left(R\sqrt{-\frac{i\omega}{\nu}}\right)} \right] \quad (5.2.18)$$

where the  $J_0$  is the zero-th order Bessel function. As for the channel case the solution for very low frequency is quasi-steady

$$u(r, t) = -\frac{K_2}{4\nu} (R^2 - r^2) \sin(\omega t) \quad (5.2.19)$$

and at very high frequencies the flow oscillates inviscidly with a 90° phase shift with respect to the pressure forcing and a stokes layer develops close to the wall:

$$u(r, t) = -\frac{K_2}{\omega} \left[ \cos(\omega t) - \sqrt{\frac{R}{r}} e^{-\eta_s} \cos(\omega t - \eta_s) \right] \quad (5.2.20)$$

where

$$\eta_s = \sqrt{\frac{\omega}{2\nu}} (R^2 - r^2) \quad (5.2.21)$$

The Stokes Reynolds Number is again a representative parameter for such a flow.

## 5.3 Steady Turbulent Pipe and Channel Flow Correlations

In the case of turbulent flow, different relations between the frictional losses and the cross-sectional mean flow velocity can be formulated in a non-dimensional form similar to (5.2.16) and (5.1.17). One first empirical relation was given by H. Blasius already in 1913 for smooth pipes [85]:

$$C_f = 0.0791 Re_{Dh}^{-1/4} \quad (5.3.1)$$

From the definition of  $C_f$  ( $C_f = 2\tau_w/(\rho U_b^2)$ ) and  $\bar{u}_\tau$  ( $\bar{u}_\tau = \sqrt{\tau_w/\rho}$ ) the following can be derived:

$$\frac{\bar{u}_\tau}{U_b} = \left(\frac{C_f}{2}\right)^{1/2} \quad (5.3.2)$$

together with (5.3.1), a relation between  $\bar{u}_\tau$  and  $Re_{Dh}$  can be obtained:

$$\bar{u}_\tau^2 = 0.03955 U_b^2 Re_{Dh}^{-1/4} \quad (5.3.3)$$

Another possibility, is to use the universal law of the wall presented in section 4.3 to describe the turbulent velocity profile:

$$\bar{u} = \bar{u}_\tau \left( \frac{1}{\kappa} \ln y^+ + C \right) \quad (5.3.4)$$

the cross sectional mean velocity,  $U_b$ , can be obtained by spatial integration as in (5.2.13) and (5.1.13) and using the definition of  $C_f$  and  $Re_{Dh}$  the following expressions can be derived:

$$\frac{1}{(4C_f)^{1/2}} = 1.99 \log [Re_{Dh}(4C_f)^{1/2}] - 1.02, \quad (5.3.5)$$

for pipe flows [85], and for rectangular Channels [85]:

$$\frac{1}{(4C_f)^{1/2}} = 2 \log [Re_{Dh}(4C_f)^{1/2}] - 1.19. \quad (5.3.6)$$

In non-isothermal flows, for the determination of the turbulent heat transfer coefficient, the Buckingham *II*-Theorem of dimensional analysis imposes the definition of three non dimensional parameters. the Prandtl number,  $Pr$  and the Reynolds number  $Re_{Dh}$  have been already introduced. A third one, the Nusselt number,  $Nu$  needs to be introduced here.

Due to the simple geometry, a channel or pipe flow can be characterized at each axial position by its cross-sectional velocity  $U_b$  and the so called cup-mixing temperature  $T_m$  defined as :

$$T_m = \frac{1}{\dot{m}} \int \rho \bar{u} \bar{T} dA, \quad (5.3.7)$$

where  $A$  is the cross sectional area and  $\dot{m}$  the mass flow. Locally, the turbulent heat flux is given by 4.2.21, but can be expressed globally as

$$q_w = h(T_w - T_m), \quad (5.3.8)$$

where  $q_w$  and  $T_w$  are the wall heat transfer and the wall temperature respectively.  $h$  is called the heat transfer coefficient and in this case relates the cup-mixing temperature  $T_m$  with the imposed wall heat transfer and/or wall temperature. The Nusselt number  $Nu$  is given by

$$Nu = \frac{hD}{\lambda} \quad (5.3.9)$$

and represents an indirect measure of the turbulent heat transfer coefficient using a characteristic dimension  $D$  and the flow heat conduction number  $\lambda$ .

Several empirical correlations are available for channel and pipe flow in the form [88]

$$Nu = C_h Re_{Dh}^\alpha Pr^\beta \quad (5.3.10)$$

for different range of Prandtl and Reynolds number. Here one of the most widely used in pipe flows is reported [88]:

$$Nu = 0.021 Pr^{0.5} Re_m^{0.8} \quad (5.3.11)$$

The Nusselt number correlations for flows between parallel plates are given in [88]. According to [88], the channel case can be viewed as a limit case of the flow in circular-tube annuli with inner and outer tubes heat flux:

$$Nu_{i/o} = \frac{Nu_{ii/oo}}{1 - (\dot{q}_{o/i}/\dot{q}_{i/o})\theta_{i/o}^*} \quad (5.3.12)$$

where the suffix  $i/o$  and  $o/i$  refer to the inner or outer tube surfaces alternatively (see Fig. 5.3.1).  $Nu_{ii}$  and  $Nu_{oo}$  represent the Nusselt number values when the inner or outer tube alone is heated. The other wall is considered insulated. In the case of a channel flow, the radius ratio ( $r^* = r_i/r_o$ ) is equal to one and the Nusselt number at the inner and outer wall are equal ( $Nu_i = Nu_o = Nu_{Ch}$ ). When considering a fix wall temperature difference, the inner and outer heat flux are equal and opposite in sign (see Fig. 8.1.1). Equation 5.3.12 becomes then:

$$Nu = \frac{Nu_{Ch}}{1 + \theta^*} \quad (5.3.13)$$

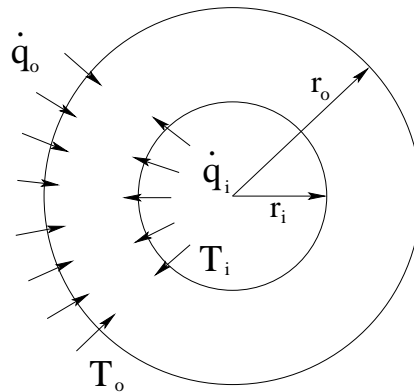


Figure 5.3.1: Nomenclature for flow and heat transfer in a circular-tube annulus.

Values of  $Nu_{Ch}$  and  $\theta^*$  are tabulated in [88] for different values of  $Re_{Dh}$ .

## 6 Pulsating Flows without Heat Transfer

In the frame of the present work the effect of pulsations on the viscous boundary layer was investigated in detail. The present results have been also published by the author in [63] and [64].

As already introduced in Chapter 4, according to the Reynolds analogy the ratio of the turbulent heat diffusivity and turbulent viscosity is assumed to be constant. Once the Reynolds analogy is supposed to be valid, the accuracy of the numerical heat transfer predictions can be indirectly measured by the accuracy of the wall shear stress prediction since they both rely on the correct estimation of the turbulent viscosity. In this sense the turbulence model accuracy in predicting the wall shear stress in unsteady isothermal flow is of interest also for the more complicated non-isothermal flow configurations. In the following, experimental measurements on isothermal pulsating and oscillating turbulent pipe and channel flows are considered for the turbulence model validation. In the next section a general overview about pulsating and oscillating pipe and channel flows is presented. For obvious reasons, the main attention is however focused on the experimental effect of pulsation amplitude and frequency on the overall wall shear stress. In section 6.2.2 a validation of the LES approach in an oscillating channel flow configuration against DNS results from Spalart and Baldwin [76] is presented. Different LES near wall approaches were compared and discussed. The URANS simulation capability are instead tested considering the experimental results of Tardu et al. [79] in section 6.4. In the same section, a comparison between URANS and scaled LES and DNS pulsating channel simulations and experimental results using characteristic non-dimensional parameters is also given.

## 6.1 Overview on Pulsating and Oscillating Pipe and Channel Flow

### 6.1.1 Pulsating and Oscillating Flow Description

One important distinction that must be made in the field of periodic flows is between 'oscillating' and 'pulsating' flows. Flows characterized by a zero temporal mean velocity field are generally defined oscillatory. Pulsating flows instead have a non-zero temporal mean and are often decomposed in their temporal steady part and a superimposed oscillating field. In the more general case of a turbulent flow, a triple decomposition is often performed as follows [37]:

$$\vec{u}(t, \vec{x}) = \vec{u}(\vec{x}) + \vec{\tilde{u}}(\vec{x}, t) + \vec{u}'(\vec{x}, t) \quad (6.1.1)$$

Here the velocity vector  $\vec{u}$  is considered at time  $t$  and at the space location  $\vec{x}$  (analogous relations can be written for any flow quantity). At each time and location a pulsating flow can be decomposed in the sum of its time-averaged values ( $\bar{u}$ ), its oscillating values ( $\tilde{u}$ ) and the turbulent fluctuations ( $u'$ ) (when the flow is in the turbulent regime). The triple decomposition above can be easily visualized considering the graph in fig. 6.1.1. In this case, the black line represents the streamwise velocity component  $u$  in time and  $\bar{u}$ ,  $\tilde{u}$  and  $u'$  are reported at a time

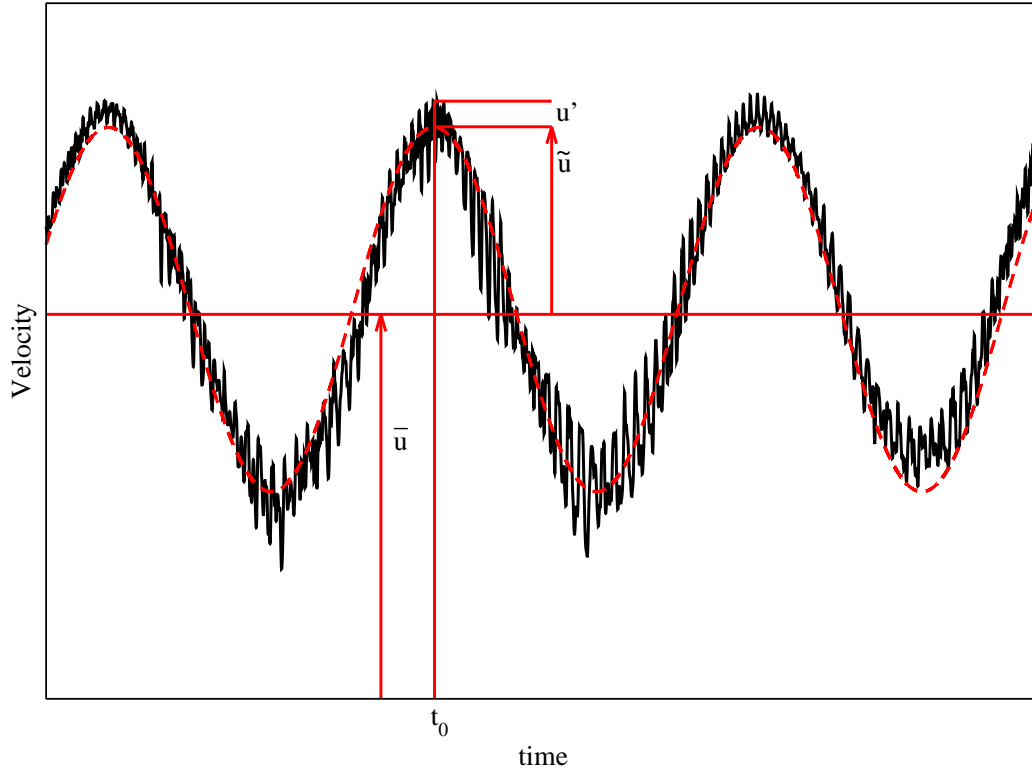


Figure 6.1.1: Triple decomposition of a periodic velocity signal

$t_0$ . If we indicate with  $\mathcal{T}$  the period of the forcing signal, we can extract the time-mean value of the velocity as follows:

$$\bar{u}(\vec{x}) = \frac{1}{n\mathcal{T}} \int_0^{n\mathcal{T}} u(t, \vec{x}) dt \quad (6.1.2)$$

with  $n$  being the number of periods considered for the total time averaging.

The so called phase-averaged quantities are generally defined using the bracket operator:

$$\langle u \rangle(t, \vec{x}) = \frac{1}{n} \sum_0^n u(t + n\mathcal{T}, \vec{x}) \quad (6.1.3)$$

In the graph of fig. 6.1.1  $\langle u \rangle$  is reported with the red dashed line and the following relation is valid:

$$\langle u \rangle(t, \vec{x}) = \bar{u}(\vec{x}) + \tilde{u}(t, \vec{x}) \quad (6.1.4)$$

In a time periodic flow, the sum of the time-averaged and oscillating quantities can be extracted performing a so called 'phase-locked' average (6.1.3) assuming the period of the

forcing frequency,  $\mathcal{T}$ . Often, the oscillating quantities are described using their amplitude and phase with respect to the forcing:

$$\langle u \rangle(t, \vec{x}) = \bar{u}(\vec{x}) + A_u(\vec{x}) \sin(\omega t + \phi_u(\vec{x})) \quad (6.1.5)$$

or

$$\langle u \rangle(t, \vec{x}) = \bar{u}(\vec{x})(1 + a_u(\vec{x}) \sin(\omega t + \phi_u(\vec{x}))) \quad (6.1.6)$$

where  $\omega$  is the angular pulsation frequency ( $\omega = 2\pi/\mathcal{T}$ ).

In conclusion a pipe or a channel in which a periodic fluid motion is realized that can be described using (6.1.5) or (6.1.6) will be referred to a pulsating channel or pipe flow and will be the subject of the present investigation.

### 6.1.2 Laminar to Turbulent Transition

Steady pipe and channel flows are characterized only by the flow Reynolds number defined as in (5.1.18). In pulsating channels, a mean Reynolds number can be defined as

$$Re_c = \frac{U_b D_h}{\nu} \quad (6.1.7)$$

Where the subscript  $c$  has been added to indicate the so called 'current alone' or steady component of the flow.  $U_b$  is the bulk velocity or cross-sectional mean flow velocity expressed as

$$U_b = \frac{\int_S \rho \vec{u} \cdot d\vec{S}}{\int_S \rho dS} \quad (6.1.8)$$

or, for incompressible flows,

$$U_b = \frac{1}{A} \int_S \vec{u} \cdot d\vec{S} \quad (6.1.9)$$

where  $S$  is the cross-sectional surface with area  $A$  and unit normal vector  $d\vec{S}$ .  $\bar{u}$  is the time averaged component as shown in the triple decomposition.

For pure oscillating flows, as discussed in Chapter 5, the Stokes length  $\delta_s$  (5.1.40) is an important parameter and consequently the Stokes Reynolds number,  $Re_{\delta_s}$  ( see definition (5.1.41)) is important too.

As reported in Hino et al. [35] an oscillating channel flow remains stable for  $Re_{\delta_s}$  values below 400. In the range between 400 and 800 the flow exhibits alternatively turbulent and laminar states over a single oscillation period. For  $Re_{\delta_s} > 800$  the flow can be considered fully turbulent.

For pipe flows, Lodahl et al. in [51] considered an analogous parameter, the wave-boundary layer Reynolds number  $Re_w$  defined as follows:



$$Re_w = \frac{A_{uc}^2}{\nu\omega} \quad (6.1.10)$$

where  $A_{uc}$  is the velocity amplitude at the channel centerline. It can be shown that  $Re_w = \frac{1}{2}Re_{\delta_s}^2$ . According to Lodhal et al. the transition from laminar to turbulence can be well described with the so called Tromans stability curve [80]. A comparison between different experiments and the linear stability analysis is reported in fig 6.1.2.

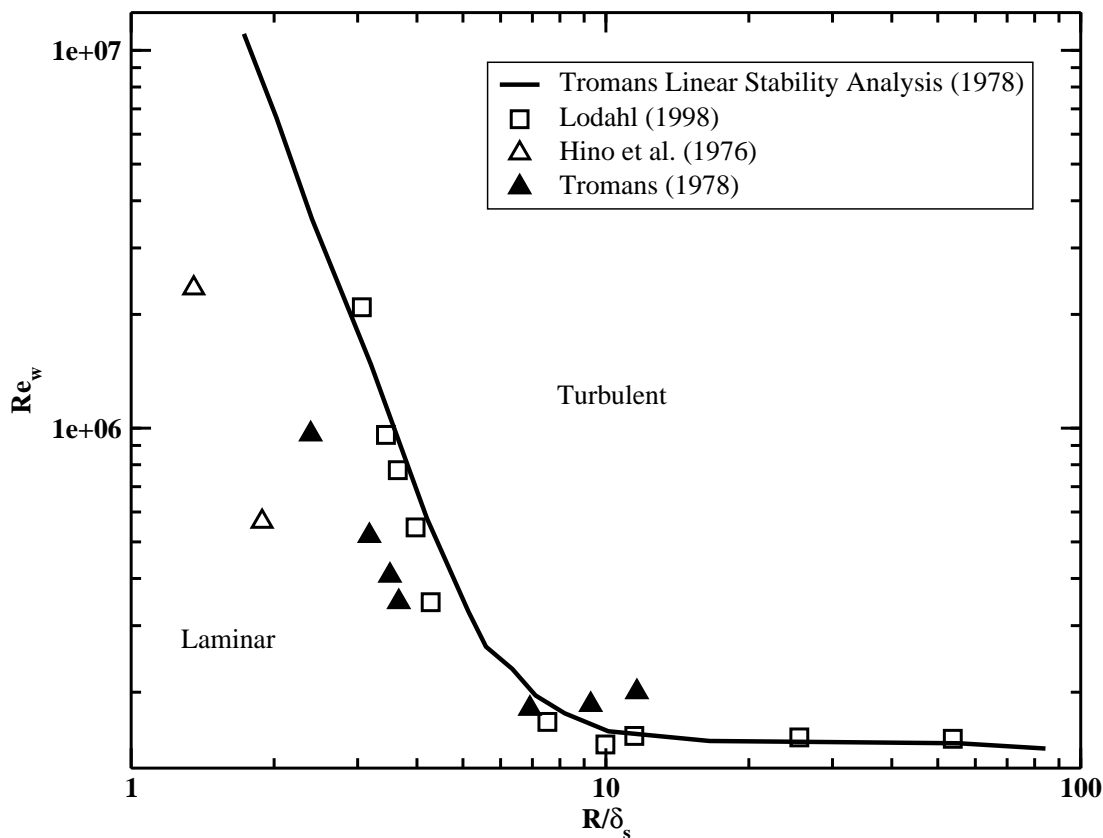


Figure 6.1.2: Transition to turbulence in oscillatory flow alone.(source [51])

As shown in the Figure (6.1.2), for oscillating pipe flows, the transition depends on the Stokes Reynolds number  $Re_{\delta_s}$  or  $Re_w$  and the ratio of the pipe radius to the Stokes length,  $R/\delta_s$ .  $R/\delta_s$  can be seen as a measure of the ratio between the boundary layer thickness and the pulsation penetration depth.

In combined current and oscillatory flow (pulsating flows), the stability curves are different, see Fig. (6.1.3). Due to the presence of a characteristic elbow in the experimental transition curve, it is clear that for a current alone flow the transition from laminar to turbulence can be delayed with a superposition of an oscillating flow. In fig. 6.1.3 the transition line is reported depending on  $Re_c$  and  $Re_w$  for different values of the parameter  $R/\delta_s$

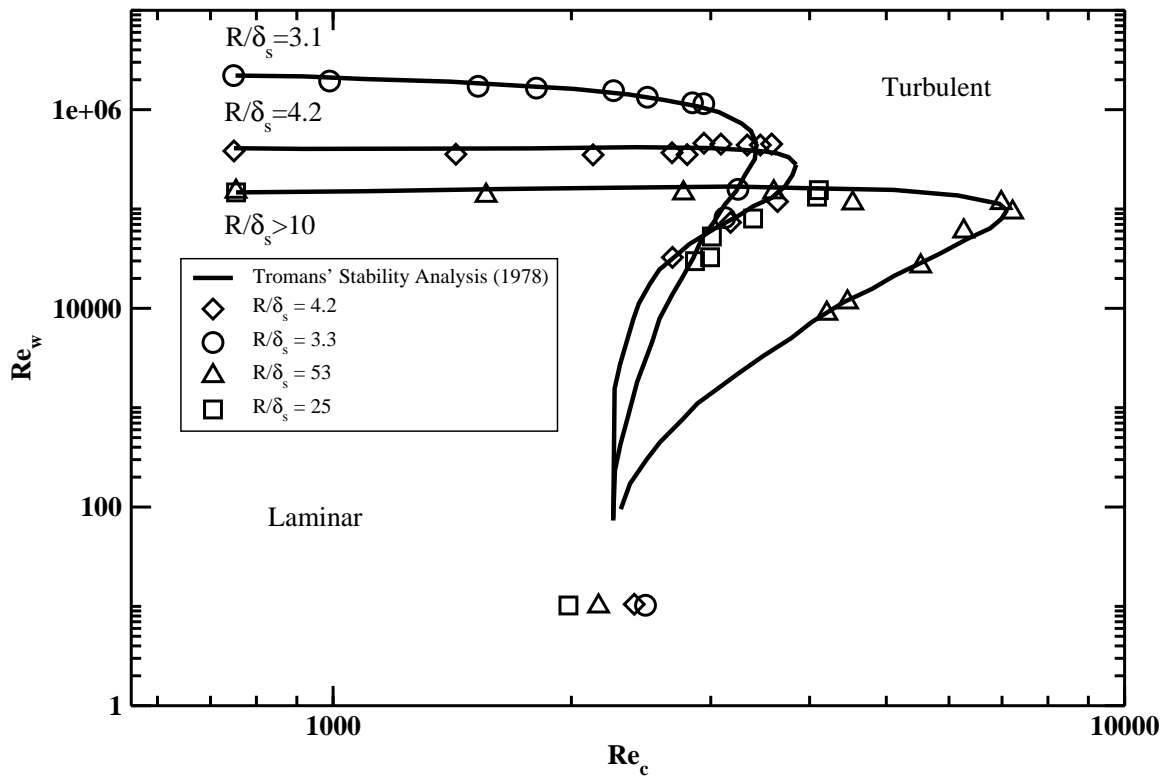


Figure 6.1.3: Transition to turbulence in combined current and oscillatory flow. (source [51])

### 6.1.3 Turbulent Pulsating Flow Regimes

The main parameters which characterize a turbulent pulsating pipe flow are: the pulsation frequency  $\omega$ , the mean bulk velocity  $U_b$ , the pulsation amplitude  $A_{uc}$ , the pipe hydraulic diameter  $D_h$  and the fluid viscosity  $\nu$ . The fundamental physical dimensions involved are mass, length and time. For the Buckingham's *II*-Theorem, the phenomenon can be fully described by the combination of 2 non-dimensional quantities.

If we define with  $\bar{u}_\tau$  the mean friction velocity, a non dimensional frequency parameter can be defined as (see also [72]):

$$\omega^+ = \frac{\omega \nu}{\bar{u}_\tau^2} \quad (6.1.11)$$

note that  $\omega^+$  can be viewed as a forcing frequency expressed in so called 'wall units'. Length and time have been non-dimensionalized using the same quantities as in the universal law of the wall. The corresponding + quantities can be viewed as typical wall quantities, hence 'wall units' (see Equation 4.3). Expressing the Stokes length in wall unit:

$$l_s^+ = \frac{\delta_s \bar{u}_\tau}{\nu} \quad (6.1.12)$$

it is easy to show that

$$\omega^+ = \frac{2}{l_s^+} \quad (6.1.13)$$

and both parameters can be used for the flow characterization.

Writing the phaselocked averaged velocity at the pipe centerline as follows:

$$\langle u_c \rangle(t, \vec{x}) = \bar{u}_c(\vec{x})(1 + a_{uc}(\vec{x})\sin(\omega t + \phi_u(\vec{x}))) \quad (6.1.14)$$

the non-dimensional pulsating flow ratio  $a_{uc}$  can be used as the amplitude parameter and both  $\omega^+$  and  $a_{uc}$  or  $l_s^+$  and  $a_{uc}$  can be used to scale the problem in physical similitude.

Depending on the parameter  $a_{uc}$ , two flow regimes can be distinguished: the wave dominant ( $a_{uc} \gg 1$ ) and the current dominant ( $a_{uc} \ll 1$ ). In the current dominant regime, the turbulent structures are little affected by the variation of  $a_{uc}$ . The flow seems to be controlled mainly by the value of  $\omega^+$  [72], [79]. For low values of  $\omega^+$  the flow can be considered quasi steady. The turbulence has time to relax to the local (in time) and spectral equilibrium. The flow can be studied as a succession of steady states and the boundary layer is not affected by flow pulsations. This situation has been sketched in Figure (6.1.4) a).

When the frequency is increased the turbulence production and dissipation start to show a phase lag. The stabilizing effect of acceleration can relaminarize the flow as also revealed by the stability curve in Figure (6.1.3). The acceleration and deceleration phases are not symmetric and frequency effects on amplitude and phase with respect of the outer flow velocity are measured for the wall shear stress [79], [72], [20]. This flow regime is often referred as the intermediate frequency range and it is characterized by the presence of a turbulent Stokes Layer similar to the one observed in laminar flows (5.1.2). This situation is sketched in Figure (6.1.4) b). Due to the non-symmetric acceleration and deceleration phase, four profile are shown instead of the three plotted in Figure (6.1.4) a). The effects of flow pulsations are confined in a turbulent Stokes Layer,  $\delta_{st}$  where overshoot and undershoot of velocity can be measured.

The thickness of the turbulent Stokes Layer decreases with the increasing forcing frequency and in the inertia dominated or quasi-laminar regime the turbulent Stokes layer thickness is comparable with the viscous sub layer. This is the case shown in Figure (6.1.4) c). In this case a flow solution can be obtained combining the laminar Stokes solution in the laminar sub-layer with a turbulent plug flow far from the wall. Despite the strong effects of pulsation on the turbulent structures, in current dominated regimes, the mean flow quantities, such as mean velocity profile and wall shear stress, seem not to be much affected by pulsations. Small increasing as well as decreasing of the mean wall shear stress were detected by different authors. For a complete review on the subject we refer to [33]. For very high frequency, the forcing start to be comparable with the current alone turbulent bursting frequency and some experiments

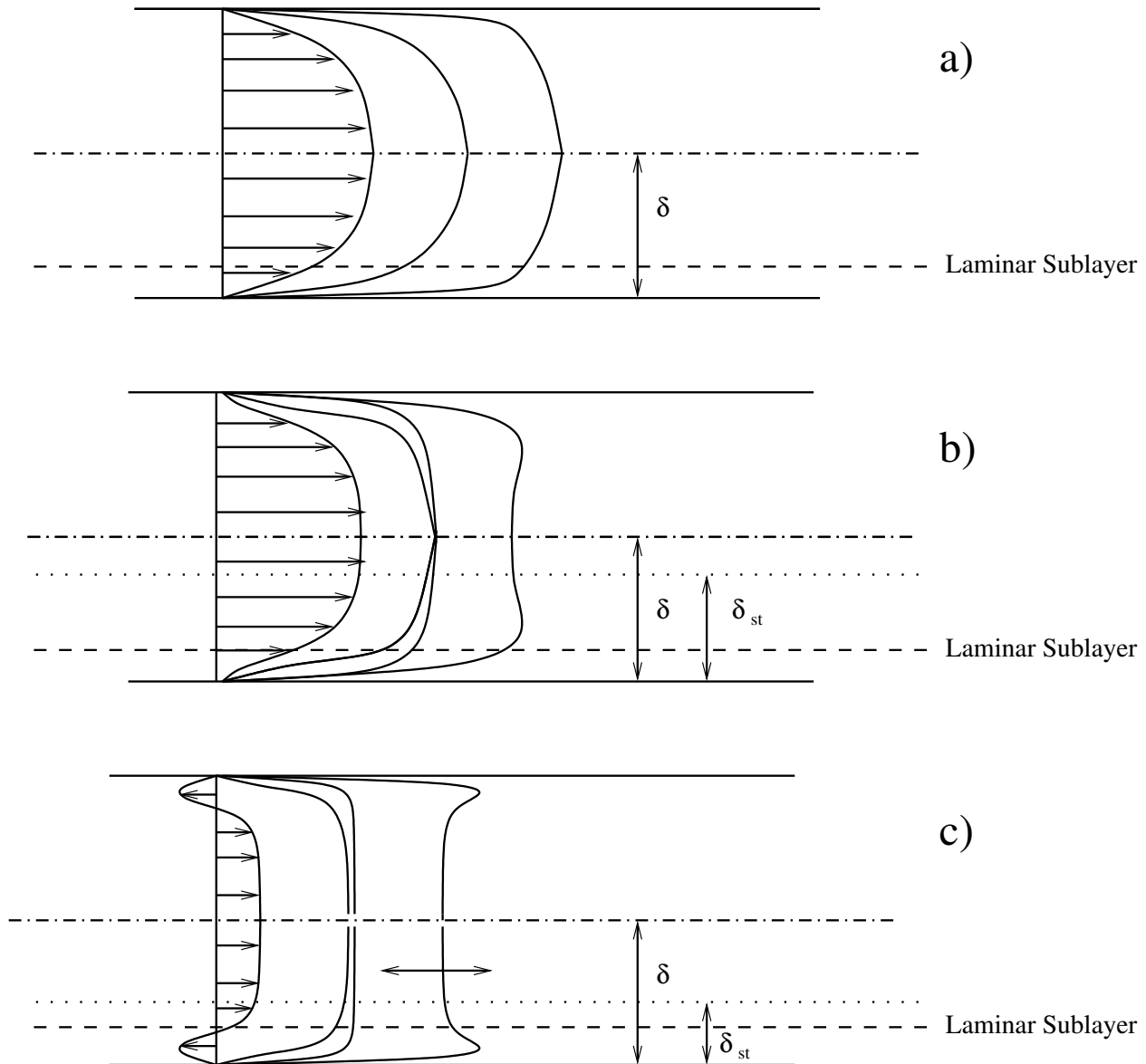


Figure 6.1.4: Turbulent Pulsating flow regimes. a) Quasi steady b) Intermediate Frequency c) Quasi Laminar

report, with considerable scattering, different effects on the amplitude and modulation of the wall shear stress. In wave dominated flows and in flows with  $a_{uc} = 1$  flow reversal in the totality of the channel or in limited areas close to the walls (see Figure 6.1.4 c) ) is experienced with a consequently strong effect on the wall shear stress and turbulent heat transfer characteristics.

## 6.2 LES simulation of Oscillating Turbulent Flow

DNS and LES computations presented in the following chapters, were performed using the AVBP code developed by CERFACS and IFP [4]. AVBP is a parallel CFD code that solves the laminar and turbulent compressible Navier-Stokes equations in two and three space dimensions on unstructured and hybrid grids. The data structure of AVBP employs a cell-vertex finite-volume approximation. The basic numerical methods are based on a Lax-Wendroff or a Finite-Element type low-dissipation Taylor-Galerkin discretization in combination with a

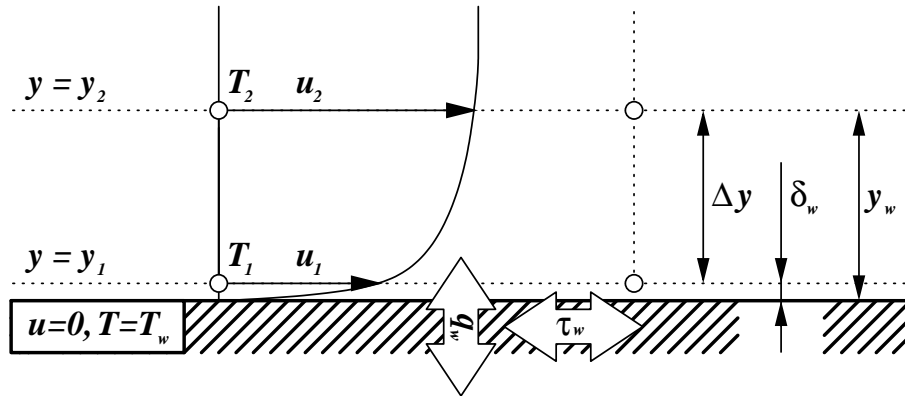


Figure 6.2.1: Typical velocity profile near the wall and notation used for near-wall quantities.

linear-preserving artificial viscosity model [4]. In this work only the Lax-Wendroff scheme was used, the study of the influence of the numerical scheme on the solution remains open for future works. The time discretization is explicit making use of a Runge-Kutta multi-stage time stepping. For turbulent compressible flows, AVBP solves the LES formulation of the Navier-Stokes equations ( see equations (4.5.6) - (4.5.8) ) and both the Smagorinsky and the WALE SGS closure can be used (see section 4.5).

### 6.2.1 Wall Functions Implementation

The wall law implemented in AVBP is described in Schmitt [71] and will be only shortly described here. As mentioned above AVBP uses a cell-vertex scheme. All quantities are thus stored at the cell-corners. For the calculation of the viscous fluxes AVBP needs the shear stresses at the cell boundary and the heat fluxes. Schmitt showed that imposing the appropriate value of velocity and temperature at the boundary plus the correct fluxes using the wall-law formulations constrains the flow too much and leads to oscillatory solutions [71]. The strategy used by Schmitt is then to impose the wall-shear stress  $\tau_w$  (and heat flux  $q_w$ ) at the boundary using the wall-function approach without fixing the value of velocity and temperature at the wall cell corners ( $u_1$  and  $T_1$  in figure 6.2.1). Only the normal component of the velocity at the wall is imposed to vanish at the wall for continuity reasons. This is equivalent as shown in figure 6.2.1 to imagine the real wall boundary shifted by a small distance  $\delta_w$  away from the computational domain. Assuming that the shift is small compared to the distance between the wall and the first point in which the wall-function is evaluated ( $\delta_w \ll y_w$ ), it can be neglected when computing the wall distance. The wall shear stress is then imposed at the boundary following the steps in Table 6.1.

### 6.2.2 LES code Validation for Oscillating Flow

In order to validate the code in a turbulent oscillating channel flow application, in the present work, the numerical data were compared with a DNS (Direct Numerical Simulation) from Spalart and Baldwin [76]. Two series of near wall treatments have been employed: the Wall Function Approach as explained in section 6.2.1 and a so called Wall-Normal Resolved approach.

Step 1	Compute $u_\tau$ iteratively from Equation. (4.3.4) with Equation. (4.3.2). Input values: $\bar{u} = u_2, \nu = \nu(T_1), y = \Delta y$ .
Step 2	Compute $\tau_w$ from Equation. (4.3.3) with $\rho = \rho_1$ .
Step 3	Apply $\tau_w$ and advance flow equations.
Step 4	Set normal component of $u_1$ to zero and go to Step 1.

Table 6.1: Working principle of the wall-function boundary condition.

	Fine Grid	Coarse Grid
Wall-Normal		
Resolved	31x31x31	21x21x21
Wall-Functions	37x15x37	31x11x31

Table 6.2: grid points and reference directory table

The computational domain consists of a cubic box of 0.006  $m$  side centered in the axis origin. On the upper and lower box-sides solid wall boundary conditions are applied. The other remaining boundaries are treated as periodic. The flow is considered aligned with the  $x$  axis. The  $y$  axis is normal to the walls and the  $z$  axis is aligned with the span-wise direction.

The flow is oscillated using a pressure source term which realize an harmonic pressure gradient:

$$-\frac{1}{\rho} \frac{\partial p}{\partial x} = K \sin(\omega t) \quad (6.2.1)$$

For the Wall-Function computations two grids, equally-spaced in the three axis direction, are used with different refinement. A wall function treatment is employed in the near wall region as explained in 6.2.1.

In the Wall-Normal Resolved computations, the grids were equally spaced in the  $x$  and  $z$  directions, but stretched in the wall-normal direction in order to resolve the boundary layer up to a  $y^+$  value of the order of 2. In a first approximation the  $y^+$  value is computed using the usual steady channel flow correlations and the maximum velocity value in the cycle. An hyperbolic tangent stretching law has been employed and two different grid refinements are presented. The number of grid points used for each computation are summarized in the table 6.2.

The fluid considered is  $N_2$  with a kinematic viscosity value of  $1.7 \cdot 10^{-5} m^2/s$ . The maximum  $\tau_w$  is calculated considering the maximum cycle velocity at the channel center line. We choose a maximum velocity amplitude,  $U_{max} \approx 70 m/s$  and a frequency of 100  $Hz$  in order to have a Reynolds number based on the Stokes length around 1000 and comparable with the results in Spalart and Baldwin [76].

In a first approximation, the pressure gradient source term was evaluated using the analytical laminar results ( see also 5.1.2 )

$$u(y, t) = -\frac{K}{\omega} e^{i\omega t} \left\{ 1 - \frac{\cosh(y\sqrt{\frac{i\omega}{\nu}})}{\cosh(\frac{h}{2}\sqrt{\frac{i\omega}{\nu}})} \right\} \quad (6.2.2)$$

In order to have an oscillating velocity at the center line as

$$U_c(y, t) = U_{max} \sin(\omega t) \quad (6.2.3)$$

we observed from 6.2.2 that K should be set as

$$K = \omega U_{max} \quad (6.2.4)$$

For large values of  $\omega$ , as already shown in section 5.1.2, (6.2.2) becomes:

$$u(y, t) = \frac{K}{\omega} \left[ \cos(\omega t) - e^{\sqrt{\omega/(2\nu)}(\frac{h}{2}-y)} \cos(\omega t - \sqrt{\frac{\omega}{2\nu}}(\frac{h}{2} - y)) \right] \quad (6.2.5)$$

and the fluid in the core oscillates inviscid, with a phase shift of 90 degree with respect to the pressure source term. The flow has been than initialized with an uniform velocity equal to  $-U_{max}$  and a white noise with typical value of  $u' = 0.02U_{max}$ . The pressure source term  $K$ , starting from the value of (6.2.4) was adjusted in order to have  $U_{max} = 70 \text{ m/s}$  and a Stokes Reynolds number very close to 1000.

For the Wall-Resolved computations, the WALE SGS [26] model has been used in order to reproduce the asymptotic behavior of the SGS turbulence terms to the wall. For the Wall-Functions computations, calculations were performed using the usual homogeneous Smagorinsky SGS model together with the wall function implementation described in section 6.2.1.

The numerical results for the Wall-Function and Wall-Normal Resolved computations are reported in figure from (6.3.1) to (6.3.5) and from (6.3.6) to (6.3.10). The result discrepancies between coarse and fine grid where negligible and for this reason only the fine grid results are reported. For each phase ( $\pi/6$ ,  $\pi/3$ ,  $2\pi/3$ ,  $5\pi/6$  and  $\pi$ ) the non-dimensional values of the wall shear stress ( $\tau_w/U_o^2$ ), the velocity distribution ( $u/U_o$ ), the fluctuation of the velocity components ( $u'/U_o, v'/U_o$  and  $w'/U_o$ ) and the dimensional pressure fluctuations ( $P'$ ) are reported in function of the non-dimensional wall distance. The value of flow quantities have been non-dimensionalized using the velocity amplitude ( $U_o$ ) and the stokes length  $\delta_l$  (5.1.40). Note that the quantity  $\tau_w/U_o^2$  can be considered non-dimensional since the density is equal to one.

The results are obtained by phase-locking averaging the numerical instantaneous values over several cycles. As we can see from the graphs, the velocity profile are quite well captured by

both near wall approaches. We noticed a non-zero value of the velocity at the wall due to the wall-function implementation as explained in section 6.2.1. In the Wall-Function computations, the value of the velocity fluctuations are not well captured at the wall as we expected for the reason that near the wall the turbulent structure are not resolved since they are instead modeled by the wall law. In contrast, the Wall-Normal Resolved computations instead, reproduce quite well the turbulent structures at the wall even if the grid is resolved only in the y-direction. The values of  $u'/U_o, v'/U_o$  and  $w'/U_o$  agree very well with the DNS results. Concerning  $\tau_w$  we observe a good agreement in both series of computations. We notice that the Wall-Normal Resolved computations predict pressure fluctuations one order of magnitude larger than the Wall-Functions computations. In figure 6.3.11 a)  $\tau_w$  is reported in phase and compared with the DNS results. A sketch of the pressure source term in time and the velocity at the channel center line is reported in figure 6.3.11 b). As we can see the Wall-Function computations seem to reproduce better the amplitude of the wall shear stress oscillations. What we notice is a little phase shift between the peak value of  $\tau_w$  that is not present in the Wall-Normal Resolved results. The Wall-Normal Resolved  $\tau_w$  predictions seem to underestimate the peak value of the wall-shear stress but seem to be more in phase with the DNS data. The overall behavior of both approach is quite good in this oscillation frequency.

The most striking discrepancy is on the pressure fluctuation prediction. Unfortunately no direct DNS data are available from [76].

In figure 6.3.12 the pressure term of the Reynolds-stress budget is than computed and compared with the DNS data available from Spalart and Baldwin [76]. The figure shows that the Wall-Normal Resolved result agree well with the DNS data. The Wall-Function results are not reported in the graph since they are out of scale.

$$P_{term} = \Pi_{12} = -\frac{1}{\rho} \left( \overline{u' \frac{\partial P'}{\partial y}} - \overline{v' \frac{\partial P'}{\partial x}} \right) \quad (6.2.6)$$

## 6.3 Conclusions

Two different LES near wall models were compared : the Wall-Function approach and the Wall-Normal Resolved approach. The first is often preferred in the simulation of complex geometry due to the lower grid resolution needed in the near wall region. The validation case proposed arises however some issues on the applicability of the Wall-Function approach in the presence of flow unsteadiness. Despite the agreement of the two near wall models in the wall shear stress prediction, it is however important to discuss the strong difference in the pressure and velocity fluctuation prediction. A comparison of figures from (6.3.1) to (6.3.5) and from (6.3.6) to (6.3.10) reveals the superiority of the Wall-Normal Resolved approach to predict the near wall velocity fluctuations. This can be of secondary importance in isothermal flows but can be extremely important in the simulation of turbulent temperature convection and in reacting flows. Both aspects must be considered in combustion chamber applications.



Concerning the wall pressure fluctuations, figure 6.3.12 confirms the accuracy of the Wall-Normal Resolved LES simulations showing at the same time the strong underestimation of the pressure fluctuation level given by the Wall-Function approach. The use of Wall-Function can be than questionable in each case accurate time resolved pressure fluctuation, in the near wall region, are required. This can be the case for the study of combustion chamber fluid-structure interactions. As shown in Section 2, the thermal and mechanical fluid structure interaction can lead to the appearance of thermo-acoustic instabilities and high wall vibrations which can badly compromise the combustion chamber components. LES simulation have shown the capability of predict quite well the appearance of combustion instabilities and for this reason have been used also in industrial combustion chamber design. In order to save computational time, the wall function approach have been widely used [69]. In this sense, the present results are very important showing the possible limitation of wall function approach.

Concerning the effect of flow pulsations on the boundary layer, it is important to point out that the oscillation frequency in the case of Spalart and Baldwin are very small. As reported by Gundogdu [33] for values of  $\omega^+ \leq 0.001$  the boundary layer behavior is quasi-steady. Since  $\omega^+$  is defined for pulsating flows using the average friction velocity  $\bar{u}_\tau$ , it is difficult to compute  $\omega^+$  for an oscillating flow. In the case of Spalart and Baldwin, considering the maximum oscillating friction velocity instead of its mean value (which is zero for oscillating flows) the  $\omega^+$  parameter is well below the quasi-steady limit. This is also confirmed by the fact that there is practical no phase shift between the wall shear stress and the velocity at the channel center line ( see figure 6.3.11 ). Hence, in this flow conditions, no strong effects are expected on the wall shear stress. For a further investigation on the wall function limitations in the other pulsation regimes, the reader can refer to section 6.5.

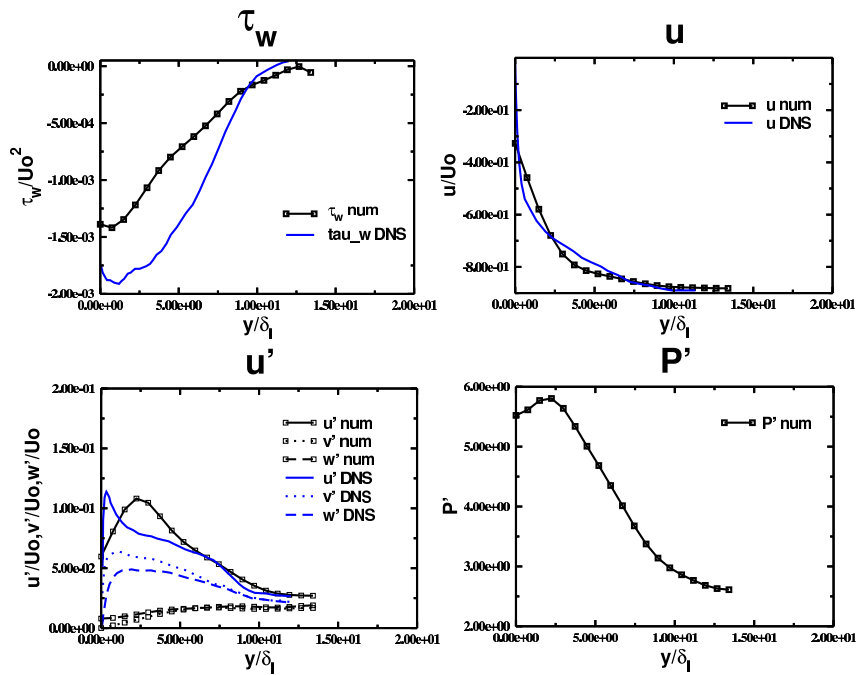


Figure 6.3.1: Phase  $\pi/6$ , Fine grid, Wall-Function Computation.

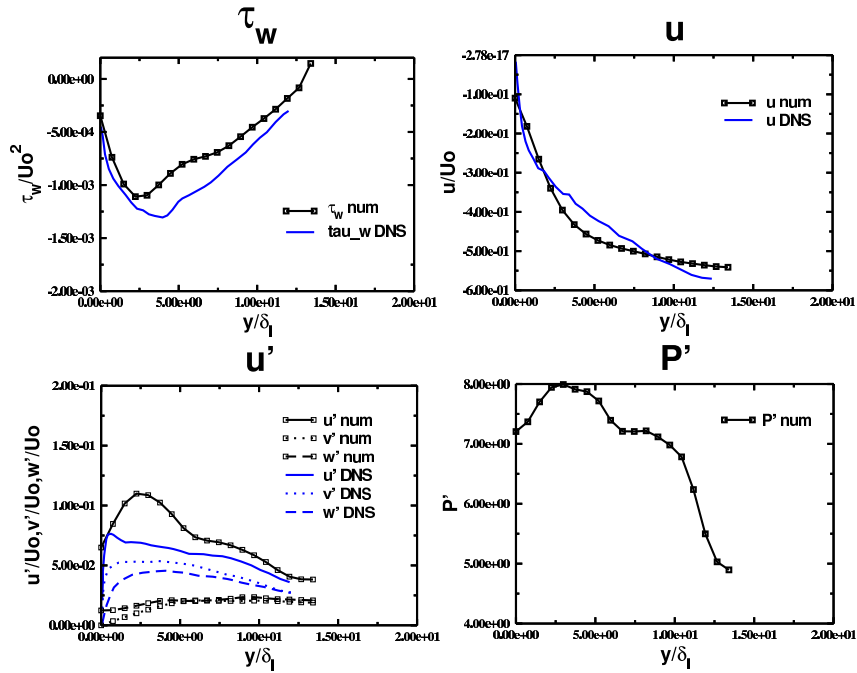


Figure 6.3.2: Phase  $\pi/3$ , Fine grid, Wall-Function Computation.

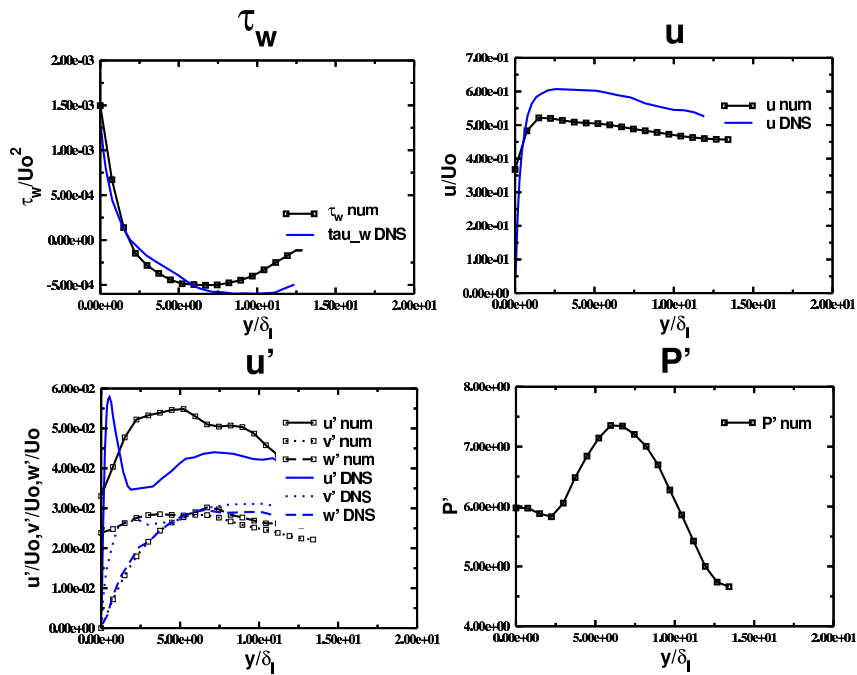


Figure 6.3.3: Phase  $2\pi/3$ , Fine grid, Wall-Function Computation.

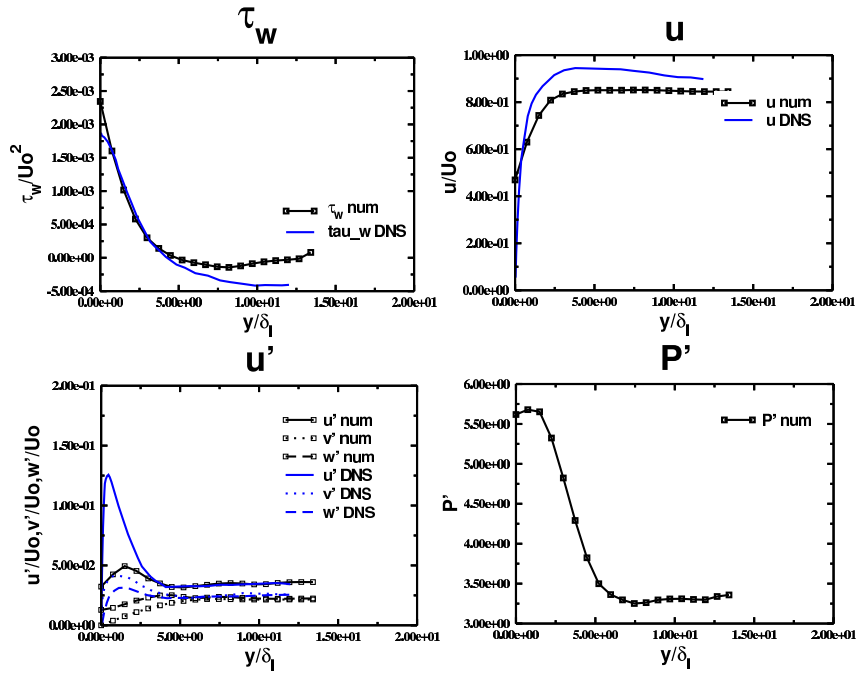


Figure 6.3.4: Phase  $5\pi/6$ , Fine grid, Wall-Function Computation.

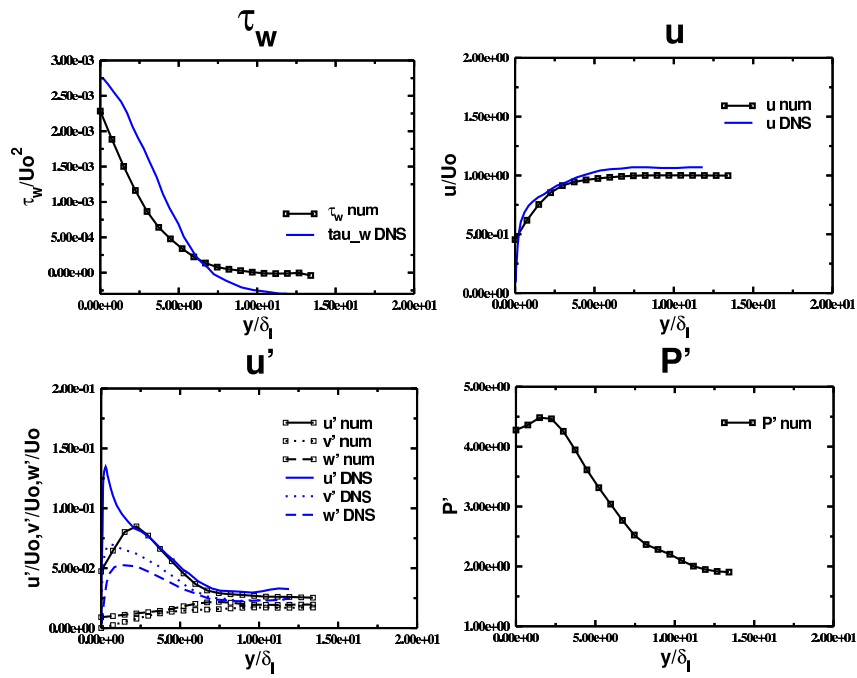


Figure 6.3.5: Phase  $\pi$ , Fine grid, Wall-Function Computation.

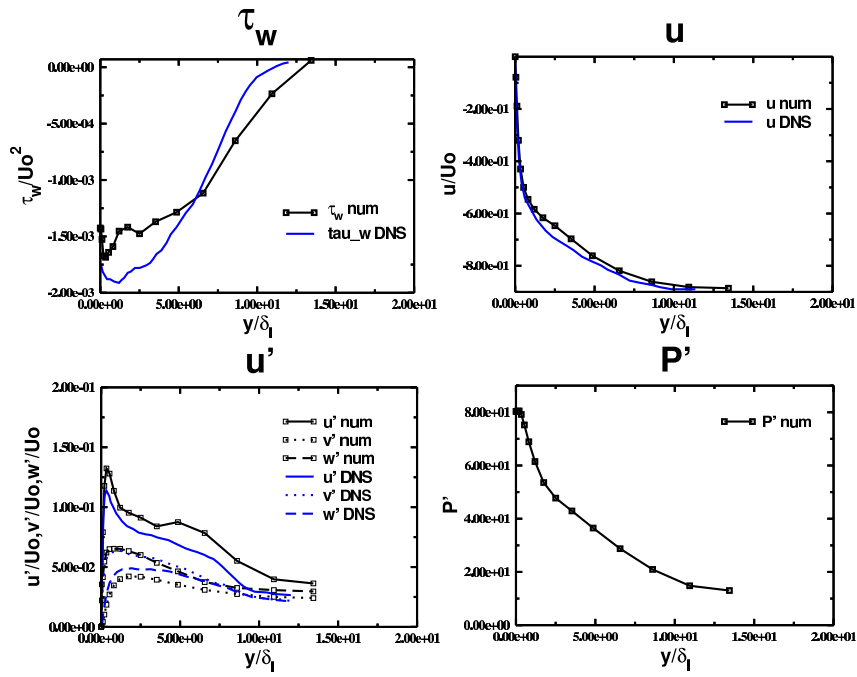


Figure 6.3.6: Phase  $\pi/6$ , Fine grid, Wall-Normal Resolved Computation.

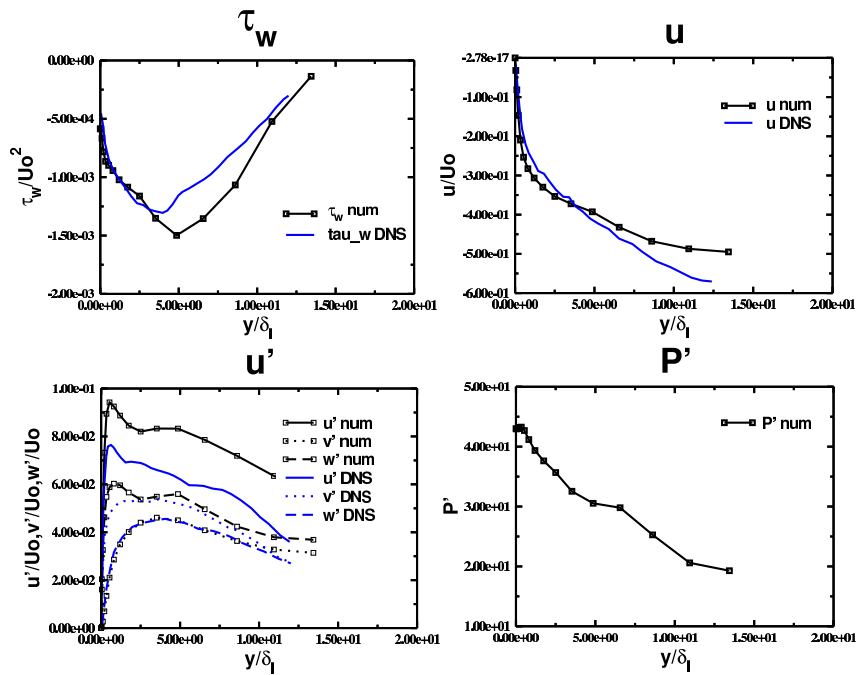


Figure 6.3.7: Phase  $\pi/3$ , Fine grid, Wall-Normal Resolved Computation.

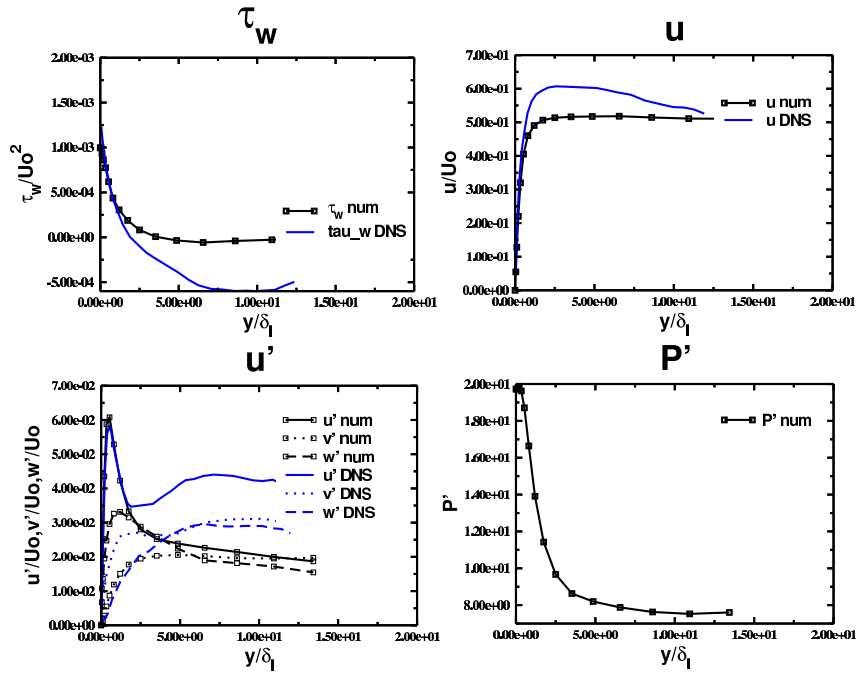


Figure 6.3.8: Phase  $2\pi/3$ , Fine grid, Wall-Normal Resolved Computation.

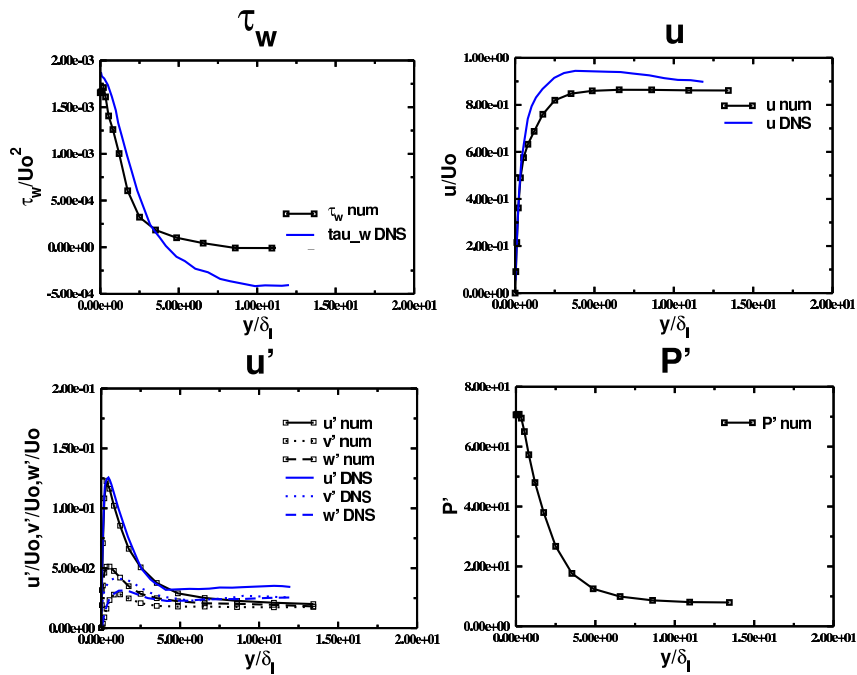


Figure 6.3.9: Phase  $5\pi/6$ , Fine grid, Wall-Normal Resolved Computation.

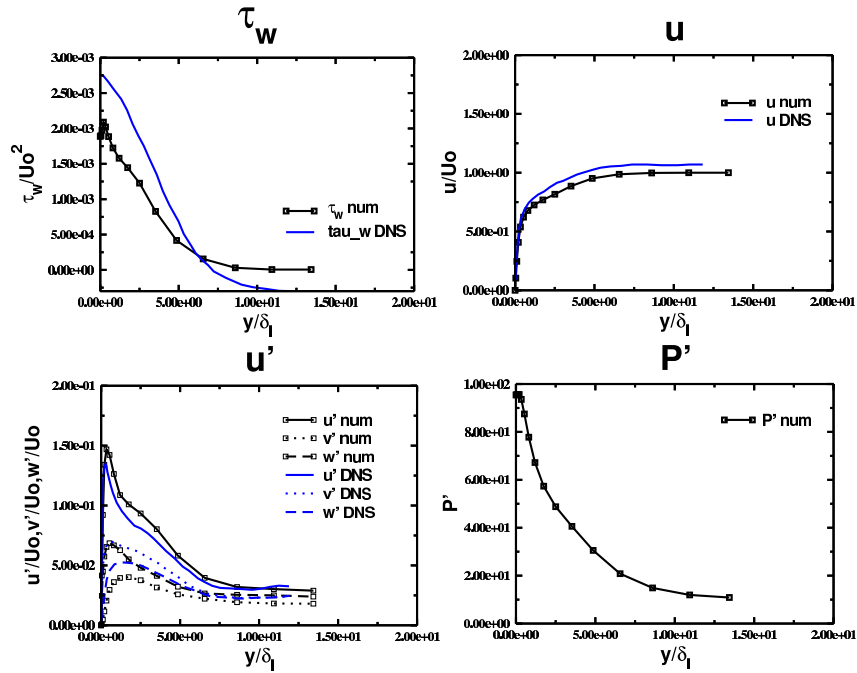


Figure 6.3.10: Phase  $\pi$ , Fine grid, Wall-Normal Resolved Computation.

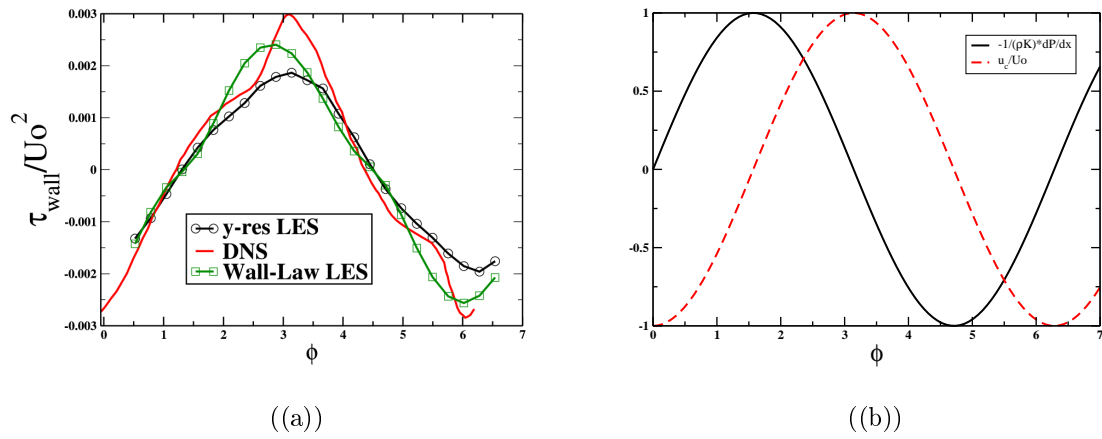


Figure 6.3.11: a) Wall-shear stress vs. oscillation phase, Fine grid, Wall-Normal Resolved and Wall Function Computation. b) pressure source term and center line velocity vs. oscillation phase

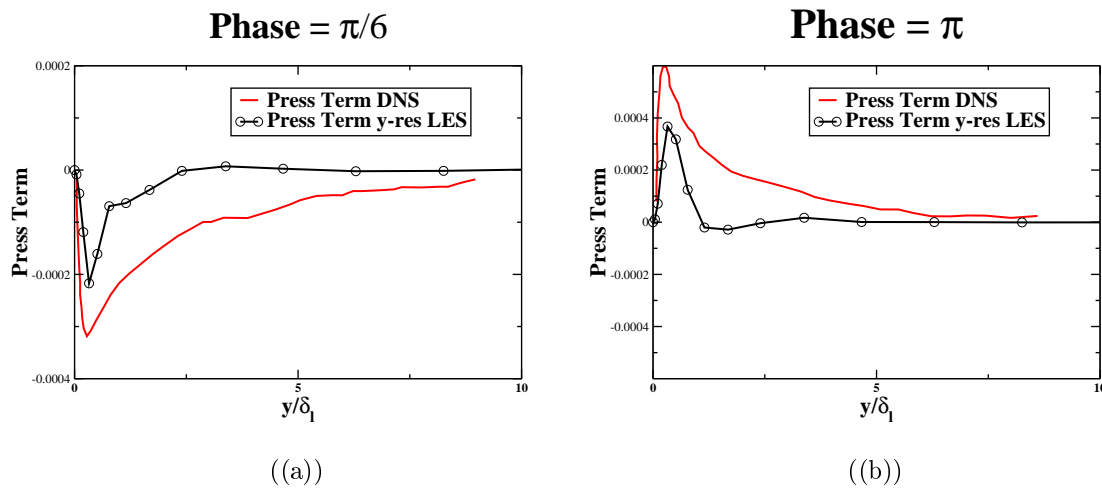


Figure 6.3.12: Pressure term profiles. Comparison with DNS [76]

## 6.4 URANS simulation of Pulsating Turbulent Flow

The URANS calculation was performed using the OpenFoam solver [6]. OpenFoam (Open Field Operation and Manipulation) is a CFD toolbox that uses finite volume discretization to solve systems of partial differential equations ascribed on any 3D unstructured mesh of polyhedral cells. OpenFoam is designed to be a flexible, programmable environment for simulation by having a top-level code that is a direct representation of the equations being solved. Each problem specific partial differential equation can be specified, in the top-level code, in a natural tensor notation. Each equation term can be then discretized and solved choosing different available numerical schemes just editing an input file. Many ready made top-level code are available for the solution of typical fluid dynamics problems. In the present work, the standard OpenFoam solver, turbFoam, for transient incompressible turbulent flows has been used.

turbFoam solves the URANS equation for a turbulent fluid flow using a robust, implicit, pressure-velocity, iterative algorithm based on the PISO scheme [39] (Pressure-Implicit with Splitting of Operators).

The URANS code is validated comparing the results with the experimental data of Tardu et al. [79]. The test channel is 100 mm in width, 2600 mm in length and 1000 mm in span. The working fluid is water and the flow is pulsated using a special device whose details are given in [79]. The flow can be considered isothermal.

Due to the pulsation, the phase locked average value of the velocity at the channel axis can be expressed as in equation (6.1.5) or (6.1.6):

$$u_c(t) = U_c(1 + a_{\bar{u}c} \cos \omega t) \quad (6.4.1)$$

or

$$u_c(t) = U_c + A_{\bar{u}c} \cos \omega t \quad (6.4.2)$$

The values of  $a_{\bar{u}c}$  are varied in the experiment in the range from 0.1 to 0.6. The value of  $U_c$  varies up to 0.5 m/s. The pulsation frequency is given in relation to dimensionless viscous Stokes layer thickness ( $l_s^+$ ) defined in (6.1.12).  $\bar{u}_\tau^2$  is the skin friction velocity of the relative steady channel case with  $U_c$  velocity at the center line.

Also for the URANS simulations, two series of near wall treatments have been employed: the Wall Function Approach as explained in section 4.4.1 together with a  $k-\epsilon$  High Reynolds Number model and a resolved boundary layer approach using the  $k-\epsilon$  Low Reynolds Number model from Launder and Sharma [49].

The grid deployed with Low Reynolds Number turbulence models ( LR-Grid ) is a two dimensional grid with 150x80 points covering the whole testing section (100x2600 mm channel). The points in the direction normal to the channel wall are stretched using a simple grading algorithm in which the ratio between the larger and the smaller cell has been set to 5. The



instantaneous values of  $y^+$ , at the first grid point, are varying during the unsteady computations but are always between 10 and one.

The grid deployed with wall functions (HR-Grid) is not stretched and it is composed of 150x40 points. As expected, the Wall Functions approach requires a minor number of computational points and the  $y^+$  values are in this case of the order of 50.

Concerning the boundary conditions, a turbulent velocity profile according to equation 6.4.3 is pulsated at the inlet and a constant static value of pressure is prescribed at the outlet.

$$u_{inl} = u_{max} \left( \frac{2y}{h} \right)^{\frac{1}{7}} \quad (6.4.3)$$

The value of the turbulent kinetic energy  $k$  is prescribed at the inlet using the experimental value on  $\overline{u'u'}$  reported by Tardu et al [79]. The value of the inlet dissipation rate of the turbulent kinetic energy has been estimated using the following mixing length hypothesis:

$$\epsilon = \frac{C_{\mu}^{0.75} k^{1.5}}{\delta} \quad (6.4.4)$$

where  $\delta$  for fully developed pipe flows can be taken as half channel width. This assumption is representative of the actual flow condition. As reported by Tardu et al in their experiment [79], the channel length is 52 times the channel half width and the flow has been observed to be well established already at  $x/h = 42$ . According to our observation, no alteration in the resulting flow field occurs due to small changes of turbulent inlet parameters.

In figure 6.4 the near-wall velocity profiles in different phases are compared with the experimental results for  $l_s^+ = 8.1$ ,  $a_{\bar{u}c} = 0.64$  and  $U_c = 0.169$  m/s. The computed skin friction velocity for the steady case is 0.92 cm/s. According to the definition of  $l_s^+$  it is possible to calculate the pulsating flow frequency:  $f = 0.41$  Hz. The high Reynolds number and low Reynolds number boundary layer treatments are indicated with HR and LR. The figure shows the first limitation of the wall law approach. In this flow regime, the magnitude of the pulsations determines the flow reversal close to the solid walls. This is not captured by the HR model even though there is quite a good agreement between the HR and LR model far from the wall.

If the wall shear stress is computed using (4.4.22) for the HR case and the following for the LR model:

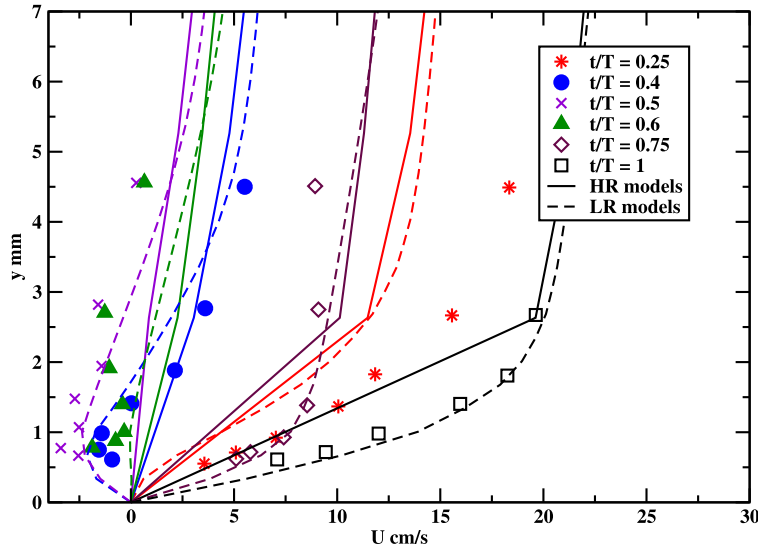


Figure 6.4.1: Instantaneous velocity profiles in the presence of reverse flow.  $U_c = 16.9 \text{ cm/s}$ ,  $a_{\bar{u}c} = 0.64$ ,  $l_s^+ = 8.1$ . Symbols from Tardu et al. [79], solid lines: High Reynolds (HR) number model with wall functions, dashed lines:  $k$ - $\epsilon$  Launder and Sharma low Reynolds (LR) number model.

$$\bar{\tau}_w = \bar{\rho}\nu \left. \frac{\partial \bar{u}}{\partial y} \right|_w \quad (6.4.5)$$

a phase shift with respect to the velocity center line of  $-8^\circ$  and  $33^\circ$  as it is shown in figure 6.6.1 can be observed. Besides the calculations done for  $l_s^+ = 8.1$ , a variety of further simulations were done for other values of  $l_s^+$ . In figure 6.6.1 the value of wall-shear stress phase shift is shown as function of the dimensionless viscous Stokes layer thickness  $l_s^+$ . The numerical results are compared with the experimental results reported by Tardu [79] (symbols in black). The graph shows the incapability of the wall law approach to predict the experimental wall-shear stress phase shift. The vertical lines separate the regimes of quasi-laminar and quasi-steady boundary layer behavior for low and high values of  $l_s^+$  respectively. As already discussed, in the quasi-steady regime, the flow can be studied as a succession of steady states and the wall function assumption seems to be still valid. When the frequency is increased the turbulence production and dissipation start to show a phase lag. In this situation a change in amplitude and phase of the wall-shear stress with respect of the outer velocity is measured as also showed in figure 6.6.1. In conclusion the time resolved behavior of the wall shear stress is correctly predicted by the low Reynolds turbulence model. The wall function approach instead failed to reproduce the effects of flow pulsations. both, the flow reversal close to the wall and the measured phase lag between the wall shear stress and the velocity center line are not captured. This can be critical in the study of combustion instabilities. As stated in section 1, the phase lag between heat wall release and pressure fluctuations can be the source of combustion instabilities. If the

Reynolds analogy is assumed to be valid, the numerical heat transfer prediction capabilities can be indirectly measured by the accuracy of the wall shear stress prediction. The present results clearly indicate the limitation of the wall function approach in the wall shear stress prediction. The main concern is the inaccuracy of the wall function model to predict the boundary layer phase response in both the intermediate and high frequency regimes (see figure 6.6.1). Low Reynolds turbulence models should be than preferred in presence of high frequency flow pulsations and hence in the study of fluid-structure interactions in presence of combustion instabilities.

## 6.5 LES and URANS Near Wall Numerical Predictions in Turbulent Pulsating Flows

In section 6.2.2 the application of the wall function approach to LES simulations in oscillating channel flow was discussed. in the test case presented, no phase-lag between centerline velocity and wall-shear stress was measured. As pointed out in section 6.3, this was expected due to the relatively small flow oscillations. In the present section a LES pulsating channel case was simulated in order to meet the values of  $l_s^+$  considered in the Tardu et al. [79] experiment. A direct comparison with the URANS simulations presented in 6.4 can be than made.

The computational domain and boundary conditions are the same as the validating oscillating case presented in section 6.2.2. Just the source term has been modified as follows:

$$-\frac{1}{\rho} \frac{\partial P}{\partial x} = K_{osc} \sin \omega t + K_m \tag{6.5.1}$$

$K_{osc}$  in first approximation has been evaluated as in section 6.2.2.  $K_m$  has been chosen, as a first approximation, to balance the wall mean value shear-stress giving a positive mean flow velocity:

$$K_m = \frac{2\bar{\tau}_w}{h} \tag{6.5.2}$$

where  $h$  is the channel height and in our case the size of the chosen cubic numerical domain.

Both wall-normal resolved and wall-function LES computation were performed at two different values of  $l_s^+$ :  $l_s^+ = 14.14$ ,  $l_s^+ = 20$ . Considering a value of  $U_c = 70 \text{ m/s}$  and an height of the channel of  $h = 0.006 \text{ m}$ , the corresponding value of  $\bar{\tau}_w$  was around  $13.88 \text{ N/m}^2$  and  $\bar{u}_\tau = 3.48 \text{ m/s}$ . The channel Reynolds number was 98800. At  $l_s^+ = 14.14$  The consequent pulsation frequency was  $1140 \text{ Hz}$ .

The pressure source term amplitude was chosen in order to have a velocity pulsation amplitude ( $A_{\bar{u}c}$ ) equal to  $20 \text{ m/s}$  in each case considered. At different  $l_s^+$  values, the oscillating frequency and the  $K_{osc}$  term have been set coherently. All the computations were then made with the same channel size ( $h = 0.006 \text{ m}$ ) and the computed values of  $U_c$  and  $A_{\bar{u}c}$  were always verified to be around  $70$  and  $20 \text{ m/s}$ .

For the Wall-Function computation an equally spaced grid  $31x31x11$  has been used. For the Wall-Normal Resolved computation a wall-normal stretched grid  $21x21x21$  with a hyperbolic tangent stretching law has been employed. For comparison, a DNS channel of  $h = 0.0015$  m with same values of  $U_c$  and  $A_{\bar{u}c}$  has also been computed. In order to match the nominal condition of  $l_s^+ = 14.14$  the pulsation frequency has been set to  $1500$  Hz. The DNS grid consisted of a wall-normal stretched grid with  $73x73x9$  points.

The wall shear-stress phase shift results are shown in figure 6.6.1.

## 6.6 Conclusions

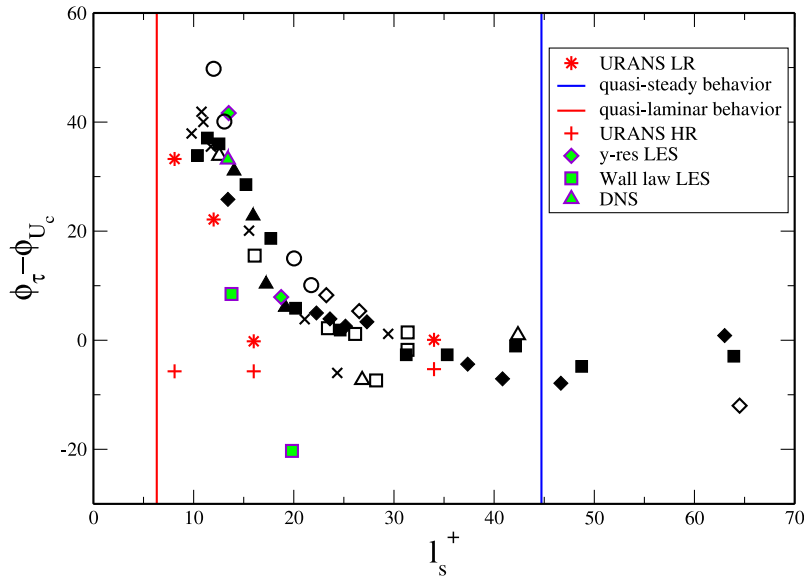


Figure 6.6.1: Wall shear stress phase shift dependence on pulsation frequency

The use of wall-functions for LES and URANS has been investigated paying special attention to the wall shear stress phase shift. In pulsating flow conditions the wall-function approach fails to reproduce the measured wall-shear stress phase shift with respect to the channel center-line velocity. This is shown in figure 6.6.1 and comparisons are given with the experimental results from Tardu et al. [79]. URANS two-dimensional simulations were performed setting the computational domain as close as possible to the Tardu et al. experimental geometry. due to the high computational resources required, this was not possible for the three-dimensional LES simulations.

LES simulations were performed on a much smaller turbulent channel flow at comparable values of the pulsation flow parameter  $l_s^+$ . A validation of the LES code and the flow configuration was given in 6.2.2.

The comparison presented in figure 6.6.1 shows clearly the limitation of the wall-function approach both in LES and URANS simulations. The use of Wall-Normal Resolved computations for LES and Low-Reynolds Turbulent models for URANS seem to drastically improve the results, capturing the unsteady effects of pulsation on the wall-shear stress phase shift. The use of wall functions seems to be accurate only in cases in which the oscillation frequency are well below the quasi-steady limit. In all the other cases the use of wall-functions in URANS and LES computations is questionable especially in applications in which phase lags can play an important role such as the prediction of thermo-acoustic instabilities.



## 7 Pulsating Flows with Heat Transfer - The Ishino et al. Test Case

The experimental work of Ishino et al. [38] is devoted to the investigation of the effect of pulsation on internal heat transfer. Due to the set up simplicity and the wide range of pulsation amplitude investigated, it has been used as an experimental test case for different numerical near wall treatments. In the next chapters a brief description of this test case is followed by a more detailed description of the numerical models used for the comparison and the simulation results.

## 7.1 Test Case Description

A pulsating flow generator composed of a blower and a piston-cylinder system [38], feeds air at ambient temperature in a circular test tailpipe section heated by feeding saturated vapor at atmospheric pressure into a concentric exterior annular pipe (see Figure 7.1.1). The heated section is of  $25\text{mm}$  inner diameter and  $2\text{m}$  length. The pipe heat transfer is measured comparing the time-averaged sectional temperature profiles in two different stream-wise locations. The measuring sections are located respectively at  $601\text{mm}$  and  $1443\text{mm}$  downstream the inlet of the heated part.

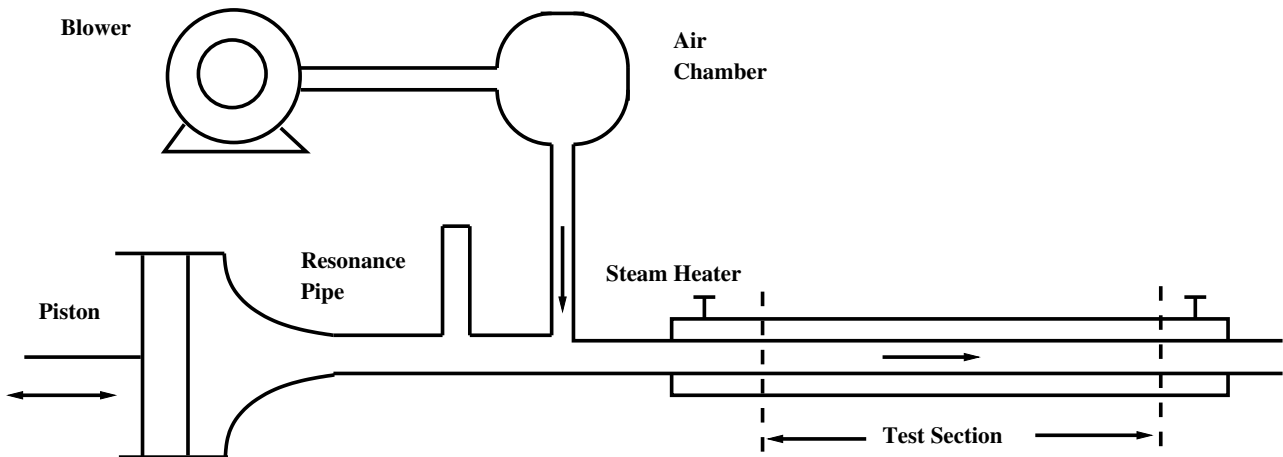


Figure 7.1.1: Ishino et. al. experimental apparatus, simplified sketch

The ensemble average of the velocity at the pipe center line realized by the pulsating device can be described as follows:

$$U(t) = V + U_b \sin(\omega t + \phi_{uc}) \quad (7.1.1)$$

The overall heat transfer coefficient  $h$  is estimated by Ishino [38] as:

$$h = mc_p \frac{T_{m2} - T_{m1}}{S \Delta \theta} \quad (7.1.2)$$

where  $m = \rho A U_m$  is the mass flow rate,  $T_{m1}$  and  $T_{m2}$  the inlet and outlet sectional-averaged temperatures and  $S = 2\pi R L$  is the surface of heat transfer. The density,  $\rho$  and specific heat at constant pressure coefficient  $c_p$  of air are assumed to be constant and  $\Delta \theta$  indicates the logarithmic mean temperature difference defined by



$$\Delta\theta = \frac{T_{m2} - T_{m1}}{\ln\left(\frac{T_w - T_{m1}}{T_w - T_{m2}}\right)} \quad (7.1.3)$$

The sectional averaged temperatures  $T_{mn}$ , with the subscript  $n$  depending on the measuring section, are calculated as

$$T_{mn} = \frac{2\pi}{U_{mn}A} \int_0^R U(y)T(y)(R - y)dy \quad (7.1.4)$$

where  $A = \pi R^2$  is the area of the pipe section,  $R$  is the pipe radius,  $y$  the distance from the pipe center line and  $U_{mn}$  is the sectional-averaged velocity at the pipe section  $n$  defined as

$$U_{mn} = \frac{2\pi}{A} \int_0^R U(y)(R - y)dy \quad (7.1.5)$$

During the experiments two non-dimensional parameter were varied: the pulsating Reynolds number ratio,  $Re_b/Re_m$  and the dimensionless pulsation frequency,  $\omega^{++} = R\sqrt{\frac{\omega}{\nu}}$  where  $Re_b$  and  $Re_m$  are the Reynolds numbers based on the pulsation amplitude  $U_b$  at the pipe center line and the time- and section-averaged velocity  $U_m$ . The fluid kinematic viscosity and the angular pulsation are indicated with  $\nu$  and  $\omega$ .

Equation (7.1.2) can be used to measure the overall heat transfer in both steady and pulsating case. If we indicate with  $h_p$  the heat transfer coefficient calculated using (7.1.2) in the pulsating case, and with  $h$  the heat transfer coefficient relative to the steady pipe flow with mean sectional velocity  $U_m$ , an interesting quantity is represented by the heat transfer coefficient ratio  $h_p/h$  as a measure of the effect of pulsation on the enhancement of the overall heat transfer. Indicating with  $\lambda_f$  the thermal conductivity of air at the film temperature  $T_f = \frac{1}{2}(T_w + \frac{1}{2}(T_{m1} + T_{m2}))$  it is possible to define an analogous Nusselt number ratio,  $Nu_p/Nu$  where

$$Nu = h \frac{R}{\lambda_f} \quad (7.1.6)$$

Ishino et al. reported the value of  $Nu_p/Nu$  for different value of  $Re_b/Re_m$  and  $\omega^{++}$ . The experimental conditions are reported in table 7.1. The values of  $\omega^{++}$  considered in the experiment of Ishino et al. were in the range 17.7 – 35.5 very close to the values of the pulsating motor tailpipe experiment of Dec and Keller [22]. In the present investigation two pulsation frequency were considered: 15 and 20 Hz at  $U_m = 5$  m/s. These conditions correspond to  $\omega^{++}$  values of 28.6 and 33 respectively. It is important to point out that these frequency correspond to  $\omega^+$  values of 0.02 and 0.015 respectively, hence they to the intermediate frequency range (see section 6).

$U_m[m/s]$	5.0				8.0			
$f[Hz]$	5	10	15	20	5	10	15	20
$U_b[m/s]$	2.9	3.0	4.3	6.9	3.2	3.6	4.0	7.5
$Re_b/Re_m$	0.58	0.60	0.86	1.38	0.40	0.45	0.50	0.94
$U_b[m/s]$	15.7	33.9	29.2	30.0	14.2	27.9	29.6	27.5
$Re_b/Re_m$	3.14	6.78	5.84	6.00	1.78	3.49	3.70	3.44

Table 7.1: Experimental Conditions of Pulsating Flows from Ishino et al. [38]

## 7.2 Numerical Simulations

### 7.2.1 URANS simulations

Several series of URANS numerical simulations were conducted in the present work with different turbulence models and at different pulsation frequency and pulsating Reynolds number ratios.

The high Reynolds number  $k$ - $\epsilon$  turbulent model with wall function was used for the so called HR computations. The computational grid in this case consisted of a pipe sector of  $20^\circ$  equally spaced in the longitudinal and radial directions. The  $100 \times 10$  point domain consisted of a single cell in the tangential direction and the boundary conditions were set in order to have a two-dimensional axisymmetric case.

For the LR computations, the low-Reynolds  $k$ - $\epsilon$  turbulence model of Launder and Sharma (see section 4.4.2) has been used. In order to better resolve the boundary layer, a simple grading algorithm was employed to stretch the grid in the wall-normal direction. The wall normal grid dimensions increased from the wall towards the channel center with a constant expansion ratio. The computational grid consisted of  $100 \times 20$  points and the ratio between the larger and the smaller cell height has been set to 20.

For comparison, computation with the  $k$ - $\omega$  SST model (see section 4.4.2.4) have been also performed on the same grid used for the LR computations.

The flow is pulsated using a pressure source term:

$$-\frac{1}{\rho} \frac{\partial p}{\partial x} = K_m + K_{osc} \sin(\omega t) \quad (7.2.1)$$

and  $K_m$  and  $K_{osc}$  are adjusted in order to have a fixed value of  $U_m$  (all the computations are performed with  $U_m = 5m/s$ ) and a variable  $U_b$  (see Equation (7.1.1)) depending on the pulsating Reynolds number ratio,  $Re_b/Re_m$ .

At the inlet and outlet no velocity profiles are prescribed imposing a zero value von Neumann boundary condition ( $\frac{\partial U}{\partial n} = 0$  at the boundaries). This condition together with the use of the pressure source term permits to obtain, after some cycles, a pulsating turbulent fully developed

profile at both inlet and outlet without restriction on the sign of the flow main direction. Due to the high values of the pulsating Reynolds number ratio in fact, the flow completely reverses in the oscillation period.

Constant temperature boundary condition of  $373.15K$  and  $293.15K$  are prescribed at the pipe walls and a at the inlet respectively. Note that depending on the flow direction, the temperature is fixed (at the inlet, flow entering the computational domain) or extrapolated from the interior (at the outlet, flow leaving the computational domain) using a so called inlet-outlet boundary condition (see OpenFoam User Guide [6]).

### 7.2.2 LES simulations

Furthermore in the present work, LES simulations were performed at different frequencies and Reynolds number ratio ( $Re_b/Re_m$ ). The grid used here consisted of 960000 hexaedrons and a transversal grid cut is reported in Fig. 7.2.1. The wall grid resolution is of about 15 wall units in radial and tangential directions. As it is shown in Fig. 7.2.1 the exahedral cells are pretty uniform and in the pipe mid region the grid is practically Cartesian and quadratic. In the longitudinal direction 800 equally spaced point are considered which gives a resolution of 50 wall unit in the stream-wise direction. The wall unit are referred to the mean value of  $u_\tau$ .

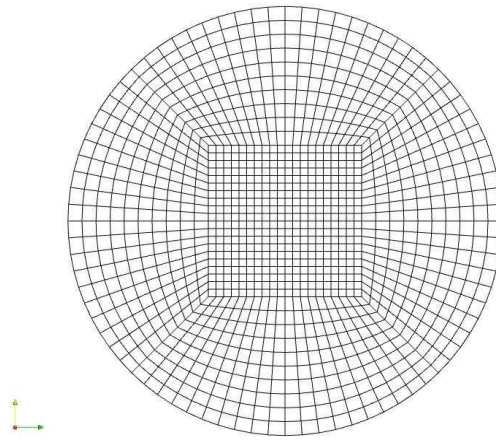


Figure 7.2.1: LES grid, transversal cut

Concerning the SGS LES model a dynamical one equation eddy viscosity model is used [31], [30] which similarly as the WALE model permits to take into account the limiting SGS wall behavior without the use of wall functions. The computational domain not only comprises the 2 meter long three-dimensional pipe test section, but also two additional  $0.25m$  long sections upstream and downstream for a total of  $2.5m$ . 800 equally spaced grid points are considered in the longitudinal direction, giving an axial resolution of circa 50 wall unit. At the inlet and outlet pipe sections, periodic boundary conditions are imposed. The standard OpenFoam LES solver coodles has been modified in order to consider two thermal and pressure extra terms. The pressure term is the same as the one used for the URANS calculations (7.2.1) and realizes the flow pulsations at the required amplitude and frequency. The energy term instead, acts

only outside of the test section in order to cool the flow down to the inlet temperature. In this way a inlet-outlet thermal boundary condition analogous to the URANS simulation is realized.

The periodical boundary conditions not only represent a simple way of handling the inlet turbulence but also, together with the pressure source term, permits to easily treat the inlet-outlet pressure boundary conditions at flow reversal.

The extended inlet and outlet sections, together with the energy sink term assure that the flow enters the test section always at the right inlet temperature independently from the flow direction and without violating the periodic temperature conditions at the inlet and outlet section of the computational domain.

The energy sink term is of the form:

$$H^* = \rho c_p \frac{1}{\tau} (T_i - T) \quad (7.2.2)$$

and it is simply added to the right hand side of 4.2.14.  $T_i$  represents the inlet temperature and  $\tau$  a time relaxation constant which must be set in order to completely cool down the flow within the recovery extra sections at the outlet/inlet region.

### 7.3 Numerical Results

In figure 7.3.1 the numerical prediction of the heat transfer enhancement ratio ( $Nu_p/Nu$ ) has been compared with the experimental results from Ishino [38].

The quasi-steady line reported in the figure is obtained under the hypothesis that the instantaneous value of the heat transfer coefficient can be correlated to the instantaneous value of the flow Reynolds number as in steady turbulent pipe flow [37]:

$$h = kRe^{0.8}. \quad (7.3.1)$$

In pulsating flow, the overall mean value of the heat transfer coefficient can be then obtained by integration as follows [45]:

$$\frac{Nu_p}{Nu} = \frac{h_p}{h_m} = \frac{1}{\mathcal{T}} \int_0^{\mathcal{T}} \left| 1 + \frac{Re_b}{Re_m} \cos(\omega t) \right|^{0.8} dt \quad (7.3.2)$$

Where  $\mathcal{T}$  represents a pulsating period. The above equation can be solved numerically showing an independence on  $\omega$ . For Reynolds number ratio between 0 and 1 Equation (7.3.2) decreases till a minimum value at  $\frac{Re_b}{Re_m} = 1$ . For  $\frac{Re_b}{Re_m} > 1$  Equation (7.3.2) increases practically linearly. As pointed out already by [45], the assumptions on which Equation (7.3.2) can be considered valid are quite open to speculations. The main concern is that the flow is always considered to be fully turbulent. This can be reasonable for values of  $\frac{Re_b}{Re_m}$  below the unity but if the flow reverses ( $\frac{Re_b}{Re_m} > 1$ ), there must be an interval in which the velocity is so low that the Reynolds number is below its laminar-turbulent critical value. In this condition it is questionable whether laminar flow conditions are ever established, or whether the turbulent history of the flow persists during the reversal of direction.

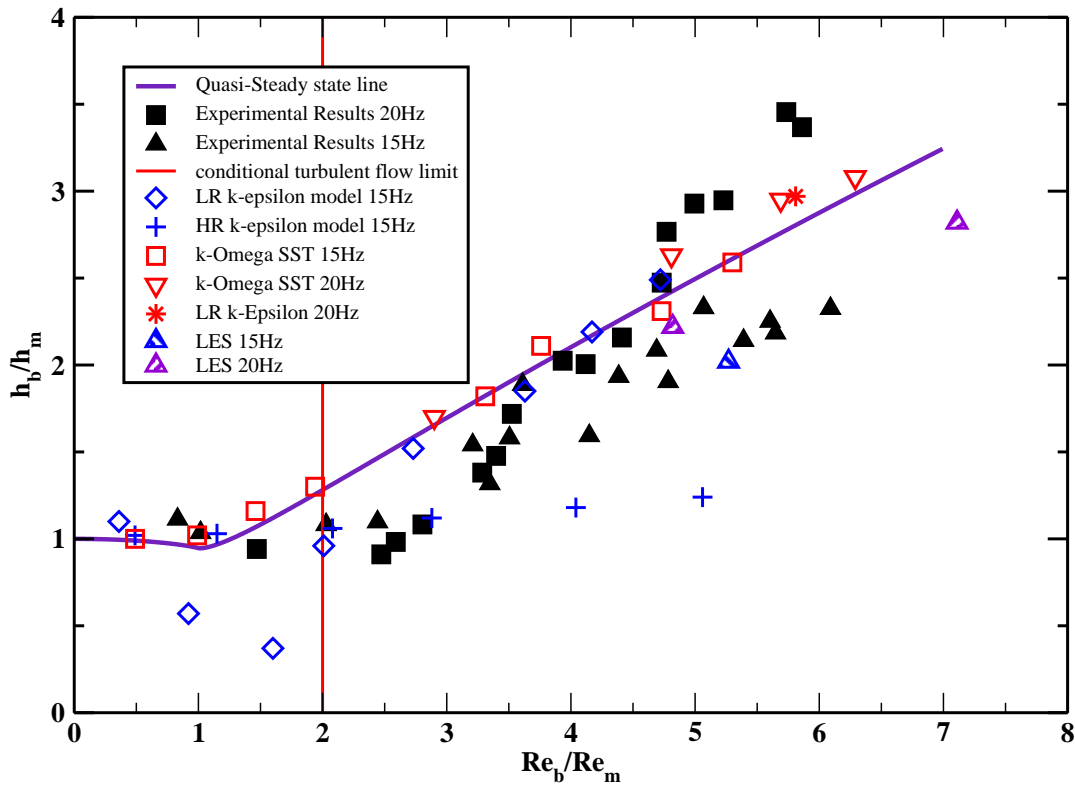


Figure 7.3.1: Effect of the amplitude ratio on heat transfer enhancement ratio, comparison with numerical results ( $U_m = 5m/s$ )

Considering Figure 7.3.1, it can be observed that the high Reynolds number  $k-\epsilon$  model with wall function seems to predict a quite constant value of Nusselt ratio ( $\frac{Nu_p}{Nu}$ ) independently from the Reynolds ratio considered. This is quite far from the experimental results especially in the case of high Reynolds number ratio and with reversing flow. The results obtained with both the Launder and Sharma low Reynolds  $k-\epsilon$  model and the  $k-\omega$  SST model seem to lay on the quasi-steady state line and are not able to take into account the effect of pulsation frequency on the Nusselt ratio found in the Ishino et al. experiment. As it is clear from the graph in fig. 7.3.1 the experiments, for the pulsation frequency case of  $20Hz$ , demonstrate a clear increasing in the overall heat transfer above the quasi-steady line for values of  $Re_b/Re_m$  above 4.5. On the contrary, the experimental data for the case of  $15Hz$  follow the quasi-steady line with an overall shifting towards smaller values of the Nusselt number ratio. The same attenuation with respect to the quasi-steady line is evident for both the 15 and  $20Hz$  case for value of  $Re_b/Re_m$  between 2 and 3.

The Launder and Sharma low Reynolds  $k-\epsilon$  model underestimate the experimental Nusselt ratio and the quasi-steady prediction for  $1 < Re_b/Re_m < 2$ . This is due to the fact that the flow simulation have the tendency to relaminarize. This is coherent with the boundary layer stability

analysis and the transition curves reported in section 6.1.2. The Reynolds current number ( $Re_m$  in the Ishino et al. notation and  $Re_c$  in Lodahl et al. notation) for the case of  $U_m = 5m/s$  is around 8000. For the frequency of  $15Hz$  the Stokes layer thickness is around  $5.6 \cdot 10^{-4}m$  and the ratio  $R/\delta$  is around 22. For  $Re_b/Re_m = 2$  the corresponding oscillatory boundary layer Reynolds number is close to 71000. The condition of  $Re_w = 71000, Re_c = 8000$  is very close to the elbow of the Tromans stability line reported in fig. 6.1.3 for  $R/\delta > 10$ . As reported in [51] flow conditions close to the stability curves are characterized by conditionally turbulent flow. This means that the flow can relaminarize partially or completely in the oscillation period. The transitional turbulent flow limit is reported in fig. 7.3.1 with the vertical red line and seems to be very close to the onset of relaminarization for the  $k-\epsilon$  computations.

Ishino et al. explained the attenuation of the Nusselt ratio in the region of  $2 < Re_b/Re_m < 4$  in the same way. By means of hot-wire anemometers they observed three flow patterns: fully turbulent flow, conditionally turbulent flow and transitional flow. The so called transitional flow was observed in the region  $2 < Re_b/Re_m < 4$  confirming the Tromans stability analysis. In this region, due to the flow pulsation almost no higher frequency velocity fluctuations were measured in the time histories, except in the acceleration period of the reverse flow [38]. The flow practically relaminarize in all other part of the pulsation cycle. When the Reynolds ratio further increases and exceeds 3.0, higher-frequency fluctuations return in the velocity profiles in some part of the cycle. The flow is then considered conditionally turbulent.

The LES computations reported in figure 7.3.1 were performed as described in Section 7.2.2. As it can be seen, at  $15Hz$  the LES results agree very well with the experimental data. Unfortunately this is not the case for the  $20Hz$  LES simulations. All the LES results remain below the quasi-steady curve and seem not to be able to predict the experimental heat transfer increasing at this frequency.

## 7.4 Conclusions

The experimental results from Ishino, showed a dependence of the heat transfer enhancement ratio on pulsation frequency and amplitude. The Launder and Sharma  $k-\epsilon$  low Reynolds model and the  $k-\omega$  SST model seem to perform much better than the  $k-\epsilon$  high Reynolds model with wall functions. This is especially true for high values of the Reynolds number ratio which correspond to the higher overall heat transfer increasing.

However, the two equation models considered seem not to be able of reproducing satisfactory the experimental dependence of heat transfer enhancement on pulsation frequency. The numerical results seem all to lie on the quasi-steady line independently from the frequency considered.

Due to the high computational costs a limited number of LES simulations were performed. The LES Nusselt number ratio predictions show a little dependence on pulsating frequency but always below the quasi-steady line.

The LES wall resolution, due to the length of the domain and the limited computational resources available, could not reach very high resolutions. This could be a cause of error. At

the same time, the Ishino results are very scattered and show a maximum deviation from the quasi steady line of 25% which is not so big considering the experimental errors. The Ishino et al results in the author opinion need to be further confirmed and validated especially in the high Reynolds ratio range. In order to shed more light on the effect of pulsation frequency on turbulence structures and heat transfer, a more extensive and accurate experimental database is needed but not available at the moment. In the mean while, higher resolution LES or DNS simulations could be helpful in understanding the physical phenomena involved.

Due to the difficult boundary conditions and large domain extension, a validation of highly resolved LES simulations and/or DNS is incompatible with the Ishino experiment geometry.

For this reason, and in order to overcome the lack of experimental data, in the next chapter a simpler flow configuration is considered.

However, some important conclusion can be drawn:

- A considerable heat transfer increasing can be obtained in wave dominant flow conditions with high amplitude pulsations. This heat transfer enhancement can be explained by the simple quasi-steady theory with a reasonable accuracy.
- The wall function approach can lead to significant errors for the prediction of the wall heat transfer in wave dominated flows.
- The Nusselt number ratio attenuation below the quasi-steady theory can be related to the presence of transitional flow conditions. This flow conditions can be however quite well be predicted using the linear stability analysis [80]





## 8 DNS of a Channel Flow with Heat Transfer

Despite the interest showed on unsteady heat transfer phenomena, there is a fundamental lack of experimental work in this field. Moreover, the development of turbulence heat transfer models rely on the availability and accuracy of near wall data which are often very difficult to be measured. In recent years DNS has shown the capability to be used as a so called “numerical experiments” and has been used to fill the gap between models and accurate statistical data. In the following, DNS results are presented in a simple channel configuration with heat transfer. The medium considered is air and temperature has been treated as a passive scalar in order to compare the numerical results with the experiments presented in the previous chapter and address the possible limitation of such an assumption. For the steady channel flow, the DNS results are validated against experimental data and very fine resolved DNS simulations available in the literature [42] [47] [52]. Results are also shown and discussed for the unsteady pulsating flow. Unfortunately neither numerical nor experimental results are available for the pulsating case involving heat transfer. In this sense the present work can be considered original and could be used as a numerical database for the development of better unsteady heat transfer models.

## 8.1 Steady Channel Flow with Heat Transfer

The flow considered in this section, hereinafter referred as Steady Channel Flow with Fix Wall Temperature Difference (SChF-FWTD), has been sketched in figure 8.1.1. A fully developed thermal and velocity field occurs between two infinite parallel plates ( $B$  and  $L \gg h$ ) which are kept at different constant temperatures ( $T_1 > T_0$ ). The flow Reynolds number ( $Re_{D_h}$ ) based on the bulk flow velocity  $U_b$  and the hydraulic diameter  $D_h = 2h$  was set to be 13636. Using the common turbulent channel flow correlations [85], it corresponds to a value of the friction velocity  $u_\tau$  of 4.43. Consequently, the Reynolds number based on the friction velocity and half wall distance is  $Re_{u_\tau} \simeq 216$ .

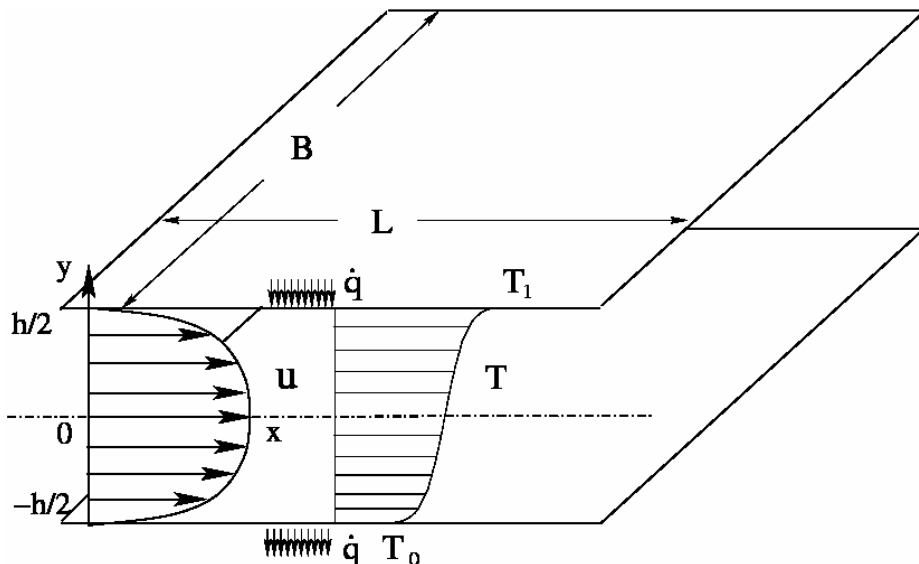


Figure 8.1.1: Flow geometry, velocity and temperature layout

The Nusselt number correlations for flows between parallel plates are given in [88] and have been already discussed in Section 5.3. A linear interpolation between the tabulated values of Nusselt number in the interval  $Re_{D_h} = 10^4 \div 3 \cdot 10^4$  gives the following dependence on  $Re_{D_h}$

$$Nu = 1.43 \cdot 10^{-3} Re_{D_h} + 8.5 \quad (8.1.1)$$

This corresponds to a Nusselt number of 28 and a correspondent friction temperature  $T_\tau = 0.23$

## 8.2 Fundamental Equations and Numerical Solution

Considering the Temperature as a passive scalar in an incompressible flow, the governing equation 4.0.1-4.0.3 can be simplified as follows:

$$\nabla \cdot (\vec{u}) = 0 \quad (8.2.1)$$

$$\frac{\partial \vec{u}}{\partial t} + \nabla \cdot (\vec{u}\vec{u}) - \nabla \cdot \frac{\tau}{\rho} + \frac{\nabla p}{\rho} = 0 \quad (8.2.2)$$

$$\frac{\partial T}{\partial t} + \nabla \cdot (T\vec{u}) = \frac{\nu}{Pr} \nabla^2 T \quad (8.2.3)$$

where, according to 4.0.7,

$$\frac{\tau}{\rho} = \nu \nabla \vec{u} + \nu \nabla \vec{u}^T - \nu \frac{2}{3} Tr(\nu \nabla \vec{u}^T). \quad (8.2.4)$$

In the present simulation a constant Prandtl number has been considered,  $Pr = 0.71$ . No further assumptions have been made to model the turbulent flow. Each term of the above equations have been discretized using a finite volume approach and a direct numerical simulation (DNS) was performed. The CFD code used (OpenFoam) solves the coupled momentum-continuity system using a PISO strategy. The time discretization used is a typical backward Euler scheme (implicit, second order accurate in time) [6]. The gradient terms were discretized using a Gauss linear scheme (second order accurate) [6]. The divergence and Laplacian terms are discretized using a Gauss linear corrected scheme (unbounded second order, conservative) [6], [83].

## 8.3 DNS Calculations of Steady Channel Flow

The computational grid consists of a cubic domain which extends about 430 wall units in the three dimensions. If the wall distance is indicate with  $y$  a wall unit is defined as:  $y^+ = (\bar{u}_\tau y)/\nu$ ; see section 4.3. The finest grid consists of  $100 \times 160 \times 100$  points and has been stretched towards the center of the channel in the wall normal direction ( $y$ -coordinate) with a geometrical progression of ratio 1.03. The resulting minimum and maximum cell dimensions in the  $y$ -direction are respectively 0.6 and 6 wall unit (cell ratio:  $R = 10$ ). The grid is equally spaced

in the span-wise ( $z$ ) and stream-wise ( $x$ ) directions with a resulting point interval of 4.3 wall units.

A coarser grid consisting of  $50 \times 80 \times 50$  points has been also employed and comparisons are given with the finer grid showing very little discrepancies. As well as the finer grid, the coarse grid is equally spaced in the span and stream-wise direction. The stretching ratio is different and has been set to  $R = 20$  giving at the wall values of  $y^+$  comparable to the finer grid.

No-slip and isothermal boundary conditions were used at the upper and lower solid walls. Periodic boundary conditions were imposed on the remaining boundaries. The flow motion was realized using a fix pressure source term in the momentum equation to balance the channel viscous losses:

$$\frac{1}{\rho} \frac{dP}{dx} = \frac{2u_\tau^2}{h}. \quad (8.3.1)$$

## 8.4 Results

For the validation of the code, in Fig. 8.4.1 the DNS temperature profile is compared with experimental values from Page et al. [58] at similar Reynolds Number. The data from [58] have been non-dimensionalized using the half channel distance and wall difference. The DNS results and the experiments agree quite well.

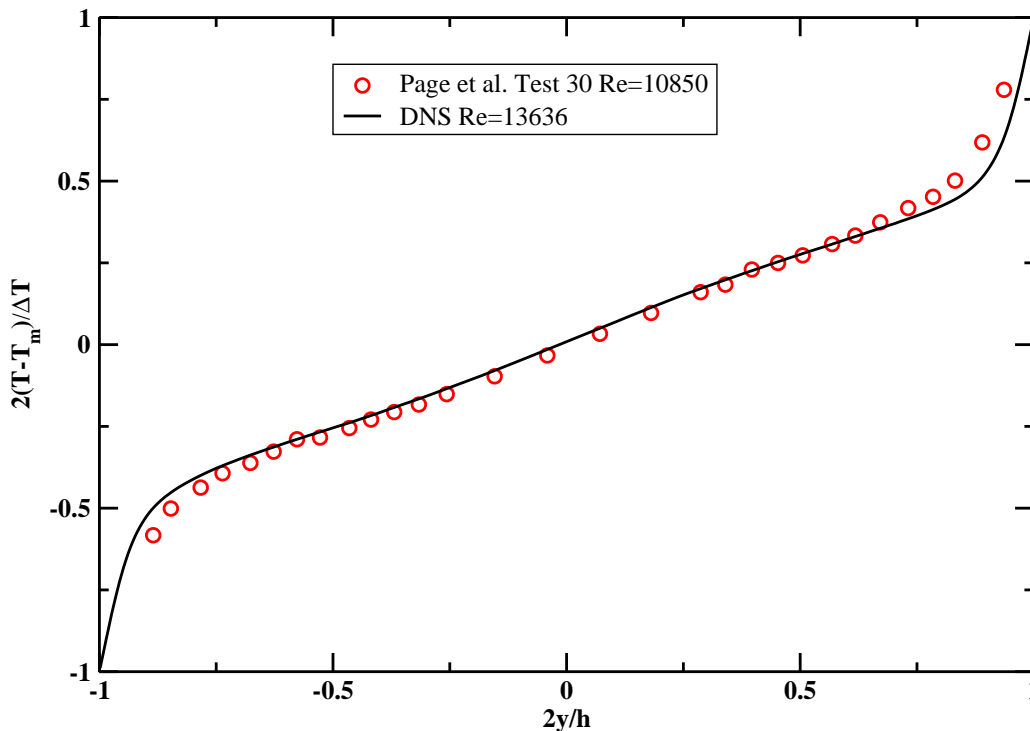


Figure 8.4.1: Temperature profiles. Comparison with experimental data from [58]

In Fig. 8.4.2 the temperature results are expressed in wall units and validated against the DNS results from Kasagi et al. [42]. In [42] the computational domain is analogous to the one used in the present work but the temperature boundary conditions are different. In [42] instead of prescribing a constant temperature difference between the channel walls, the flow is heated with a positive constant heat flux coming from the solid walls. This kind of heating configuration will be hereinafter referred as Steady Channel Flow with Constant Heat Flux (SChF-CHF) configuration and can be easily described using the classical Nusselt correlation for pipe flows [88]:

$$Nu = 0.021Pr^{0.5}Re_m^{0.8} \quad (8.4.1)$$

where  $Re_m$  is the mean flow Reynolds number based on the bulk flow velocity and the wall distance ( $Re_{D_h} = 2Re_m$ ).

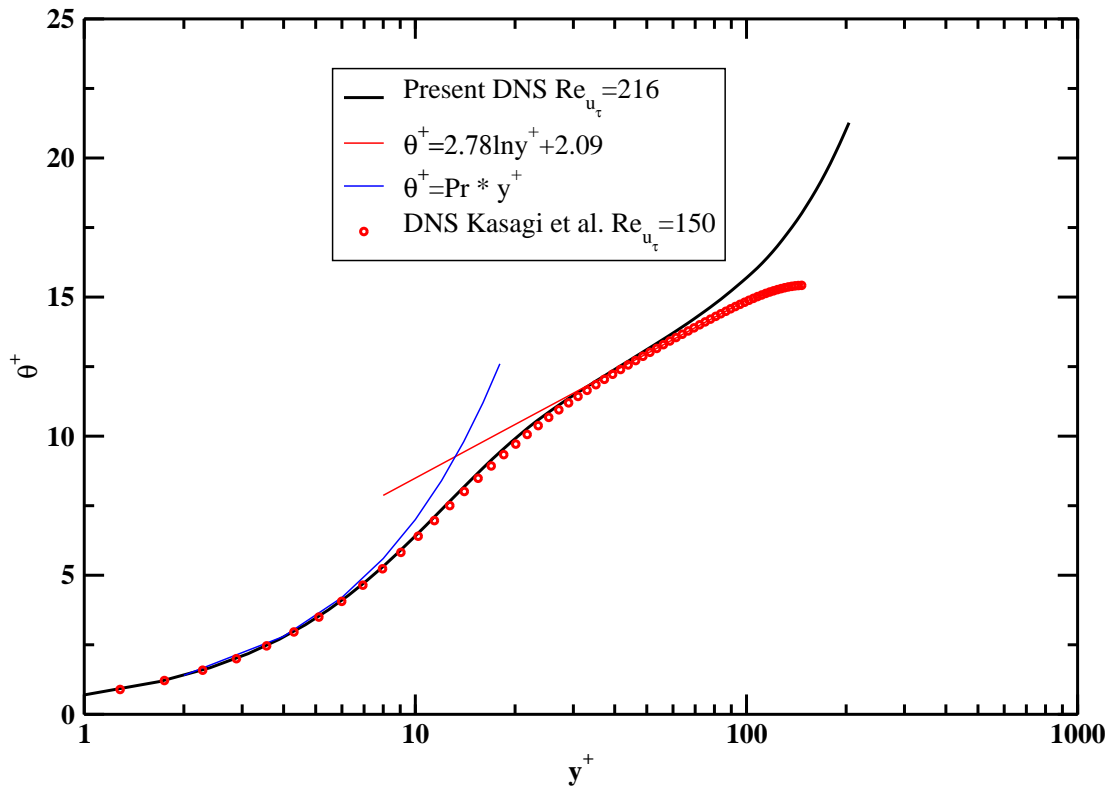


Figure 8.4.2: Dimensionless temperature profiles. Comparison with DNS data from [42]

Despite the boundary condition difference, both approaches are equivalent when the temperature profile is expressed in wall units (see Section 4.3):

$$\theta^+ = \frac{\bar{T} - T_w}{T_\tau} \quad (8.4.2)$$

where

$$\bar{T}_\tau = -\frac{\bar{q}_w}{\bar{\rho}c_p\bar{u}_\tau} \quad (8.4.3)$$

In both configurations, in the near wall region, the temperature wall law is valid. Differences occur approaching the channel center due to the different heating as shown also by Kawamura [43].

A more direct validation of the numerical results can be done against the numerical data from [52]. In [52] both geometry and thermal boundary conditions are similar to the present case. The only difference is in the value of  $Re_\tau$  which, in the present case is 50% higher than in [52]. As shown by [43] for  $Pr = 0.71$  (as in the present case) no appreciable Reynolds number effects are expected on the temperature wall profile which practically do not differ from the classic temperature wall law (see Section 4.3). In the present study a higher steady Reynolds number flow has been considered in order to consider later in Section 8.5 the effect of superimposed pulsations on the turbulence level. In Section 8.5 in fact comparison were made with LES and DNS results of [72] performed at higher Reynolds Number.

In Fig. 8.4.3, the budget of the temperature variance is reported. Comparison were made with the DNS data from [52] and the experiment from [47].

As pointed out by [52], the results obtained in the SChF-FWTD configuration compare well, in the near wall region ( $y^+ < 40$ ), with the experiments or DNS in steady channel or flat plate configurations with fix wall temperature or heat transfer. In the SChF-FWTD configuration the presence of a non-vanishing temperature gradient at the center of the channel determines a positive contribution of the Production term in 4.4.38 which needs to be balanced by a non-vanishing dissipation term of the same intensity. In [42] and in the experiment of Krishnamoorthy and Antonia [47] instead, (see Fig. 8.4.3) both the production and the dissipation term rapidly decrease towards zero value approaching the center of the channel.

In Fig. 8.4.4 the  $\epsilon_\theta$  budget is reported. A comparison can be made with the DNS data from [42] keeping in mind the already mentioned difference due to the presence of the non-vanishing contribution of the temperature gradient at the center of the channel.

Another interesting budget equation which can be directly compared with the DNS results in [42] is the turbulent kinetic energy budget and has been reported in Fig. 8.4.5. The budget equation can be obtained by summation ( $k = \frac{1}{2}u_i u_i$ ) of the fluctuating momentum equations. The fluctuating momentum equation can be infer subtracting the ensemble averaged momentum equation 4.2.13 from its instantaneous form 4.0.2.

The good agreement between the present results with the data from [42] and [52] represents a good validation of the solver and the grid resolution used. The difference between the coarse and fine mesh results in the prediction of the budget quantities reported in figures from 8.4.3 to 8.4.5 are quite small. The budget behavior is similar as well as the position of maxima and minima of each budget term. This allows to use the coarser resolution to study qualitatively the dynamic behavior of the near wall turbulence.

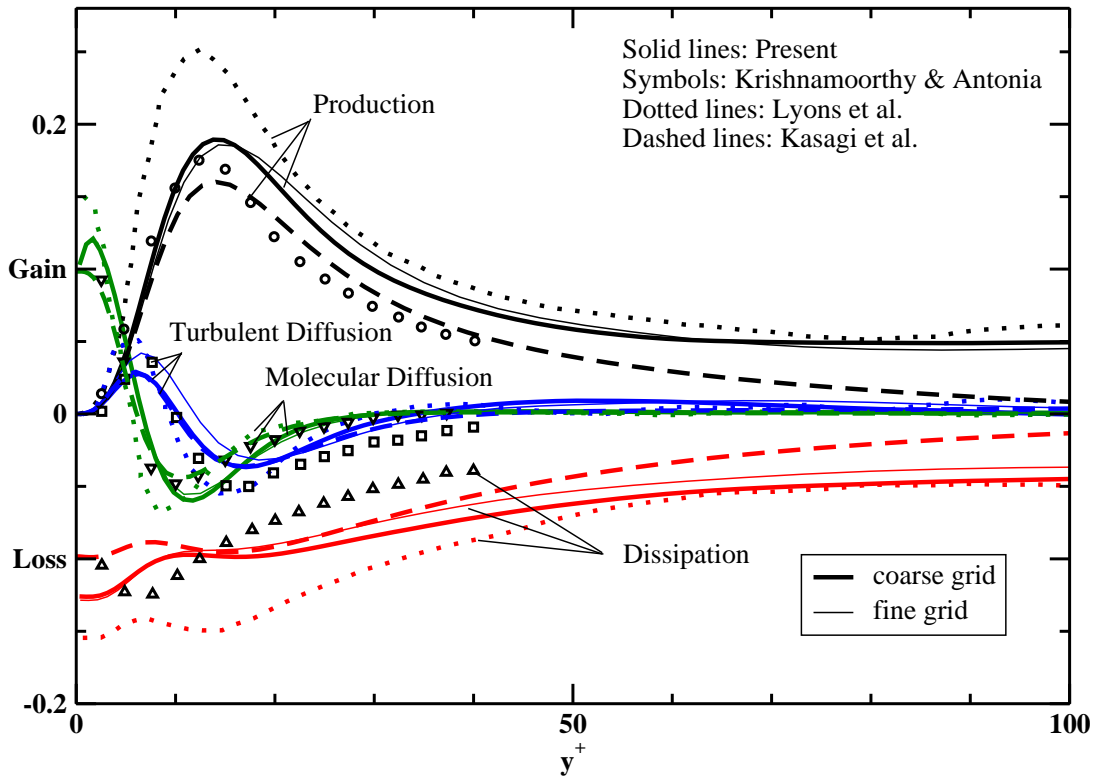


Figure 8.4.3: Dimensionless  $k_\theta$  budget. Comparison with DNS data from Lyons et al. [52], Kasagi et al. [42] and experiments from Krishnamoorthy and Antonia [47].

## 8.5 Unsteady Channel Flow with Heat Transfer

In order to realize a pulsating flow within the channel, a pressure source term of the form:

$$\frac{1}{\rho} \frac{\partial P}{\partial x} = K_m - K_{osc} \sin(\omega t) \quad (8.5.1)$$

has been used. The flow geometry and boundary conditions considered are the same as in the SChF-FWTD configuration. In order to distinguish the pulsating channel from its steady counterpart the pulsating case will be referred hereinafter as the PulsChF-FWTD case.

In order to investigate the effect of pulsation frequency on the viscous-thermal boundary layer behavior, three different values of the non dimensional frequency parameter  $\omega^+$  have been considered. Each value considered is representative of a different pulsation regime: quasi-laminar, intermediate frequency range and quasi-steady.

Moreover, in order to explain the non-linear effects of overall heat transfer enhancement in presence of very high amplitude oscillations reported by Ishino et al. in [38], additional computations were performed at high values of pulsating Reynolds number ratio ( $Re_b/Re_m = 6$ ).

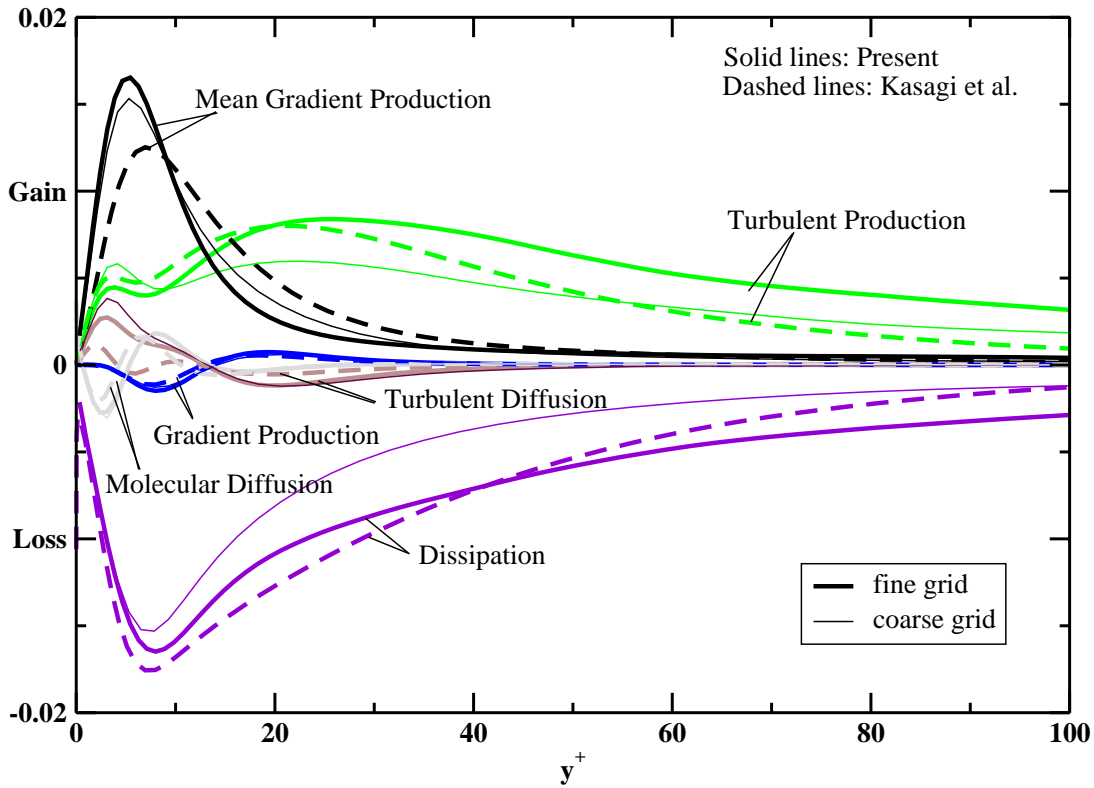


Figure 8.4.4: Dimensionless  $\epsilon_\theta$  budget. Comparison with DNS data from, Kasagi et al. [42]

In Table 8.1 an overview of the investigated parameter field together with the different pulsating flow regimes is reported.

Depending on the amplitude parameter  $a_{uc}$  two pulsation case were distinguished: the 'Low-Reverse flow' case and the 'Wave Dominated Flow' case. In the Low-Reverse flow case the pulsation amplitude parameter is below 1.0 but high enough to cause the flow reversal in the boundary layer. As it has been already shown in the Chapter 6 this is a quite critical condition for many turbulence models. In the Wave Dominated Flow case the amplitude of the velocity pulsations is several times the mean flow component. In this conditions the flow is very close to the pure oscillatory flow case. In this case the oscillating flow component is much stronger than the mean counterpart. As it will be shown later on, the unsteady results in the Low-Reverse

	Quasi-Laminar Regime	Intermediate	Quasi-Steady Regime
Low-Reverse Flow	$a_{uc} = 0.7; l_s^+ = 7$	$a_{uc} = 0.7; l_s^+ = 14$	$a_{uc} = 0.7; l_s^+ = 35$
Wave Dominated Flow	$a_{uc} = 6; l_s^+ = 7$	$a_{uc} = 6; l_s^+ = 14$	-

Table 8.1: DNS computations, pulsating parameter and investigated flow regimes.



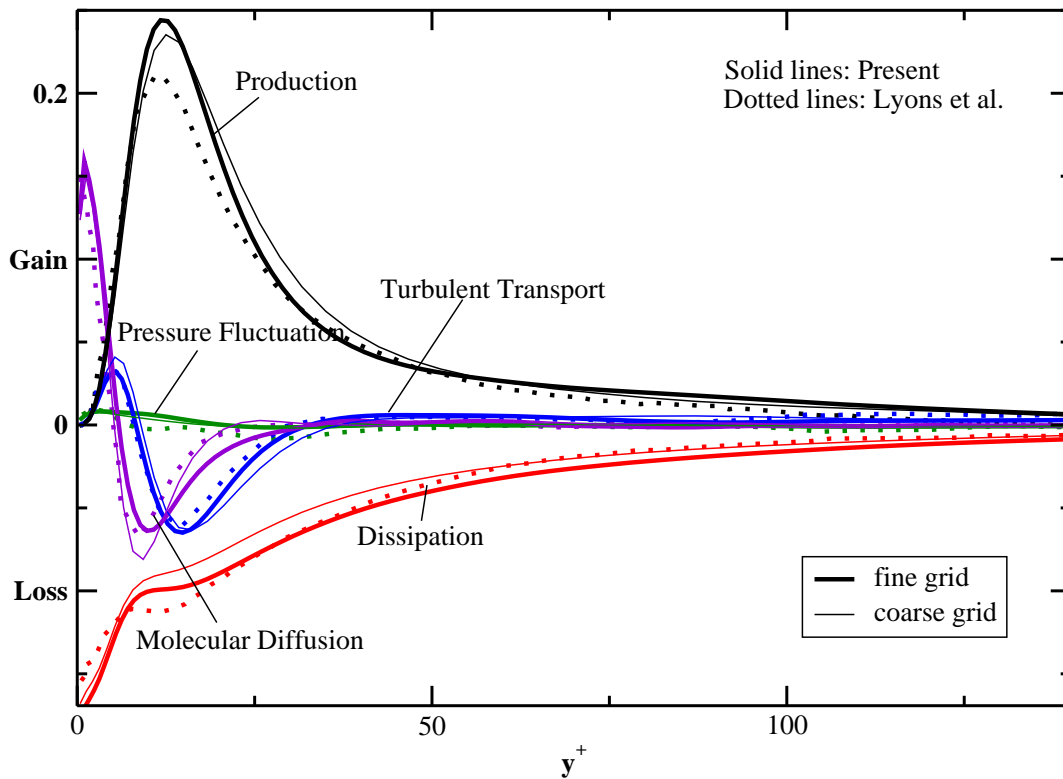


Figure 8.4.5: Dimensionless turbulent kinetic energy budget. Comparison with DNS data from, Kasagi et al. [42]

Flow case, have a resolution comparable with other DNS and very accurate LES cases. In the case of Wave Dominated Flow, the high velocity amplitude involved determines a radical change in the scale of the turbulent structures. Being the grid fixed, at high velocity, i.e. high Reynolds Number, the accuracy of the calculation is considerably reduced. For this reason, the present high amplitude simulations should be regarded more as very large eddy simulation than as DNS.

### 8.5.1 Low-Reverse Flow Results

The velocity profiles and the tangential Reynolds shear stress ( $\overline{u'v'}$ ) are reported in Fig. 8.5.1 and 8.5.6. The present unsteady results are compared with the isothermal LES/DNS simulations of [72]. The small differences in the plot profiles are most likely due to the different values of  $Re_{u_\tau}$  considered. In [72] the steady part of the pressure forcing ( $K_m$ ) was set in order to have a current alone  $Re_{u_\tau} = 395$ . In the present case  $Re_{u_\tau} \simeq 216$ . A smaller Reynolds number has been chosen in order to save computational resources. In this way, it was possible to consider a wider range of flow amplitude. The non-dimensional parameter considered by [72] ( $a_{uc}$  and  $l_s^+$ ) have been limited to the case of Low-Reverse Flow. Despite the small difference in the

mean flow Reynolds number, the near wall boundary layers are comparable and the turbulent Reynolds shear stress seem to exhibit a similar behavior. This was expected since the pulsation parameter were considered equal and the difference in Reynolds number affected just the ratio between the channel eight and the stokes length. As in [72], the oscillating pressure term ( $K_{osc}$ ) has been set in order to have at the channel centerline a pulsating amplitude ratio of 0.7 ( $a_{uc} = 0.7$ ):

$$\langle u_c \rangle(t) = \bar{u}_c(1 + a_{uc}\sin(\omega t + \phi_{uc})) \quad (8.5.2)$$

where  $\langle u_c \rangle(t)$  represents the phase-locked ensemble average of the axial velocity component at the channel centerline.

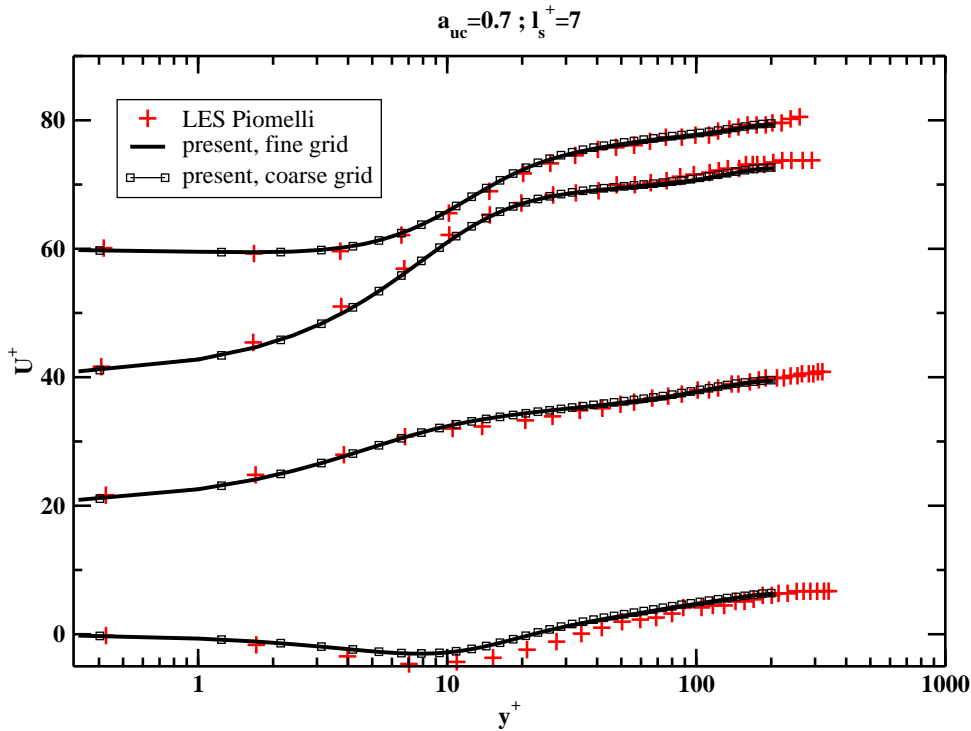


Figure 8.5.1: Velocity profiles, comparison with LES data from [72],  $l_s^+ = 7$ . Profiles are plotted every  $T/4$  and offset in the vertical direction; the bottom plot corresponds to phase  $\pi$  with respect to the pressure forcing.

The effect of flow pulsations on the velocity profile can be seen in Figures from 8.5.1 to 8.5.2. Starting from bottom to top the profiles refer to phase  $\pi$ ,  $\pi/2$ , 0 and  $3\pi/4$  with respect to the pressure forcing. Observing the curves, it is evident that there is practically a phase shift of  $90^\circ$  between the pressure forcing and the velocity at the channel centerline (the velocity profiles at phase 0 in Figures from 8.5.1 to 8.5.2 present always the maximum values of velocity at channel centerline). This can be explained due to the fact that, even in the case of  $l_s^+ = 35$ , the flow pulsations are high enough to be in the limiting case of very high flow pulsations (see Equation 5.1.36 in Section 5.1.2). In this case, similar to the laminar channel theory, the velocity and

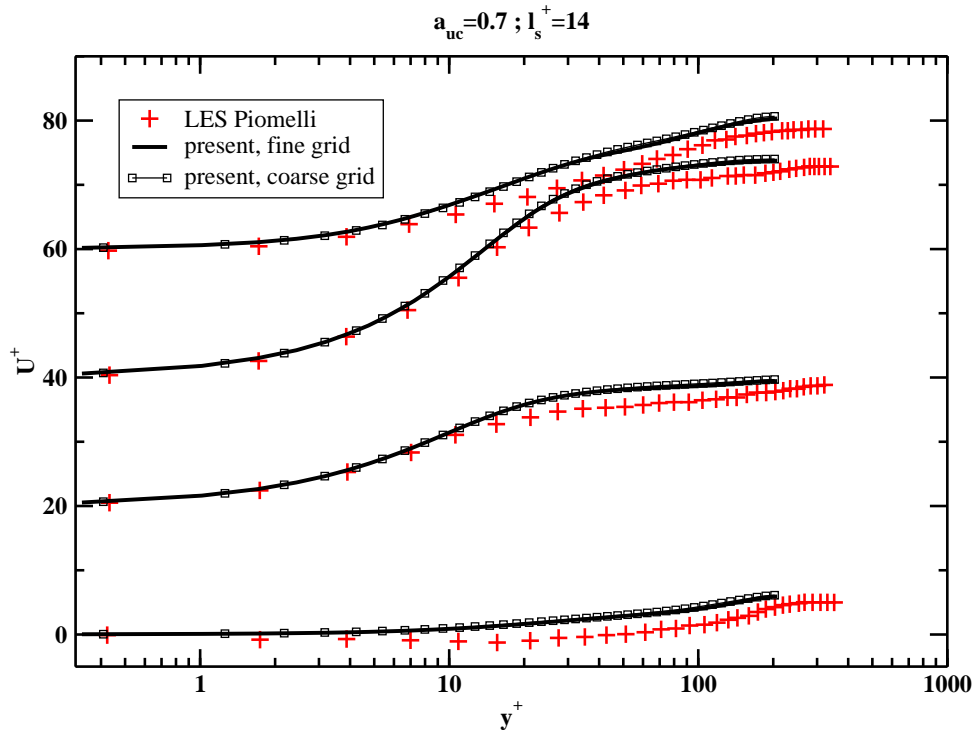


Figure 8.5.2: Velocity profiles, comparison with LES data from [72],  $l_s^+ = 14$ . Profiles are plotted every  $T/4$  and offset in the vertical direction; the bottom plot corresponds to phase  $\pi$  with respect to the pressure forcing.

pressure source term are expected to be shifted of  $90^\circ$ . At the channel centerline, the flow oscillates with practically the same amplitude and phase in all the three pulsation frequency considered. However the shape of the velocity profiles seem to be quite different. Considering the velocity profiles at phase  $\pi$  ( bottom lines in figures from 8.5.1 to 8.5.2 ), it is evident that at high flow pulsation ( $l_s^+ = 7$ ) a small portion of the boundary layer, up to  $y^+ = 30$ , is reversed. At phase  $\pi/2$  the difference between the velocity profiles at different pulsation frequencies are more intense. At  $l_s^+ = 7$ ,  $y^+$  and  $U^+$  seem to exhibit a logarithmic dependence in practically the whole channel domain.

The effect of flow pulsation on the Reynolds shear stress is even stronger. Observing the Reynolds stress profiles reported in Figures from 8.5.4 to 8.5.6 several considerations can be drawn. The Reynolds shear stress maximum peak decreases with the increase of pulsation. Comparing Figure 8.5.6 with 8.5.4 it is evident that the maximum Reynolds stress at  $l_s^+ = 35$  is two times larger than the maximum Reynolds stress at  $l_s^+ = 7$ . On the other side, at low pulsation frequency (see Figure 8.5.6) the flow is practically laminar for half of the pulsation period showing an intense burst immediately before the starting of the decelerating flow phase. At higher pulsation frequency (see Figure 8.5.5) the Reynolds stress intensity burst seems to be somehow delayed. The maximum intensity is realized at  $3\pi/4$  (top graph in Figure 8.5.5) and  $\pi$  (bottom graph in Figure 8.5.4) respectively. As shown already by Scotti and Piomelli in [72] the flow pulsation have a huge impact on the turbulence structure especially in the intermediate

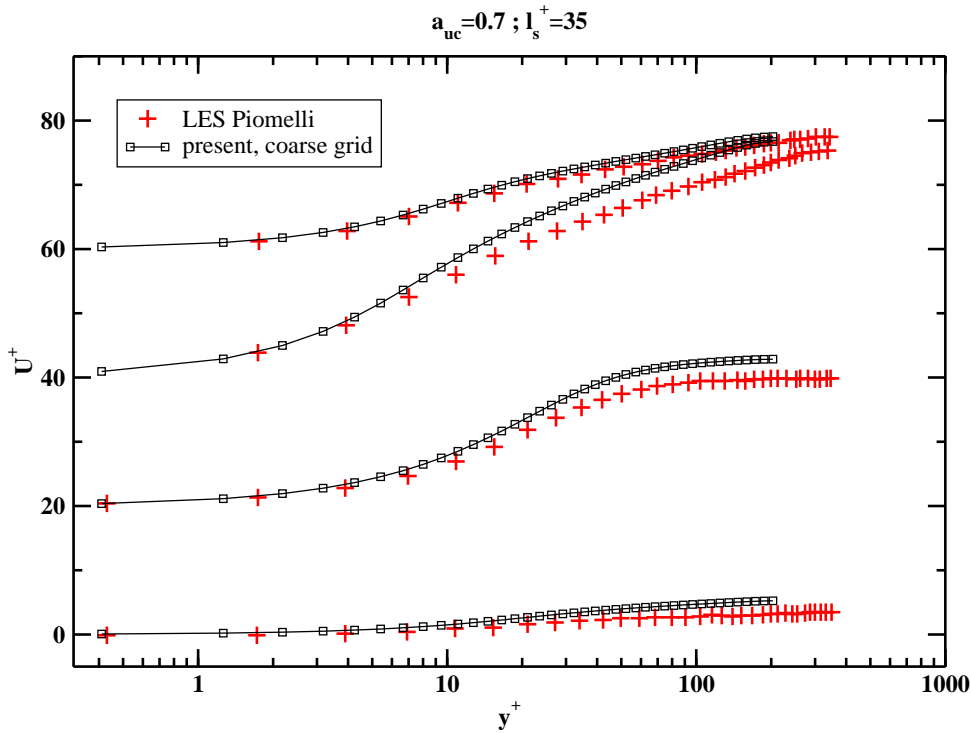


Figure 8.5.3: Velocity profiles, comparison with LES data from [72],  $l_s^+ = 32$ . Profiles are plotted every  $T/4$  and offset in the vertical direction; the bottom plot corresponds to phase  $\pi$  with respect to the pressure forcing.

frequency range. In the present study the effect on the changing of turbulent structure on the heat transfer is also studied.

In Figure 8.5.7, the phase-locked averaged Nusselt number is reported for different frequency parameter values and in the case of small amplitude oscillations. The increased frequency seems to have a higher impact on the phase and amplitude of the Nusselt number than on its mean value. In Figure 8.5.7 the phase is reported again with respect to the pressure source term oscillation. According to the quasi-steady theory, an analytical behavior of the oscillating Nusselt number can be derived. Assuming valid 5.3.11, at each time  $t$  the Nusselt number can be expressed as:

$$Nu(t) = 0.021Pr^{0.5} \left( \frac{2hU_b(1 + a_{uc}\cos(\omega t))}{\nu} \right)^{0.8} \quad (8.5.3)$$

The quasi-steady line is than in phase with the velocity pulsation and presents a  $90^\circ$  phase shift with respect to the pressure term. The Nusselt number behavior at  $l_s^+ = 35$  presents a similar behavior. The maximum and minimum Nusselt number values are however delayed of  $\pi/4$  and  $\pi/2$  with respect of the quasi-steady line respectively. Increasing the frequency the Nusselt number amplitude decreases and the phase shift increases till the velocity and the heat transfer reach practically an opposition of phase.

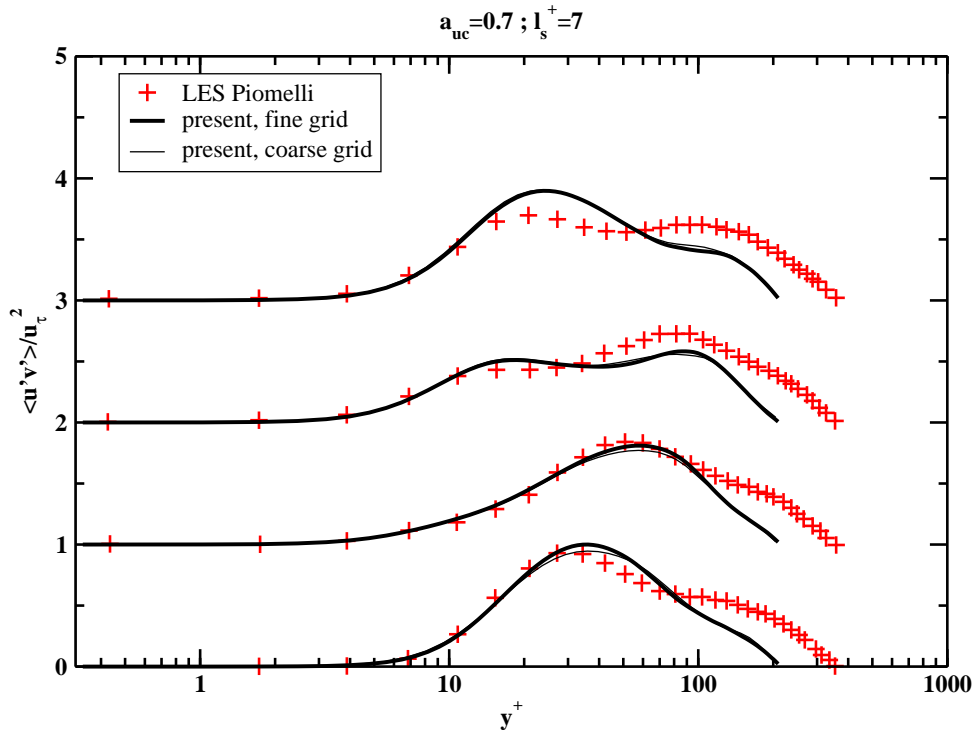


Figure 8.5.4: Reynolds stress profiles, comparison with LES data from [72],  $l_s^+ = 7$ . Profiles are plotted every  $T/4$  and offset in the vertical direction; the bottom plot corresponds to phase  $\pi$  with respect to the pressure forcing.

It is evident that the changing in amplitude and phase cannot be predicted within the quasi-steady theory.

In Section 8.5.2 the  $k_\theta$ ,  $k$  and  $\epsilon_\theta$  budget are reported for different phases and different oscillating parameters. In Fig. 8.5.8, 8.5.9 and 8.5.10 a comparison between fine and coarse grid results is presented in the case of  $a_{uc} = 0.7$  and  $l_s^+ = 7$  showing a good overall grid independence of the results. For this reason, in the following plots, just the coarse grid results are presented.

The main purpose of the present DNS campaign is in fact to give a better inside on the imbalance phenomena of  $k_\theta$  and  $\epsilon_\theta$  production and dissipation. As it is clear from Fig. 8.5.8, 8.5.9 and 8.5.10, this can be done quite accurately using the coarse grid configuration permitting in this way a considerable save in the computational time especially for higher value of the  $l_s^+$  parameter and hence for lower frequency regimes. All the budget terms have been averaged over more than 50 cycles which corresponds in the case of lower frequency to a conspicuous amount of computational time over several processors.

In all the graphs, comparisons are given with the steady channel flow case with mean pulsating bulk velocity. In the case of the turbulent temperature variance and turbulent kinetic energy budgets, the DNS data of [52] in the SChF-FWTD configuration are used. Concerning the  $\epsilon_\theta$  budget, comparison are made instead with the DNS data of Kasagi et al. [42] in the SChF-IFBC case.

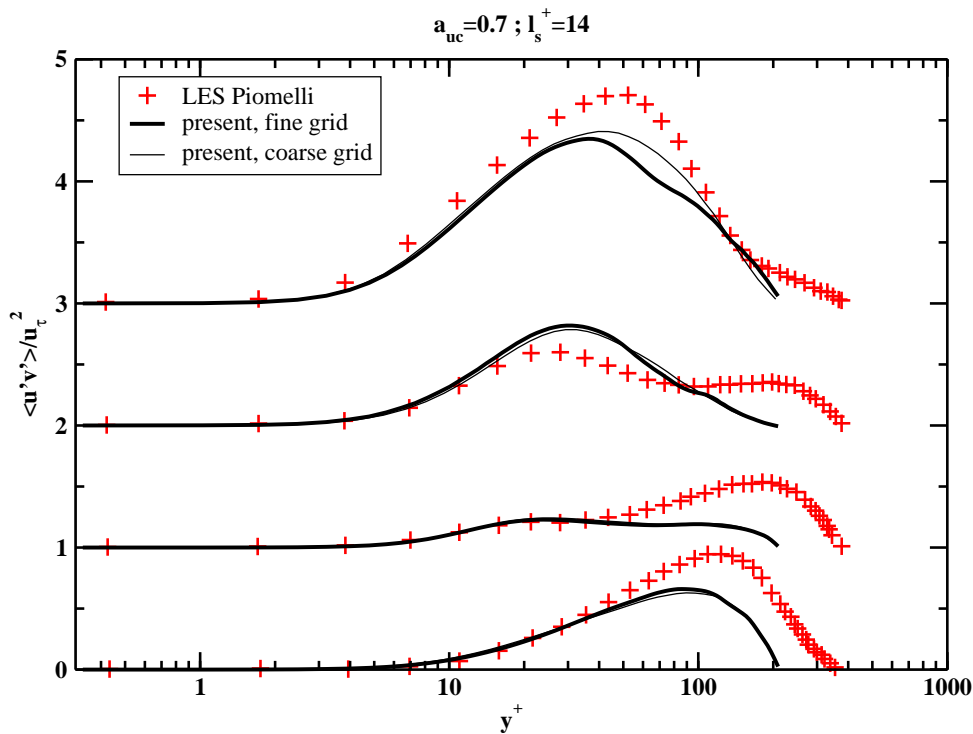


Figure 8.5.5: Reynolds stress profiles, comparison with LES data from [72],  $l_s^+ = 14$ . Profiles are plotted every  $T/4$  and offset in the vertical direction; the bottom plot corresponds to phase  $\pi$  with respect to the pressure forcing.

In Fig. 8.5.8 the  $k_\theta$  budget is reported in the case of  $a_{uc} = 0.7$  and  $l_s^+ = 7$ . As can be seen from Fig. 8.5.8 (a) to (d) the turbulent production and dissipation are almost frozen. The picture correspond to the deceleration phase. The production and dissipation maxima are slightly lower than the steady channel flow case. At phase  $\pi$  the flow reaches the velocity minimum and starts to accelerate. The effect of the change in flow direction seems to affect first the production term of  $k_\theta$  (Fig. 8.5.8 (e) and (f)) and than the dissipation term. The peak of turbulent production is however at phase  $5\pi/4$ . In the intermediate frequency range:  $l_s^+ = 14$  the  $k_\theta$  production and dissipation seem to be more affected by the flow pulsations. In the deceleration phase (Fig. 8.5.11 (a) to (d)) an increasing in the turbulent production peak is evident followed by a decreasing from phase  $\pi$  to  $7\pi/4$  which continues up to the new cycle start. The decreasing of  $k_\theta$  production can be addressed also to the flow relaminarization due to the small velocity. If we consider in fact the case of  $l_s^+ = 35$  close to the quasi-steady regime,  $k_\theta$  production and dissipation are in balance and comparable to the levels of the steady channel till phase  $3\pi/4$ . From phase  $3\pi/4$  to  $3\pi/2$  the level of turbulence is very low as can be seen also analyzing the kinetic energy budget results in Fig. 8.5.15 (d) to (g). At the flow top velocity inversion point (Fig. 8.5.15 (h)) the  $k$  turbulent production have a sudden increase which corresponds also with the little increasing of the  $k_\theta$  production from Fig. 8.5.14 (g) to (h). It is important to notice that the analogy between  $k$  and  $k_\theta$  behavior is observed just in the quasi-steady flow condition. For  $l_s^+ = 7$  and  $l_s^+ = 14$  the  $k$  production term exhibits a

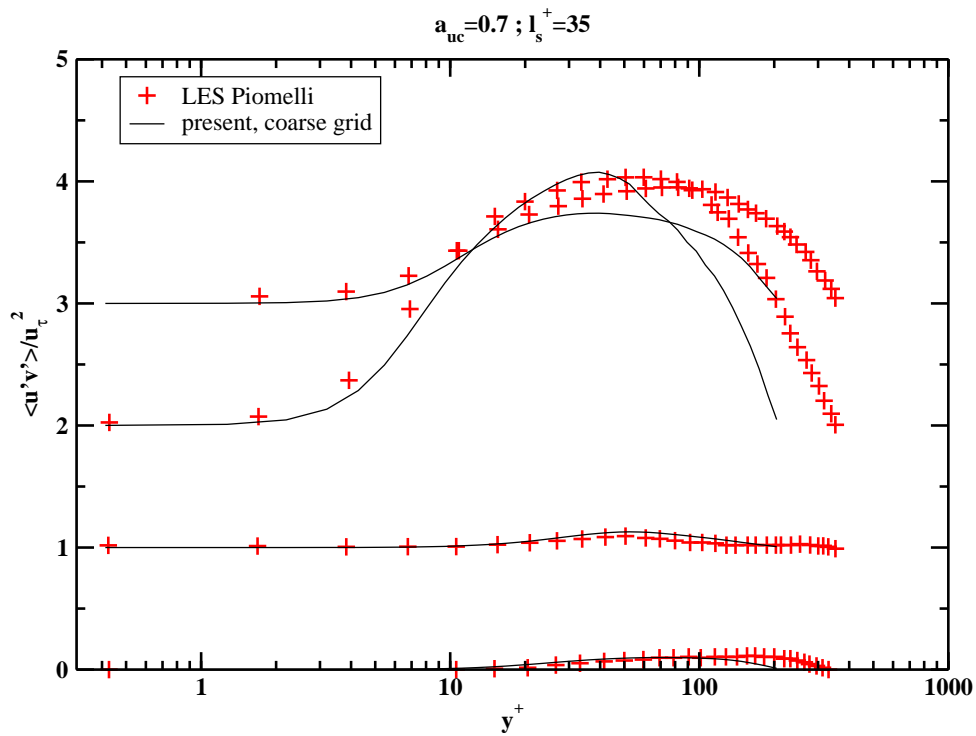


Figure 8.5.6: Reynolds stress profiles, comparison with LES data from [72],  $l_s^+ = 35$ . Profiles are plotted every  $T/4$  and offset in the vertical direction; the bottom plot corresponds to phase  $\pi$  with respect to the pressure forcing.

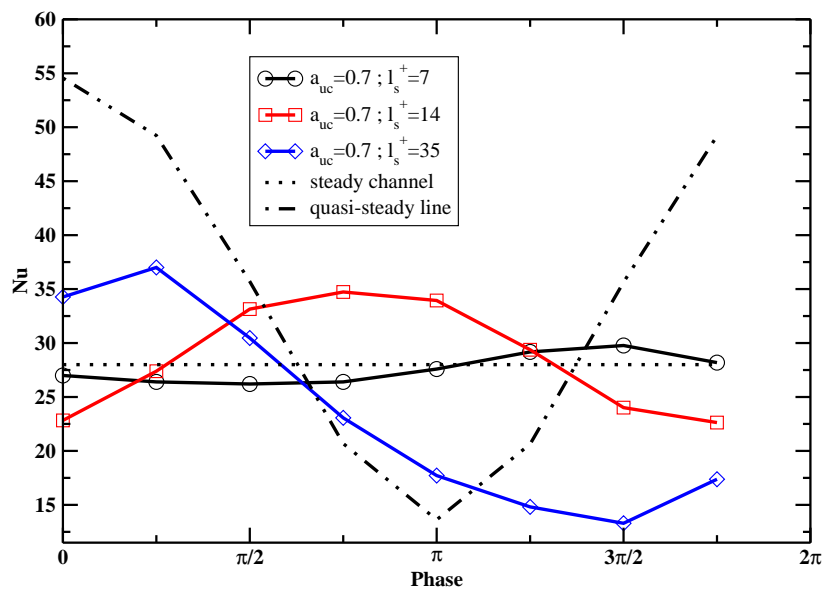


Figure 8.5.7: Pulsating channel flow, Phase-locked averaged Nusselt number comparison

similar behavior in phase. The maximum  $k$  production level in both cases is revealed at phase  $\pi/4$  immediately after the peak velocity and in the decelerating phase. Similarly, the  $k$  start to

increase again at phase  $3\pi/2$  when the acceleration decrease till the maximum velocity inversion point. This is not the case for  $k_\theta$  which seems to be frozen in the case of  $l_s^+ = 7$  but not in the case of  $l_s^+ = 14$ . Concerning the turbulent kinetic energy budget, another interesting feature regards the location of the turbulent production maximum. Both in the intermediate frequency range and in the quasi-steady flow conditions, the turbulent production peak is always located at  $y^+ \simeq 15$  or practically inexistent due to the relaminarization effects. In the case of  $l_s^+ = 7$  the position of the maximum oscillates cyclically between  $y^+ \simeq 15$  and  $y^+ \simeq 25$ . Concerning the budget of  $\epsilon_\theta$  is it possible to observe a behavior similar to  $k_\theta$ . At  $l_s^+ = 7$  and in the deceleration phase the production terms seem to be little affect by the flow velocity changes. In the acceleration phase instead the sharp peak of the mean velocity gradient production term seem to change much more. The most interesting behavior concerns the turbulent production term. In the steady channel flow case it presents a local maximum closer to the wall respect to the location of its global maximum value. At  $l_s^+ = 7$  in the deceleration phase this local maximum is practically inexistent. It shows up again at phase  $3\pi/4$  increasing in intensity till phase  $5\pi/4$  to disappear again at the end of the cycle (Fig. 8.5.10 (d) to (h)). An opposite behavior can be observed in Fig. 8.5.13 (a) to (e) in the case of  $l_s^+ = 14$ . The higher peak of the mean temperature gradient production term is always very close to the wall at the usual location of the steady channel local maximum. At  $l_s^+ = 35$  the two peak instead practically merge at each phase considered. An exception is the phase  $7\pi/4$  where only the wall closer peak is visible.



### 8.5.2 Pulsating Channel Flow with Heat Transfer, $k_\theta$ , $k$ and $\epsilon_\theta$ budget plots

In this section the budget plots of  $k_\theta$ ,  $k$ , and  $\epsilon_\theta$  are reported at different pulsating phase. Comparison were given with the steady channel case of Kasagi et al. [42] and Lyons et al. [52]

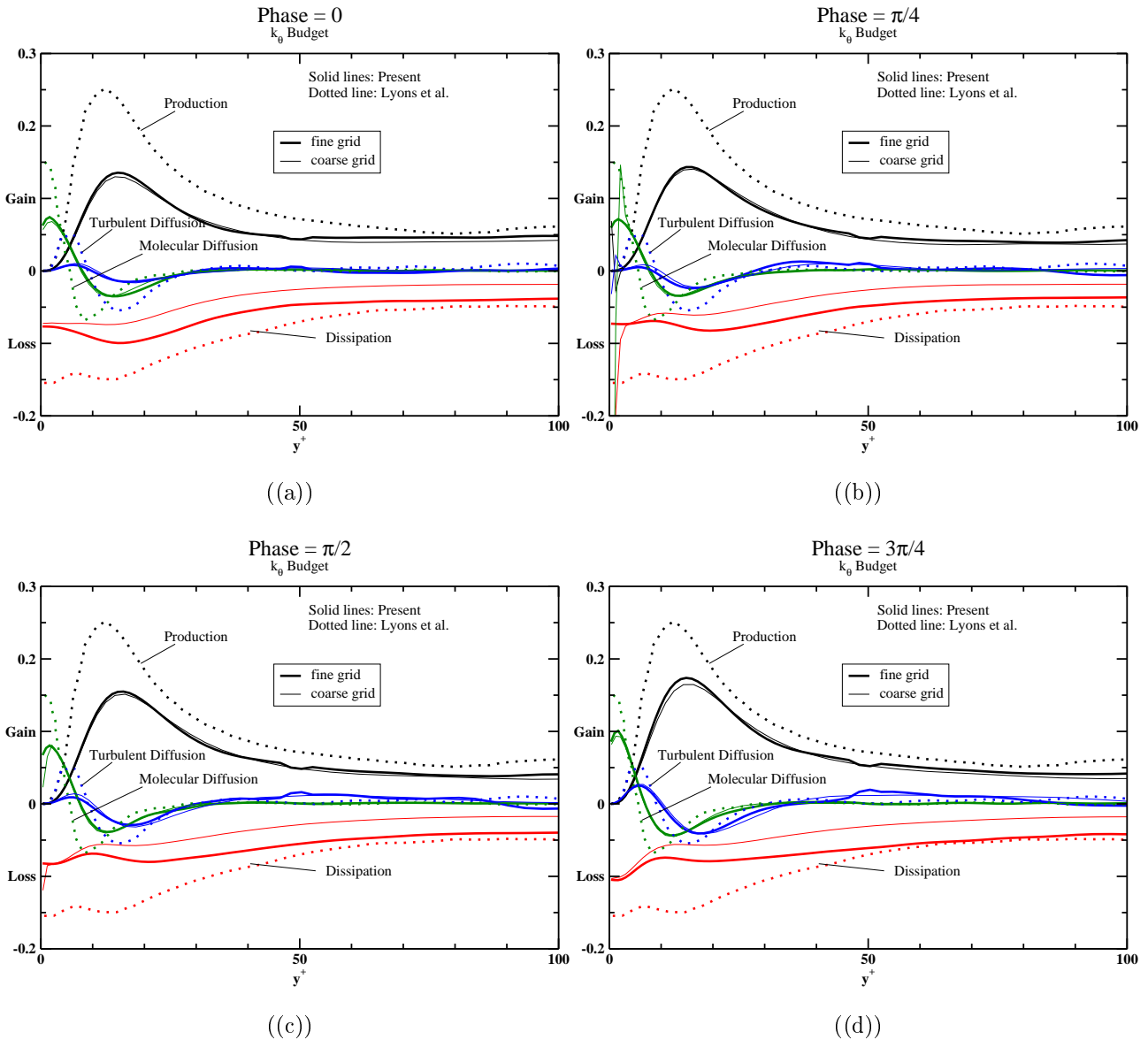


Figure 8.5.8: Budget of  $k_\theta$ , pulsating flow computations on fine and coarse grid,  $a_{uc} = 0.7$ ,  $l_s^+ = 7$ , comparison with steady channel flow DNS data from [52]

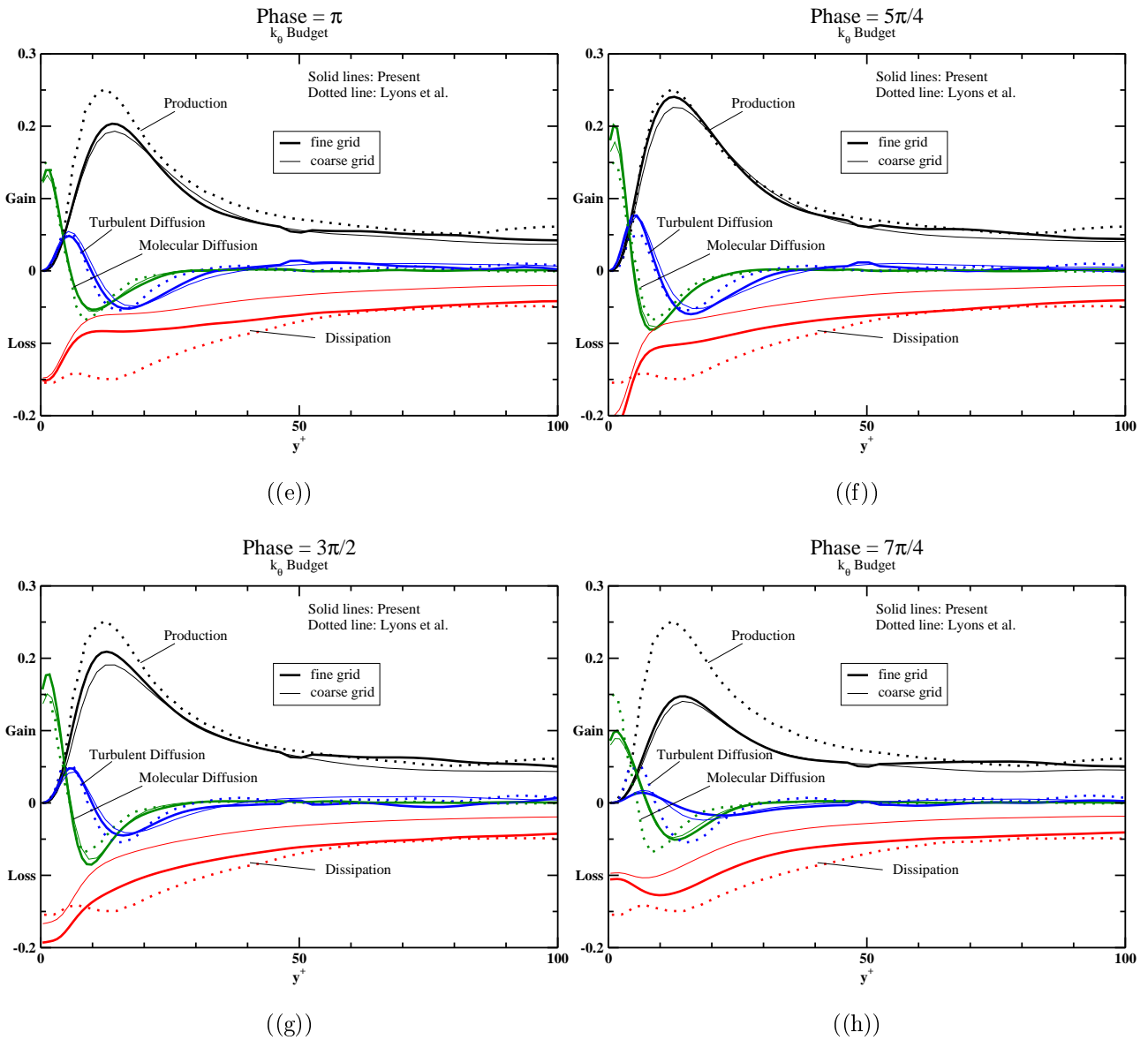


Figure 8.5.8: Budget of  $k_\theta$ , pulsating flow computations on fine and coarse grid,  $a_{uc} = 0.7$ ,  $l_s^+ = 7$ , comparison with steady channel flow DNS data from [52] (continue)

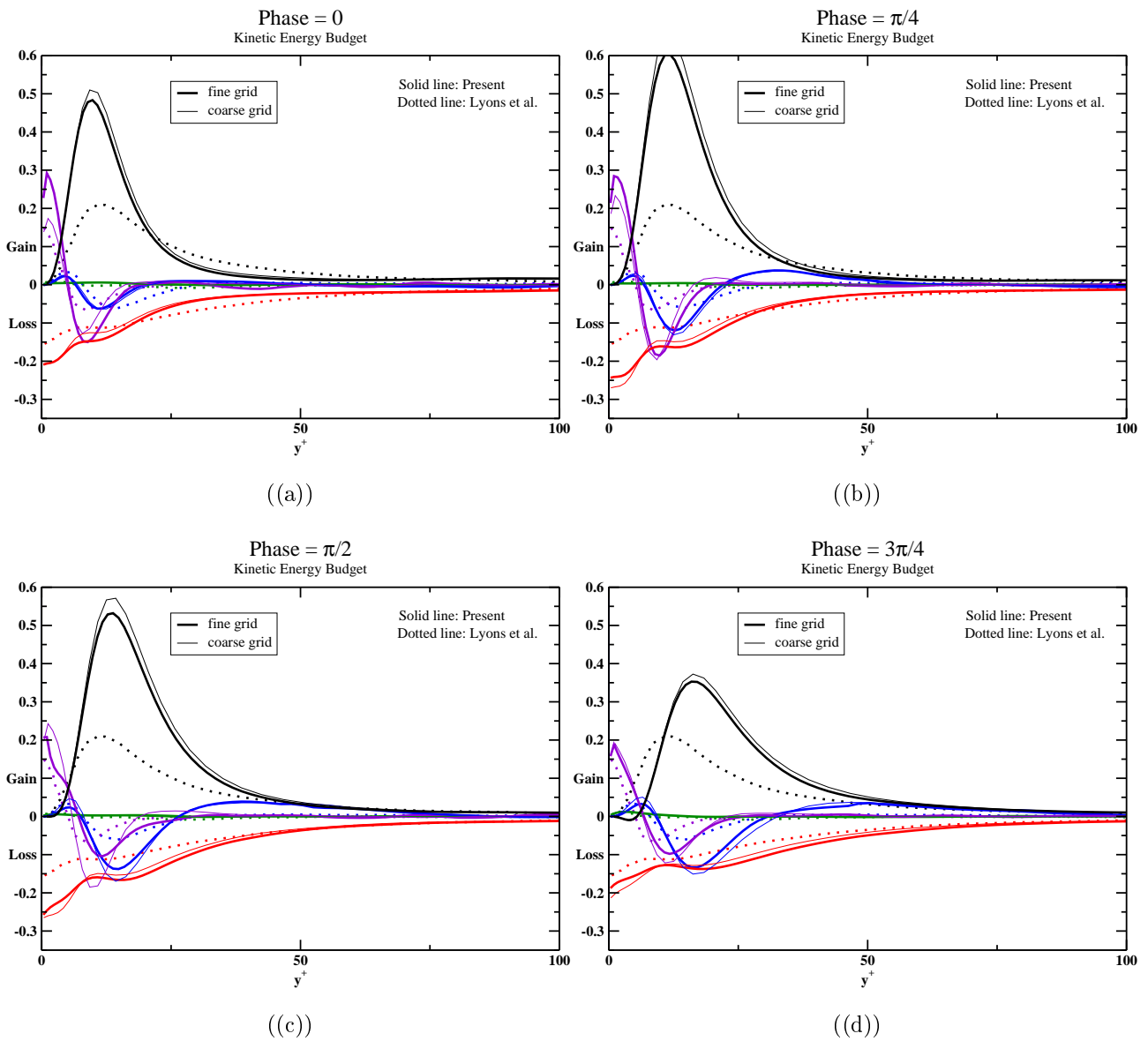


Figure 8.5.9: Budget of kinetic energy, pulsating flow computations on fine and coarse grid,  $a_{uc} = 0.7$ ,  $l_s^+ = 7$ , comparison with steady channel flow DNS data from [42]

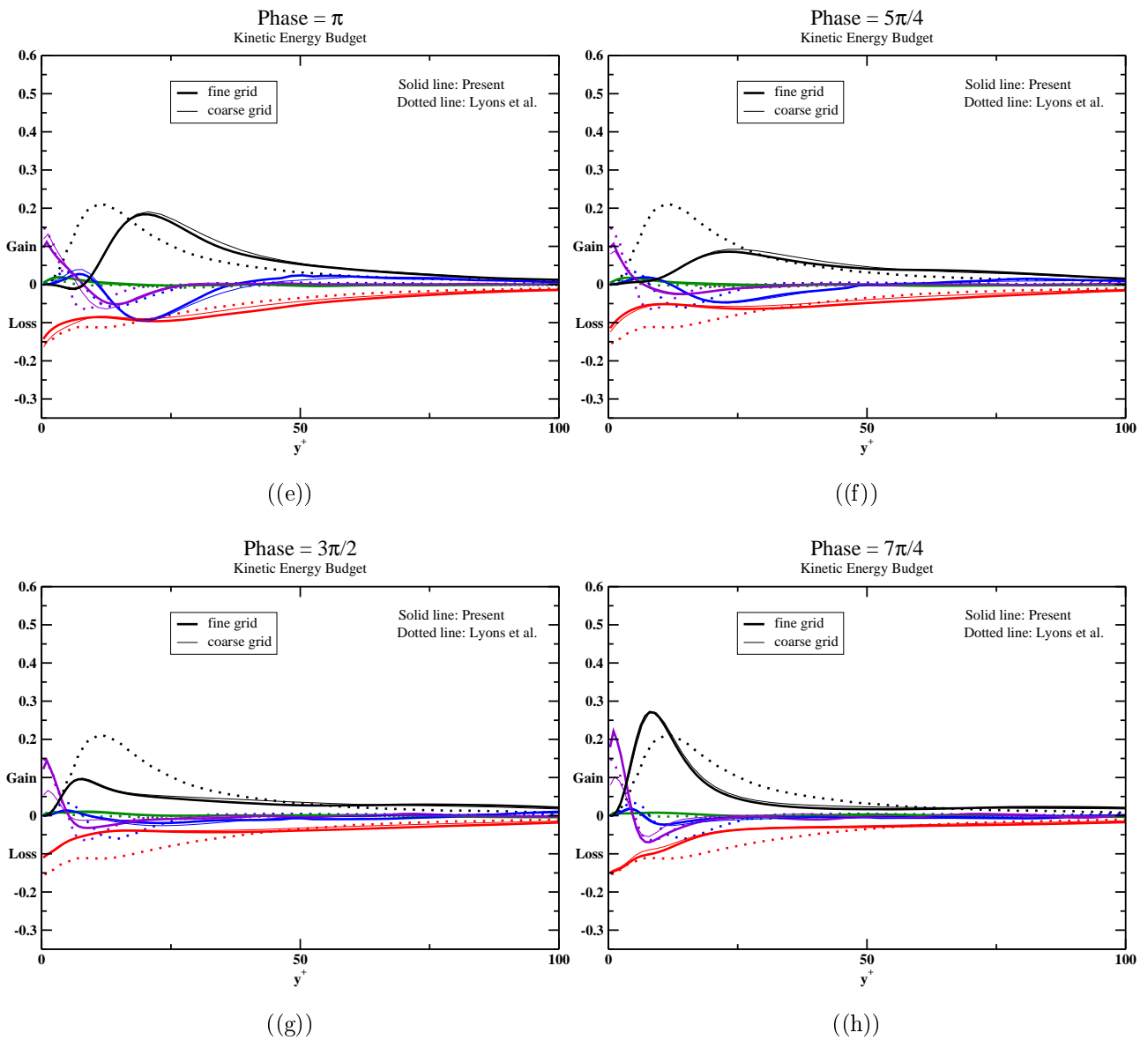


Figure 8.5.9: Budget of kinetic energy, pulsating flow computations on fine and coarse grid,  $a_{uc} = 0.7$ ,  $l_s^+ = 7$ , comparison with steady channel flow DNS data from [42] (continue)

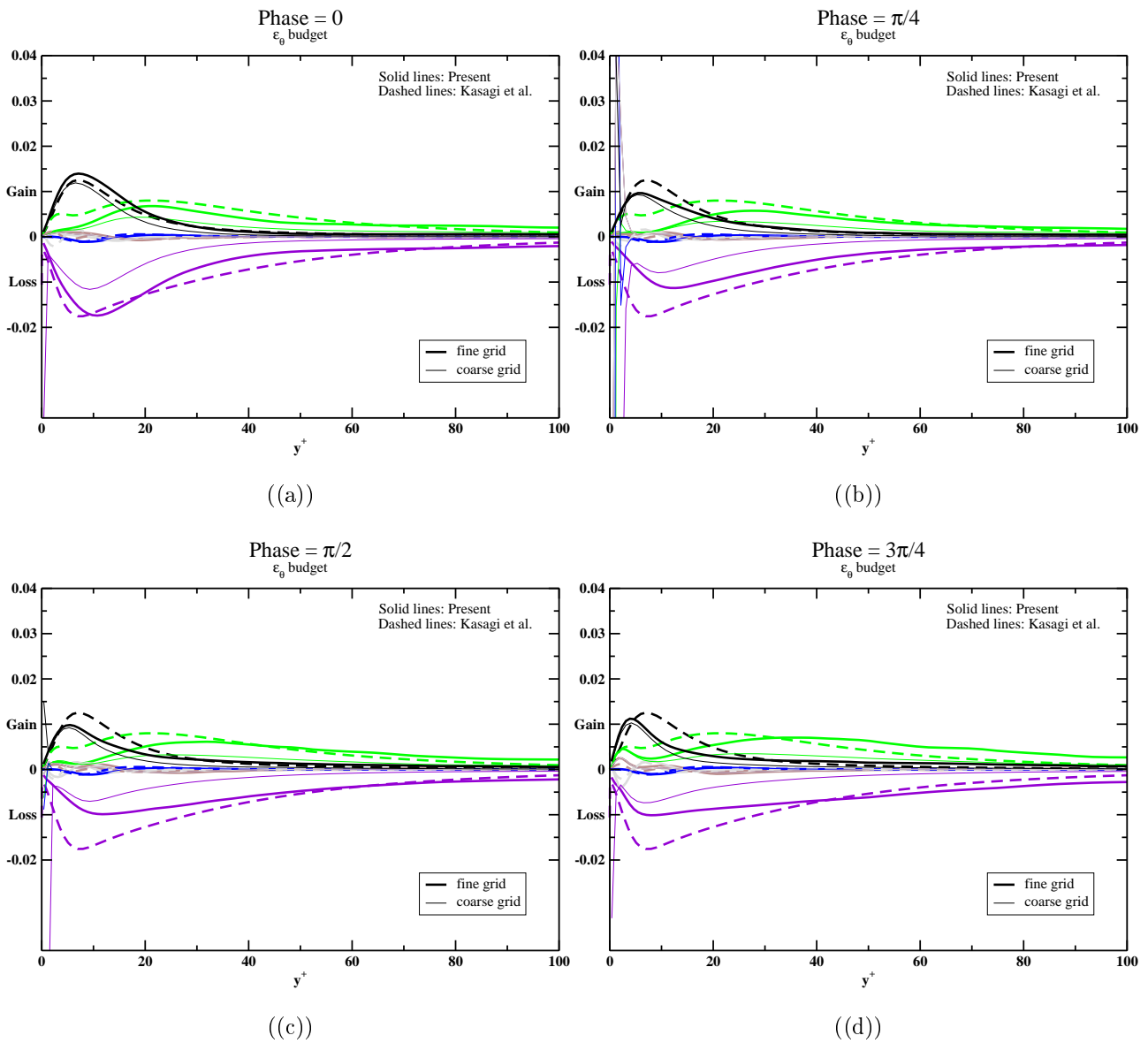


Figure 8.5.10: Budget of  $\epsilon_\theta$ , pulsating flow computations on fine and coarse grid,  $a_{uc} = 0.7$ ,  $l_s^+ = 7$ , comparison with steady channel flow DNS data from [42]

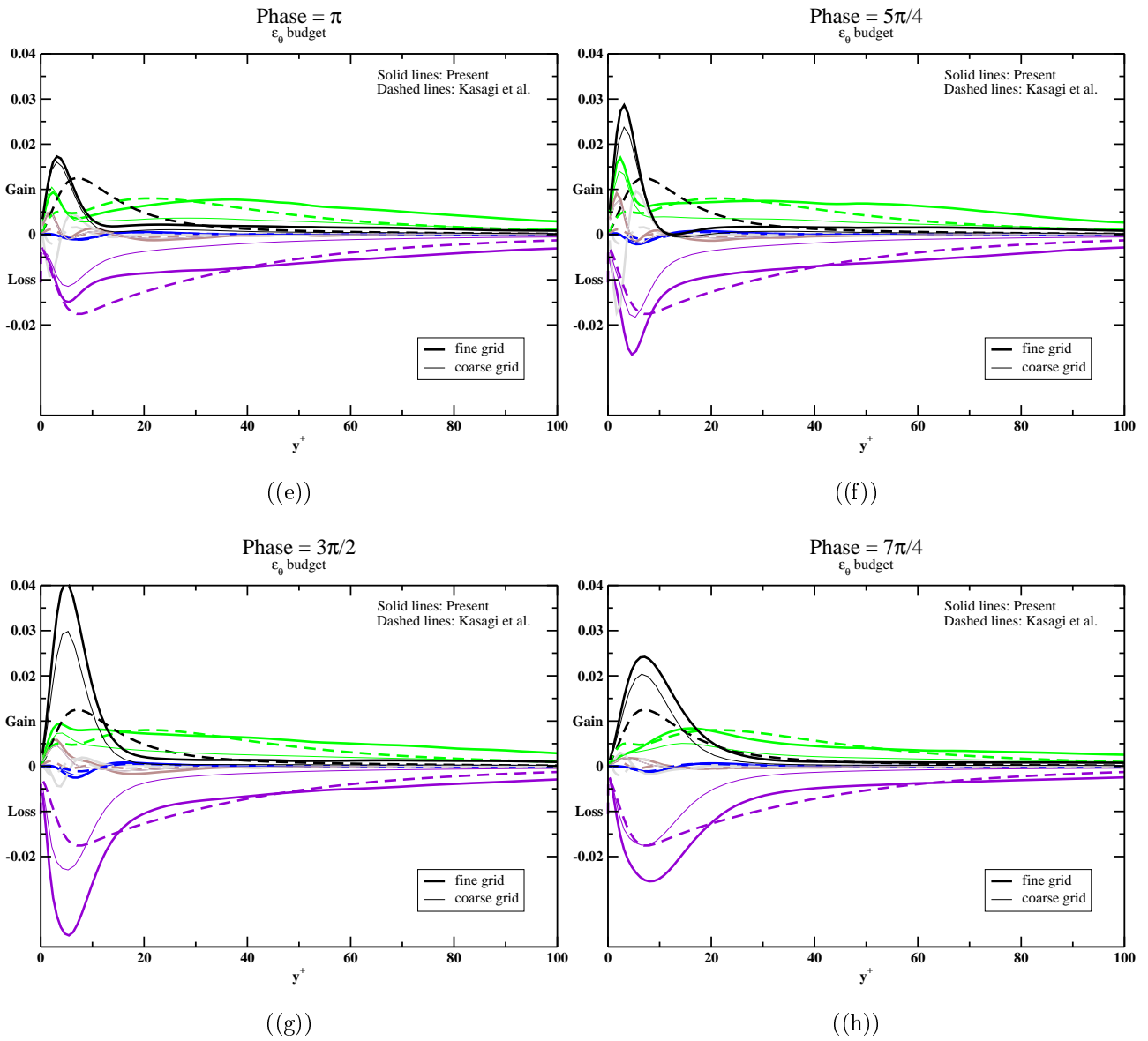


Figure 8.5.10: Budget of  $\epsilon_\theta$ , pulsating flow computations on fine and coarse grid,  $a_{uc} = 0.7$ ,  $l_s^+ = 7$ , comparison with steady channel flow DNS data from [42] (continue)

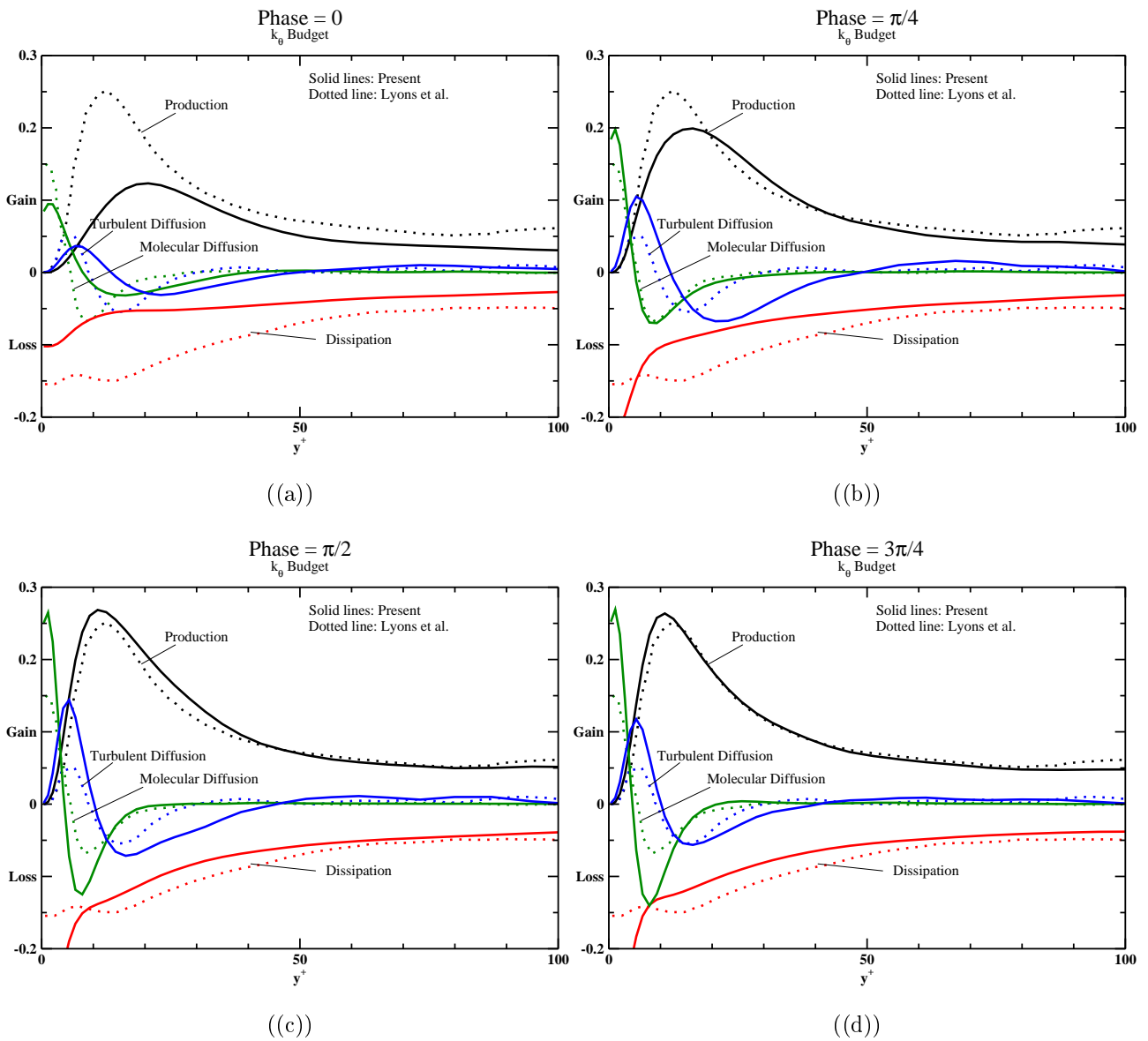


Figure 8.5.11: Budget of  $k_\theta$ , pulsating flow computations on fine and coarse grid,  $a_{uc} = 0.7$ ,  $l_s^+ = 14$ , comparison with steady channel flow DNS data from [52]

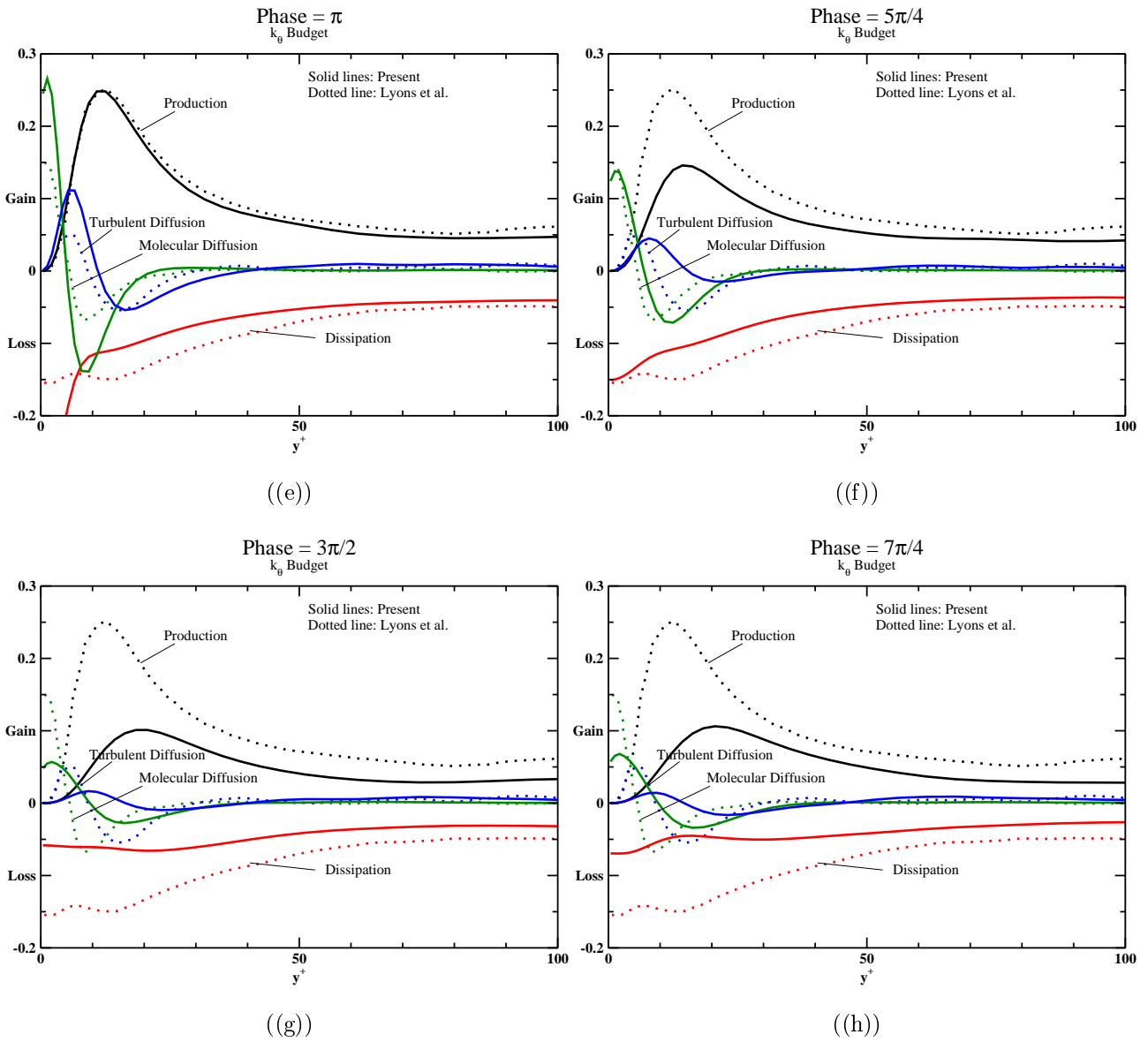


Figure 8.5.11: Budget of  $k_\theta$ , pulsating flow computations on fine and coarse grid,  $a_{uc} = 0.7$ ,  $l_s^+ = 14$ , comparison with steady channel flow DNS data from [52] (continue)



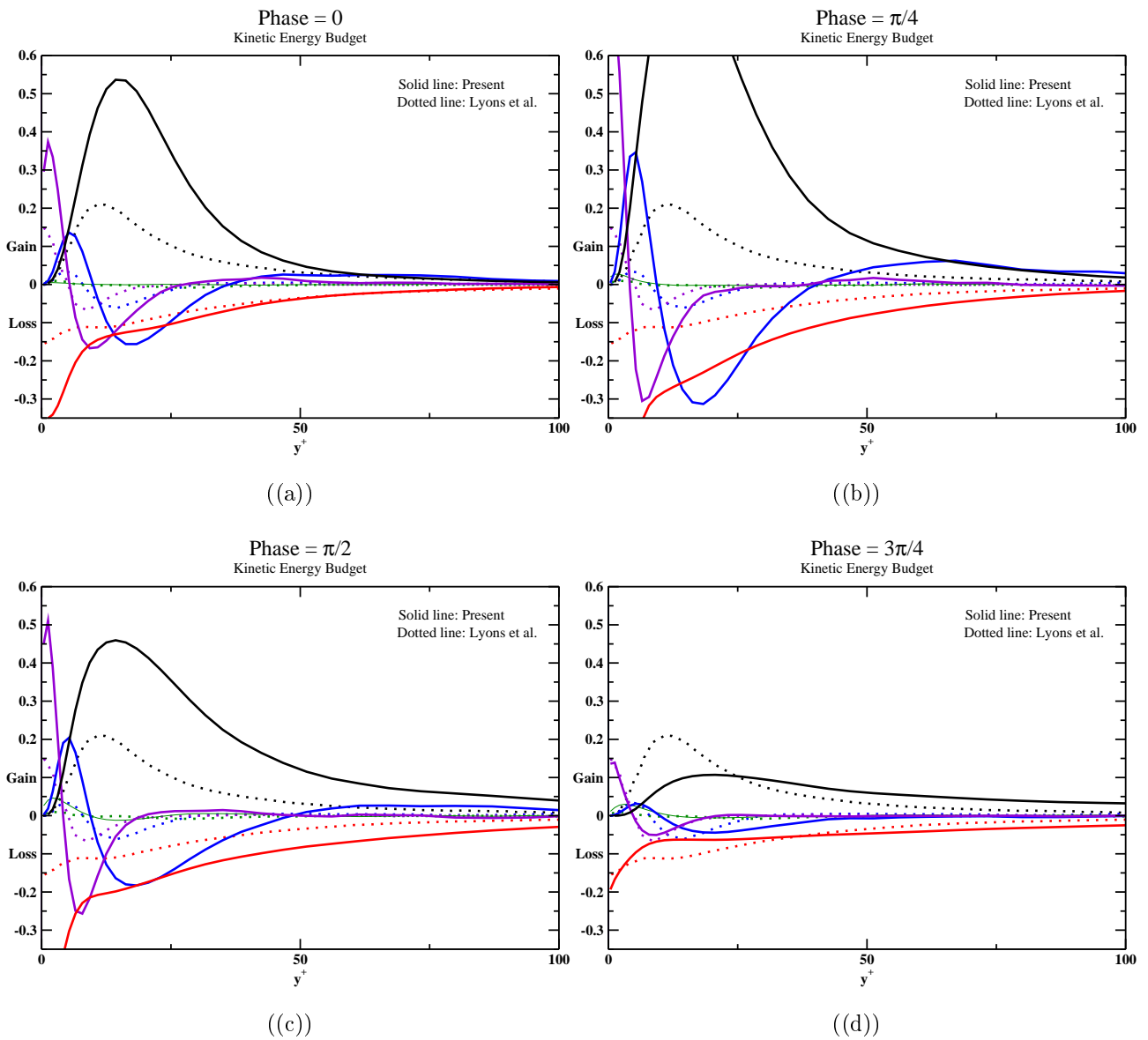


Figure 8.5.12: Budget of kinetic energy, pulsating flow computations on coarse grid,  $a_{uc} = 0.7$ ,  $l_s^+ = 14$ , comparison with steady channel flow DNS data from [42]

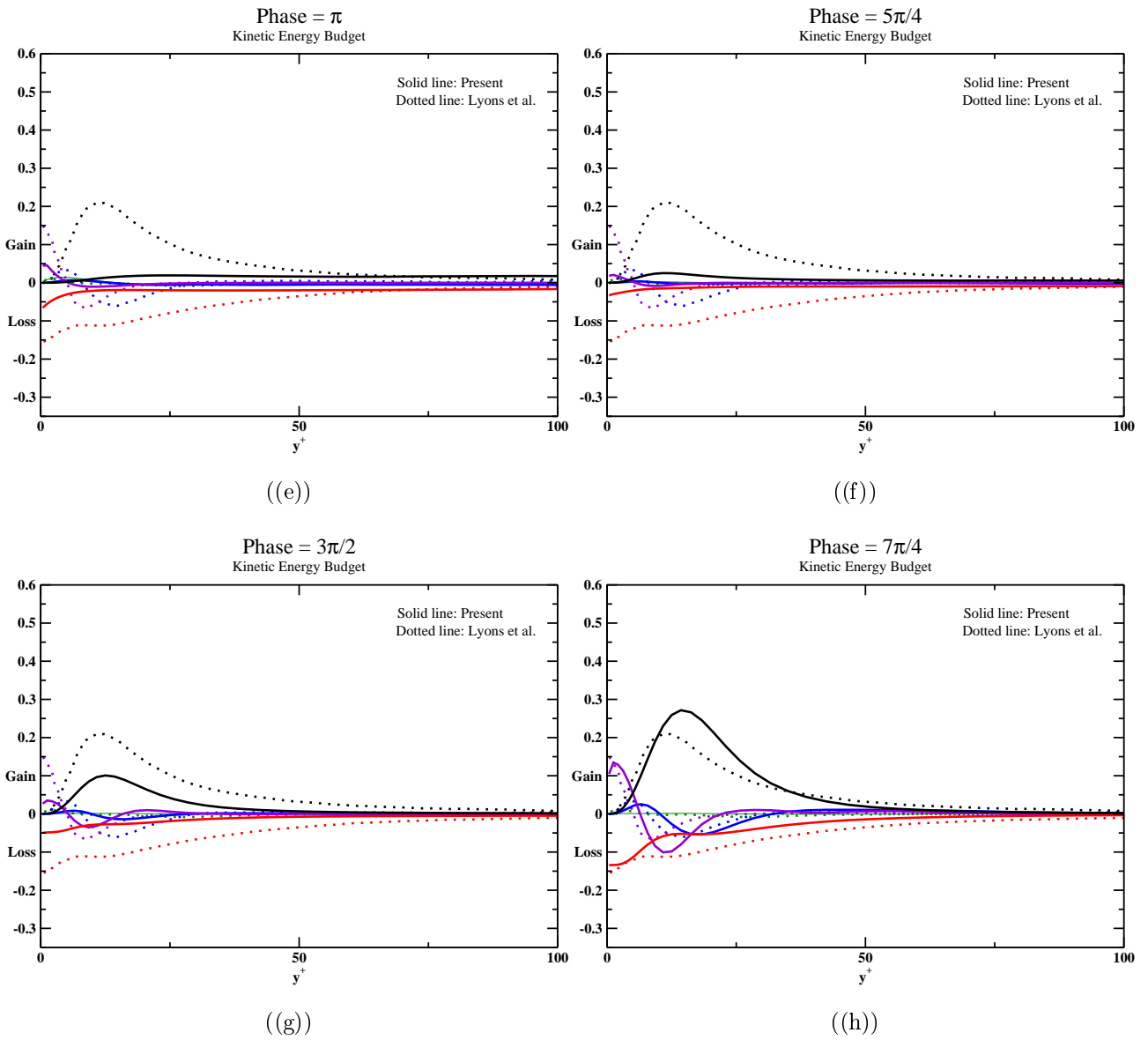


Figure 8.5.12: Budget of kinetic energy, pulsating flow computations on coarse grid,  $a_{uc} = 0.7$ ,  $l_s^+ = 14$ , comparison with steady channel flow DNS data from [42] (continue)

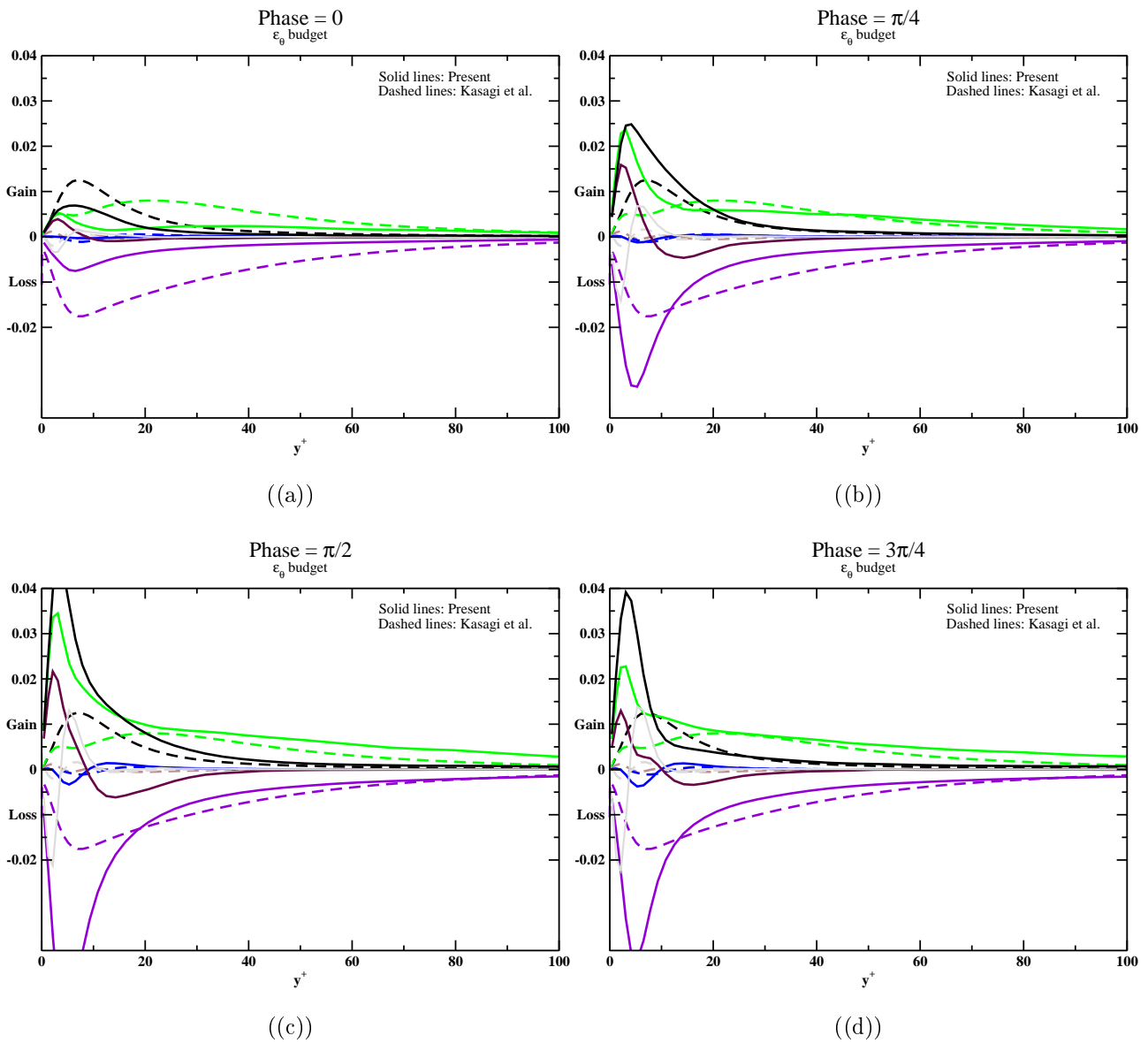


Figure 8.5.13: Budget of  $\epsilon_\theta$ , pulsating flow computations on fine and coarse grid,  $a_{uc} = 0.7$ ,  $l_s^+ = 14$ , comparison with steady channel flow DNS data from [42]

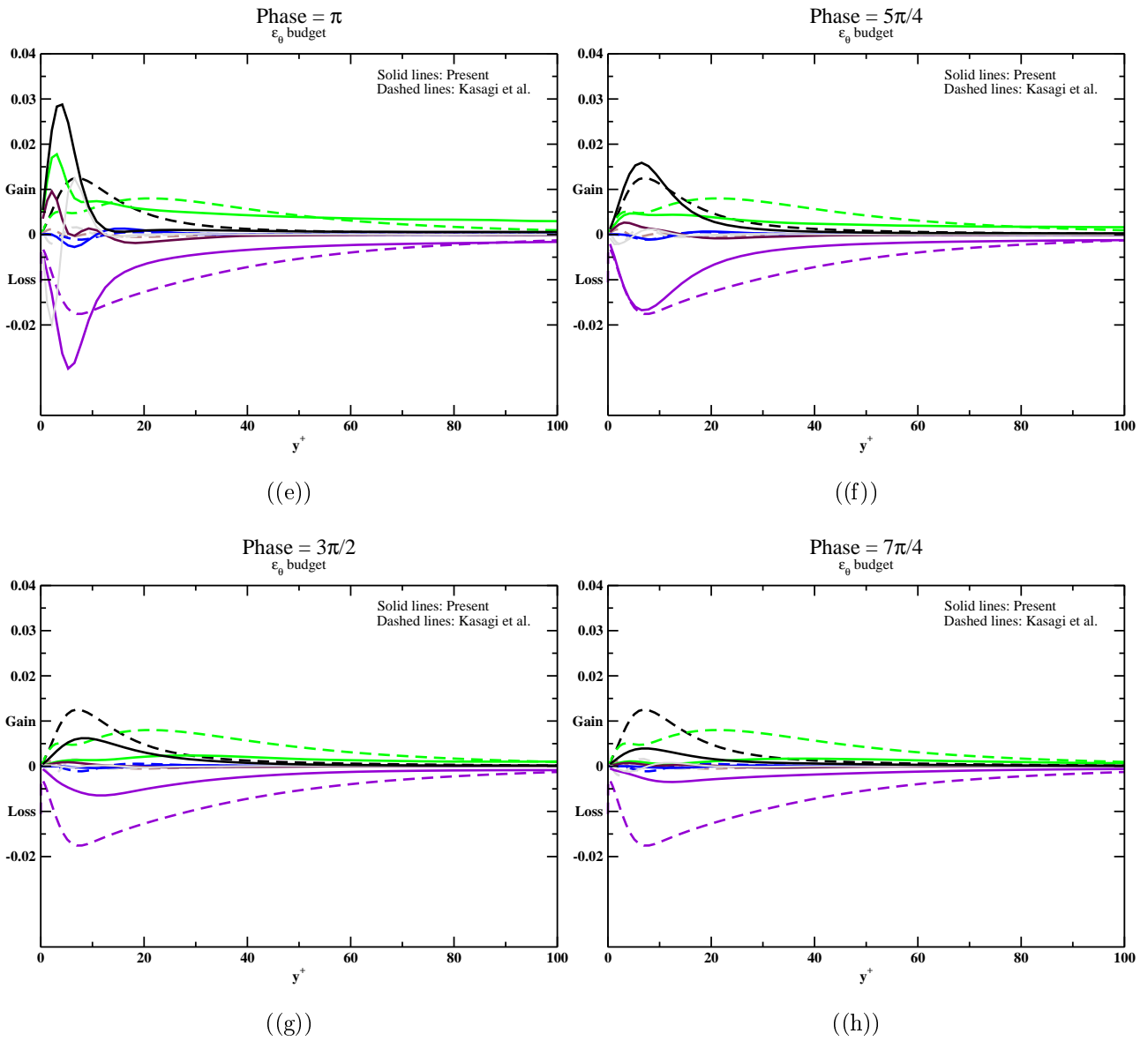


Figure 8.5.13: Budget of  $\epsilon_\theta$ , pulsating flow computations on fine and coarse grid,  $a_{uc} = 0.7$ ,  $l_s^+ = 14$ , comparison with steady channel flow DNS data from [42](continue)

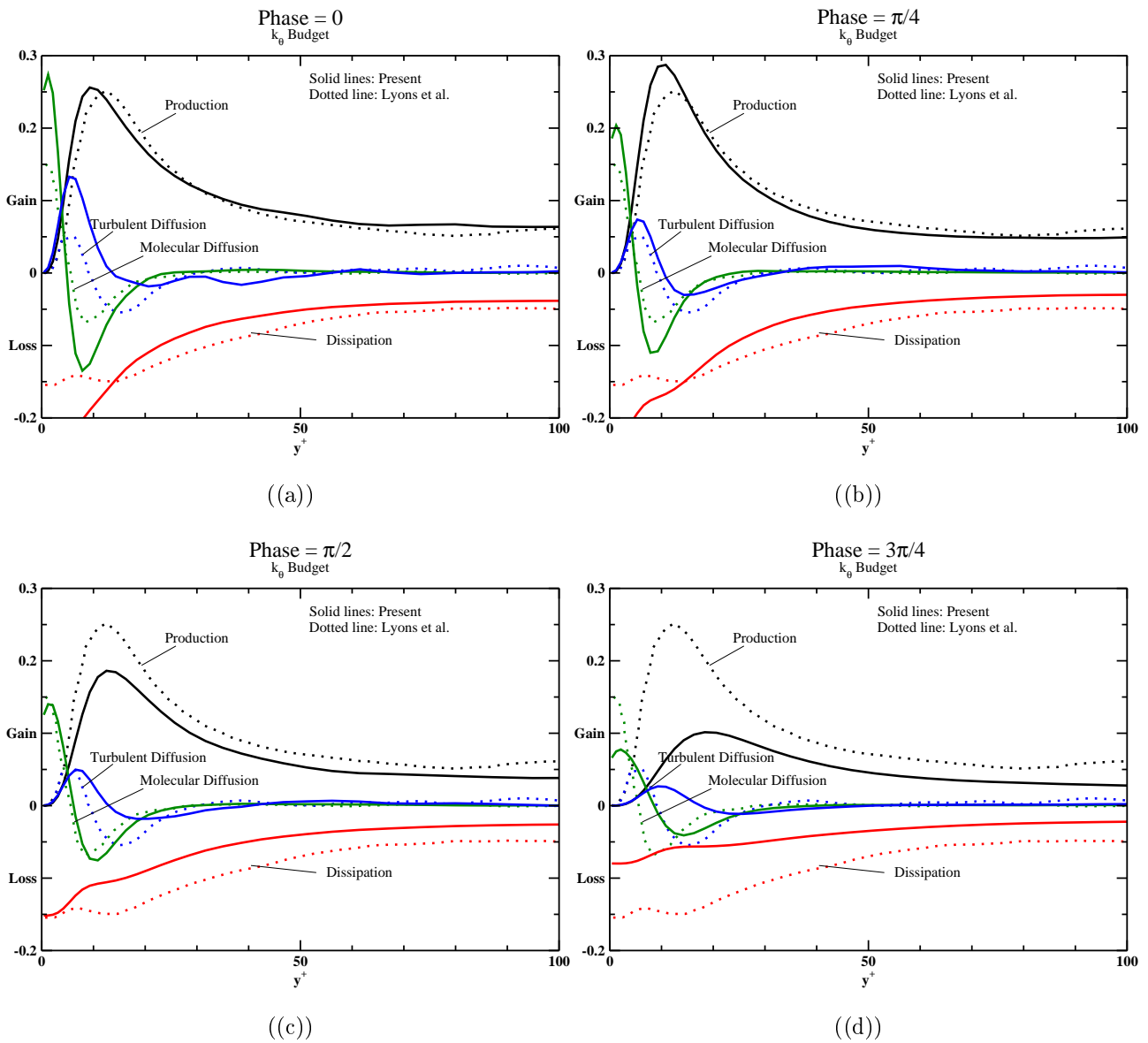


Figure 8.5.14: Budget of  $k_\theta$ , pulsating flow computations on fine and coarse grid,  $a_{uc} = 0.7$ ,  $l_s^+ = 35$ , comparison with steady channel flow DNS data from [52]

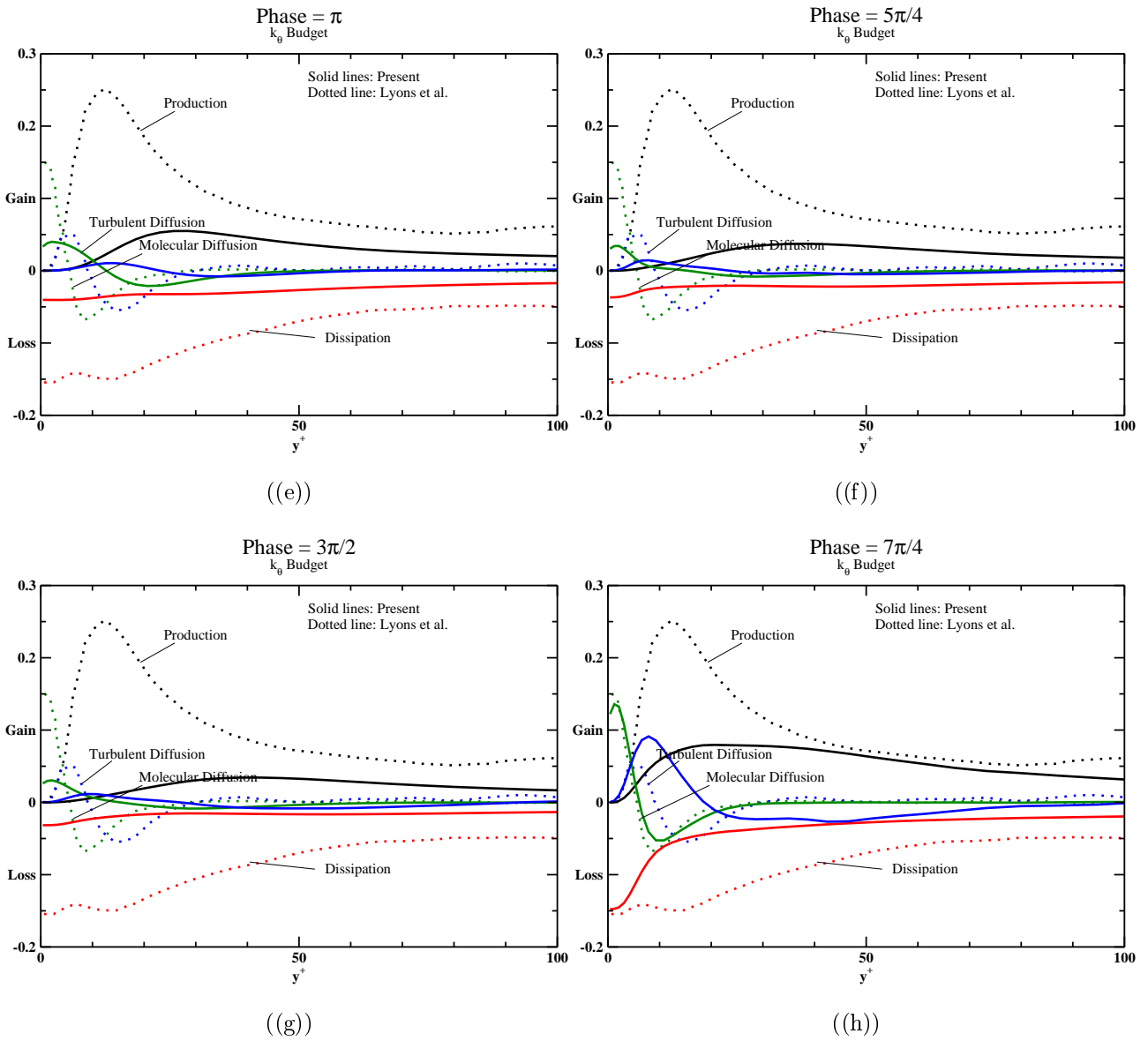


Figure 8.5.14: Budget of  $k_\theta$ , pulsating flow computations on fine and coarse grid,  $a_{uc} = 0.7$ ,  $l_s^+ = 35$ , comparison with steady channel flow DNS data from [52] (continue)

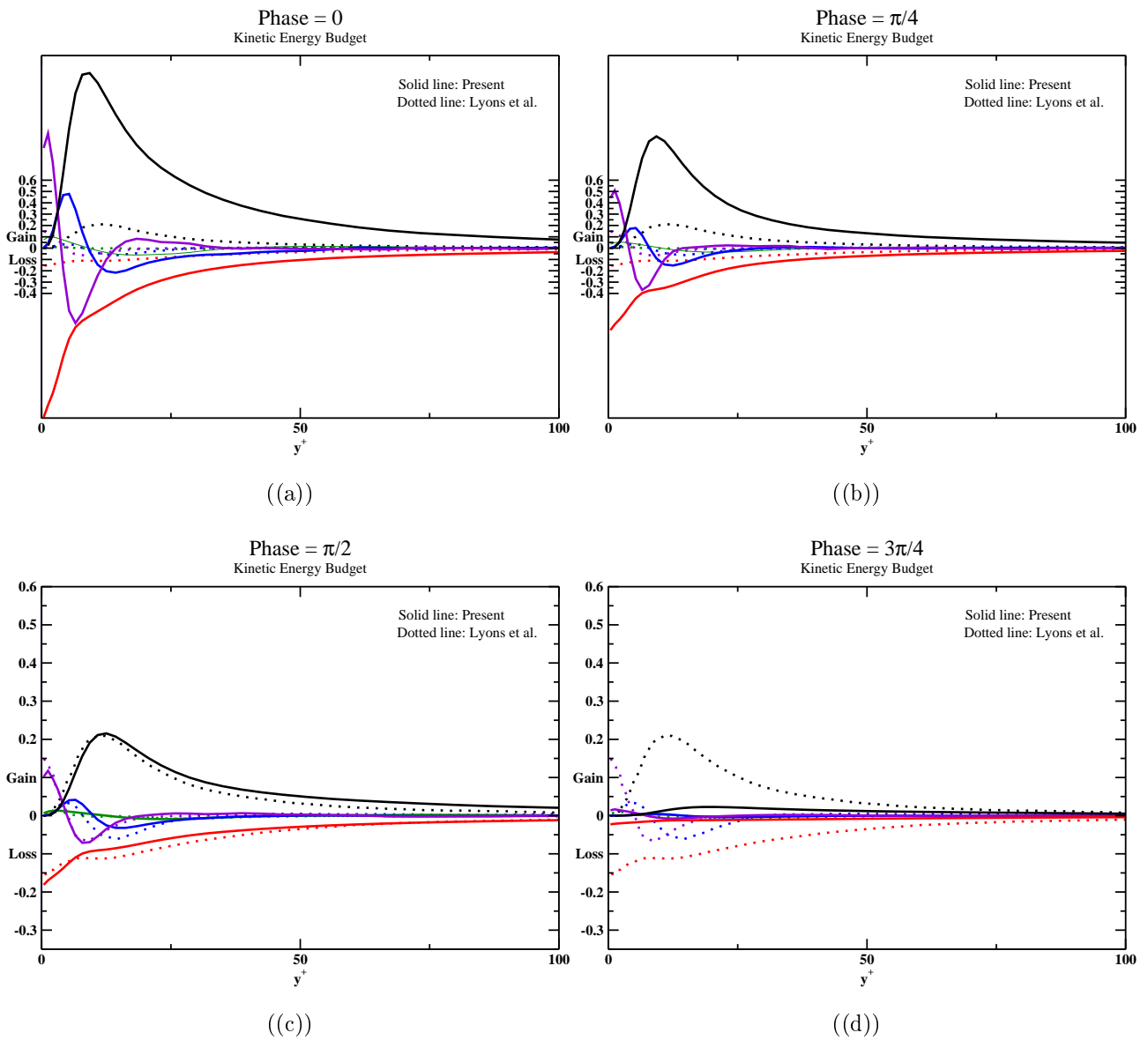


Figure 8.5.15: Budget of kinetic energy, pulsating flow computations on coarse grid,  $a_{uc} = 0.7$ ,  $l_s^+ = 35$ , comparison with steady channel flow DNS data from [42]

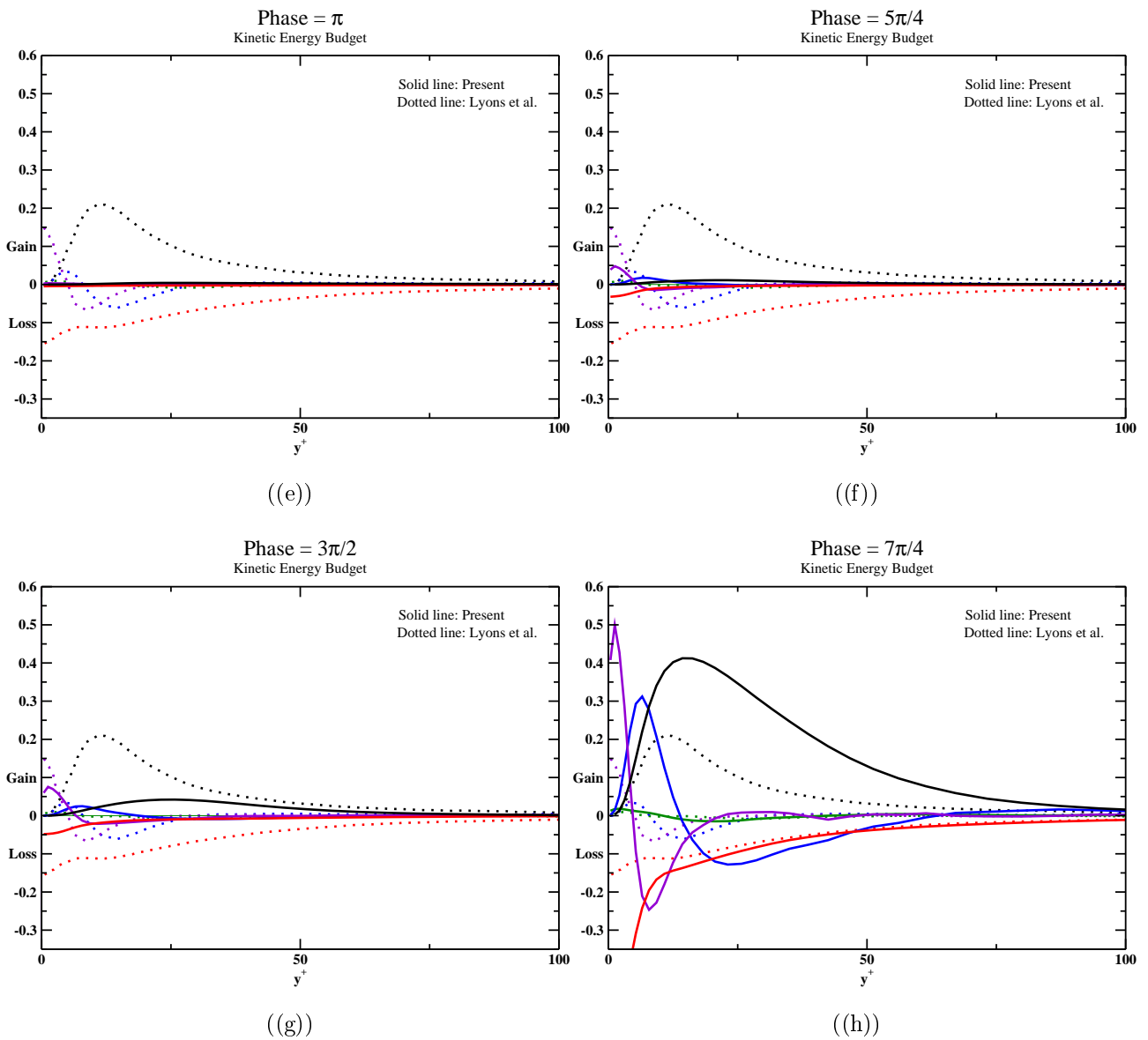


Figure 8.5.15: Budget of kinetic energy, pulsating flow computations on coarse grid,  $a_{uc} = 0.7$ ,  $l_s^+ = 35$ , comparison with steady channel flow DNS data from [42] (continue)



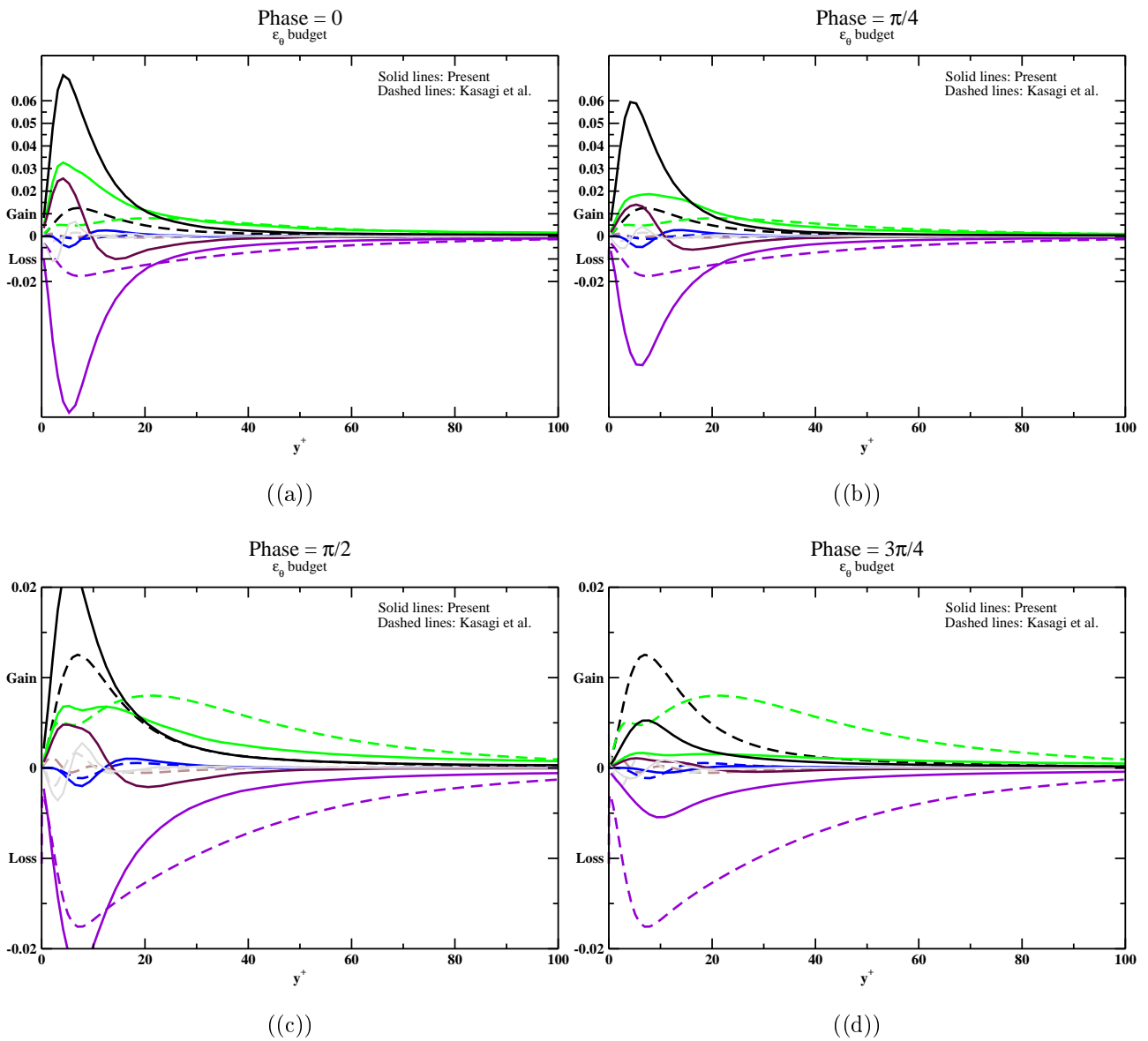


Figure 8.5.16: Budget of  $\epsilon_\theta$ , pulsating flow computations on fine and coarse grid,  $a_{uc} = 0.7$ ,  $l_s^+ = 35$ , comparison with steady channel flow DNS data from [42]

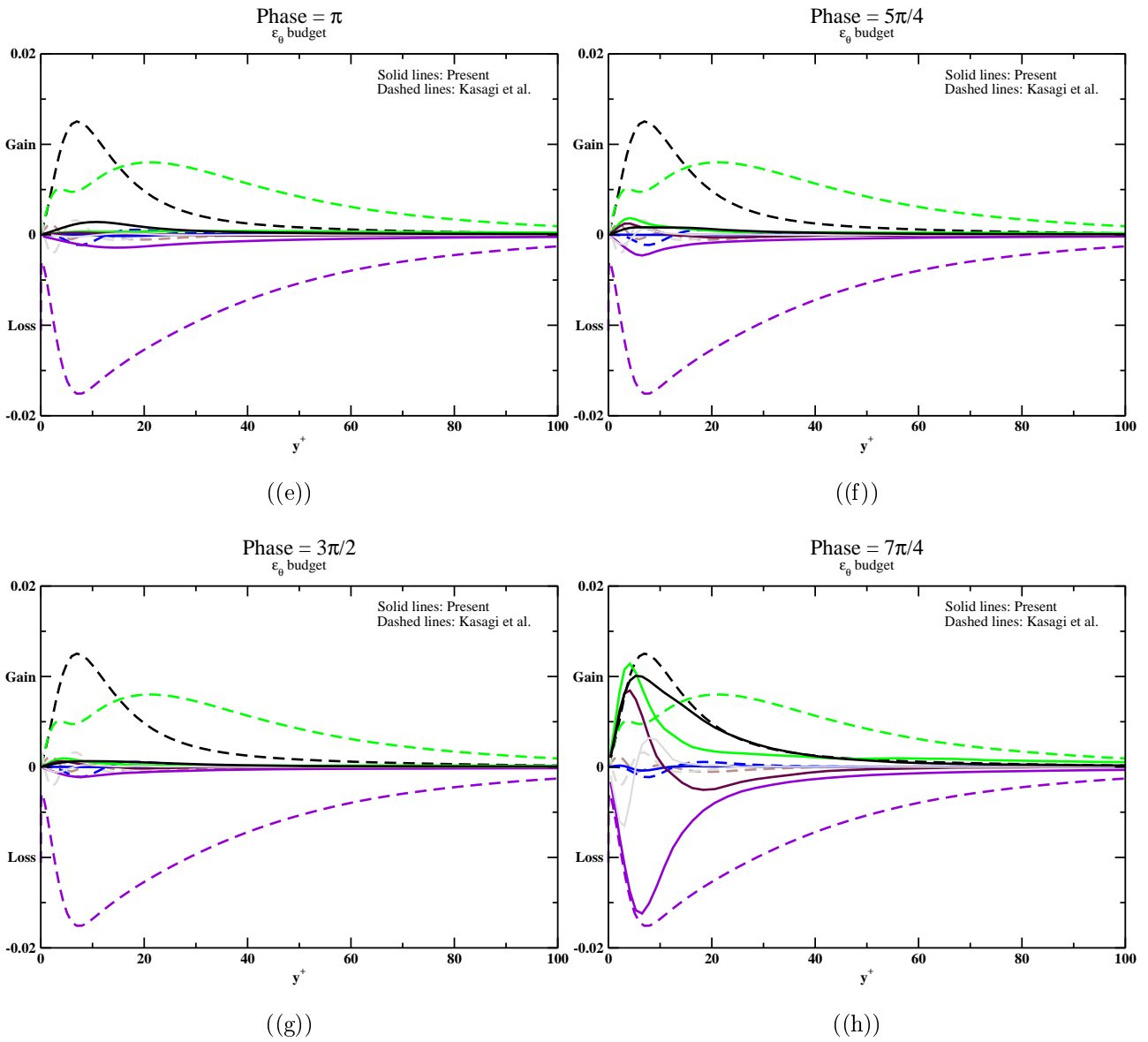


Figure 8.5.16: Budget of  $\epsilon_\theta$ , pulsating flow computations on fine and coarse grid,  $a_{uc} = 0.7$ ,  $l_s^+ = 35$ , comparison with steady channel flow DNS data from [42] (continue)

### 8.5.3 Turbulent Prandtl Number

In the Figures From 8.5.17 to 8.5.19 the phase-locked averaged turbulent Prandtl Number,

$$Pr_t = \frac{\overline{w'v'} \frac{dT}{dy}}{\overline{v'T'} \frac{dU}{dy}} \quad (8.5.4)$$

has been plotted in time and for different pulsation frequencies. At high frequency pulsation (Figure 8.5.17), the turbulent Prandtl number oscillates between very high positive and negative values ( region  $y^+ < 20$ ). This can be explained due to the fact that in the near wall region, because of the partial flow reversal, the velocity profile changes curvature very sharply. In the outer flow the turbulent Prandtl number remains close to one oscillating from 0.9 to 1.25. In the intermediate frequency range (Figure 8.5.18) a similar behavior can be observed. Very high values of turbulent Prandtl number are observed at the wall but no negative values are present. In the outer flow, the turbulent Prandtl number profiles oscillate between 0.8 and 1.1 but with a different phase. Finally for the case of  $l_s^+ = 35$  the turbulent Prandtl number shows the highest variation in time and space showing values spanning from 0.8 up to 1.4

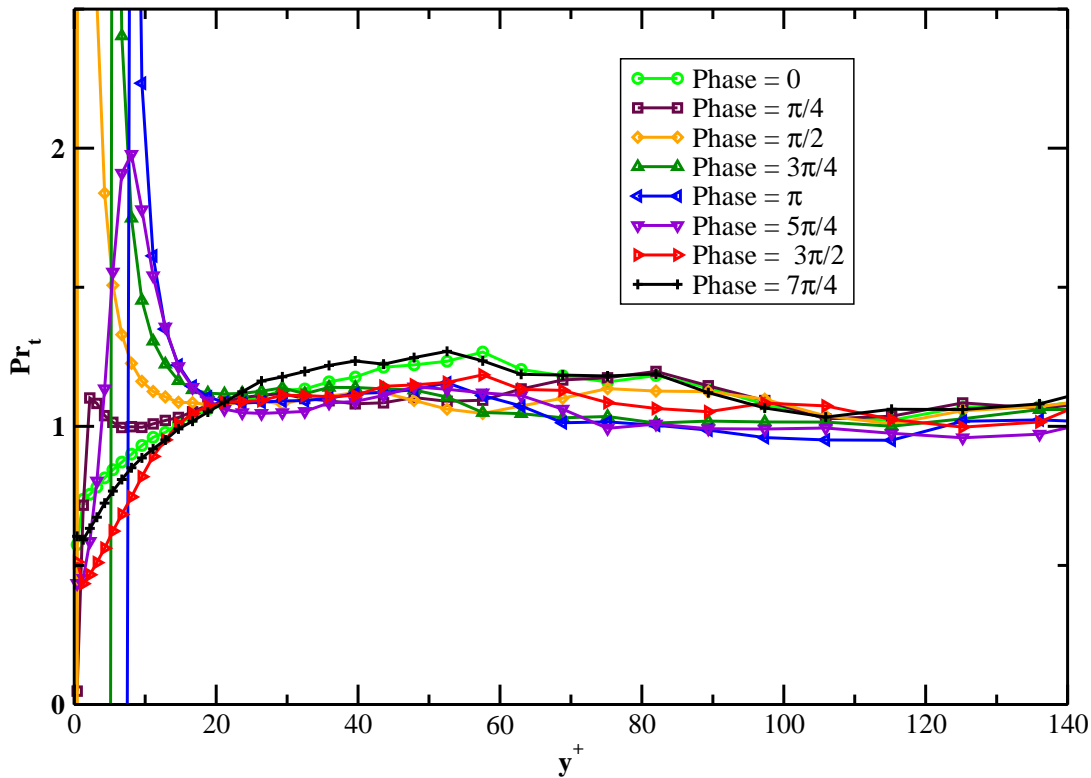


Figure 8.5.17: Phase-locked averaged Turbulent Prandtl Number, case  $a_{uc} = 0.7$   $l_s^+ = 7$

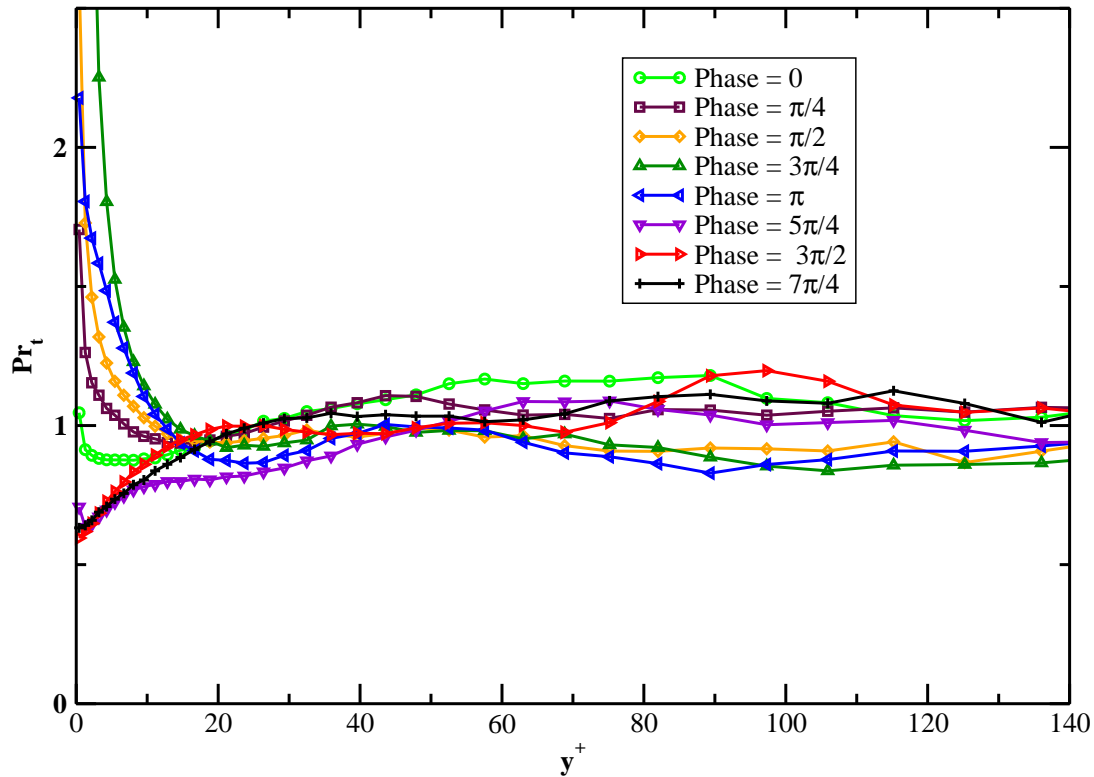


Figure 8.5.18: Phaselocked averaged turbulent Prandtl Number, case  $a_{uc} = 0.7$   $l_s^+ = 14$

The average value of turbulent Prandtl number is reported in Figure 8.5.20 for different pulsation numbers. For comparison, the turbulent Prandtl number profile for the steady channel case is reported. In the case of  $l_s^+ = 7$  a maximum value of  $Pr_t = 1.2$  at  $y^+ = 50$  is evident. Far from the wall the turbulent Prandtl number recovers the steady case behavior. In the intermediate frequency range ( $l_s^+ = 14$ ), close to the wall ( $y^+ < 40$ ), the turbulent Prandtl number is lower than the steady case and then asymptotically increases towards 1.0. At  $l_s^+ = 35$  the turbulent Prandtl number behavior is more similar to the steady case but surprisingly shifted around 1.2.

#### 8.5.4 Wave Dominated Flow

In the present section the results in the Wave Dominated Flow conditions are reported. In Fig. 8.5.21 the phase-locked averaged Nusselt number is reported in phase. As expected, there is a big difference between the present results at  $l_s^+ = 7$  and  $l_s^+ = 14$  and the quasi-steady theory. The increased frequency seems to reduce not only the Nusselt number amplitude but also its overall mean value. This trend seems to be opposite to the experimental evidences in [38].

Due to the mentioned reduced accuracy of the simulations no-budgets are reported.

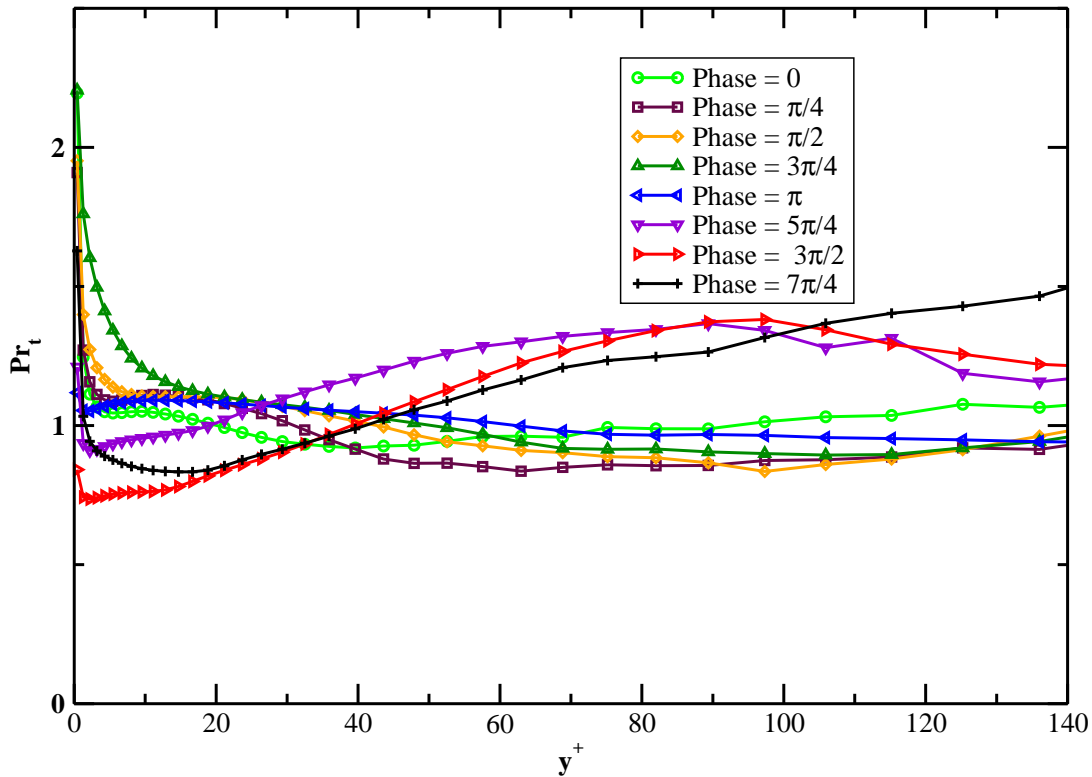


Figure 8.5.19: Phase-locked averaged turbulent Prandtl Number, case  $a_{uc} = 0.7 l_s^+ = 35$

## 8.6 Conclusions

In the present chapter the effect of flow pulsations on the turbulent structures and wall heat transfer has been investigated in detail by means of DNS simulations. From the results shown several conclusion can be drawn.

- Depending on the flow pulsations, the near wall velocity profiles can be strongly affected by the outer flow pulsations. Flow reversal can occur at high frequency also in the case of relatively small pulsation amplitudes ( $a_{uc} = 0.7$  and  $l_s^+ = 7$ ).
- Flow pulsations affect not only the mean velocity profiles but also the turbulent structures and hence the level of near wall velocity fluctuations. As it is clearly shown by the behavior of the turbulent shear stress (Figure from 8.5.4 to 8.5.6), the stabilizing and destabilizing effects of flow acceleration and deceleration have a strong impact on the turbulent velocity fluctuations. The phase and amplitude of the shear stress response depends strongly with the flow frequency. At low frequency relaminarization, as well a sudden increase of Reynolds stress intensity, can occur within a pulsation period. The phase and amplitude of the Reynolds stress bursts depend also on the flow frequency.

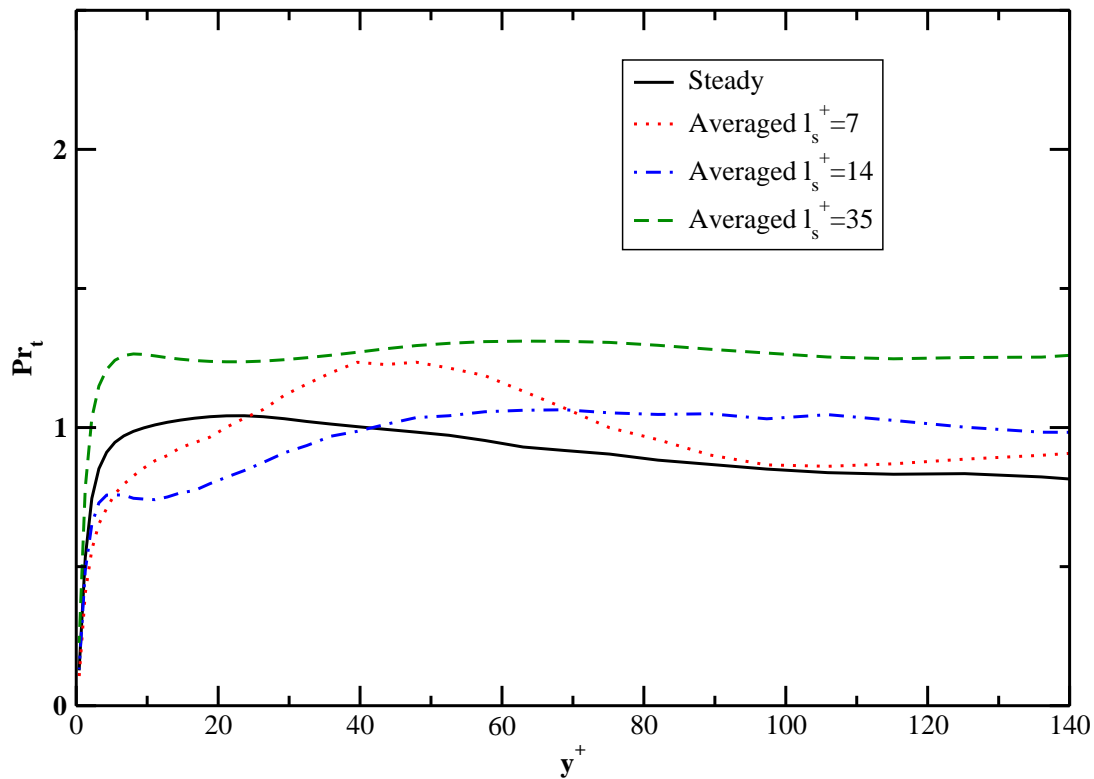


Figure 8.5.20: Averaged turbulent Prandtl Number, comparison with steady flow.

- The  $k$ ,  $k_\theta$  and  $\epsilon_\theta$  budget analysis has shown interesting differences between the time response of each budget term.  $k$  and  $k_\theta$  seem to behave quite differently at high frequency pulsation.  $k_\theta$  production and dissipation seem to be frozen at high pulsations frequency whereas  $k$  is strongly affected by flow acceleration and decelerations.
- As shown in section 8.5.3, the mean and phase-locked averaged turbulent Prandtl number is clearly affected by flow pulsation. In order to correctly predict the overall heat transfer in presence of flow pulsations the assumption of a constant turbulent Prandtl number should be released.
- The unsteady heat transfer is strongly affected by flow pulsations in both phase and amplitude especially in the case of high pulsation amplitude ( $a_{uc} = 6$ ). The pulsation frequency increase determines an unsteady heat transfer amplitude decrease. The pulsation frequency however have a small effect on the overall value of heat transfer in the case of small pulsation amplitude. Considering Figure 8.5.7 it is clear that the flow pulsation affects the mean value of Nusselt number just of few percents, remaining always close to the steady channel value. On the contrary, in the case of high amplitude pulsations (see Figure 8.5.21) the mean value of the Nusselt number increases up to 2 times its steady

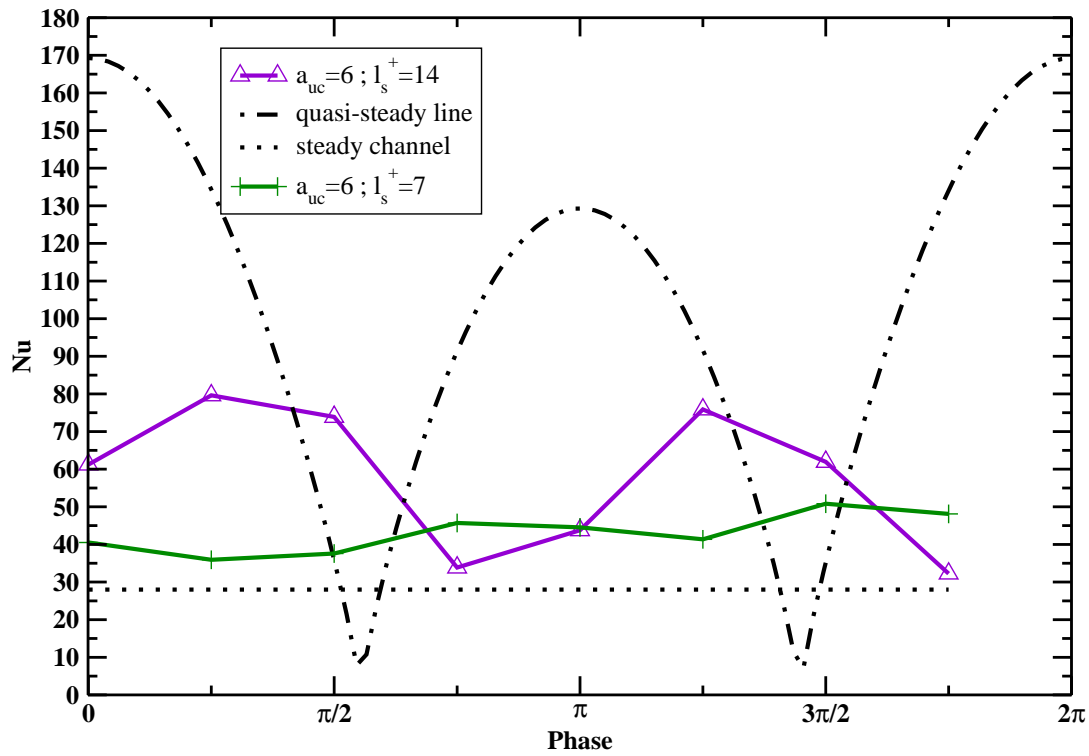


Figure 8.5.21: Pulsating channel flow, Phase-locked averaged Nusselt number comparison, wave dominated flow.

channel value but below the value predicted by the quasi-steady assumption. This finding however seems to be in opposition to the experimental evidences of Ishino et al. [38].





# 9 Turbulent Heat Transfer Modeling

Production	Dissipation	Mol. Diff.	Turb. Diff.
$\mathcal{P}_\theta = -\overline{u'_j T'} \frac{\partial \bar{T}}{\partial x_j}$	$\epsilon_\theta = -\alpha \overline{\frac{\partial T'}{\partial x_j} \frac{\partial T'}{\partial x_j}}$	$-\frac{\partial \overline{u'_j k'_\theta}}{\partial x_j}$	$\frac{\partial}{\partial x_j} \left( \alpha \frac{\partial k_\theta}{\partial x_j} \right)$

Table 9.1:  $k_\theta$  transport equation: turbulent production, dissipation, molecular diffusion and turbulent diffusion terms.

As shown by the DNS results in Chapter 8, flow pulsations do have an effect on the turbulent temperature and velocity fluctuations, hence on the unsteady heat transfer. In Chapter 4, several URANS and LES turbulent model have been presented and, in Chapter 7, their capability to predict unsteady heat transfer has been investigated. All the presented models rely on the assumption of a constant turbulent Prandtl Number which, in Chapter 8, has been proven to be questionable. In the present chapter, such an assumption has been released and, two equation turbulent heat transfer closures are discussed more in details. A particular attention is given to the model proposed by Abe et al. in [10] and outlined in the Section 4.4.3. In section 9.2, the implementation and validation of the model using the OpenFOAM CFD toolbox is discussed. Results and possible model improvements for pulsating channel flow configurations are discussed and compared with the DNS data from Chapter 8.

## 9.1 Two Equation Turbulent Heat Transfer Closures

As proposed by [55], a promising strategy for a turbulent heat transfer closure which does not require any questionable assumptions for the turbulent Prandtl number makes use of two additional transport equations for the fluctuating temperature variance ( $k_\theta$ ) and its dissipation rate ( $\epsilon_\theta$ ).

As already mentioned in 4.4.3, the exact transport equation for  $k_\theta$ , according to [48], has been presented first by [19] and can be obtained by multiplying the temperature equation (4.0.9) by the fluctuating temperature ( $T'/2$ ) and ensemble averaging:

$$\frac{Dk_\theta}{Dt} = -\overline{u'_j T'} \frac{\partial \bar{T}}{\partial x_j} - \alpha \overline{\frac{\partial T'}{\partial x_j} \frac{\partial T'}{\partial x_j}} - \frac{\partial \overline{u'_j k'_\theta}}{\partial x_j} + \frac{\partial}{\partial x_j} \left( \alpha \frac{\partial k_\theta}{\partial x_j} \right). \quad (9.1.1)$$

Where

$$k_\theta = \frac{1}{2} \overline{T'^2} \quad (9.1.2)$$

and

$$k'_\theta = \frac{1}{2} T'^2 \quad (9.1.3)$$

The terms on the righthandside are referred as: Production, Dissipation, Turbulent Diffusion and Molecular Diffusion respectively (see table 9.1).

The dissipation term is often referred as  $\epsilon_\theta$ :

	Prod. by Mean T Grad.	Grad. Prod.	Prod. by Mean U Grad.
Mean Grad. Prod. Terms	$-2\alpha \overline{\frac{\partial T'}{\partial x_j} \frac{\partial u'_k}{\partial x_j} \frac{\partial \bar{T}}{\partial x_k}}$	$-2\alpha \overline{u'_k \frac{\partial T'}{\partial x_j} \frac{\partial^2 \bar{T}}{\partial x_k \partial x_j}}$	$-2\alpha \overline{\frac{\partial T'}{\partial x_j} \frac{\partial T'}{\partial x_j} \frac{\partial \bar{u}_k}{\partial x_j}}$

Table 9.2:  $\epsilon_\theta$  transport equation, mean gradient production terms: production by mean temperature gradient, gradient production, production by mean velocity gradient.

Turb. Prod.	Dissipation	Mol. Diff.	Turb. Diff.
$-2\alpha \overline{\frac{\partial T'}{\partial x_j} \frac{\partial u'_k}{\partial x_j} \frac{\partial T'}{\partial x_k}}$	$-2 \left( \alpha \frac{\partial^2 T'}{\partial x_j \partial x_k} \right)^2$	$\frac{\partial}{\partial x_k} \left( \alpha \frac{\partial \epsilon_\theta}{\partial x_k} \right)$	$-\frac{\partial \overline{\epsilon'_\theta u'_k}}{\partial x_k}$

Table 9.3:  $\epsilon_\theta$  transport equation: turbulent production, dissipation, molecular diffusion and turbulent diffusion terms.

$$\epsilon_\theta = \alpha \overline{\frac{\partial T'}{\partial x_j} \frac{\partial T'}{\partial x_j}} \quad (9.1.4)$$

As introduced in Section 4.4.3, an exact equation can be derived also for  $\epsilon_\theta$ :

$$\begin{aligned} \frac{D\epsilon_\theta}{Dt} = & -2\alpha \overline{\frac{\partial T'}{\partial x_j} \frac{\partial u'_k}{\partial x_j} \frac{\partial \bar{T}}{\partial x_k}} - 2\alpha \overline{u'_k \frac{\partial T'}{\partial x_j} \frac{\partial^2 \bar{T}}{\partial x_k \partial x_j}} \\ & -2\alpha \overline{\frac{\partial T'}{\partial x_j} \frac{\partial T'}{\partial x_j} \frac{\partial \bar{u}_k}{\partial x_j}} - 2\alpha \overline{\frac{\partial T'}{\partial x_j} \frac{\partial u'_k}{\partial x_j} \frac{\partial T'}{\partial x_k}} \\ & -2 \left( \alpha \frac{\partial^2 T'}{\partial x_j \partial x_k} \right)^2 - \frac{\partial \overline{\epsilon'_\theta u'_k}}{\partial x_k} + \frac{\partial}{\partial x_k} \left( \alpha \frac{\partial \epsilon_\theta}{\partial x_k} \right), \end{aligned} \quad (9.1.5)$$

where

$$\epsilon'_\theta = \alpha \overline{\frac{\partial T'}{\partial x_j} \frac{\partial T'}{\partial x_j}} \quad (9.1.6)$$

The  $\epsilon_\theta$  equation is obtained by taking the derivative of the temperature equation with respect of  $x_k$  (4.0.9), multiplying by  $2\alpha \partial T' / \partial x_k$  and ensemble averaging. The terms on the righthandside of (4.4.39) are referred as: Production by Mean Temperature Gradient, Gradient Production, Production by Mean Velocity Gradient, Turbulent Production, Dissipation, Turbulent Diffusion and Molecular Diffusion term (see table 9.2 and 9.3).

In order to obtain a time scale ( $\tau_\theta$ ) representative of the turbulent heat transfer,  $k_\theta$  and  $\epsilon_\theta$  can be combined as follows:

$$\tau_\theta = \frac{k_\theta}{\epsilon_\theta} \quad (9.1.7)$$

This is analogous to the definition of a turbulent time scale by means of  $k$  and  $\epsilon$ :

$$\tau_t = \frac{k}{\epsilon}. \quad (9.1.8)$$

The turbulent time scale, as expressed in 9.1.8, has been already used in the definition of the turbulent viscosity in section 4.4.1:

$$\nu_t = C_\mu k \tau_t = C_\mu \frac{k^2}{\epsilon} \quad (9.1.9)$$

The eddy diffusivity  $\nu_t$ , which has the dimension of [ $m^2/s$ ], can be defined by the product of a specific turbulent energy scale  $k$  and a characteristic turbulent time scale,  $\tau_t$ .

The thermal eddy diffusivity  $\alpha_t$  has the same dimensions as  $\nu_t$  and is generally related to the eddy diffusivity by the definition of a constant turbulent Prandtl number,  $Pr_t$ :

$$Pr_t = \frac{\nu_t}{\alpha_t} \quad (9.1.10)$$

This strict assumption, can be released in analogy to (9.1.9) upon the definition of reasonable time and energy scales characteristic of the turbulent heat transport phenomena.

Furthemore, for the correct modeling of the turbulent heat transfer phenomena, it is extremely important to consider the mutual interaction between velocity- and temperature-field scales, which makes the turbulent heat transfer modeling very challenging.

Even considering the temperature field as a passive scalar, turbulent heat transfer depends on both velocity fluctuation and temperature fluctuation. For this reason, the thermal eddy viscosity must be defined using a mixed time scale,  $\tau_m$ .

Combining  $\tau_t$  and  $\tau_\theta$ , different formulations of  $\tau_m$  can be proposed. Many classical works use the following generalized formula [10]:

$$\tau_m = \tau_t^l \tau_\theta^m \quad (l + m = 1) \quad (9.1.11)$$

The turbulent heat diffusivity can be then expressed, in analogy to (9.1.9), with

$$\alpha_t = C_\alpha k \tau_m = C_\alpha k \tau_t R^m \quad (9.1.12)$$

where  $R$  represents the time scale ratio:

$$R = \frac{\tau_\theta}{\tau_t} \quad (9.1.13)$$

Substituting (9.1.9) in (9.1.12) the turbulent Prandtl number can be obtained as follows:

$$Pr_t \propto R^{-m} \quad (9.1.14)$$

Often  $l$  and  $m$  are chosen equal ( $l = m = \frac{1}{2}$ ) and  $Pr_t$  is given by

$$Pr_t \propto \frac{1}{C_\alpha} \sqrt{\frac{k_\theta}{\epsilon_\theta}} \frac{\epsilon}{k} \quad (9.1.15)$$

In conclusion, giving a mixing time scale formulation (9.1.11) the turbulent Prandtl number can be expressed as a function of the time scale ratio  $R$  and hence of the  $k_\theta$ -  $\epsilon_\theta$ -fields. The accuracy of the turbulent heat transfer model resides than in the correct estimation of the mixed time scale ( $\tau_m$ ) and on the correct closure of the  $k_\theta$  and  $\epsilon_\theta$  transport equations in (4.4.38) and (4.4.39).

In the  $k_\theta$  equation, assuming the dissipation term ( $\epsilon_\theta$ ) known from its transport equation, the only term which needs to be modelled is the turbulent diffusion term. Generally isotropic diffusion and a gradient transport is assumed:

$$\frac{\overline{\partial u'_j k_\theta}}{\partial x_j} = \frac{\partial}{\partial x_j} \left( \frac{\alpha_t}{\sigma_h} \frac{\partial k_\theta}{\partial x_j} \right) \quad (9.1.16)$$

leading to a formulation analogous to (4.4.41) and here reposed:

$$\frac{\partial k_\theta}{\partial t} + \bar{u}_j \frac{\partial k_\theta}{\partial x_j} = \frac{\partial}{\partial x_j} \left\{ \left( \alpha + \frac{\alpha_t}{\sigma_h} \right) \frac{\partial k_\theta}{\partial x_j} \right\} - \alpha_t \frac{\partial \bar{T}}{\partial x_j} \frac{\partial \bar{T}}{\partial x_j} - \epsilon_\theta \quad (9.1.17)$$

The modeling of the  $\epsilon_\theta$  transport equation is much more difficult due to the different turbulent scales involved. For wall-bounded flows as it is also confirmed by the DNS simulations in Chapter 8, the main contributions are given by the terms of turbulent production, dissipation and production by mean gradients. As outlined by [48], the main requirements for the  $\epsilon_\theta$  transport equation are the following:

- 1) The  $\epsilon_\theta$  dissipation term should be dependent on both velocity and temperature time scales.
- 2) The  $\epsilon_\theta$  production term should be sensitive to changes in both turbulence production and temperature fluctuation production.
- 3) There is a little point in worrying about how the diffusion terms of  $\epsilon_\theta$  can be treated until the form of the creation and destruction terms is settled.

These considerations follow from basic physical observations. Despite the fact that Launder [48] stressed the need for accurate measurements of thermal turbulence in simple flows already in 1976, up to now little has been done in this direction. In this sense, DNS simulations could represent a powerfull tool for the transport equation closure and the present work can be viewed as a part of this strategy.

According to 1) the most obvious approximation of the  $\epsilon_\theta$  dissipation term is to use two terms proportional to  $\epsilon_\theta/\tau_t$  and  $\epsilon_\theta/\tau_\theta$ .

According to 2) the  $\epsilon_\theta$  production term can be also modelled using two terms proportional to  $\frac{\mathcal{P}_\theta}{\tau_t}$  and  $\frac{\mathcal{P}_\theta}{\tau_\theta}$ , where  $\mathcal{P}_\theta$  is the  $k_\theta$  production term:

$$\mathcal{P}_\theta = -\alpha_t \frac{\partial \bar{T}}{\partial x_j} \frac{\partial \bar{T}}{\partial x_j}. \quad (9.1.18)$$

Moreover Lumley and Khajeh-Nouri [48] proposed that the rate of creation of  $\epsilon_\theta$  should be proportional to  $\epsilon_\theta \mathcal{P}/k$ , where  $\mathcal{P}$  is given in (4.4.6).

The turbulent diffusion term is generally modeled assuming simply gradient transport:

$$-\frac{\overline{\partial \epsilon_\theta' u_k'}}{\partial x_k} = \frac{\partial}{\partial x_j} \left( \frac{\alpha_t}{\sigma_\phi} \frac{\partial \epsilon_\theta}{\partial x_j} \right), \quad (9.1.19)$$

giving a closed approximation for the  $\epsilon_\theta$  transport equation of the form:

$$\begin{aligned} \frac{\partial \epsilon_\theta}{\partial t} + \bar{u}_j \frac{\partial \epsilon_\theta}{\partial x_j} &= \frac{\partial}{\partial x_j} \left\{ \left( \alpha + \frac{\alpha_t}{\sigma_{\epsilon_\theta}} \right) \frac{\partial \epsilon_\theta}{\partial x_j} \right\} \\ &\quad - C_{P1} \frac{\epsilon_\theta}{k_\theta} \alpha_t \frac{\partial \bar{T}}{\partial x_j} \frac{\partial \bar{T}}{\partial x_j} - C_{P2} \frac{\epsilon_\theta}{k} \nu_t \left( \frac{\partial \bar{u}_j}{\partial x_i} + \frac{\partial \bar{u}_i}{\partial x_j} \right) \frac{\partial \bar{u}_i}{\partial x_j} \\ &\quad - C_{P3} \frac{\epsilon}{k} \alpha_t \frac{\partial \bar{T}}{\partial x_j} \frac{\partial \bar{T}}{\partial x_j} - C_{D1} \frac{\epsilon_\theta^2}{k_\theta} - C_{D2} \frac{\epsilon \epsilon_\theta}{k}. \end{aligned} \quad (9.1.20)$$

Considering  $C_{P2} = 0$ , which seems to give better results in wall-bounded flows [75], (9.1.20) is very similar to (4.4.41).

## 9.2 Model Validation

### 9.2.1 Channel Flow

The first validation case considered is the DNS channel flow simulation from Kasagi et al. [42]. These results have been already used for comparisons in chapter 8. Kasagi et al. [42] considered a cubical computational domain of  $2355x942x300$  wall units in the three coordinate dimensions (x, y and z, being y the wall-normal, x the streamwise and z the spanwise directions respectively). The half channel height Reynolds number  $Re_h$  (see (5.1.19)) was set to 4580 which corresponds to a value of  $Re_{u_\tau}$  (see (5.1.22)) of 150. The DNS results were obtained using a spectral code which details are given in [42]. A time averaged constant heat flux boundary condition was imposed on the two walls so that the local mean temperature increased linearly in the streamwise direction. Air was chosen as a fluid, and the Prandtl number  $Pr$  was set to 0.71. The temperature was considered as a passive scalar and the time averaged constant wall isoflux condition was prescribed in order to have no temperature fluctuations at the wall, which is consistent with the choice of the fluid Prandtl number for most wall materials [41]. Kasagi [41] showed that depending on the fluid/material heat properties, the condition of constant heat flux on the channel outer wall (this is the case of many experimental setup) can lead to wall temperature fluctuations. The two extreme cases are the ideal wall isoflux condition and the ideal wall isothermal condition [41]. In the first case a constant wall heat flux is prescribed on a infinitely thin surface. In this case the temperature fluctuations at the wall are the highest.

This condition can be easily reproduced in a DNS flow simulation simply imposing a constant temperature gradient at the wall. In common experiments however, where air and metallic walls are used, the temperature fluctuations at the wall are negligible. This is due to the wall thickness and the fluid/wall thermal diffusivity ratio. Hence, to correctly reproduce the experimental condition it is necessary to prescribe a time averaged constant heat flux condition or to model the complex wall conjugate heat transfer problem.

The statistics obtained in the work of [42] are very accurate and concern: root-mean-square temperature fluctuations, turbulent heat fluxes, turbulent Prandtl number and each term in the budget equations of  $k_\theta$  and  $\epsilon_\theta$ . This, together with the relative simple geometry and boundary conditions make the test case very well suited for a turbulence heat transfer model validations.

In the present URANS calculations, a quadratic two-dimensional computational domain of  $20 \times 60$  points in the x and y direction was used. Periodic boundary were prescribed in the streamwise-x direction and the flow was sustained using a constant pressure source term counteracting the channel hydraulic losses. The pressure source term and the channel dimension were set in order to have a Reynolds number close to the Kasagi et al. test case ( $Re_h=4167$ ).

The rhoTurbFoam default solver, a transient solver for incompressible flow with variable density, has been modified in order to prescribe a fix pressure source term and the Abe, Kin and Nagano (AKN) model (see section 4.4.3) has been implemented in an additional OpenFoam turbulence model library. The rhoTurbFoam solver solves the discretized system of momentum-continuity and enthalpy equations reported in (4.2.12) to (4.2.14) using a PISO strategy which details are already given in [39]. The time discretization used is a typical backward Euler scheme (implicit, second order accurate in time)[6]. The gradient terms were discretized using a Gauss linear scheme (second order accurate)[6]. The divergence and Laplacian terms are discretized using a Gauss linear corrected scheme (unbounded second order, conservative) [6], [83]. The Reynolds stress tensor and the turbulent heat flux in (4.2.12) to (4.2.14) are closed using (4.2.20) and (4.2.21) with the turbulent eddy viscosity and thermal diffusivity given from the solution of the AKN transport equations ( $k$ ,  $\epsilon$ ,  $k_\theta$  and  $\epsilon_\theta$ ). The model equations and constant are reported in Section 4.4.3.

In Figure 9.2.1 (a) the velocity profiles are compared with the data from Kasagi et al. [42] showing a very good agreement.

At the wall a temperature gradient is imposed such as that  $T_\tau = 0.198$ . This determines a constant temperature growing in the channel. The temperature profiles non-dimensionalized using the classical wall units ( $\theta^+ = (T_w - T)/T_\tau$  and  $y^+ = (yu_\tau)/\nu$ ) are drawn in Figure 9.2.1 (b) and compared with the data from Kasagi et al. [42].

The agreement with the DNS is also in this case very good. In Figure 9.2.2 the Production and Dissipation terms of the budget equation for  $k_\theta$  and  $\epsilon_\theta$  transport equations are compared with the DNS data. Note that the DNS  $\epsilon_\theta$  production term in Figure 9.2.2 consists of the sum of the mean gradient production terms (see Table 9.2) and the turbulent production term in 9.3. This is compared with the second and third term at the right hand side of 4.4.41. The

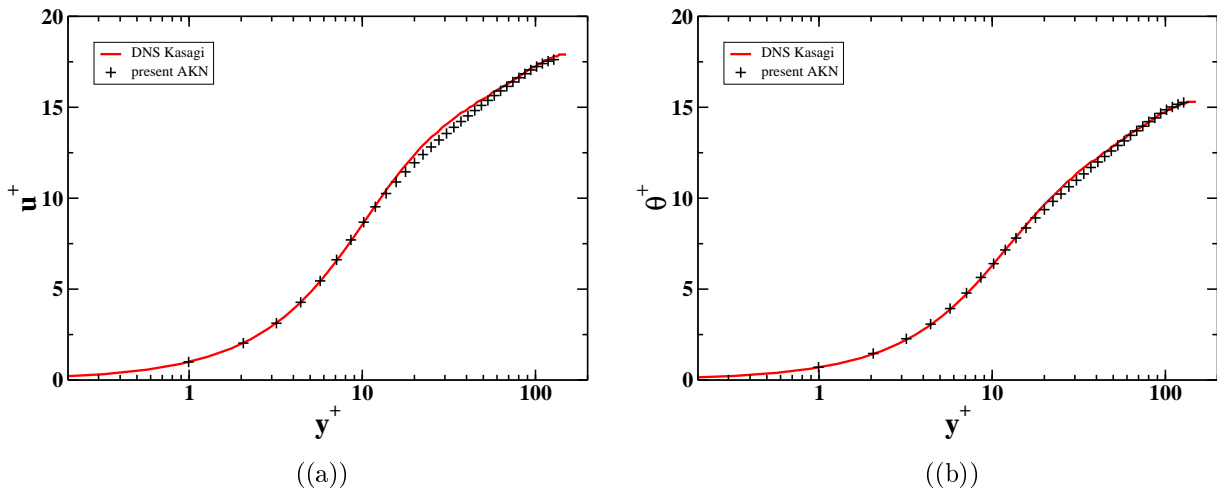


Figure 9.2.1: Velocity (a) and Temperature (b) profiles. Comparisons with DNS data from [42].

DNS dissipation term in 9.3 instead is compared with the sum of the forth and fifth term at the right hand side of equation (4.4.41).

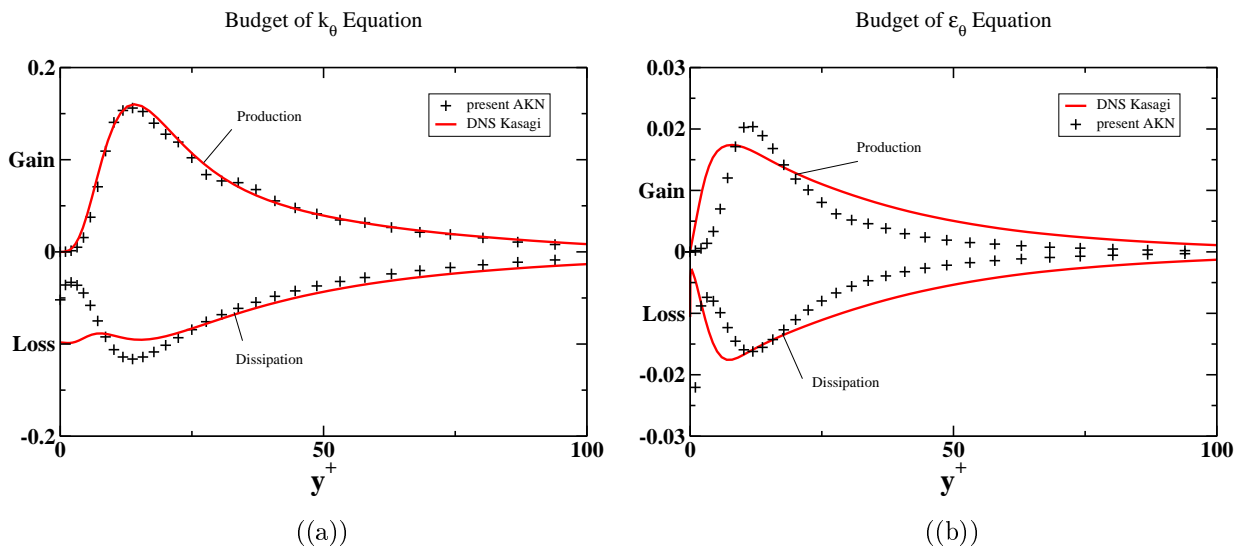


Figure 9.2.2: Budget of  $k_\theta$  (a) and  $\epsilon_\theta$  (b). Comparison with DNS data from [42]

In such a simple configuration, the AKN model seems to reproduce very well not only the velocity and temperature profiles, but also the production and dissipation terms in (4.4.38) and (4.4.39).

In conclusion, the results shown confirm the accuracy of the AKN model to predict boundary layer flows and at the same time represent a validation of the model implementation in OpenFoam.

### 9.2.2 Backward Facing Step

As a more challenging model validation, the backward-facing step experiment from Vogel and Eaton [81] has been computed. The case has been already simulated by Abe et al. in [10]



showing the promising capability of the AKN model to predict separating and reattaching flows. The case not only represents an ultimate validation for the present model implementation, but it is also representative of the turbulent combustor flows. The backward-facing step geometry, indeed, is characterized, close to the wall, by a bi-dimensional recirculation region followed by a reattaching zone which can be viewed as a two-dimensional simplification of the complex three-dimensional corner vortex typical of modern swirled combustor design (see section 2).

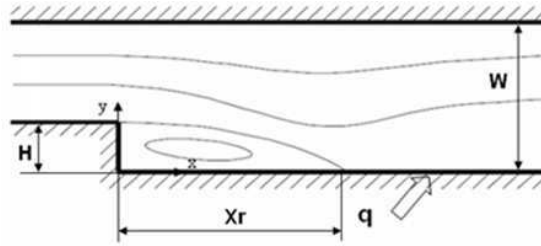


Figure 9.2.3: Experimental setup and coordinate system

The geometry of the two-dimensional sudden expansion channel experiment ([81]) and the coordinate system are depicted in Figure 9.2.3. Air enters the computational domain upstream of the step. Across the bottom wall, downstream of the step, a constant heat flux is prescribed. The top wall can be considered adiabatic and no-slip velocity boundary condition were employed. The geometry parameters based on the step height  $H$  (see Figure 9.2.3) are the following: the length of the domain, downstream of the step, is  $40H$  and upstream  $1.1H$ , the expansion ratio ( $W/(W - H)$ ) is 1.25. The Reynolds number based on the step height was fixed to 28000.

In order to better resolve the zone with stronger velocity and temperature gradients, the computational domain consisted of 44264 cells highly concentrated close to the solid boundaries and in the shear layer zone after the step (see Figure 9.2.4).

The turbulent inlet conditions were prescribed in order to match the experimental values given in [11] at the position  $x/H = -0.8$  upstream the step.

For the URANS simulations the standard rhoTurbFoam solver has been used (see Chapter 9.2.1 for a brief code description). The predicted velocity profiles with three different turbulence models are reported in Fig. 9.2.5 (a). As sketched in Fig. 9.2.3  $X_r$  corresponds to the reattachment length, and the x-axis origin has been set at the lower step edge. The velocity profiles are non-dimensionalized using the bulk inlet velocity  $U_0$  and the step height,  $H$ . The predicted reattachment length slightly differs from the predictions of Abe et al. [9] [10] and the experimental value of  $6.67H$ . The present  $X_r$  results are summarized in Table 9.4 and compared with the numerical results from [9], [10]. Simulations have been performed with three different turbulence models: the  $k-\epsilon$  Launder and Sharma model (LS), the modified  $k-\epsilon$  Nagano and Tagawa model (NTT) and the  $k-\epsilon$   $k_\theta-\epsilon_\theta$  Abe et al. turbulent heat transfer model (AKN). The Launder and Sharma model has been briefly described in Section 4.4.2.1. In Sections 4.4.3 and 9.1 a general discussion on two equation heat transfer closures and the AKN

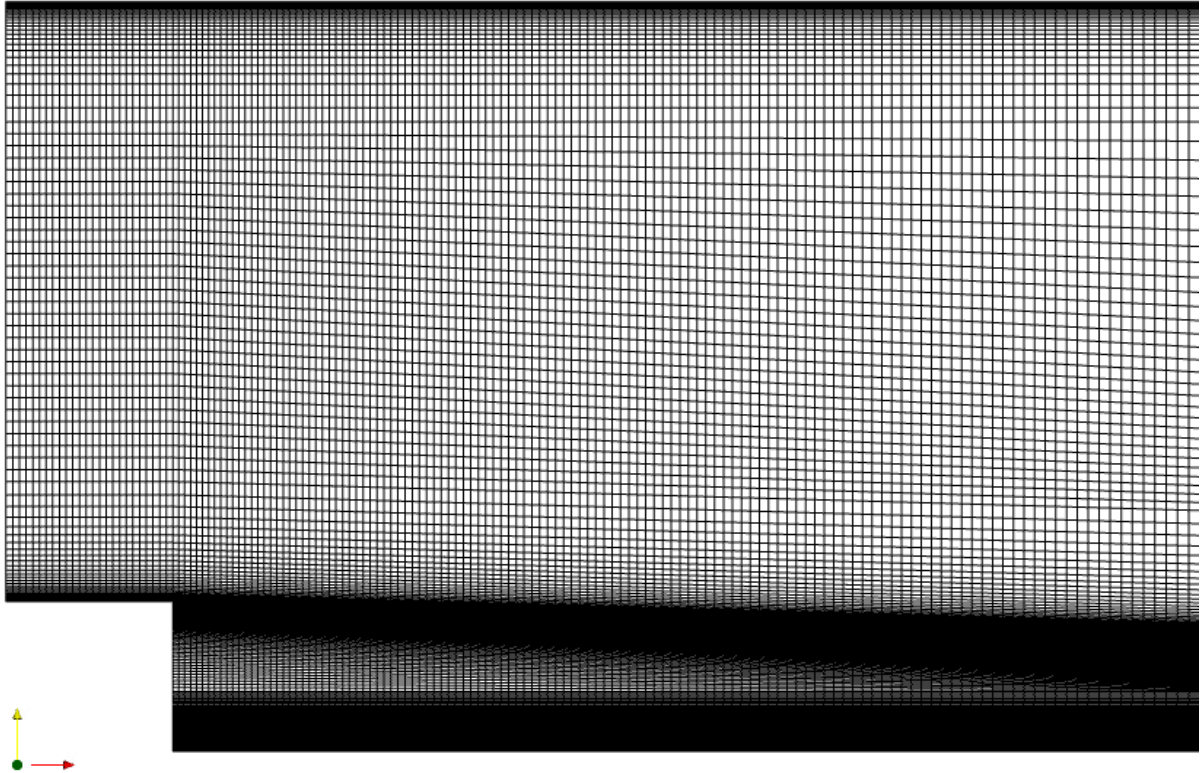


Figure 9.2.4: Computational domain, cut off

model has been given. As discussed in detail, the Launder and Sharma model, as all the two equation low-Reynolds models, rely on the assumption of a constant turbulent Prandtl number. In the present computations the turbulent Prandtl number has been set to 1.0. On the contrary, the AKN model uses two additional transport equation for the variance of temperature fluctuation,  $k_\theta$  and its dissipation rate,  $\epsilon_\theta$  in order to independently define the turbulent heat diffusivity,  $\alpha_t$  and consequently the turbulent Prandtl number. The NTT model instead uses the AKN formulation for the definition of the turbulent viscosity, but no additional equations are used for the turbulent heat diffusivity. Similarly to the Launder and Sharma model, a constant turbulent Prandtl number of 1.0 is assumed. The differences between the NTT and AKN temperature prediction can be than addressed only to the relaxation of the Reynolds analogy hypothesis, showing directly the AKN model improvements respect with the classical two equation turbulence model closures.

As pointed out in [11] the position of the reattachment point is very sensitive to very slight geometrical differences, even under controlled conditions. Adams suggested that the simulations should be focused on predicting the correct physics of the reattachment zone rather than

	NTT	AKN	LS	Exp. Vogel & Eaton
$X_r/H$ (present)	6.1	6.1	5.6	6.67
$X_r/H$ Abe et al.	6.69	6.69	—	6.67

Table 9.4: Flow reattachment length ( $X_r$ ) comparisons.

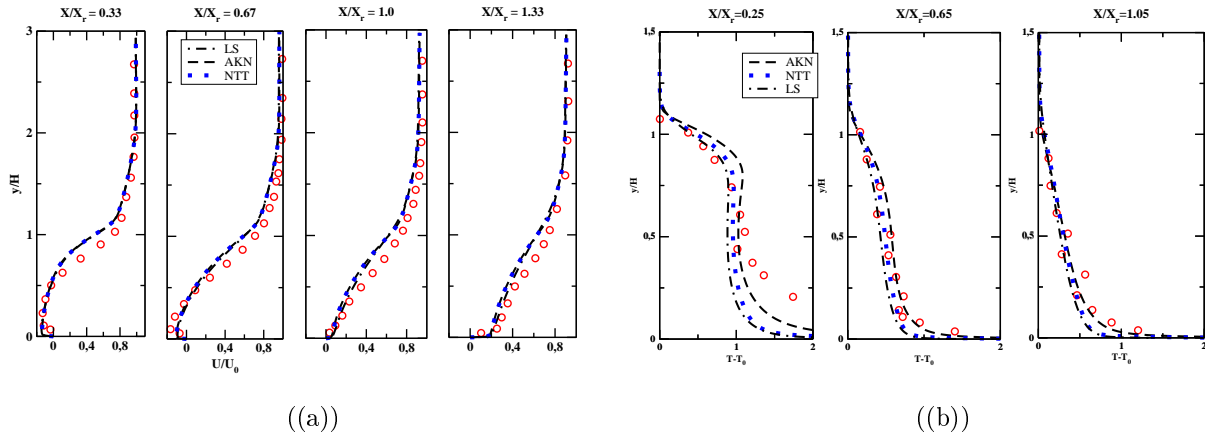


Figure 9.2.5: Velocity (a) and Temperature (b) distributions. Comparison with experimental data from [81] (LS=Lauder and Sharma, AKN= Abe et al., NTT=Nagano and Tagawa

attempting to predict reattachment length within  $\pm 0.2$ . In this sense the insignificant difference between the present AKN model implementation and the results from the paper of Abe et al. can be explained by small deviations in the computational models and in the boundary condition considered. The important improvement in the NTT formulation is the use of the velocity scale  $u_\epsilon$  in the definition of the wall damping function:

$$u_\epsilon = (\nu\epsilon)^{1/4}. \tag{9.2.1}$$

In separating flows  $u_\epsilon$  represents a more reliable scale with respect to  $u_\tau$  which is not defined at the reattachment point. To overcome the limitation of the use of  $u_\tau$  in the definition of the wall damping functions, the LS models alternative is to consider the turbulent Reynolds number,  $R_T$ . Despite the differences between the reattachment length predictions, the LS velocity profiles compare well with the AKN and NTT results and with the experimental values (see Fig. 9.2.5 (a)).

In Fig. 9.2.5 (b) the temperature profiles at different axial positions have been reported. The difference between the models is more pronounced especially in the wall region and in the shear zone immediately after the step ( $y/H \simeq 1$  and  $x/X_r$  close to zero). The biggest differences are in the wall temperature prediction. In Fig. 9.2.6 (b) the wall Stanton number distribution is reported. The Stanton number is defined as below:

$$St = \frac{q_w}{\rho c_p U_0 (T_w - T_0)} \tag{9.2.2}$$

where  $T_w$  and  $T_0$  are the wall and inlet temperatures respectively. Despite the good agreement concerning the overall velocity and temperature profiles, the LS models seems to deliver the worst results concerning the wall quantities. In Fig. 9.2.6 (a) the skin friction coefficient,  $C_f$  is also reported:

$$C_f = \frac{\tau_w}{\frac{1}{2}\rho U_0^2}. \quad (9.2.3)$$

In the regions far from the reattaching point, the NTT and the LS models seem to give a similar Stanton number distribution. In the recovery region and in the region far downstream of the recirculation zone both model seem to perform similarly. The assumption of a constant Prandtl number close to unity, in fact, has been proven accurate only in air flows close to fully developed conditions. Close to the reattaching point, the NTT model performs better than the LS model probably due to the  $u_e$  scaling. However the Stanton number seems to be considerably overpredicted. The AKN Stanton number distribution agrees very well with the experimental values showing a considerable improvement with respect to the NTT model.

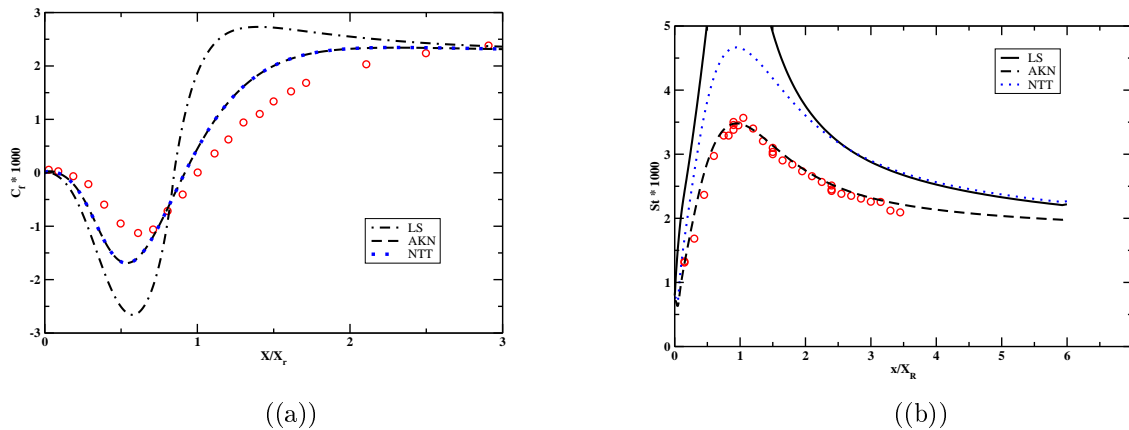


Figure 9.2.6: Skin friction coefficient (a) and Stanton number (b) wall distributions. Comparison with experimental data from [81]

The present AKN model implementation show very similar results as the one presented by Abe et al. in [10] and [9]. The AKN model represents a considerable improvement with respect to the traditional  $k-\epsilon$  low Reynolds number model especially in the separating flow regions where the assumption of a constant Prandtl number is questionable. For this reason the model application to combustor flow seems promising. As already explained, in such application due to the presence of high temperature gradients, a correct wall temperature prediction is very important for the design of the wall cooling system. An open question remains the model capabilities in the presence of flow unsteadiness, which is of particular interests in the case of a thermo-acoustic combustion instabilities. In order to answer this question in the next sections the AKN model will be tested in pulsating flow conditions and comparison are given with the DNS data reported in Chapter 8

### 9.2.3 Steady Channel Flow with Fix Wall Temperature Difference

In order to investigate the effects of flow pulsation on the unsteady turbulent heat transfer, in section 8 DNS data have been collected in the SChF-FWTD and PulsChF-FWTD configuration (see section 8.5 and 8.1). Before considering the more complex pulsating channel case (PulsChF-FWTD configuration), the AKN model has been first tested in the steady channel flow case with constant wall temperature difference (SChF-FWTD) and the numerical results are reported below.

In Section 8.3 the analogies and differences between the Isoflux Boundary Conditions (IFBC) used in the test case of Kasagi [42] and the Fix Wall Temperature Difference (FWTD) configuration used for the DNS calculations have been already discussed. As also confirmed by the experiments of Krishnamoorthy and Antonia [47], the turbulence quantities in the two flow configurations are analogous in the very near wall region ( $y^+ < 50$ ), but considerably differ in the mid channel section. In the FWTD condition the temperature gradient at the channel centerline does not vanish as in the IFBC case. This determines a positive contribution of the turbulent production terms in both the  $k_\theta$  and  $\epsilon_\theta$  budget equations (see Fig. 8.4.3 and 8.4.4).

Despite the good results given by the AKN model in the Kasagi configuration [42] (hereinafter referred as: Steady Channel Flow with Isoflux Boundary Conditions case, SChF-IFBC), the model seems to perform quite poorly in the SChF-FWTD case as will be shown here.

A calculation was performed using a two-dimensional grid with the same resolution of the DNS steady and pulsating flow calculations in 8.3 and 8.5. Same boundary conditions and pressure source term were used.

The model overpredicted the turbulent heat diffusivity of a factor of two in comparison with the DNS data. In Fig. 9.2.7 the turbulent kinetic energy,  $k$  and the turbulent temperature variance  $k_\theta$  and their respective dissipation rates,  $\epsilon$  and  $\epsilon_\theta$  are presented. The model seems to predict quite reasonably the velocity turbulent fluctuations (Fig. 9.2.7 (a) and (b)), but overpredicts considerably the temperature fluctuations (Fig. 9.2.7 (c) and (d))

As it can be seen from a closer look at the  $k_\theta$  and  $\epsilon_\theta$  budgets reported in Fig. 9.2.3, the modelled production and dissipation terms in the AKN transport equations (4.4.41) exhibit a different behavior compared with the DNS results.

Note that for comparison, two different wall scales are used in Fig. 9.2.3 (a) and (b). In Fig. 9.2.3 (b) each term is plotted in function of  $y^*$  whereas in Fig. 9.2.3 (a) the more classical wall units ( $y^+$ ) are used. Similarly to  $y^+$ ,  $y^*$  is defined as follows:

$$y^* = \frac{yu_\epsilon}{\nu}, \quad (9.2.4)$$

In order to take into account near-wall and low-Reynolds-number effects, the use of  $u_\epsilon$  instead of  $u_\tau$  have the advantage of not vanishing neither at flow separation nor in the flow reattaching zone [9]. For this reason most of the near wall damping function in 4.4.41 are expressed using  $y^*$  instead of  $y^+$ .

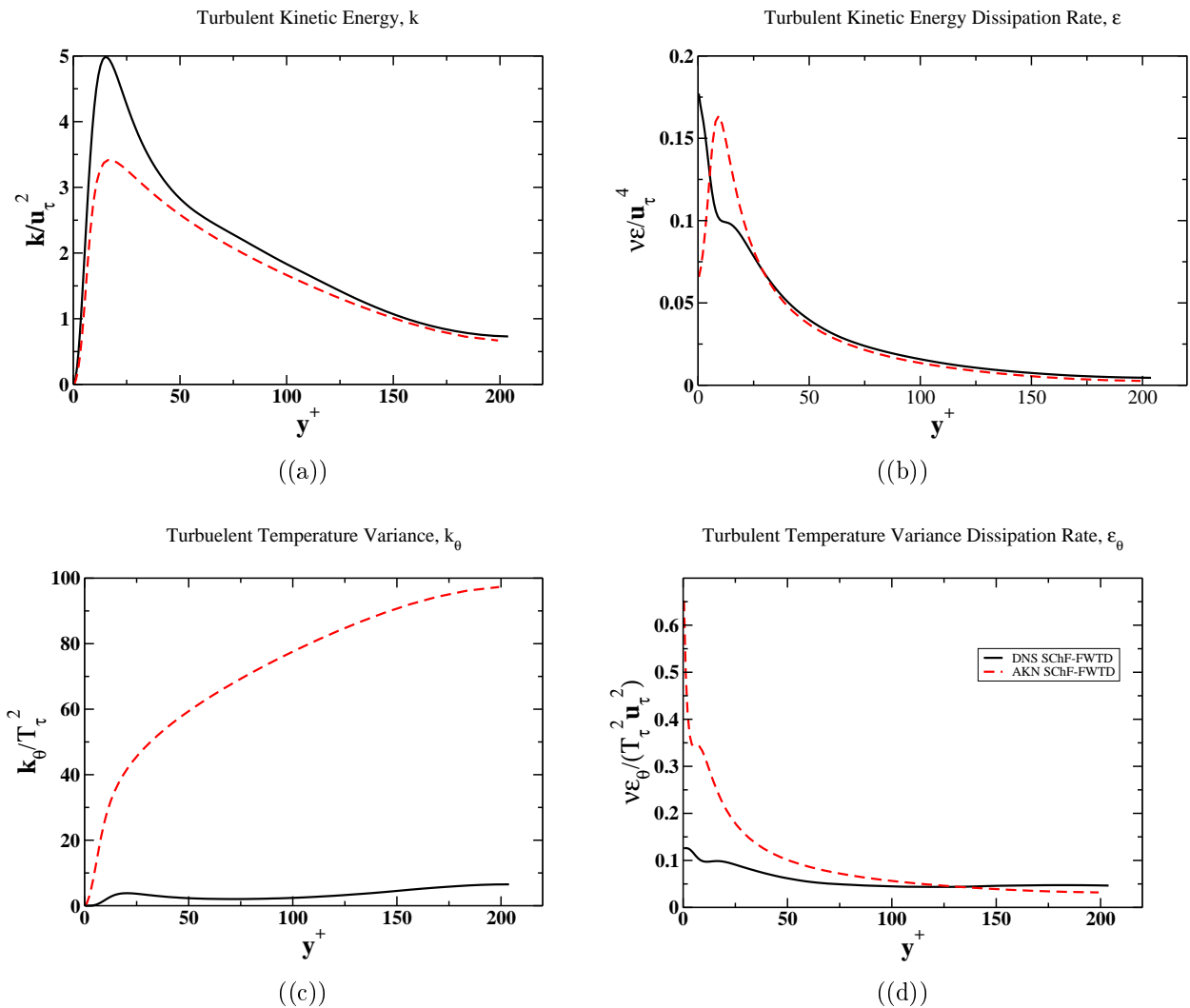


Figure 9.2.7: AKN model, comparison with DNS in the SChF-FWTD configuration, turbulent kinetic energy,  $k$  (a), turbulent kinetic energy dissipation rate,  $\epsilon$  (b), turbulent temperature variance,  $k_\theta$  (c) and turbulent temperature variance dissipation rate,  $\epsilon_\theta$  (d).

Considering the modelled  $\epsilon_\theta$  transport equation in 4.4.41, both production and dissipation terms seem to vanish at the channel centerline as in the SChF-IFBC configuration. However, this is not the case for the turbulent production and dissipation terms in the exact budget equation of  $\epsilon_\theta$  (4.4.39) as computed from the DNS calculation in Section 8.1. Moreover the magnitude of the  $\epsilon_\theta$  dissipation close to the wall is overestimated.

Concerning the  $k_\theta$  budget equation, the AKN modelled terms seem to correctly mimic the DNS near wall behavior with a general magnitude overprediction (9.2.3 (a)). An exception is constituted by the modelled turbulent diffusion term which does not vanish at the channel center line as expected from the DNS data. The result is a negative contribution of the same order of magnitude of the dissipation term which is not counterbalanced by the production.

In Fig. 9.2.9 the channel temperature profiles are compared with the experimental data from [58]. The accuracy of the AKN model temperature prediction here are considerably worse than in the isoflux test case presented in the validation section 9.2.1.

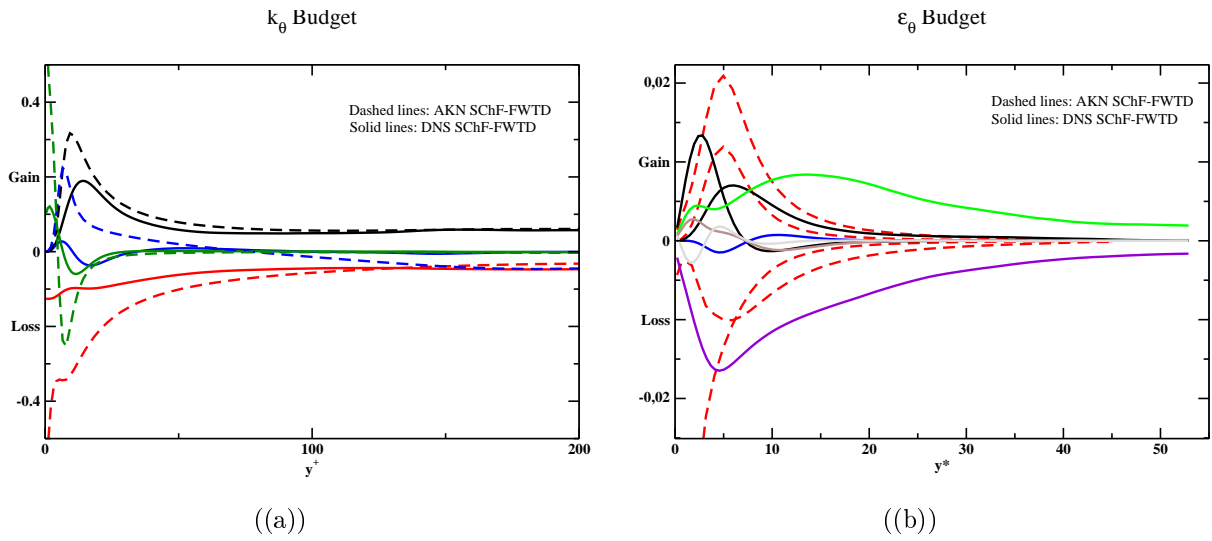


Figure 9.2.8: AKN model, comparison with DNS in the SChF-FWTD configuration, turbulent temperature variance budget,  $k_\theta$  (a), turbulent temperature variance dissipation rate budget,  $\epsilon_\theta$  (b).

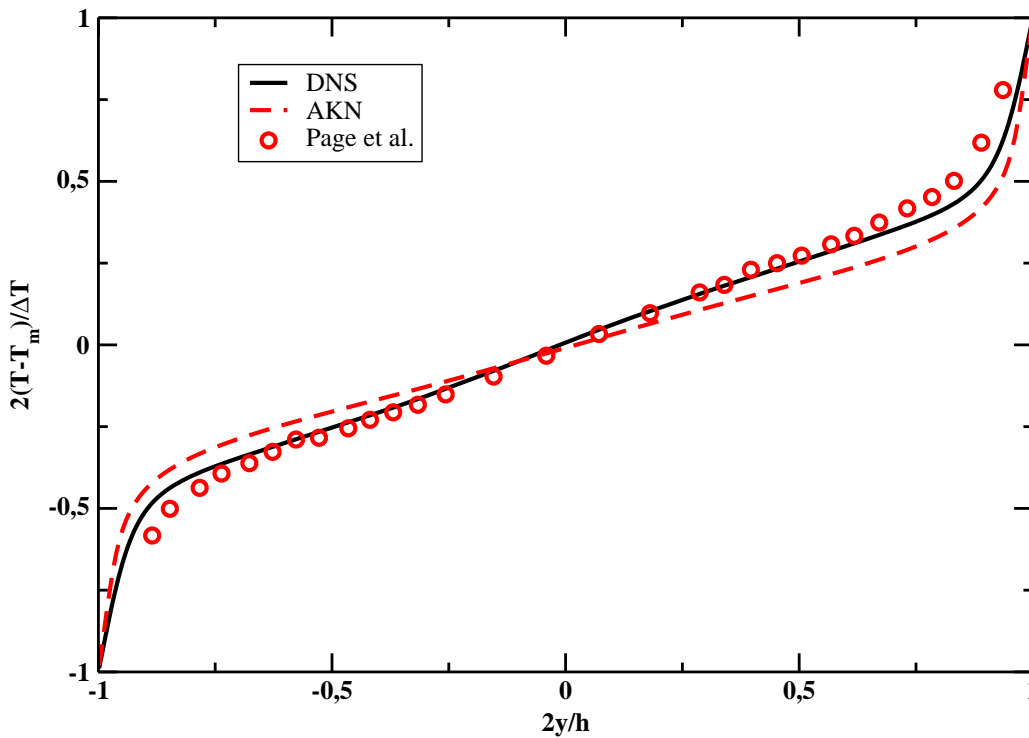


Figure 9.2.9: Temperature profiles, comparison between URANS, DNS and experimental data from [58]

### 9.3 Model Modification

In the present chapter a modification of the AKN turbulent closure is presented in order to overcome the model limitations discussed in the previous sections.

As already introduced (9.1), due to the different turbulent scales involved, the modeling of the  $\epsilon_\theta$  transport equation represents a real challenge for the two-equation turbulence heat transfer closures. The main requirements for the  $\epsilon_\theta$  transport equation outlined by [48] plus the Lumley and Khajeh-Nouri [48] hypothesis suggests a general equation form as in (9.1.20) and reported below for clarity:

$$\begin{aligned} \frac{\partial \epsilon_\theta}{\partial t} + \bar{u}_j \frac{\partial \epsilon_\theta}{\partial x_j} &= \frac{\partial}{\partial x_j} \left\{ \left( \alpha + \frac{\alpha_t}{\sigma_{\epsilon_\theta}} \right) \frac{\partial \epsilon_\theta}{\partial x_j} \right\} \\ &+ C_{P1} \frac{\epsilon_\theta}{k_\theta} \mathcal{P}_\theta + C_{P2} \frac{\epsilon_\theta}{k} \mathcal{P}_k + C_{P3} \frac{\epsilon}{k} \mathcal{P}_\theta \\ &- C_{D1} \frac{\epsilon_\theta^2}{k_\theta} - C_{D2} \frac{\epsilon \epsilon_\theta}{k}. \end{aligned} \quad (9.3.1)$$

Here we indicate with  $\mathcal{P}_\theta$  and  $\mathcal{P}_k$  the production term of the  $k_\theta$  and  $k$  transport equations in (9.1.17) and (4.4.8) respectively. Three production and two dissipation terms are present on the right hand side of (9.3.1). The first production term, hereinafter referred to  $P1$ , considers the contribution of the  $k_\theta$  production ( $\mathcal{P}_\theta$ ) scaled using the temperature time scale,  $\tau_\theta$ . Similarly to this term, the fourth term at the right hand side of (9.3.1) ( $P3$  term) considers the turbulent time scale  $\tau_t$  instead of  $\tau_\theta$ . The last production term,  $P2$ , considers instead a mixed contribution of the turbulent kinetic energy production,  $\mathcal{P}_k$  and an hybrid time scale obtained by the ratio of  $k$  and  $\epsilon_\theta$ .

As can be noticed comparing the general formulation in 9.3.1 and the AKN model in (4.4.41), Abe et al. considered the contribution of just the  $P1$  and  $P2$  terms. This choice, as also reported by [75], seems to give better results in wall-bounded flow applications, while for free turbulence cases the use of  $P3$  instead of  $P1$  seems to yield a better agreement with the turbulence characteristics. However, In a jet in cross flow application, Ivanova et al. [40] have shown that limiting the contribution of  $P2$ , a considerable improvement in the temperature profile prediction can be achieved without the need of introducing a  $P3$  term.

In the pulsating channel case (SChF-FWTD configuration), as it is clearly shown in Fig. 9.2.3 (b), both  $P1$  and  $P2$  term vanish in the central zone of the channel which does not resemble at all the behavior of the  $\epsilon_\theta$  turbulent production and dissipation terms obtained from the DNS simulations.

In the following, a term analogous to  $P3$  is proposed in order to improve the numerical prediction in both the far field and the near wall region:

$$P_D = C_{PD} f_D k \left| \frac{\partial T}{\partial x_j} \right|^2 \quad (9.3.2)$$

The complete model, hereinafter referred as AKN<sub>D</sub>, is reported below:



$C_\lambda$	$C_{D1}$	$C_{D2}$	$C_{P1}$	$C_{P2}$	$A_{D1}$	$A_{D2}$	$A_D$	$\sigma_h$	$\sigma_{\epsilon_\theta}$	$C_{PD}$
0.1	2.5	0.9	1.95	0.55	1.0	5.8	12.0	1.6	1.6	0.11

Table 9.5: Constants for the AKN model modification (AKN<sub>D</sub>),  $k_\theta$  and  $\epsilon_\theta$  equations.

$f_{D2}$	$f_{P1} = f_{D1}$	$f_{P2}$
$-\frac{0.3C_\epsilon 2e^{-(Rt/6.5)^2}}{C_{D2}} \left\{ 1 - e^{-\frac{(\nu\epsilon)^{1/4}y}{A_{D2}\nu}} \right\}^2$	$\left\{ 1 - e^{-\frac{(\nu\epsilon)^{1/4}y}{\nu}} \right\}^2$	1.0
$f_d$	$f_D$	$R$
$e^{-(Rt/200)^2}$	$\left\{ 1 - e^{-\frac{(\nu\epsilon)^{1/4}y}{A_D\nu}} \right\}^4$	$\frac{k_\theta\epsilon}{\epsilon_\theta k}$

Table 9.6: functions for the AKN model modification (AKN<sub>D</sub>),  $k_\theta$  and  $\epsilon_\theta$  equations.

$$\begin{aligned}
\frac{\partial k_\theta}{\partial t} + \bar{u}_j \frac{\partial k_\theta}{\partial x_j} &= \frac{\partial}{\partial x_j} \left\{ \left( \alpha + \frac{\alpha_t}{\sigma_h} \right) \frac{\partial k_\theta}{\partial x_j} \right\} \alpha_t \frac{\partial \bar{T}}{\partial x_j} \frac{\partial \bar{T}}{\partial x_j} - \epsilon_\theta \\
\frac{\partial \epsilon_\theta}{\partial t} + \bar{u}_j \frac{\partial \epsilon_\theta}{\partial x_j} &= \frac{\partial}{\partial x_j} \left\{ \left( \alpha + \frac{\alpha_t}{\sigma_{\epsilon_\theta}} \right) \frac{\partial \epsilon_\theta}{\partial x_j} \right\} + \\
&C_{P1} f_{P1} \frac{\epsilon_\theta}{k_\theta} \alpha_t \frac{\partial \bar{T}}{\partial x_j} \frac{\partial \bar{T}}{\partial x_j} + C_{P2} f_{P2} \frac{\epsilon_\theta}{k_\theta} \nu_t \left( \frac{\partial \bar{u}_j}{\partial x_i} + \frac{\partial \bar{u}_i}{\partial x_j} \right) \frac{\partial \bar{u}_i}{\partial x_j} \\
&+ C_{PD} f_D k \left| \frac{\partial \bar{T}}{\partial x_j} \right|^2 \\
&- C_{D1} f_{D1} \frac{\epsilon_\theta^2}{k_\theta} - C_{D2} f_{D2} \frac{\epsilon \epsilon_\theta}{k}
\end{aligned} \tag{9.3.3}$$

where  $\alpha_t$  is defined below

$$\alpha_t = C_\lambda \left[ \frac{k^2}{\epsilon} \sqrt{2R} + 3\sqrt{k} \left( \frac{\nu^3}{\epsilon} \right)^{1/4} \frac{\sqrt{2R}}{Pr} f_d \right] \left[ 1 - e^{-\frac{(\nu\epsilon)^{1/4}y}{14\nu}} \right] \left[ 1 - e^{-\frac{Pr^{1/2}(\nu\epsilon)^{1/4}}{14\nu}} \right] \tag{9.3.4}$$

and the model constants and functions are summarized in Table 9.5 and 9.6

In Fig. 9.3,  $k, \epsilon, k_\theta$  and  $\epsilon_\theta$  profiles are compared with the DNS results in the SChF-FWTD configuration. The numerical predictions are considerably improved in comparison with the original AKN model results reported in Fig.9.2.7.

This is closely related to the effect of the  $P3$  term on the  $\epsilon_\theta$  Budget reported in Fig. 9.3. The agreement with the DNS  $\epsilon_\theta$  budget is remarkably improved with a consequent positive effect on the temperature numerical prediction (see Fig. 9.3.3)

As it can be noticed comparing Table 9.6 and 4.6, the constant set in the AKN<sub>D</sub> model little differs from the one used by Abe et al. Moreover the damping function  $f_D$  has been chosen in order to limit the effect of the  $P_D$  term close to the wall. This was intentionally made in order

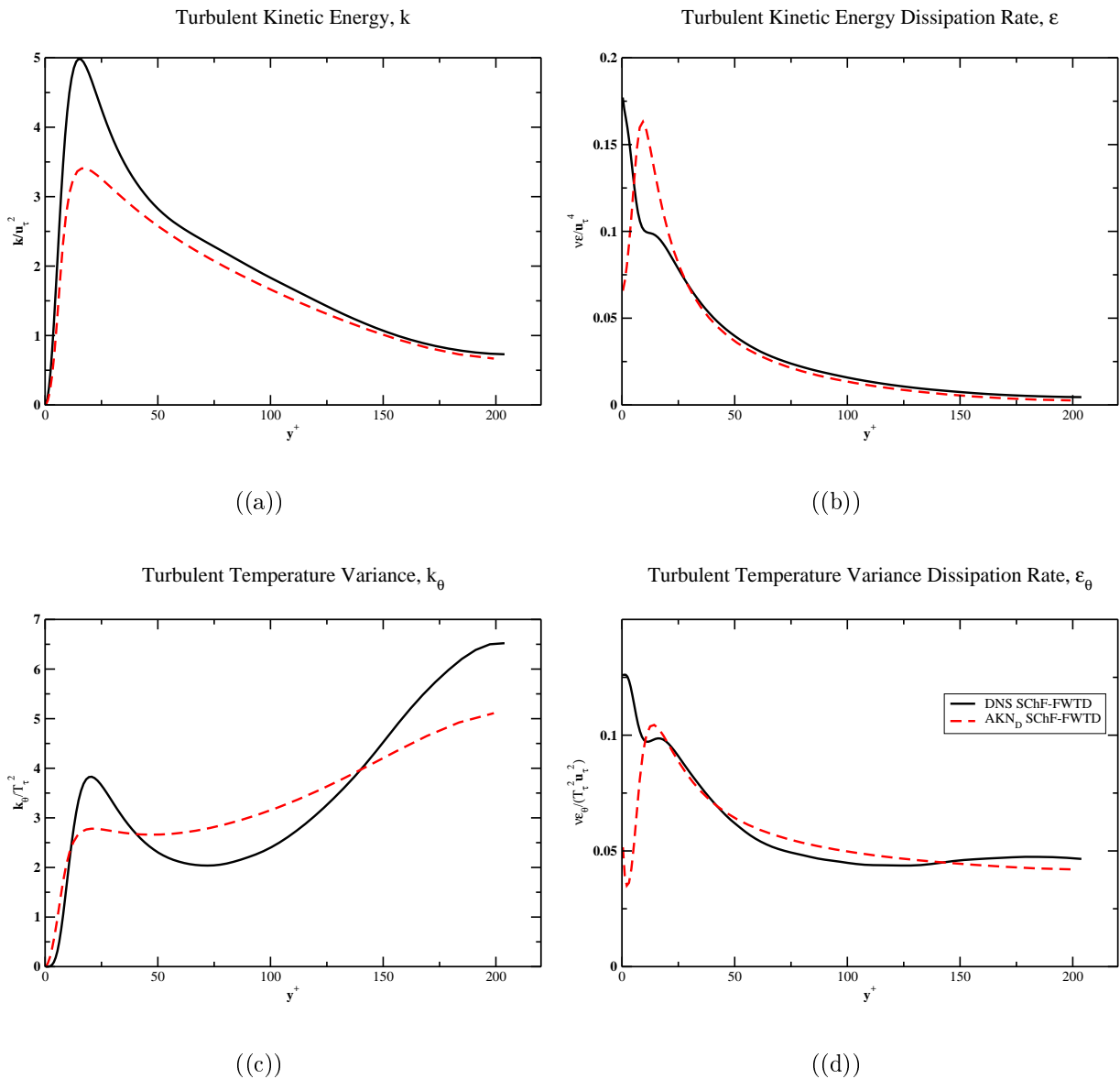


Figure 9.3.1: AKN<sub>D</sub> model, comparison with DNS in the SChF-FWTD configuration, turbulent kinetic energy,  $k$  (a), turbulent kinetic energy dissipation rate,  $\epsilon$  (b), turbulent temperature variance,  $k_\theta$  (c) and turbulent temperature variance dissipation rate,  $\epsilon_\theta$  (d).

to affect just the freestream flow and preserving the original AKN modeling close to the solid boundaries. The original AKN model in fact, as already emphasized in the previous section, has shown very good results in the near wall region of separating and reattaching flows and this feature is believed to be of great importance also for pulsating flows and more in general for combustor flow applications.

Before considering the performances of the model correction in the backward facing step case, the Kasagi et al. test case has been simulated in order to address the effect of the  $P_D$  term in the isoflux channel configuration. In Fig. 9.3.4 the modelled  $k_\theta$  and  $\epsilon_\theta$  budget is compared with the DNS data from [42].

As expected, the results are very close to the ones obtained with the AKN original formulation. An unexpected result instead arises considering the mean temperature profile in Fig.

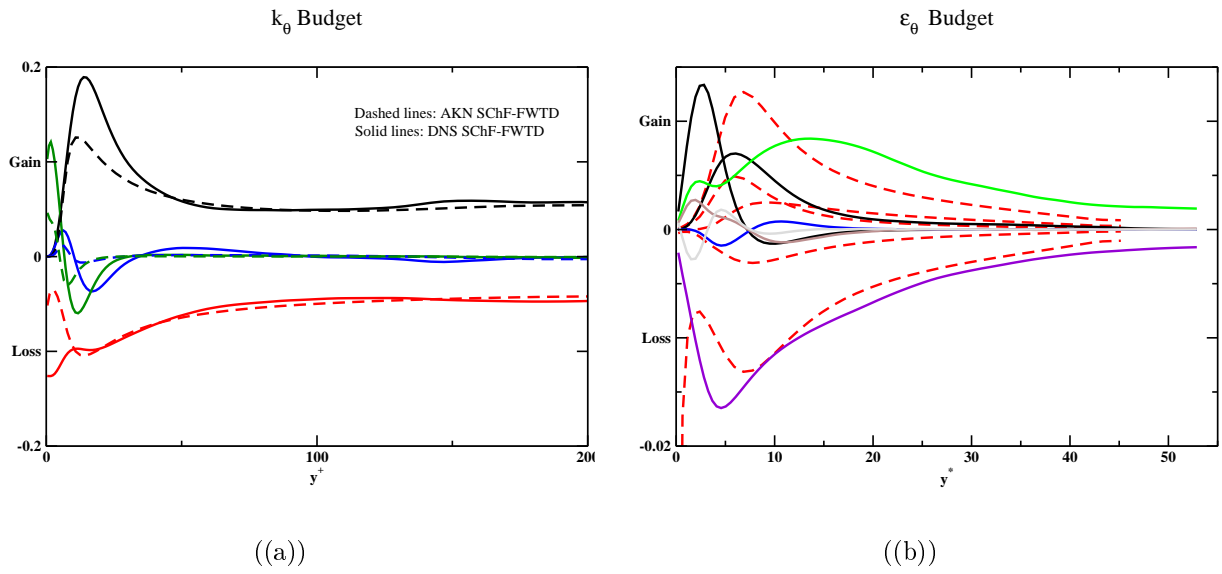


Figure 9.3.2:  $AKN_D$  model, comparison with DNS in the SChF-FWTD configuration, turbulent temperature variance budget,  $k_\theta$  (a), turbulent temperature variance dissipation rate budget,  $\epsilon_\theta$  (b).

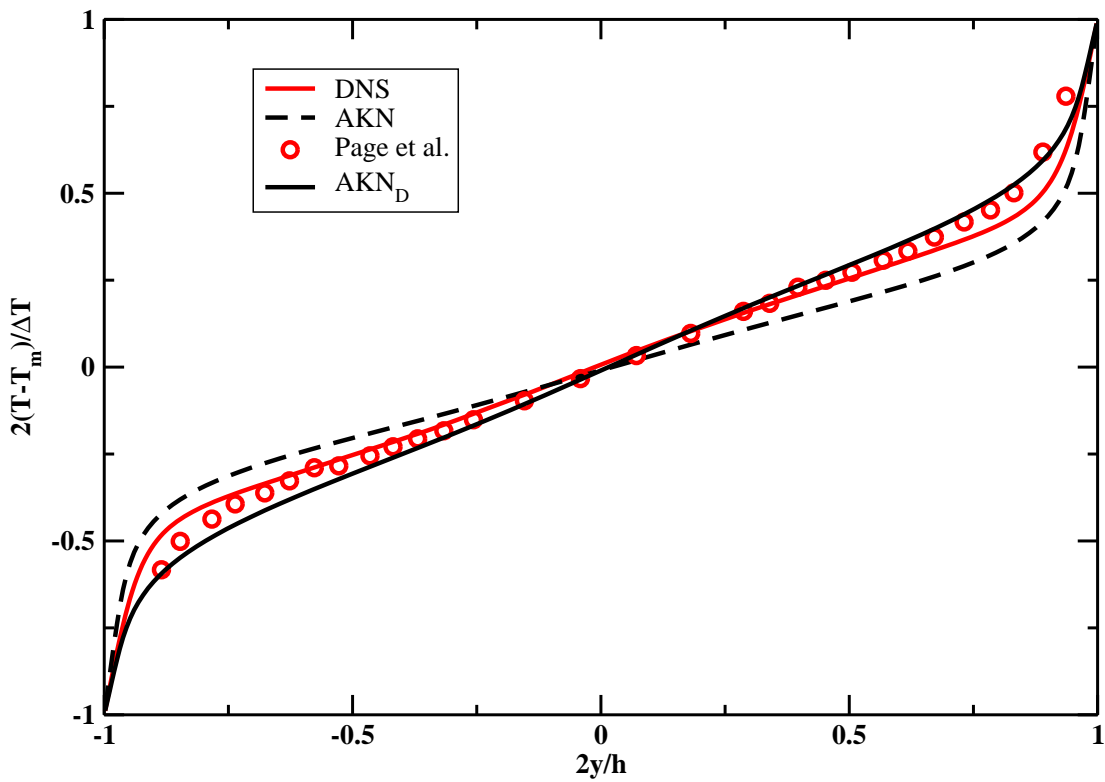


Figure 9.3.3: Temperature profiles, comparison between URANS, DNS and experimental data from [58]

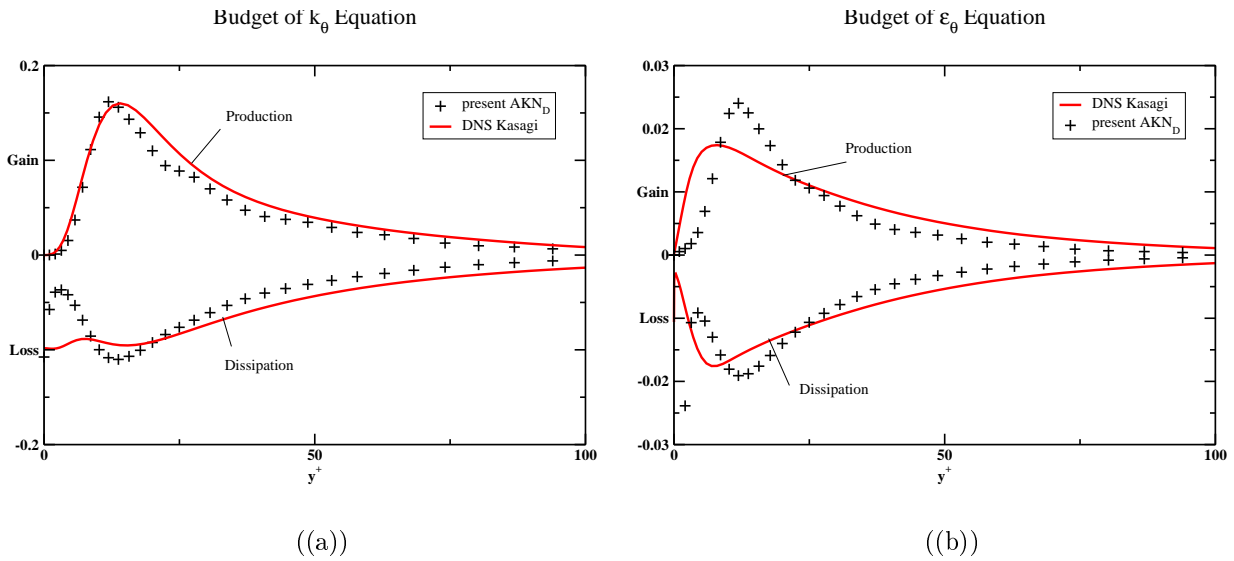


Figure 9.3.4: Budget of  $k_\theta$  (a) and  $\epsilon_\theta$  (b). AKN<sub>D</sub> model, comparison with DNS data from [42]

9.3.5. The AKN model modification seems to predict a logarithmic thermal wall law with same  $\kappa_\theta$  as in [42] but with a slightly different value of  $A_\theta$ . However as in Kasagi et al. [42]  $A_\theta$  seems to be higher as the commonly accepted values obtained using (4.3.8) which confirms a positive trend.

Finally in Fig. 9.3.6 and 9.3.7 the Stanton number predictions and the temperature profiles in the backward facing step case from Vogel and Eaton [81] are presented. The AKN<sub>D</sub> model results are very close to the original AKN formulation and the experimental data showing a consistent improvement in comparison with the NTT model.

In conclusion, a modification of the AKN model is proposed which do not rely on the assumption of a constant turbulent Prandtl number and seems to be able to overcome the original model limitations in the simulation of the SChF-FWTD configuration. Moreover, the new proposed model gives satisfactory results in the SChF-IFBC case and, more importantly, in separating and reattaching flow configurations which are highly interesting for combustor flow applications.

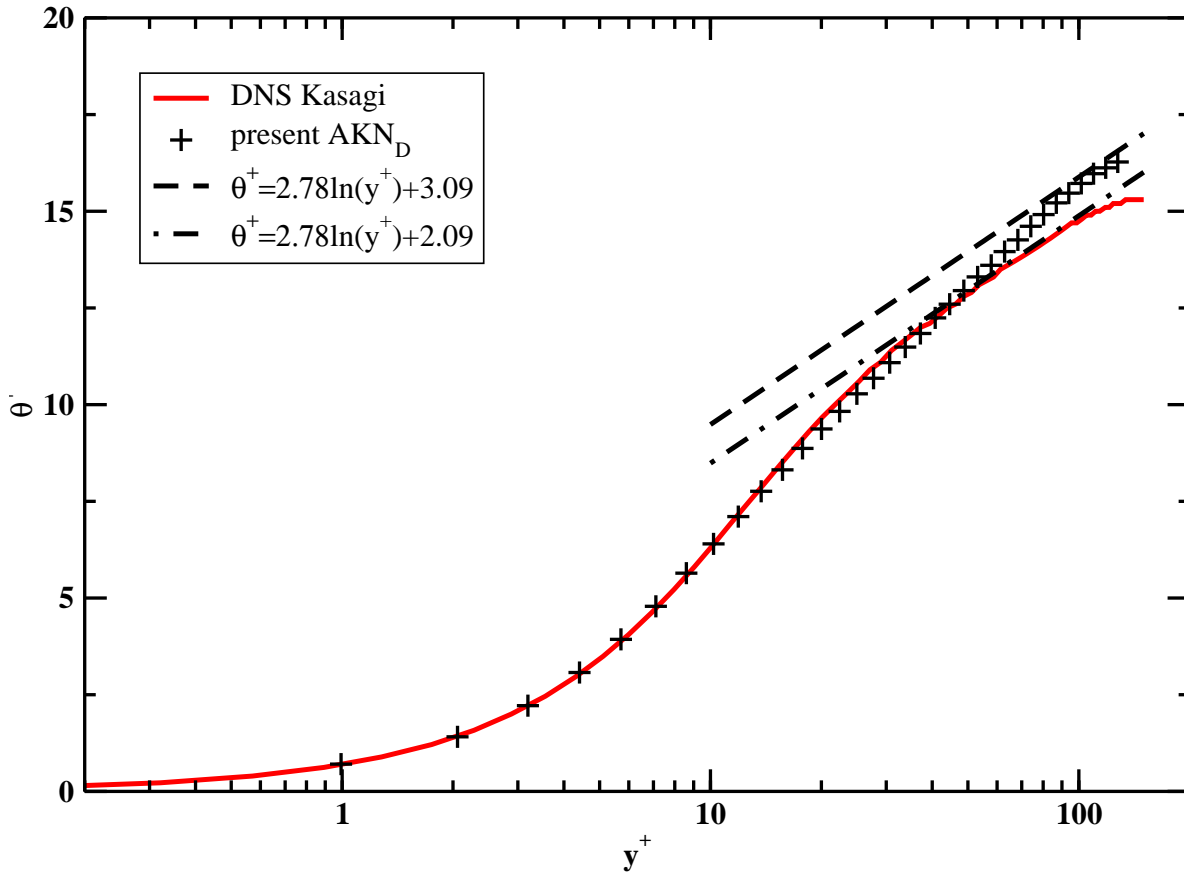


Figure 9.3.5:  $AKN_D$  model. Comparisons with DNS data from [42].

## 9.4 Pulsating Channel Flow

In the present section the pulsating, non-isothermal channel flow (PulsChF-FWTD case) is simulated using the AKN model and the proposed ( $AKN_D$ ) modification. Comparisons are given with the DNS results presented in 8.5. The grid and boundary conditions are the same as in the steady channel computation ( see Section 9.2.3). The oscillating pressure source term was set as for the pulsating flow DNS computations.

The Nusselt number predictions in phase are reported in Fig. 9.4.1 at different frequencies ( $l_s^+ = 7; l_s^+ = 14$  and  $l_s^+ = 35$ ) keeping the same amplitude parameter ( $a_{uc} = 0.7$ ) constant. The DNS results are reported for comparison. In Fig. 9.4.1 (a) the AKN model results are presented. A considerable overestimation of the Nusselt number compared with the DNS results is evident. On the other side, the Nusselt Number phase shift depending on the pulsating frequency is underestimated. The DNS results show an almost opposition of phase between the lower and higher pulsation frequency. Both the URANS computations instead predict a maximum phase difference of about  $\pi/4$ . The results obtained with the proposed  $AKN_D$  modification are reported in Fig. 9.4.1 (b). The agreement with the DNS data is quite good

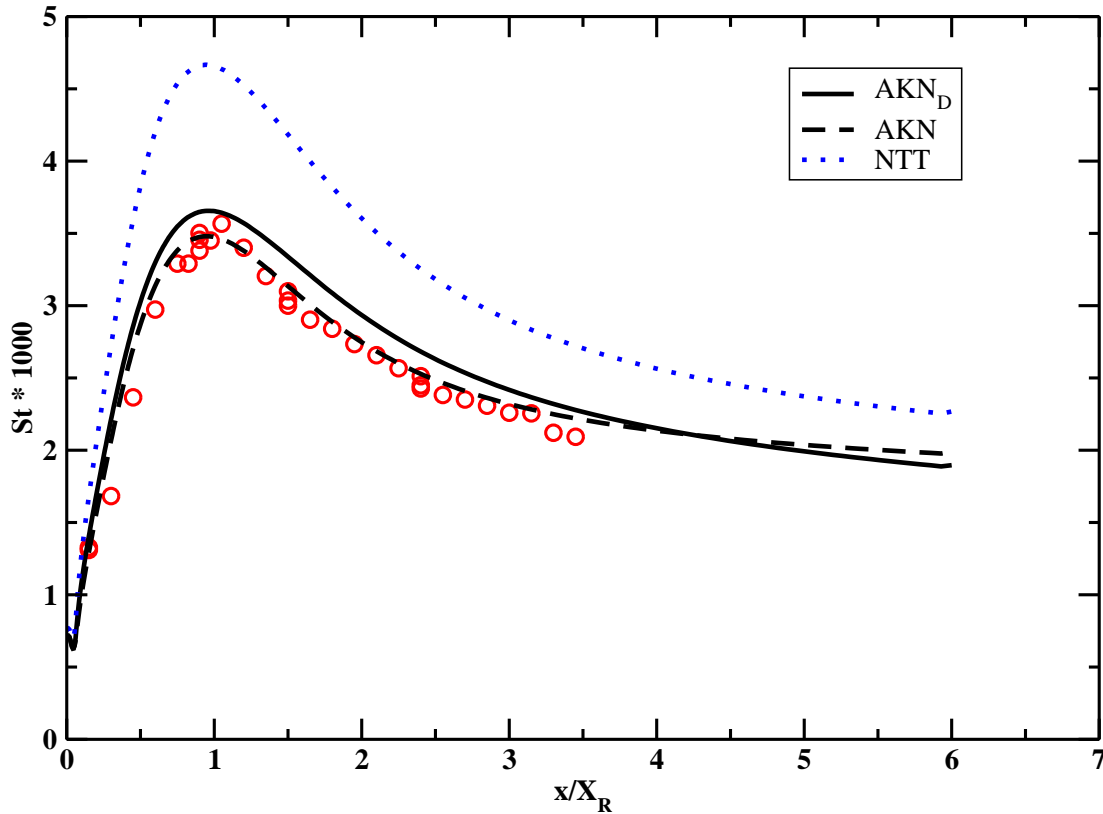


Figure 9.3.6:  $AKN_D$  model. Backward facing step case, Stanton number, comparisons with experimental data from [81].

for conditions close to the quasi-steady regime conditions ( $l_s^+ = 35$ ). The Nusselt number pulsation amplitude in all the three frequency cases considered is comparable with the DNS predictions. An increasing underestimation of the mean Nusselt number can be noticed passing from  $l_s^+ = 35$  to  $l_s^+ = 14$  and 7.

Thus it can be concluded that the proposed model modification is not only able to give accurate results in steady flow conditions but seems to predict quite accurately the magnitude and mean values of the wall heat transfer in pulsating flow conditions as well. Discrepancies have been found concerning the Nusselt number wall phase shift. It seems that despite the fact that the assumption of a constant turbulent Prandtl number was released, the proposed two equation turbulent heat transfer closures cannot predict correctly the turbulence time relaxation phenomena especially not in the intermediate and quasi-laminar regime. In Fig. from 9.4.2 to 9.4.7 the modelled budget terms in the transport equations for  $k_\theta$  and  $\epsilon_\theta$  are compared with the DNS data. In all the frequency regimes investigated, the  $AKN_D$  model seems to have a tendency of overpredicting the  $k_\theta$  production and dissipation terms in the deceleration phase (Figures (a) to (d)) and underpredicting them in the acceleration phase (Figures (e) to (h)). For  $l_s^+ = 7$  in Figure 9.4.3 the model is not able to predict the 'frozen' state of  $k_\theta$  production in the deceleration phase described in Section 8.5.1. As in the case of

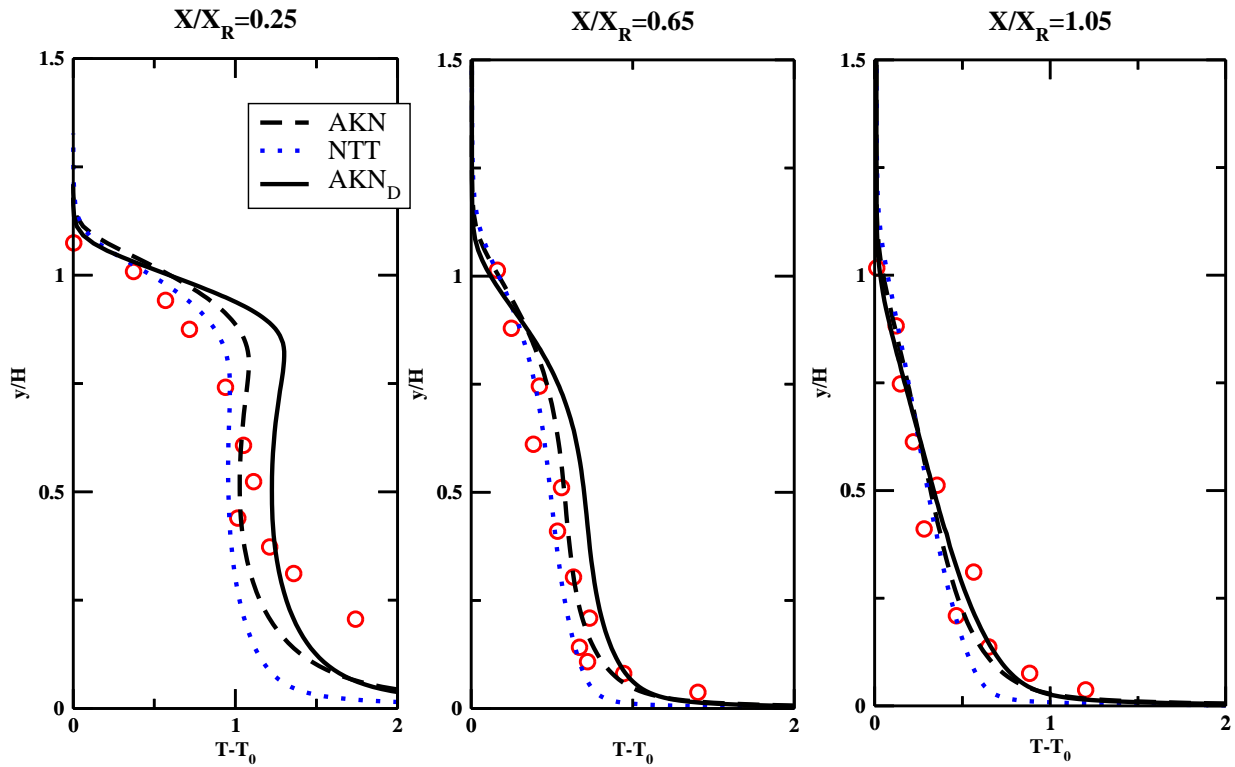


Figure 9.3.7:  $AKN_D$  model. Backward facing step case, temperature profiles comparison.

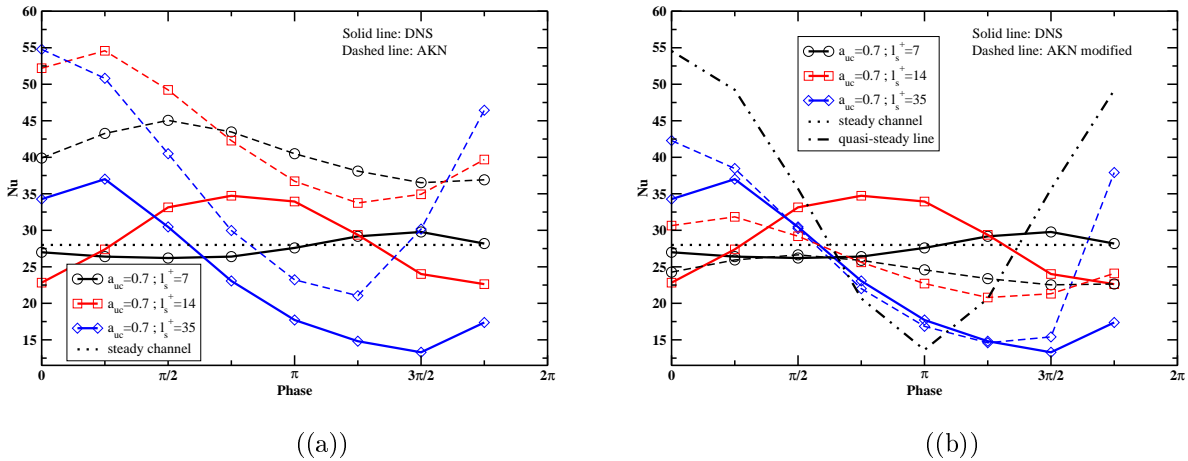


Figure 9.4.1: Nusselt number predictions. Comparison with DNS results from Section 8.5. AKN model (a) and proposed  $AKN_D$  modification (b).

$l_s^+ = 14$  and  $l_s^+ = 35$ , it predicts the maximum value of turbulent production at phase  $\pi/4$  which is correct just for lower values of pulsation frequency. In the acceleration phase instead (Figures 9.4.3 (e) to (h)) the production and dissipation terms appear to be little affected from the velocity changes. This opposite behavior between URANS and DNS is also confirmed by the opposition of phase of the Nusselt number results in Figure 9.4.1. At  $l_s^+ = 14$  the highest discrepancy between DNS results and the  $AKN_D$  model results are at phase  $\pi$  and  $5\pi/4$  where

the peak of turbulent production at  $y^+ \simeq 20$  is completely smoothed out by the URANS predictions. At  $l_s^+ = 35$  the model seems to perform quite well. The consistent reduction of  $k_\theta$  production and dissipation at phases from  $\pi$  to  $3\pi/2$  is correctly predicted. This means that the model can take into account also the relaminarization effect already discussed in Section 8.5.1. However the onset of turbulence and the relative increasing in  $k_\theta$  production at phase  $7\pi/4$  is considerably overpredicted thus explaining also the discrepancy in the Nusselt number prediction at that phase in Figure 9.4.1. The important model limitations are clear from the analysis of the  $\epsilon_\theta$  budget graphs (Figures 9.4.2, 9.4.4 and 9.4.6). The model overpredicts the peaks of mean temperature and mean velocity gradient productions in the deceleration phase and it is often not able to predict the sharp peak of mean gradient velocity productions close to the wall ( $y^+ < 10$ ). The present results show that a better modeling of the  $\epsilon_\theta$  equation is fundamental for improving the turbulent heat transfer closure performance in steady and unsteady flow conditions. However, as already stressed, due to the different scales involved in equation (4.4.39) this task remains quite challenging especially in the case of unsteady flows.



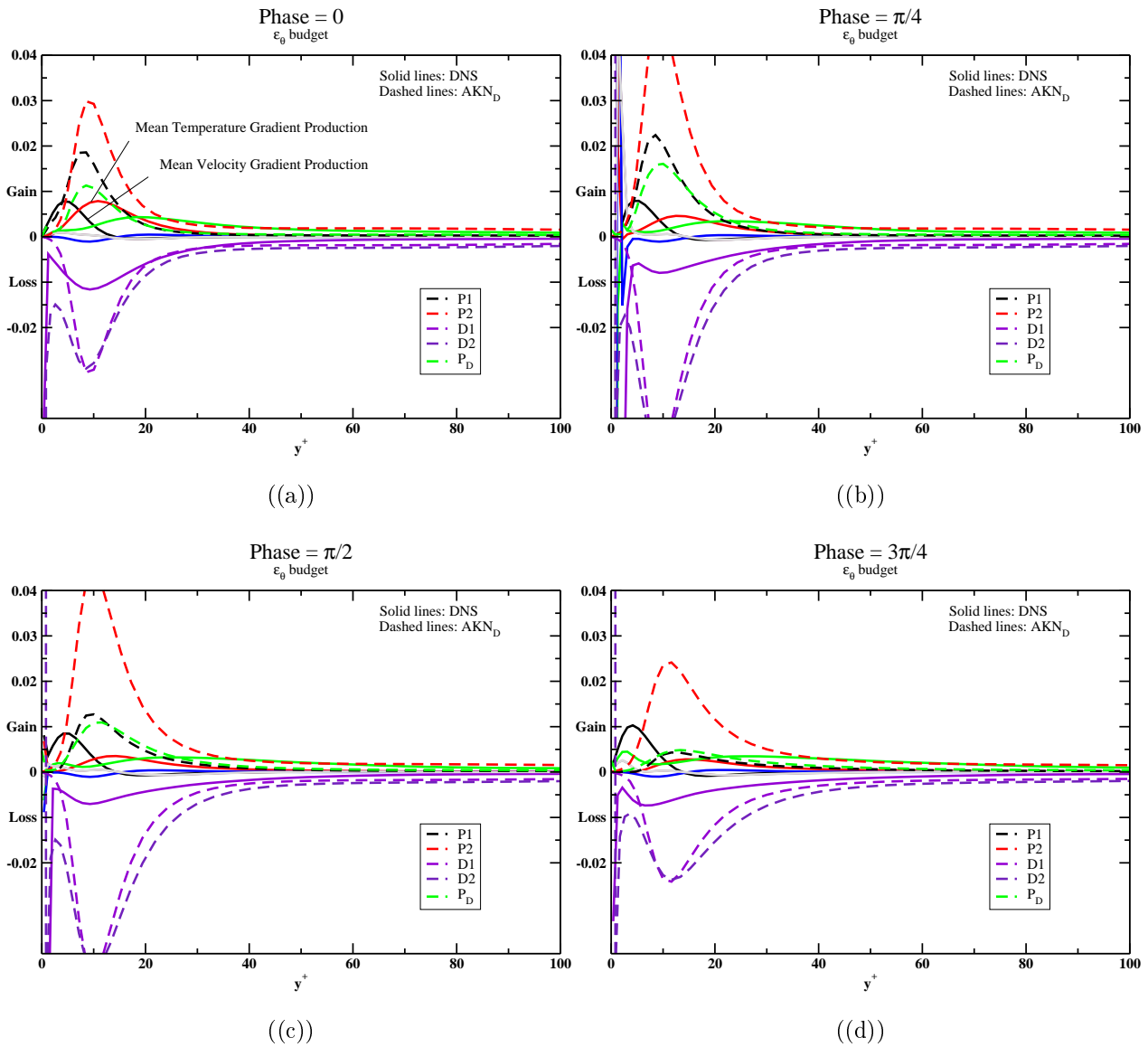


Figure 9.4.2: Budget of  $\epsilon_\theta$ ,  $AKN_D$  model results with pulsating flow ( $a_{uc} = 0.7, l_s^+ = 7$ ). Comparison with DNS on coarse grid.

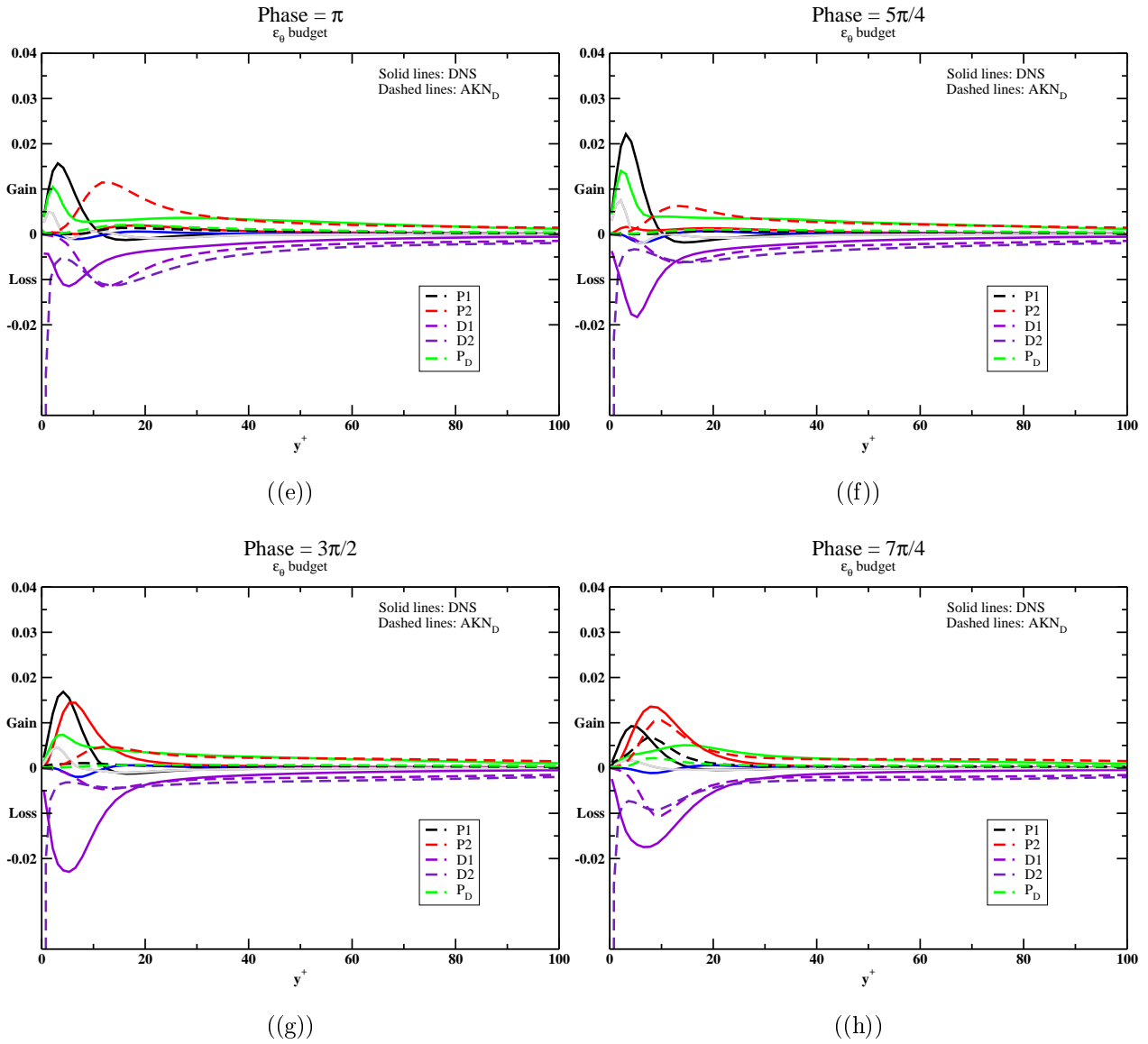


Figure 9.4.2: Budget of  $\epsilon_\theta$ , AKN<sub>D</sub> model results with pulsating flow ( $a_{uc} = 0.7, l_s^+ = 7$ ). Comparison with DNS on coarse grid (continue).

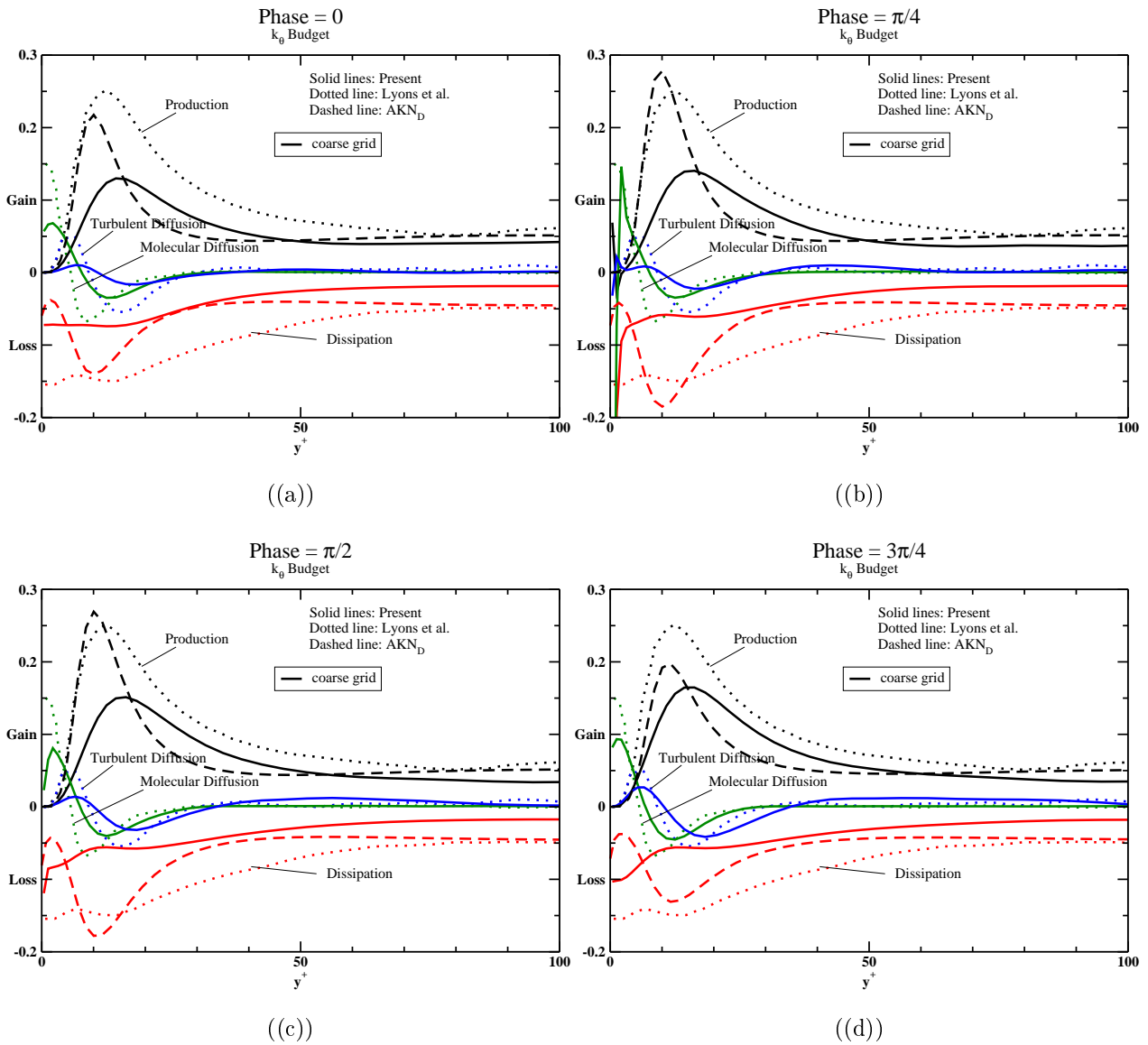


Figure 9.4.3: Budget of  $k_\theta$ ,  $AKN_D$  model results with pulsating flow ( $a_{uc} = 0.7, l_s^+ = 7$ ). Comparison with DNS on coarse grid and steady channel flow DNS data from [52]

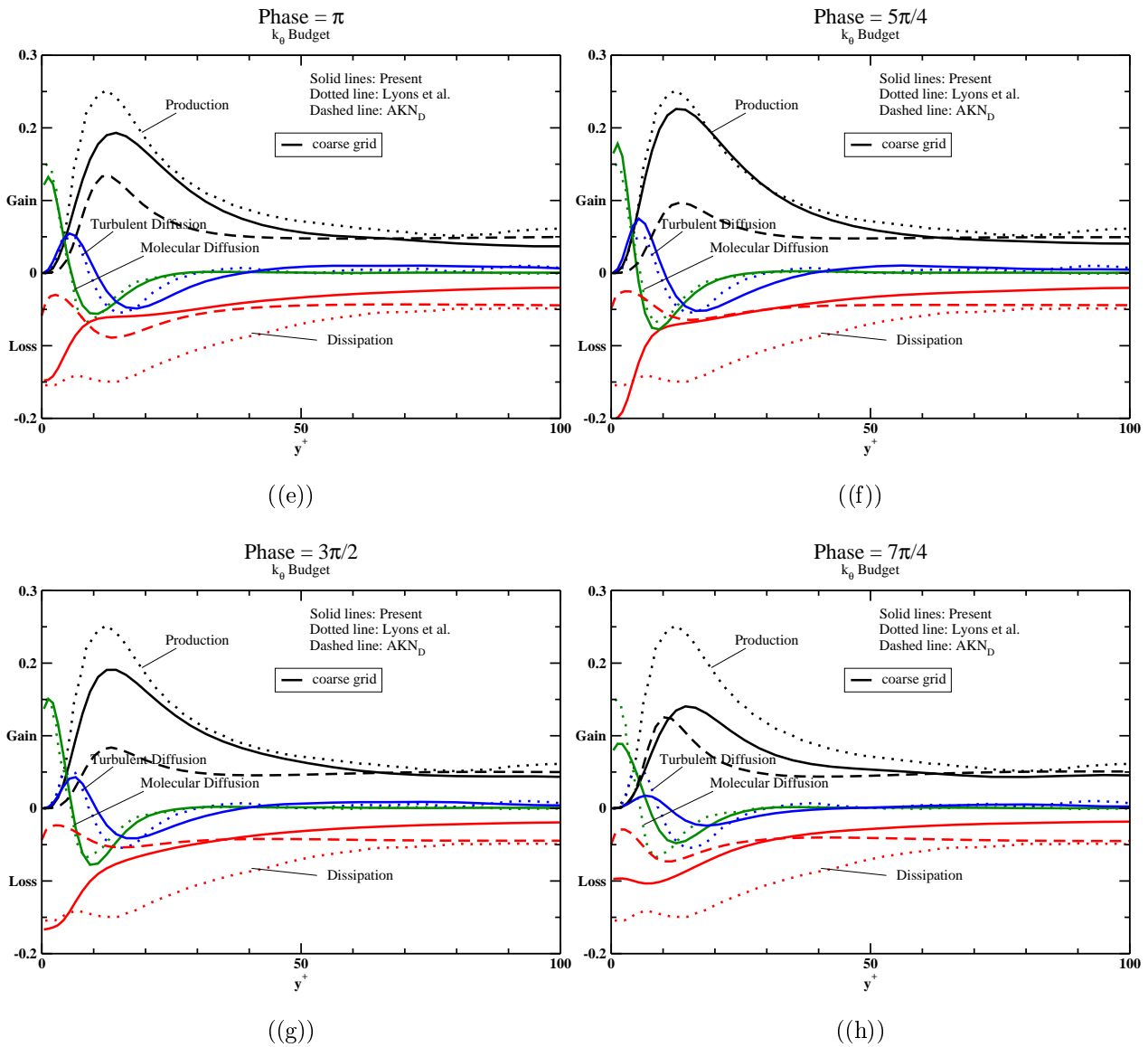


Figure 9.4.3: Budget of  $k_\theta$ ,  $AKN_D$  model results with pulsating flow ( $a_{uc} = 0.7, l_s^+ = 7$ ). Comparison with DNS on coarse grid and steady channel flow DNS data from [52] (continue)

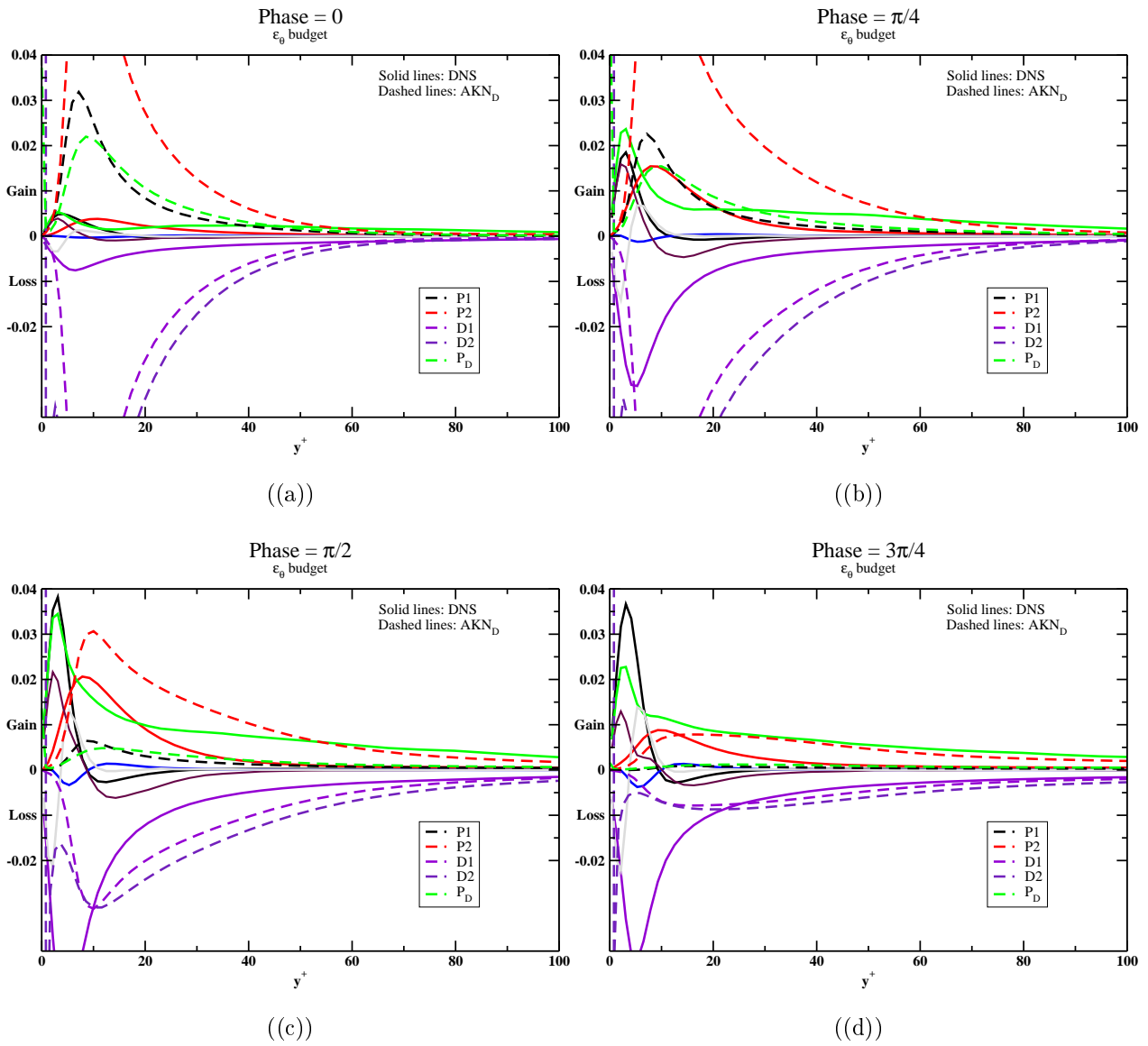


Figure 9.4.4: Budget of  $\epsilon_\theta$ ,  $AKN_D$  model results with pulsating flow ( $a_{uc} = 0.7, l_s^+ = 14$ ). Comparison with DNS on coarse grid

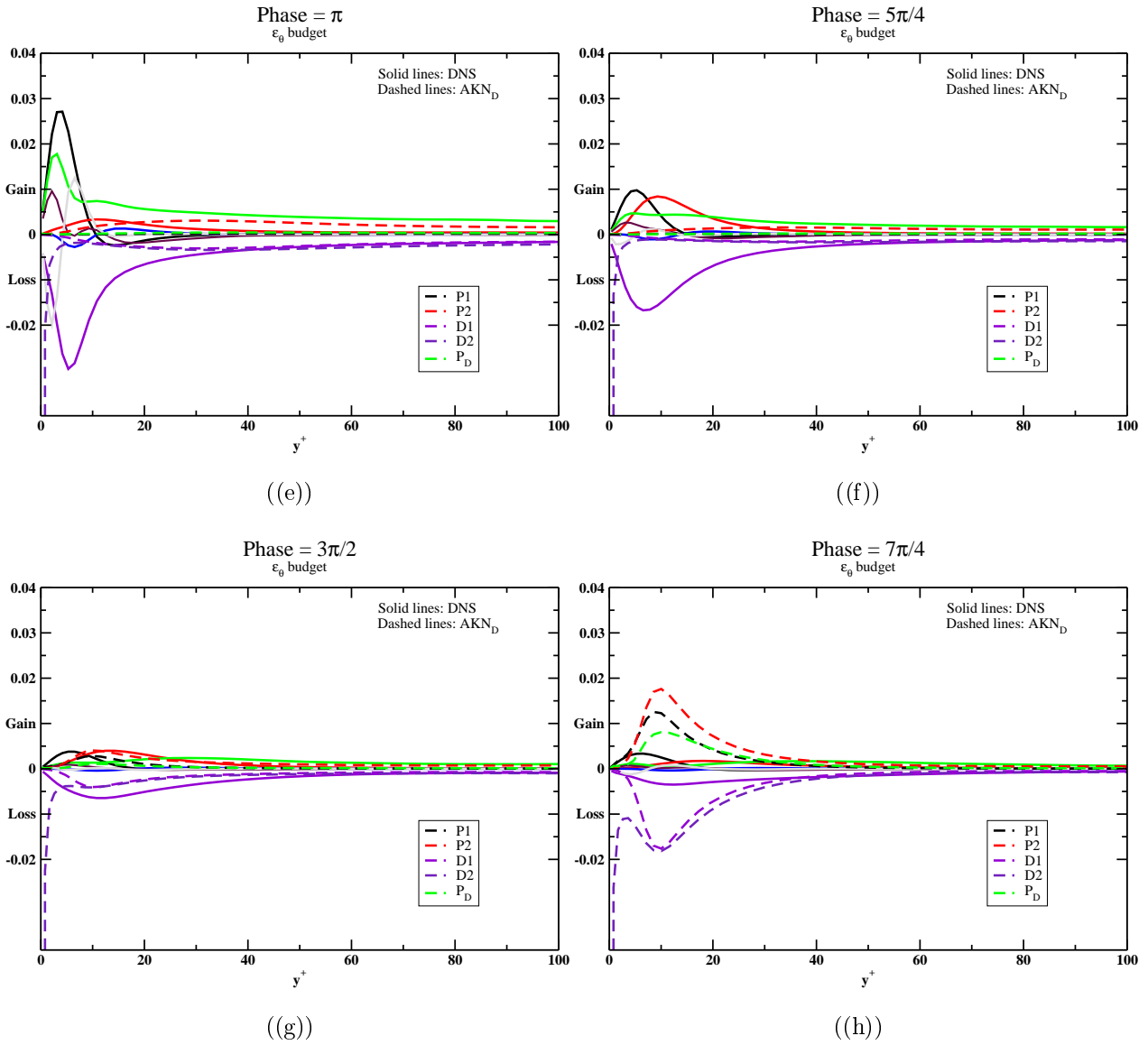


Figure 9.4.4: Budget of  $\epsilon_\theta$ ,  $AKN_D$  model results with pulsating flow ( $a_{uc} = 0.7, l_s^+ = 14$ ). Comparison with DNS on coarse grid (continue)

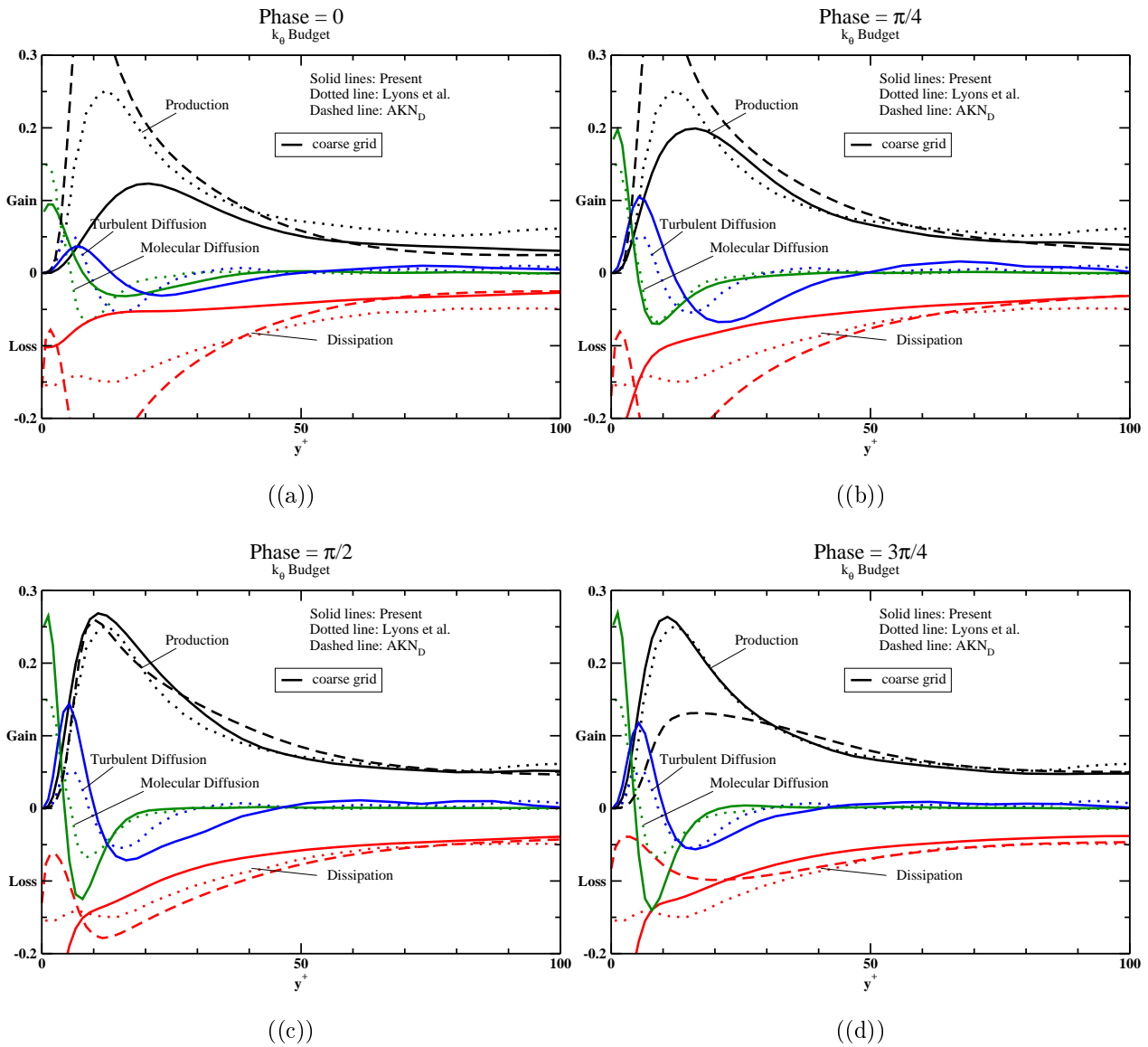


Figure 9.4.5: Budget of  $k_\theta$ ,  $AKN_D$  model results with pulsating flow ( $a_{uc} = 0.7, l_s^+ = 35$ ). Comparison with DNS on coarse grid and steady channel flow DNS data from [52]

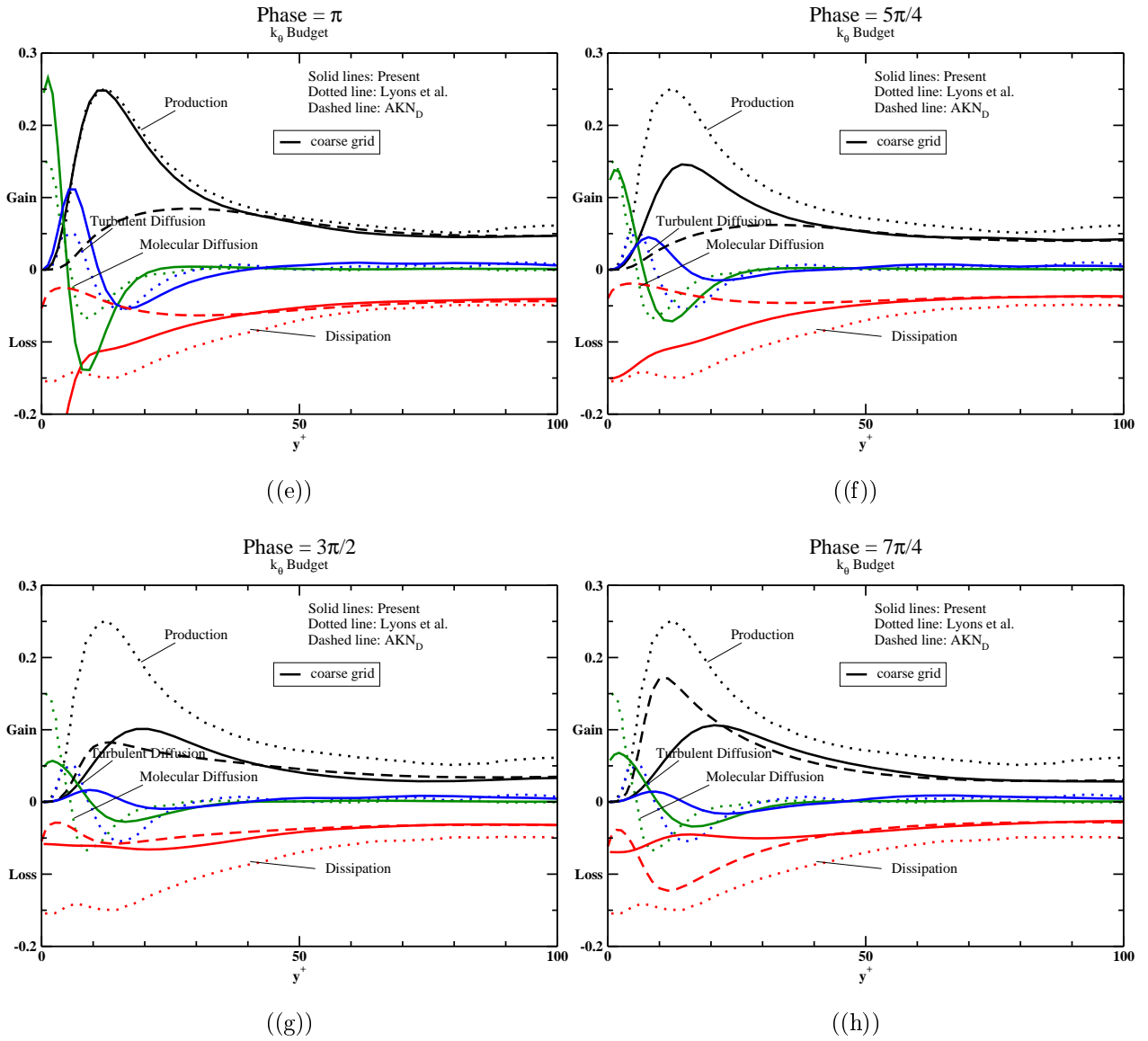


Figure 9.4.5: Budget of  $k_\theta$ , AKN<sub>D</sub> model results with pulsating flow ( $a_{uc} = 0.7, l_s^+ = 35$ ). Comparison with DNS on coarse grid and steady channel flow DNS data from [52] (continue)



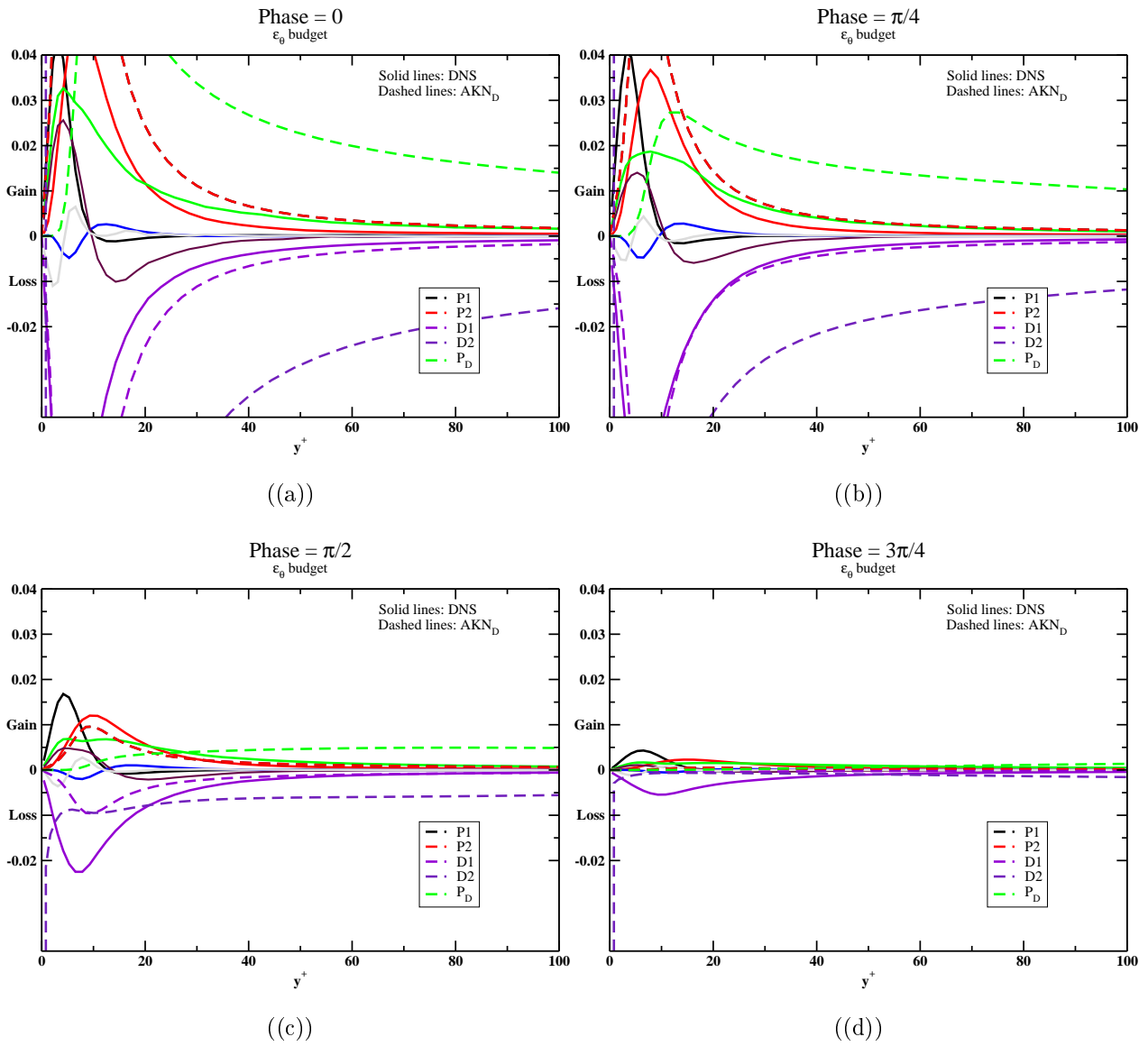


Figure 9.4.6: Budget of  $\epsilon_\theta$ ,  $AKN_D$  model results with pulsating flow ( $a_{uc} = 0.7, l_s^+ = 14$ ). Comparison with DNS on coarse grid

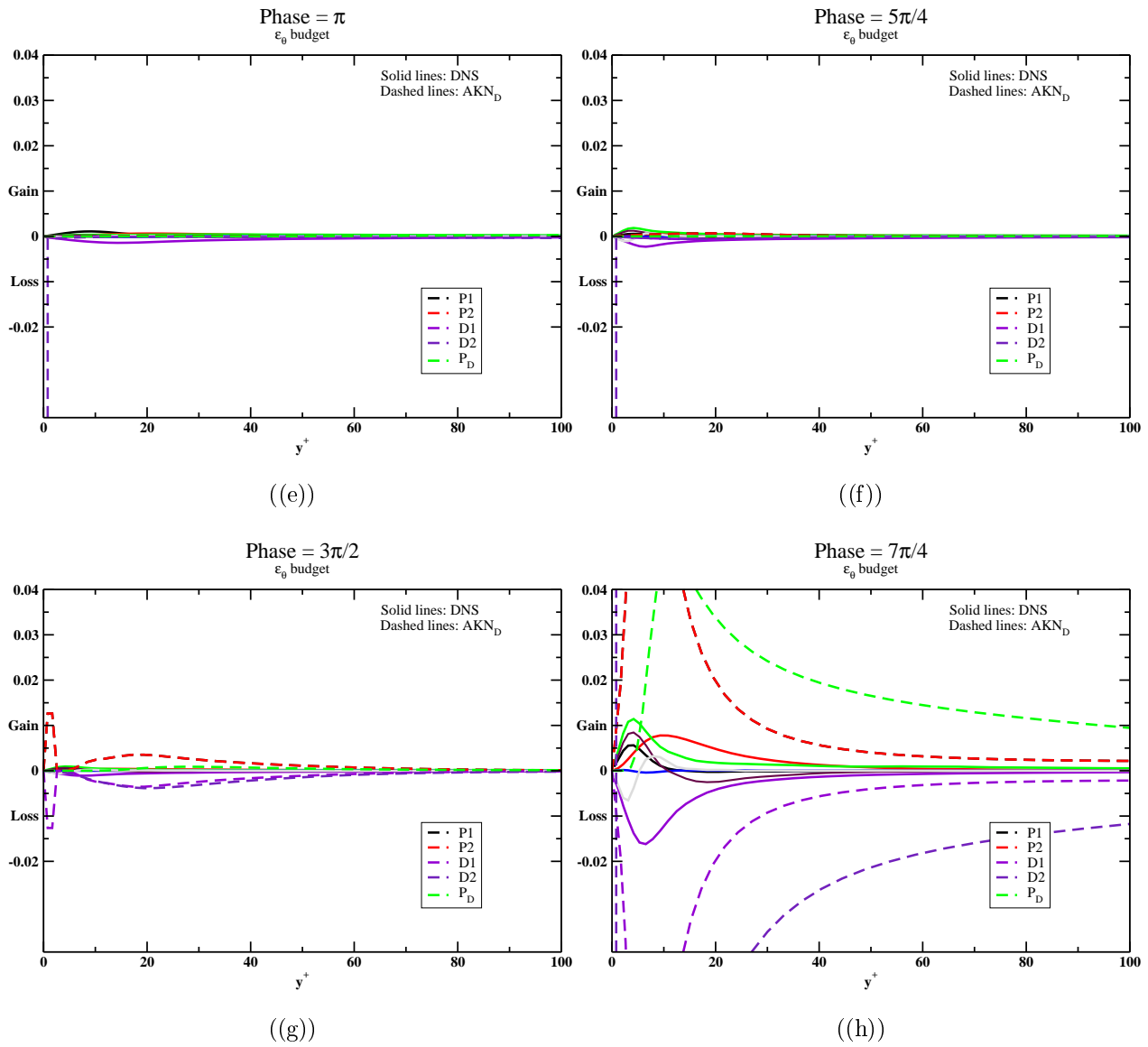


Figure 9.4.6: Budget of  $\epsilon_\theta$ , AKN<sub>D</sub> model results with pulsating flow ( $a_{uc} = 0.7, l_s^+ = 14$ ). Comparison with DNS on coarse grid (continue)

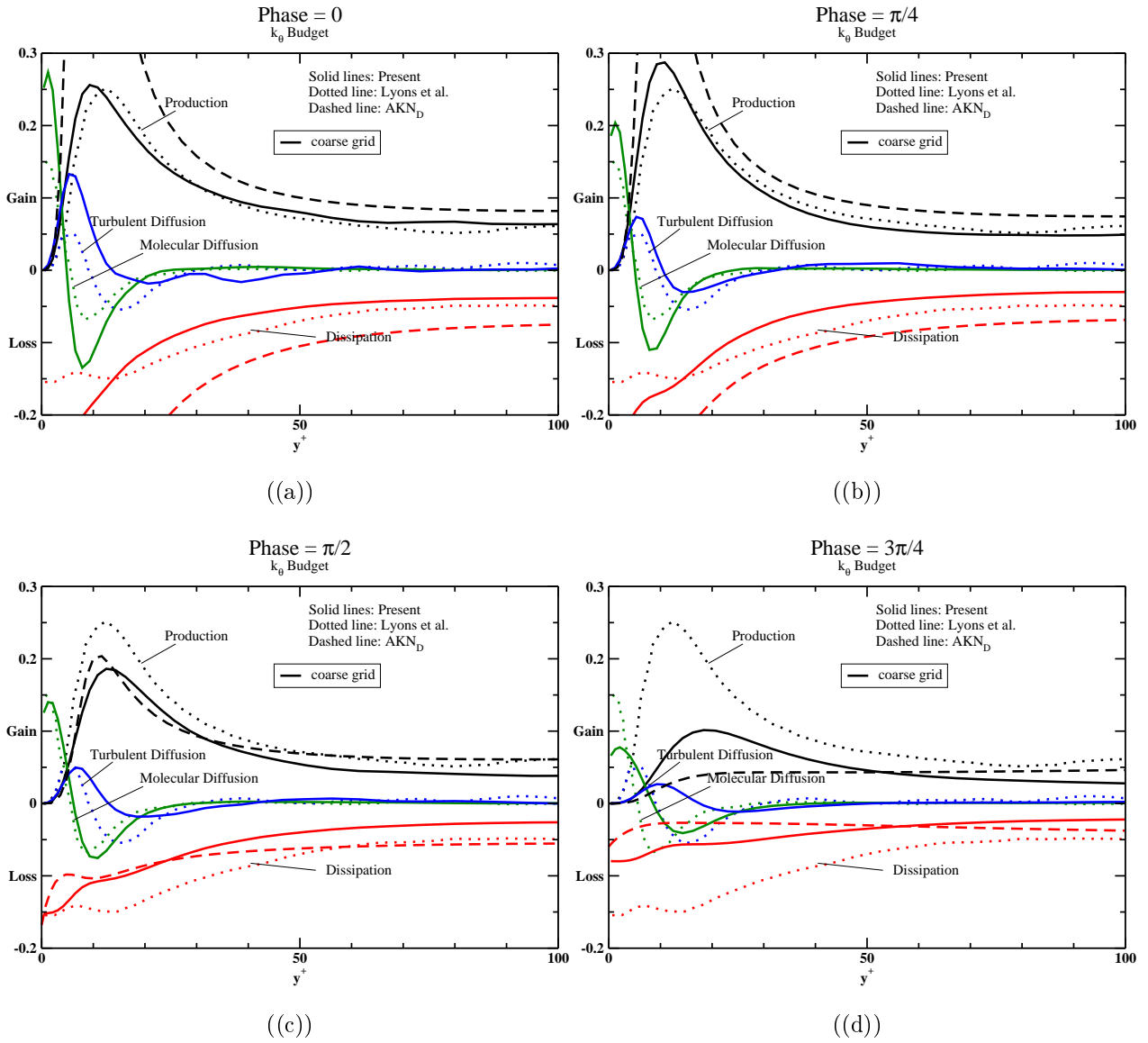


Figure 9.4.7: Budget of  $k_\theta$ ,  $AKN_D$  model results with pulsating flow ( $a_{uc} = 0.7, l_s^+ = 35$ ). Comparison with DNS on coarse grid and steady channel flow DNS data from [52]

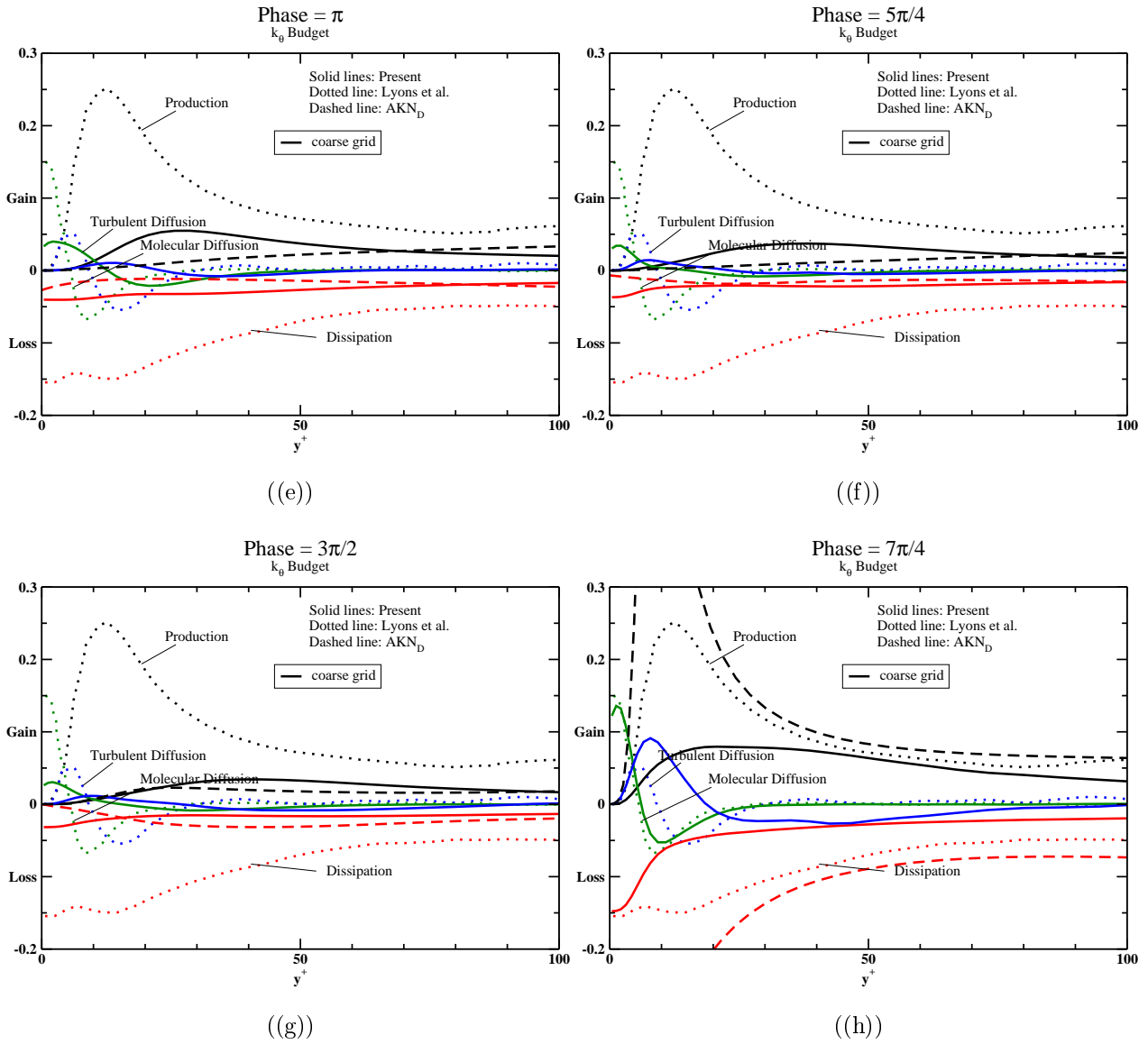


Figure 9.4.7: Budget of  $k_\theta$ , AKN<sub>D</sub> model results with pulsating flow ( $a_{uc} = 0.7, l_s^+ = 35$ ). Comparison with DNS on coarse grid and steady channel flow DNS data from [52](continue)

# 10 Conclusions

In the present work the numerical simulation of wall heat transfer in combustor flow and in the presence of thermo-acoustic instabilities has been treated.

In order to reveal the state of art of commercial numerical simulations in this field, the wall heat load in a model combustion chamber equipped with a full scale SIEMENS burner has been computed. These calculations involved the simulation of the turbulent mixing of fuel and air in the mixing passages, the modelling of combustion, turbulent convection, heat conduction in the solid walls and heat radiation. Computations for steady and unsteady conditions were performed showing significant differences in the overall predictions of the wall heat transfer. The unsteady computations were in a better agreement with the experimental measurements arising some interesting issues concerning accuracy and best CFD combustor design practice in presence of combustion instabilities.

Making use of simplified but well defined academic test cases, as well as DNS simulations, the following topics were in detail investigated:

#### **Steady-unsteady computations:**

In the field of industrial CFD combustor simulation, the use of highly costing unsteady simulations can be justified only when simple analytical models or steady computations cannot deliver results within the requested accuracy. In the present work the critical pulsating-flow non-dimensional parameters have been studied. Depending on the amplitude parameter  $a_{uc}$  and the frequency parameter  $l_s^+$  the critical pulsation regimes were found. Two amplitude (current dominated and wave dominated flow) and three pulsation regimes (quasi-steady, intermediate and quasi-laminar flow) were identified. The present work showed that flow unsteadiness can considerably affect the overall wall heat transfer especially if the pulsation amplitude is big compared with the mean flow velocity (wave dominated flow). In this cases when the pulsation frequency is low (quasi-steady flow) the overall heat transfer increase can be reasonably predicted by the steady-state theory. In all the other cases accurate unsteady simulations should be performed.

#### **Near wall turbulence modeling:**

When unsteady simulations are required, in order to save computational time and resources, the near wall grid resolution together with the choice of the turbulence model become critical. In both LES and URANS simulations the use of wall function can considerably save the computational costs due to the lower near wall grid resolution required. In the present work, the limitations of the wall function approach in pulsating flow applications have been studied. The present results have shown that in presence of flow reversal (wave dominated flow) the use of wall function can considerably underestimate the overall heat transfer both in URANS and LES applications. Better results are delivered by the low Reynolds turbulent models or, in the case of LES, by the use of dynamic SGS models or the WALE approach.

In the intermediate pulsation regime, comparisons have been presented with the experiments of Tardu et al. [79]. Both low Reynolds turbulence models and wall resolved LES simulations seem to be able to correctly predict the wall shear stress phase shift phenomena typical of this pulsation frequency range. Which was not the case for the wall function approach.

The capability of a turbulence model of correctly predict the wall shear stress is often used as a measure of the model capability to predict the wall heat transfer. However, due to the lack of experiments involving flow pulsations and wall heat transfer, this cannot be definitely proven. In the present work DNS simulations of a pulsating channel flow with fixed wall temperature difference were performed at different flow pulsations and amplitude. The acquired DNS database was used to study the effect of flow pulsation on the unsteady heat transfer. The DNS results indicated in the intermediate frequency range an imbalance between turbulence production and dissipation terms. Moreover the DNS results showed a different time response of temperature fluctuation to flow unsteadiness with respect to turbulence production and dissipation. The DNS data were used to develop and validate a turbulent heat transfer closure which satisfactorily predicts the wall heat transfer not only in pulsating but also in separating and reattaching flow regions. The turbulent model proposed was compared with the low Reynolds Launder and Sharma model as well as with the turbulent heat transfer model of Abe et al. showing a considerable improvement. In pulsating flow conditions the new model correctly predicts the mean value and the pulsation amplitude of the unsteady wall heat flux. Discrepancies are however observed in the phase shift prediction between wall heat transfer and centerline velocity. The present DNS database can be very useful for future unsteady heat transfer closure development and represents a highly valuable and unique work.

### **Boundary layer response vs. Thermo-acoustic combustion instabilities:**

Thermo-acoustic combustion instabilities are due to a complex feed back cycles which could involve the thermo-acoustic answer of the solid boundaries. In this case not only an accurate prediction of the mean value and amplitude of the wall heat load is required, but it is also important to quantify the relative phase shift between flame heat release and wall heat transfer. In the present work the classical low Reynolds turbulence models, the two equation turbulent heat transfer closure model of Abe et al. together with a new Abe et al. model modification were compared. None of the model were able to predict the Nusselt number phase shift and the complex imbalance phenomena between temperature fluctuation production and dissipation in presence of flow oscillations. Future work must be done in this direction. The present work however offers a very useful and unique DNS database for the development and validation of unsteady heat transfer turbulence closures.

Altogether it can be concluded that for the correct prediction of the combustion chamber heat load in presence of combustion instabilities many physical phenomena must be accurately

simulate. The turbulent mixing of fuel and air, the modelling of combustion, turbulent convection, heat conduction in the solid walls and heat radiation are only the main phenomena. The simulation of combustor models such as the ITS test-rig presented here represents a too complex task for the study of each detailed phenomena involved. On the contrary the present work, making use of simplified but well defined test cases and well aimed DNS simulations was able to address some of the most important issues related to the simulation of the unsteady wall heat load in combustion chamber applications.



# Appendix



# A - Tensor Notation in General Coordinates Systems

If we consider two different coordinate systems, for example:

- Cartesian:  $(\overline{Ox^1x^2x^3}$  or  $\overline{Oxyz}$ )
- Cylindrical polar:  $(\overline{Oy^1y^2y^3}$  or  $\overline{Or\phi x}$ )

it is always possible to express the coordinate transformation as follows:

$$y^1 = f_1(x^1, x^2, x^3) \quad (\text{A.0.1})$$

$$y^2 = f_2(x^1, x^2, x^3) \quad (\text{A.0.2})$$

$$y^3 = f_3(x^1, x^2, x^3) \quad (\text{A.0.3})$$

which in the specific case becomes,

$$r = \sqrt{x^2 + y^2} \quad (\text{A.0.4})$$

$$\phi = \text{arctg}\left(\frac{y}{x}\right) \quad (\text{A.0.5})$$

$$z = z \quad (\text{A.0.6})$$

The coordinate transformation is generally non linear but in the neighborhood of a point the transformation is fully characterized by the definition of the Jacobian matrix

$$\underline{J} = \frac{\partial y^i}{\partial x^j} \quad (\text{A.0.7})$$

Provided that the determinant of  $J$  exists and does not vanish, the coordinate transformation can be inverted and expressions can be derived for the transformations of tensor fields and their spatial and temporal derivatives from one coordinate system to the other. In particular two classes of vector transformation, the contravariant and covariant vector transformation can be defined as follows:

$$\bar{a}^i = \frac{\partial y^i}{\partial x^j} a^j \quad (\text{A.0.8})$$

$$\bar{a}_i = \frac{\partial x^j}{\partial y^i} a^j \quad (\text{A.0.9})$$

For the law of partial differentiation, it is easy to show that passing from one reference system to the other the coordinate components transform as a contravariant vector and the coordinate base vectors as covariant vectors.

Indicating with  $\vec{x} = (x^1, x^2, x^3)$  the coordinate base vectors are given from

$$\vec{g}_{(j)} = \frac{\partial \vec{x}}{\partial x^j} \quad (\text{A.0.10})$$

The Cartesian coordinate base vectors are in fact defined as follows:

$$\vec{x} = (1, 0, 0) = \left( \frac{\partial x}{\partial x}, \frac{\partial x}{\partial y}, \frac{\partial x}{\partial z} \right) \quad (\text{A.0.11})$$

$$\vec{y} = (0, 1, 0) = \left( \frac{\partial y}{\partial x}, \frac{\partial y}{\partial y}, \frac{\partial y}{\partial z} \right) \quad (\text{A.0.12})$$

$$\vec{z} = (0, 0, 1) = \left( \frac{\partial z}{\partial x}, \frac{\partial z}{\partial y}, \frac{\partial z}{\partial z} \right) \quad (\text{A.0.13})$$

Changing from Cartesian to the cylindrical reference system, the base vectors become

$$\vec{g}_{(k)} = \frac{\partial \vec{x}}{\partial y^k} = \frac{\partial x^j}{\partial y^k} \vec{g}_{(j)} \quad (\text{A.0.14})$$

or

$$\vec{r} = \left( \frac{\partial x}{\partial r}, \frac{\partial y}{\partial r}, \frac{\partial z}{\partial r} \right) = (\cos(\phi), \sin(\phi), 0) \quad (\text{A.0.15})$$

$$\vec{\phi} = \left( \frac{\partial x}{\partial \phi}, \frac{\partial y}{\partial \phi}, \frac{\partial z}{\partial \phi} \right) = (-r \sin(\phi), r \cos(\phi), 0) \quad (\text{A.0.16})$$

$$\vec{z} = \left( \frac{\partial x}{\partial z}, \frac{\partial y}{\partial z}, \frac{\partial z}{\partial z} \right) = (0, 0, 1) \quad (\text{A.0.17})$$

The inverse transformation is in fact

$$x = r \sin \phi \quad (\text{A.0.18})$$

$$y = r \cos \phi \quad (\text{A.0.19})$$

$$z = z \quad (\text{A.0.20})$$

and A.0.15 - A.0.17 come directly from differentiation of A.0.18 - A.0.20.

Any Cartesian vector can be expressed in terms of the base vectors as follows:

$$\vec{a} = a^1 \vec{g}_{(1)} + a^2 \vec{g}_{(2)} + a^3 \vec{g}_{(3)} \quad (\text{A.0.21})$$

In the new coordinate system using A.0.14

$$\vec{a} = \bar{a}^k \vec{g}_{(k)} = \bar{a}^k \frac{\partial x^j}{\partial y^k} \vec{g}_{(j)} = a^i \vec{g}_{(i)} \quad (\text{A.0.22})$$

and

$$a^i = \bar{a}^k \frac{\partial x^j}{\partial y^k} \quad (\text{A.0.23})$$

Comparing equations A.0.23 with the definitions in A.0.14 and A.0.8 of contravariant and covariant transformations it is clear that changing from one reference system to the other the

coordinate components transform as contravariant vectors and the coordinate base vectors as covariant.

The base vectors define the metric tensor as follows

$$g_{ij} = \vec{g}_{(i)} \cdot \vec{g}_{(j)} \quad (\text{A.0.24})$$

and from A.0.14

$$g_{ij} = \sum_{p=1}^3 \frac{\partial x^p}{\partial y^i} \frac{\partial x^p}{\partial y^j} \quad (\text{A.0.25})$$

A.0.24 for the cylindrical coordinate system becomes

$$g_{11} = g_{rr} = \vec{r} \cdot \vec{r} = 1 \quad (\text{A.0.26})$$

$$g_{22} = g_{\phi\phi} = \vec{\phi} \cdot \vec{\phi} = r^2 \quad (\text{A.0.27})$$

$$g_{33} = g_{zz} = \vec{z} \cdot \vec{z} = 1 \quad (\text{A.0.28})$$

$$g_{12} = g_{21} = g_{13} = g_{31} = g_{23} = g_{32} = 0 \quad (\text{A.0.29})$$

The partial derivative of a generic vector,  $\vec{a}$  is than given:

$$\vec{a} = a^i \vec{g}_{(i)}, \quad (\text{A.0.30})$$

$$\frac{\partial \vec{a}}{\partial y^k} = \frac{\partial a^i}{\partial y^k} \vec{g}_{(i)} + a^i \frac{\partial \vec{g}_{(i)}}{\partial y^k} \quad (\text{A.0.31})$$

Considering A.0.24, the partial derivative of  $\vec{g}_{(i)}$  in the last term of the above expression can be regarded as

$$\frac{\partial \vec{g}_{(i)}}{\partial y^k} = \frac{\partial \vec{g}_{(i)}}{\partial y^k} \cdot \vec{g}_{(i)} \cdot \vec{g}^{(j)} \quad (\text{A.0.32})$$

where  $\vec{g}^{(j)}$  is the  $j^{\text{th}}$  reciprocal base vector for which the following is valid:

$$\vec{g}^{(i)} \cdot \vec{g}_{(j)} = \delta_j^i \quad (\text{A.0.33})$$

It can be shown that the reciprocal base vectors transform as contravariant vectors. A generic vector can be expressed also in terms of the reciprocal base vectors:

$$\vec{a} = a_k \vec{g}^{(k)} = a^k \vec{g}_{(k)} \quad (\text{A.0.34})$$

and the following is also valid

$$\vec{a} \cdot \vec{g}_{(j)} = a_j = a^i \vec{g}_{(i)} \cdot \vec{g}_{(j)} = a^i g_{ij} \quad (\text{A.0.35})$$

It can be also shown that  $a_k$  transform as a covariant vector which explains the notation used. Covariant vectors and components are indicated with affixes in the upper position. Contravariant quantities are instead indicated with lower indices. The metric tensor transform the covariant components in contravariant and vice versa. If we indicate with  $g^{ij}$  the inverse of the metric matrix  $g_{ij}$  the following relations can be derived

$$a_j = a^i g_{ij} \quad (\text{A.0.36})$$

and

$$a^i = a_j g^{ij} \quad (\text{A.0.37})$$

Considering the derivative of the metric tensor

$$\frac{\partial g_{ij}}{\partial y^k} = \frac{\partial \vec{g}_{(i)}}{\partial y^k} \cdot \vec{g}_{(j)} + \vec{g}_{(i)} \frac{\partial \vec{g}_{(j)}}{\partial y^k} \quad (\text{A.0.38})$$

and its definition in A.0.25 the term  $\frac{\partial \vec{g}_{(i)}}{\partial y^k} \cdot \vec{g}_{(j)}$  can be expressed as

$$\frac{\partial \vec{g}_{(i)}}{\partial y^k} \cdot \vec{g}_{(j)} = \sum_{p=1}^3 \frac{\partial^2 x^p}{\partial y^i \partial y^k} \frac{\partial x^p}{\partial y^j} \quad (\text{A.0.39})$$

Considering the system of equations

$$\frac{\partial g_{ij}}{\partial y^k} = \sum_{p=1}^3 \frac{\partial^2 x^p}{\partial y^i \partial y^k} \frac{\partial x^p}{\partial y^j} + \sum_{p=1}^3 \frac{\partial x^p}{\partial y^i} \frac{\partial^2 x^p}{\partial y^j \partial y^k} \quad (\text{A.0.40})$$

$$\frac{\partial g_{ik}}{\partial y^j} = \sum_{p=1}^3 \frac{\partial^2 x^p}{\partial y^i \partial y^j} \frac{\partial x^p}{\partial y^k} + \sum_{p=1}^3 \frac{\partial x^p}{\partial y^i} \frac{\partial^2 x^p}{\partial y^j \partial y^k} \quad (\text{A.0.41})$$

$$\frac{\partial g_{jk}}{\partial y^i} = \sum_{p=1}^3 \frac{\partial^2 x^p}{\partial y^i \partial y^j} \frac{\partial x^p}{\partial y^k} + \sum_{p=1}^3 \frac{\partial x^p}{\partial y^j} \frac{\partial^2 x^p}{\partial y^i \partial y^k} \quad (\text{A.0.42})$$

A.0.39 can be reformulate in terms of  $g_{ij}$  derivatives as

$$\frac{\partial \vec{g}_{(i)}}{\partial y^k} \cdot \vec{g}_{(j)} = \sum_{p=1}^3 \frac{\partial^2 x^p}{\partial y^i \partial y^k} \frac{\partial x^p}{\partial y^j} = \frac{1}{2} \left( \frac{\partial g_{ij}}{\partial y^k} + \frac{\partial g_{ik}}{\partial y^j} - \frac{\partial g_{jk}}{\partial y^i} \right) = [ik, j] \quad (\text{A.0.43})$$

where  $[jk, i]$  is called the Christoffel symbol of first kind. Using the above expression, A.0.32 can be finally rewritten as

$$\frac{\partial \vec{g}_{(i)}}{\partial y^k} = \frac{\partial \vec{g}_{(i)}}{\partial y^k} \cdot \vec{g}_{(i)} \cdot \vec{g}^{(j)} = [ik, j] \vec{g}^{(j)} \quad (\text{A.0.44})$$

or using A.0.37

$$\frac{\partial \vec{g}_{(i)}}{\partial y^k} = \frac{\partial \vec{g}_{(i)}}{\partial y^k} \cdot \vec{g}_{(i)} \cdot \vec{g}^{(j)} = [ik, j] g^{jm} \vec{g}_{(m)} = \Gamma_{ik}^m \vec{g}_{(m)} \quad (\text{A.0.45})$$

where  $\Gamma_{ik}^m$  is called the Christoffel symbol of second kind. For a generic orthogonal coordinate system the metric tensor  $g_{ij}$  is a diagonal matrix ( $g_{ij} = h_i^2 \delta_i^j$ ) and the inverse is simply given by  $g^{ij} = 1/h_i^2$  and using A.0.43 and A.0.45 the Christoffel symbols become

$$[pq, r] = \begin{cases} 0 & p \neq q \neq r \\ h_i \frac{\partial h_i}{\partial y^j} & \text{when } \begin{cases} p = q = r \Rightarrow i = j = r \\ q = r \neq p \Rightarrow i = r, p = j \\ r = p \neq q \Rightarrow i = r, q = j \end{cases} \\ -h_i \frac{\partial h_i}{\partial y^j} & p = q \neq r \Rightarrow i = p, r = j \end{cases} \quad (\text{A.0.46})$$

$$\Gamma_{pq}^r = \begin{cases} 0 & p \neq q \neq r \\ \frac{1}{h_i} \frac{\partial h_i}{\partial y^j} & \text{when } \begin{cases} p = q = r \Rightarrow i = j = r \\ q = r \neq p \Rightarrow i = r, p = j \\ r = p \neq q \Rightarrow i = r, q = j \end{cases} \\ -\frac{h_i}{h_j^2} \frac{\partial h_i}{\partial y^j} & p = q \neq r \Rightarrow i = p, r = j \end{cases} \quad (\text{A.0.47})$$

In the case of the cylindrical coordinate the only nonvanishing symbols are  $\Gamma_{\phi\phi}^r = -r$  and  $\Gamma_{r\phi}^\phi = \Gamma_{\phi r}^\phi = 1/r$ .

Using A.0.45 if we consider the generic vector  $\vec{a}$  from A.0.34 the gradient of  $\vec{a}$ ,  $\nabla \vec{a}$  is a tensor of the form

$$\nabla \vec{a} = a^i_{,k} = \left[ \frac{\partial a^i}{\partial y^k} + \Gamma_{jk}^i a^j \right] \vec{g}_{(i)} \quad (\text{A.0.48})$$

The velocity vector in dimensional cylindrical coordinates is generally expressed as

$$\nabla \vec{u} = u_r \vec{r} + u_\phi \vec{\phi} + u_z \vec{z} \quad (\text{A.0.49})$$

where  $u_r$ ,  $u_\phi$  and  $u_z$  have the dimension of a velocity ( $[m, s^{-1}]$ ). In order to be consistent with A.0.18-A.0.18, where the distance are given using two linear and one angular dimensions, the velocity should be expressed as follows:

$$\vec{u} = h_i a^i \vec{e}_{(i)} = u_r \vec{r} + r \dot{\phi} \vec{\phi} + u_z \vec{z} \quad (\text{A.0.50})$$

where  $\dot{\phi}$  is an angular velocity,  $h_i$  the scale factors and  $\vec{e}_{(i)}$  are the coordinate versors. If we consider the gradient of the velocity vector in cylindrical coordinate is than given by A.0.48 as



$$\nabla \vec{u} = \begin{pmatrix} \frac{\partial u_r}{\partial r} & \left( \frac{\partial \dot{\phi}}{\partial r} + \frac{\dot{\phi}}{r} \right) r & \frac{\partial u_z}{\partial r} \\ \frac{\partial u_r}{\partial \phi} - r \dot{\phi} & \left( \frac{\partial \dot{\phi}}{\partial \phi} + \frac{u_r}{r} \right) r & \frac{\partial u_z}{\partial \phi} \\ \frac{\partial u_r}{\partial z} & \left( \frac{\partial \dot{\phi}}{\partial z} \right) r & \frac{\partial u_z}{\partial z} \end{pmatrix} \quad (\text{A.0.51})$$

It is important to notice that the matrix elements in this case have different dimensions depending on the metric used. The dimensioned velocity gradient (whose element have all the dimension of  $[s^{-1}]$ ) is than obtained as

$$\nabla \vec{u} = \begin{pmatrix} \frac{\partial u_r}{\partial r} & \left( \frac{\partial u_\phi/r}{\partial r} + \frac{u_\phi/r}{r} \right) r & \frac{\partial u_z}{\partial r} \\ \frac{1}{r} \left( \frac{\partial u_r}{\partial \phi} - u_\phi \right) & \frac{1}{r} \left( \frac{\partial u_\phi/r}{\partial \phi} + \frac{u_r}{r} \right) r & \frac{1}{r} \frac{\partial u_z}{\partial \phi} \\ \frac{\partial u_r}{\partial z} & \left( \frac{\partial u_\phi/r}{\partial z} \right) r & \frac{\partial u_z}{\partial z} \end{pmatrix} \quad (\text{A.0.52})$$

and in general, for an orthogonal coordinate system the following is valid

$$\nabla \vec{a} = a^i_{,k} = \frac{1}{h_k} \left[ \frac{\partial a^i}{\partial y^k} + \Gamma^i_{jk} a^j \right] \vec{g}^{(i)} \quad (\text{A.0.53})$$

$a^i_{,k}$  is infact a covariant vector and the physical component of a covariant vector  $A(i)$  are obtained from the covariant vector components dividing for the scale factors ( $A(i) = A_i/h_i$ ).



# Bibliography

- [1] *Ansys cfx-solver, release 10.0:theory, discrete transfer model*, <http://www.ansys.com>, p. 236.
- [2] *Ansys cfx-solver, release 10.0:theory, eddy dissipation model*, <http://www.ansys.com>.
- [3] *Ansys cfx-solver, release 10.0:theory, spectral models*, <http://www.ansys.com>, p. 237.
- [4] *The avbp code, user guide*, [http://www.cerfacs.fr/cfd/avbp\\_code.php](http://www.cerfacs.fr/cfd/avbp_code.php).
- [5] *DESIRE : Design and demonstration of highly reliable low NO<sub>x</sub> combustion systems for gas turbines*, Contract No NNE5/388/2001. Start June 2002.
- [6] *The open source cfd toolbox, user guide*, <http://www.opencfd.co.uk/openfoam/index.html>.
- [7] *Measurement of the heat transfer at combustor walls, Siemens V64.3A-burner*, 2002, University of Karlsruhe Internal Report.
- [8] *K.-U. Schildmacher, private communication at Siemens Mülheim*, December 2007.
- [9] K. Abe, T. Kondoh, and Y. Nagano, *A new turbulence model for predicting fluid flow and heat transfer in separating and reattaching flows - i. flow field calculations*, International Journal of Heat and Mass Transfer **37** (1994), no. 8, 139–151.
- [10] ———, *A new turbulence model for predicting fluid flow and heat transfer in separating and reattaching flows - ii. thermal field calculations*, International Journal of Heat and Mass Transfer **38** (1995), no. 8, 1467–1481.
- [11] E. W. Adams, J. P. Johnston, and J. K. Eaton, *Experiments on the structure of turbulent reattaching flow*, Tech. Report MD-43, Stanford University, May 1984.
- [12] M. A. Al-Nimr and M. A. Hader, *Transient conjugated heat transfer in developing laminar pipe flow*, Journal of Heat Transfer **116** (1994), 234–337.
- [13] V. S. Arpaci, J. E. Dec, and J. O. Keller, *Heat transfer in pulse combustion tailpipes*, Combustion Science and Technology **94** (1993), 131–146.
- [14] P. Bradshaw, D. Ferris, and N. Atwell, *Calculation of boundary layer development using the turbulent energy equation*, Journal of Fluid Mechanics **28** (1967), no. 3, 593–616.

- [15] H. S. Carslaw and J. C. Jaeger, *Conduction of heat in solids*, University Press, 1959.
- [16] A. Chatelain, F. Ducros, and O. Metais, *LES of turbulent heat transfer: proper convection numerical schemes for temperature transport*, International Journal for Numerical Methods in Fluids **44** (2004), 1017–1044.
- [17] F. H. Clauser, *The turbulent boundary layer*, Adv. in Appl. Mech. **4** (1956), 1–51.
- [18] D. E. Coles, *The law of the wake in the turbulent boundary layer*, Journal of Fluid Mechanics **1** (1956), 191–226.
- [19] S. Corrsin, Journal of Applied Physics **23** (1952), 113.
- [20] J. Cousteix and R. Houdeville, *Effects of unsteadiness on turbulent boundary layers*, VKI Lecture Series 1983-03, vol. 43, Von Karman Institute for Fluid Dynamics, 1983.
- [21] R. Dannecker, B. Noll, M. Aigner, K.-U. Schildmacher, M. Hase, W. Krebs, and R. Koch, *Impact of radiation on the wall heat load at a test bench gas turbine combustion chamber: Measurements and cfd simulation*, Proceedings of GT2007 ASME Turbo Expo 2007: Power for Land, Sea and Air, May 2007.
- [22] J. E. Dec and J. O. Keller, *Time-resolved gas temperature in the oscillating turbulent flow of a pulse combustor tail pipe*, Combustion and Flame **80** (1990), 358–370.
- [23] J. E. Dec, J. O. Keller, and V. S. Arpaci, *Heat transfer enhancement in the oscillating turbulent flow of a pulse combustor tail pipe*, Int. J. Heat Mass Transfer **35** (1992), no. 9, 2311–2325.
- [24] J. E. Dec, J. O. Keller, and I. Hongo, *Time-resolved velocities and turbulence in the oscillating flow of a turbulent flow of a pulse combustor tail pipe*, Combustion and Flame **83** (1991), 271–292.
- [25] E. Divo, E. Steinhorsson, F. Rodriguez, A. J. Kassab, and J. S. Kapat, *Glenn-ht/bem conjugate heat transfer solver for large-scale turbomachinery models*, Tech. Report NASA/CR-2003-212195, NASA Glenn Research Center, April 2003.
- [26] F. Ducros, F. Nicoud, and T. Poinso, *Wall-adapting local eddy-viscosity models for simulations in complex geometries.*, ICFD (1998), 293–300.
- [27] P. A. Durbin and B. A. Petterson-Reif, *Statistical theory and modeling for turbulent flows*, John Wiley and Sons, 2001.
- [28] M. Fallen, *Waermeuebergang im Rohr mit ueberlagerter Stroemungspulsation*, Waerme- und Stoffuebertragung **16** (1993), 89–99.
- [29] S. Fan and B. Lakshminarayana, *Low-reynolds-number  $k - \epsilon$  model for unsteady turbulent boundary-layer flows*, AIAA Journal **31** (1993), no. 10, 1777–1784.

- [30] C. Fureby and F. F. Grinstein, *Large eddy simulation of high-reynolds-number free and wall-bounded flows*, Journal of Computational Physics **181** (2002), 68–97.
- [31] C. Fureby, G. Tabor, H. G. Weller, and A. D. Gosman, *A comparative study of subgrid scale models in homogeneous isotropic turbulence*, Physics of Fluids **9** (1997), no. 5, 1416–1428.
- [32] L. G. Genin, A. P. Koval, S. P. Manchkha, and V. G. Sviridov, *Hydrodynamics and heat transfer with pulsating fluid flow in tubes*, Thermal Engineering **39** (1992), no. 5, 30–34.
- [33] M. Y. Gündogdu and M. Ö. Carpinlioglu, *Present state of art on pulsatile flow theory*, JSME int. Journal **42** (1999), no. 3, 389–410.
- [34] R. Hatami, *Pulsating flow in heat exchanger*, Waerme- und Stoffuebertragung **14** (1980), 109–118.
- [35] M. Hino, M. Kashiwayanagi, A. Nakayama, and T. Hara, *Experiments on the turbulence statistics and the structure of a reciprocating oscillatory flow*, Journal of Fluid Mechanics **131** (1983), no. 63, 363–400.
- [36] C. Hirsch, *Numerical computation of internal and external flows*, John Wiley and Sons, 2001.
- [37] H. Schlichting and K. Gersten, *Boundary layer theory*, Springer, 1999.
- [38] Y. Ishino, M. Suzuki, T. Abe, N. Ohiwa, and S. Yamaguchi, *Flow and heat transfer characteristics in pulsating pipe flows (effects of pulsation on internal heat transfer in a circular pipe flow)*, Heat Transfer-Japanese Research **25** (1996), no. 5, 323–341.
- [39] R. I. Issa, *Solution of the implicitly discretised fluid flow equations by operator-splitting*, Journal of Computational physics **62** (1985), 40–65.
- [40] E. Ivanova, B. Noll, M. Di Domenico, and M. Aigner, *Improvement and assessment of rans scalar transport models for jets in crossflow*, 46th Aerospace Sciences Meeting and Exhibit, American Institute of Aeronautics and Astronautics, January 2008.
- [41] N. Kasagi, A. Kuroda, and M. Hirata, *Numerical investigation of near-wall turbulent heat transfer taking into account the unsteady heat conduction in the solid walls*, ASME Journal of Heat Transfer **111** (1989), 385–392.
- [42] N. Kasagi, Y. Tomita, and A. Kuroda, *Direct numerical simulation of passive scalar field in a turbulent channel flow*, Journal of Heat Transfer **114** (1992), 598–606.
- [43] H. Kawamura, H. Abe, and K. Shingai, *DNS of turbulence and heat transport in a channel flow with different Reynolds and Prandtl numbers and boundary conditions*, 3rd International Symposium on Turbulence, Heat and Mass Transfer.

- [44] W. M. Kays, *Turbulent Prandtl number - where are we?*, Journal of Heat Transfer **116** (1992), 284–294.
- [45] R. H. Keil and M. H. I. Baird, *Enhancement of heat transfer by flow pulsation*, Ind. Chem. Process Des. Develop. **10** (1971), no. 4, 473–478.
- [46] W. Krebs, *Technical combustion systems: Combustion dynamics and control*, Clean Combustors for Industrial Gas Turbines, VKI 2004-03, von Karman Institute for Fluid Dynamics, February 2004.
- [47] L. V. Krishnamoorthy and R. A. Antonia, *Temperature-dissipation measurements in a turbulent boundary layer*, Journal of Fluid Mechanics **176** (1987), 265–281.
- [48] B. E. Launder, *Heat and mass transport*, second ed., Topics in Applied Physics, vol. 12, Springer, 1976.
- [49] B. E. Launder and B. I. Sharma, *Application of the energy dissipation model of turbulence to the calculation of flow near a spinning disc.*, Letters in Heat and Mass Transfer **1** (1974), 131–138.
- [50] R. Lemlich, *Vibration and pulsation boost heat transfer*, Chemical Engineering **15** (1961), 171–176.
- [51] C. R. Lodahl, B. M. Sumer, and J. Fredsoe, *Turbulent combined oscillatory flow and current in a pipe*, Journal of Fluid Mechanics **373** (1998), 313–348.
- [52] S. L. Lyons, T. J. Hanratty, and J. B. McLaughlin, *Direct numerical simulation of passive heat transfer in a turbulent channel flow*, International Journal of Heat and Mass Transfer **34** (1991), no. 4/5, 1149–1161.
- [53] F. R. Menter, *Two-equation eddy-viscosity turbulence models for engineering applications*, AIAA Journal **32** (1994), no. 8, 1598–1605.
- [54] M. F. Modest, *Radiative heat transfer*, Elsevier science, USA, 2003.
- [55] Y. Nagano and C. Kim, *A two-equation model for heat transport in wall turbulent shear flows*, Journal of Heat Transfer **110** (1988), 583–589.
- [56] J. Nikuradse, *Stoemungsgesetze in rauhen Rohren*, Forsch. Arb. Ing.-Wes. (1933), no. 361.
- [57] M. N. Ozisik, *Heat conduction*, Wiley-Interscience, New York, 1980.
- [58] F. Page, W. H. Corcoran, W. G. Schlinger, and B. H. Sage, *Temperature and velocity distributions in uniform flow between parallel plates*, Industrial and Engineering Chemistry **44** (1952), no. 2, 419–423.

- [59] D. Panara, *Tascflow and finflo: a comparison between two different Navier-Stokes CFD codes in strong curvature applications*, M.sc., University of Florence, 2003.
- [60] D. Panara, R. Dannecker, and B. Noll, *Transient combustion and near-wall aero-thermal investigation for low emission and high efficient combustion energy systems*, Proc. of the 14th Sustainable Energy 'Marie Curie' Research Training Fellowships Conference under fp6, Commission of the European Communities, DG XII, Directorate-General for Research, October 2004.
- [61] D. Panara, M. Hase, W. Krebs, and B. Noll, *Numerical simulation of wall heat load in combustor flow*, AIP Conference Proceedings, ICNAAM, International Conference on Numerical Analysis and Applied Mathematics, 2007, pp. 659 – 662.
- [62] D. Panara and B. Noll, *A coupled solver for the solution of the unsteady conjugate heat transfer problem*, Computational Methods for Coupled Problems in Science and Engineering 2, Coupled Problems 2007 (Eccomas Thematic Conference) (M. Papadrakakis E. Onate and B. Schrefler, eds.), ECCOMAS, 2007.
- [63] D. Panara, M. Porta, R. Dannecker, and B. Noll, *Wall functions and boundary layer response to pulsating and oscillating turbulent channel flows.*, Proceedings of the 5th International Symposium on Turbulence, Heat and Mass Transfer THMT06, 5th International Symposium on Turbulence, Heat and Mass transfer, September 2006.
- [64] D. Panara, M. Porta, and T. Schoenfeld, *LES and URANS unsteady boundary layer strategies for pulsating and oscillating turbulent channel flow applications*, European Conference on Computational Fluid Dynamics ECCOMAS CFD 2006, September 2006.
- [65] V. C. Patel, W. Rodi, and G. Scheuerer, *Turbulence models for near-wall and low Reynolds number flows: A review*, AIAA Journal **23** (1985), no. 9, 1308–1319.
- [66] S. B. Pope, *Turbulent flows*, Cambridge University Press, 2000.
- [67] L. Prandtl, *Ueber die ausgebildete Turbulenz*, Z. Angew. Math. Mech. **5** (1925), 136–139.
- [68] O. Reynolds, *On the dynamical theory of incompressible viscous flows and the determination of the criterion*, Philos. Trans. R. Soc. London Ser. A **174**, 123–161.
- [69] P. Ryzhakov, M. Porta, R. Rossi, and T. Shoenfeld, *On the FSI in combustion chambers*, ECCOMAS Coupled Problems, 2007.
- [70] K.-U. Schildmacher, R. Koch, S. Wittig, W. Krebs, and S. Hoffmann, *Experimental investigations of unsteady flow phenomena in high intents combustion systems*, Proceedings of the 6th European Conference on Industrial Furnaces and Boilers, 2002.

- [71] P. Schmitt, *Simulation aux grandes échelles de la combustion étagée dans les turbines à gaz et son interaction stabilité - polluants-thermique - th/cfd/05/45.*, Ph.D. thesis, Institut National Polytechnique de Toulouse, 2005.
- [72] A. Scotti and U. Piomelli, *Numerical simulation of pulsating turbulent channel flow*, *Physics of Fluids* **13** (2001), no. 5, 1367–1384.
- [73] J. G. Simmonds, *A brief on tensor analysis*, second ed., Springer, 1994.
- [74] J. Smagorinsky, *General circulation experiments with the primitive equations, i. the basic experiment*, *Monthly Weather Review* **91** (1963), no. 3, 99–164.
- [75] R. M. C. So and C. G. Speziale, *A review of turbulent heat transfer modeling*, vol. 10, Begell House, Inc., 1999.
- [76] P. R. Spalart and B.S. Baldwin, *Direct simulation of a turbulent oscillating boundary layer*, *Turbulent shear Flows*, vol. 6, Springer-Verlag, 1989.
- [77] D. B. Spalding, *A single formula for the law of the wall*, *Journal of Fluid Mechanics* **28** (1961), 455–457.
- [78] J. Sucec and A. M. Sawant, *Unsteady, conjugated, forced convection heat transfer in a parallel plate duct*, *Int. J. Heat Mass Transfer.* **27** (1984), no. 1, 95–101.
- [79] S. F. Tardu, G. Binder, and R. F. Blackwelder, *Turbulent channel flow with large-amplitude velocity oscillations*, *Journal of Fluid Mechanics* (1994), no. 267, 109–151.
- [80] P. S. Tromans, *Stability and transition of periodic pipe flows*, Ph.D. thesis, Cambridge University, 1978.
- [81] J. C. Vogel and J. K. Eaton, *Combined heat transfer and fluid dynamic measurements downstream of a backward-facing step*, *Journal of Heat Transfer* **107** (1985), 922–929.
- [82] T. von Karman, *Mechanical similitude and turbulence*, NASA Technical Memorandums (1931), no. 611, Reprint from *Nachrichten von der Gesellschaft der Wissenschaften zu Goettingen*, 1930.
- [83] H.G. Weller, G. Tabor, H. Jasak, and C. Fureby, *A tensorial approach to computational continuum mechanics using object orientated techniques*, *Computers in Physics* **12** (1998), no. 6, 620 – 631.
- [84] F. B. West and A. T. Taylor, *The effect of pulsations on heat transfer*, *Chemical Engineering Progress* **48** (1952), no. 1, 39–43.
- [85] F. M. White, *Viscous fluid flow*, McGraw-Hill, 1991.



- 
- [86] D. C. Wilcox, *Reassessment of the scale-determining equation for advanced turbulence models*, AIAA Journal **26** (1988), no. 11, 1299–1310.
- [87] D. C. Wilcox and M. W. Rubesin, *Progress in turbulence modeling for complex flow fields including effects of compressibility*, Tech. Report TP-1517, NASA, April 1980.
- [88] W. Kays, M. Crawford, and B. Weigand, *Convective heat and mass transfer*, McGraw and Hill, 2005.



# Lebenslauf

## Persönliche Daten

Name	Daniele Panara
Geburtsdatum	19.10.1976
Geburtsort	Guardiagrele (Italien)
Staatsangehörigkeit	Italienisch

## Schulbildung

1982-1987	Scuola elementare "Sant' Andrea", Chieti
1987-1990	Scuola media "G. Chiarini", Chieti
1990-1995	Liceo Scientifico "F. Masci", Chieti

## Studium

1995-2003	Università degli Studi di Firenze, Facoltà di Ingegneria Meccanica, Florenz
Januar 2003	Laurea in Ingegneria Meccanica
2003-2004	Von Karman Institute for Fluid Dynamics, Bruxelles

## Berufliche Tätigkeit

Januar 2003 - April 2003	Entwicklung und Optimierung eines Strömungscodes am "Thermodynamic Laboratory", TKK-Helsinki University of Technology, Helsinki
Juni 2003 - September 2003	Quality Engineer, Nuovo Pignone GE Oil & Gas, Florenz
September 2004 - September 2007	Marie Curie Research Training Network, Fluid Structure interaction for Combustion Systems (FLUISTCOM project : MRTN-CT-2003-504183), DLR-Institute für Verbrennungstechnik, Stuttgart
September 2007 - Juli 2008	Wissenschaftlicher Mitarbeiter, DLR-Institute für Verbrennungstechnik, Stuttgart
Seit Juli 2008	Centrifugal and Axial Compressor Lead Engineer, Nuovo Pignone GE Oil & Gas, Florenz







Herausgeber

Deutsches Zentrum  
für Luft- und Raumfahrt e.V.

Institut für  
Verbrennungstechnik

Pfaffenwaldring 38-40  
70569 Stuttgart

Telefon  
Telefax

(0 7 11) 68 62 - 3 08  
(0 7 11) 68 62 - 5 78

Als Manuskript gedruckt.  
Abdruck oder sonstige Verwendung  
nur nach Absprache mit dem Institut gestattet

D93, Stuttgart